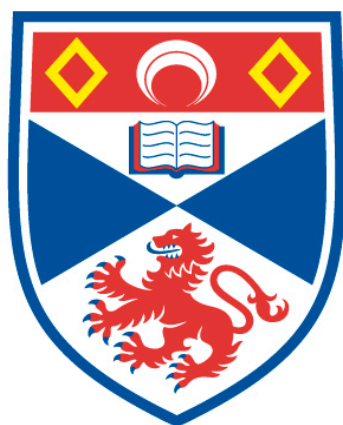# New thermally activated delayed fluorescence emitters and room-temperature organic long-persistent luminescence

Wenbo Li

A thesis submitted for the degree of PhD
at the
University of St Andrews

2021

Full metadata for this item is available in
St Andrews Research Repository
at:
http://research-repository.st-andrews.ac.uk/

Identifier to use to cite or link to this thesis:

DOI: https://doi.org/10.17630/sta/99

Candidate's declaration

I, Wenbo Li, do hereby certify that this thesis, submitted for the degree of PhD, which is approximately 49,000 words in length, has been written by me, and that it is the record of work carried out by me, or principally by myself in collaboration with others as acknowledged, and that it has not been submitted in any previous application for any degree.

I was admitted as a research student at the University of St Andrews in September 2016.

I, Wenbo Li, received assistance in the writing of this thesis in respect of language and grammar, which was provided by Peter Brown.

I received funding from an organisation or institution and have acknowledged the funder(s) in the full text of my thesis.

Date   16.11.2020   Signature of candidate

Supervisor's declaration

I hereby certify that the candidate has fulfilled the conditions of the Resolution and Regulations appropriate for the degree of PhD in the University of St Andrews and that the candidate is qualified to submit this thesis in application for that degree.

Date   16.11.2020   Signature of supervisor

Permission for publication

In submitting this thesis to the University of St Andrews we understand that we are giving permission for it to be made available for use in accordance with the regulations of the University Library for the time being in force, subject to any copyright vested in the work not being affected thereby. We also understand, unless exempt by an award of an embargo as requested below, that the title and the abstract will be published, and that a copy of the work may be made and supplied to any bona fide library or research worker, that this thesis will be electronically accessible for personal or research use and that the library has the right to

migrate this thesis into new electronic forms as required to ensure continued access to the thesis.

I, Wenbo Li, have obtained, or am in the process of obtaining, third-party copyright permissions that are required or have requested the appropriate embargo below.

The following is an agreed request by candidate and supervisor regarding the publication of this thesis:

Printed copy

No embargo on print copy.

Electronic copy

Embargo on all of electronic copy for a period of 2 years on the following ground(s):

- Publication would preclude future publication

Supporting statement for electronic embargo request

Some data will be published later.

Title and Abstract

- I agree to the title and abstract being published.

Date   16.11.2020   Signature of candidate

Date   16.11.2020   Signature of supervisor

Underpinning Research Data or Digital Outputs

Candidate's declaration

I, Wenbo Li, understand that by declaring that I have original research data or digital outputs, I should make every effort in meeting the University's and research funders' requirements on the deposit and sharing of research data or research digital outputs.

Date   16.11.2020   Signature of candidate

Permission for publication of underpinning research data or digital outputs

We understand that for any original research data or digital outputs which are deposited, we are giving permission for them to be made available for use in accordance with the requirements of the University and research funders, for the time being in force.

We also understand that the title and the description will be published, and that the underpinning research data or digital outputs will be electronically accessible for use in accordance with the license specified at the point of deposit, unless exempt by award of an embargo as requested below.

The following is an agreed request by candidate and supervisor regarding the publication of underpinning research data or digital outputs:

Embargo on all of electronic files for a period of 2 years on the following ground(s):

- Publication would preclude future publication

Supporting statement for embargo request

Some data will be published later

Title and Description

- I require an embargo on the title and description

Date   16.11.2020   Signature of candidate

Date   16.11.2020   Signature of supervisor

Acknowledgements

Funding

Research Data/Digital Outputs access statement

Digital outputs underpinning this thesis are available at https://doi.org/10.17630/24c82e40-099d-4bbd-9a3d-6f76a1c7593c

List of Published Papers

2020

1) **Li W**, Li Z, Si C, Wong MY, Jinnai K, Gupta AK, Kabe R, Adachi C, Huang W, Zysman‑Colman E, Samuel ID. Organic Long‑Persistent Luminescence from a Thermally Activated Delayed Fluorescence Compound. **Advanced Materials**. 2020, 32, 2003911.

2) Li C, **Li W**, Henwood AF, Hall D, Dordes DB, Slawin AM, Lemaur V, Oliver Y, Samuel ID, Zysman-Colman E. Luminescent Dinuclear Copper(I) Complexes Bearing an Imidazolylpyrimidine Bridging Ligand. **Inorganic Chemistry**. 2020, 59, 20, 14772–14784.

2019

3) Li Z, **Li W**, Keum CM, Archer E, Zhao B, Slawin AM, Huang W, Gather MC, Samuel ID, Zysman-Colman E. 1, 3, 4-Oxadiazole-Based Deep-Blue Thermally Activated Delayed Fluorescence Emitters for Organic Light Emitting Diodes. **The Journal of Physical Chemistry C**. 2019, 123, 40, 24772–24785.

4) Rajamalli P, Chen D, **Li W**, Samuel ID, Cordes DB, Slawin AM, Zysman-Colman E. Enhanced thermally activated delayed fluorescence through bridge modification in sulfone-based emitters employed in deep blue organic light-emitting diodes. **Journal of Materials Chemistry C**. 2019,7, 6664-6671.

5) Brown CM, Li C, Carta V, **Li W**, Xu Z, Stroppa PH, Samuel ID, Zysman-Colman E, Wolf MO. Influence of Sulfur Oxidation State and Substituents on Sulfur-Bridged Luminescent Copper (I) Complexes Showing Thermally Activated Delayed Fluorescence. **Inorganic Chemistry**. 2019, 58, 11, 7156–7168.

6) Sharma N, Spuling E, Mattern CM, **Li W**, Fuhr O, Tsuchiya Y, Adachi C, Bräse S, Samuel ID, Zysman-Colman E. Turn on of sky-blue thermally activated delayed fluorescence and circularly polarized luminescence (CPL) via increased torsion by a bulky carbazolophane donor. **Chemical Science**. 2019, 10, 6689-6696.

2018

7) Wong MY, Krotkus S, Copley G, **Li W**, Murawski C, Hall D, Hedley GJ, Jaricot M, Cordes DB, Slawin AM, Olivier Y, Beljonne D, Muccioli L, Moral M, Sancho-Garcia J, Gather MC, Samuel ID, Zysman-Colman E. Deep-blue oxadiazole-containing thermally activated delayed fluorescence emitters for organic light-emitting diodes. **ACS Applied Materials & Interfaces**. 2018, 10, 39, 33360–33372.

8) Keum CM, Kronenberg NM, Murawski C, Yoshida K, Deng Y, Berz C, **Li W**, Wei M, Samuel ID, Gather MC. The Role of Metallic Dopants in Improving the Thermal Stability of the Electron Transport Layer in Organic Light-Emitting Diodes. **Advanced Optical Materials**. 2018, 6, 1800496.

Abstract

Organic light-emitting diodes (OLEDs) have attracted a lot of attentions because of their high performance in display applications. Organic emitters are still being developed to improve efficiency, colour gamut and sustainability, and thermally activated delayed fluorescence (TADF) materials are widely regarded as one of the most promising next-generation OLED emitters. To date, green TADF emitters have been developed, and the corresponding OLEDs show high light-emitting efficiency and long operation lifetimes. However, the performance of red and blue TADF OLEDs still lag their green-emitting counterparts. For this reason, this work focuses on developing new red and deep-blue TADF materials. A group of red and blue TADF emitters were designed and synthesized. Their photophysical properties and electroluminescence performance were also studied. In addition, it was found that doping some of these new emitters into common host materials, such as 2,8-bis(diphenyl-phosphoryl)dibenzo[b,d]thiophene (PPT), 2,2',2"-(1,3,5-Benzinetriyl)-tris(1-phenyl-1-H-benzimidazole) (TPBi) or poly(methyl methacrylate) (PMMA), can lead to organic long-persistent luminescence (OLPL) lasting for thousands of seconds at room temperature. As traditional room-temperature OLPL materials are based on exciplex emitters, the new OLPL systems discovered here demonstrates that exciplex formation is not required for harvesting OLPL. This enables a wide range of host materials to be used including materials as simple as PMMA. Expanding this concept further, the author developed a method for large-scale PMMA-based OLPL sample fabrication to take full advantage of its low expense. This method gives thick (> 2 mm) and clear OLPL products, and all the required equipment is easily accessed in lab condition. Combining the flexible design of TADF emitters and mature PMMA industry, this work opens the 'door' of large-scale, colour tuneable and cost-efficient room-temperature OLPL materials. At the same time, the light-emitting properties and mechanism of these new OLPL emitters were studied, which provides a guideline for further OLPL emitter improvements.

Contents

List of Abbreviations

APS - Ambient pressure photoemission spectroscopy

CBP - 4,4′-Bis(N-carbazolyl)-1,1′-biphenyl

CT - Charge transfer

^{1}CT - Charge transfer singlet state

^{3}CT - Charge transfer triplet state

CTRW - Continuous-time random walk

CV - Cyclic voltammetry

CzSi - 9-(4-tert-Butylphenyl)-3,6-bis(triphenylsilyl)-9H-carbazole

DBP - tetraphenyldibenzoperiflanthene

DCM (or CH_2Cl_2) – Dichloromethane

DCM2 - 4-(dicyanomethylene)-2-methyl6-julolidyl-9-enyl-4H-pyran

DF - Delayed fluorescence

DFT - Density functional theory

DPEPO - Bis[2-(diphenylphosphino)phenyl]ether oxide

DPV - Differential pulse voltammetry

DSC - Differential scanning calorimetry

DTA - Differential thermal analysis

EL - Electroluminescence

EQE - External quantum efficiency

FRET - Förster resonance energy transfer

HFC - Hyperfine coupling

HOMO - Highest occupied molecular orbital

IC - Internal conversion

iCCD - Intensified charged coupled device

IQE - Internal quantum efficiency

ISC - Intersystem crossing

ITL - Isothermal luminescence

^{1}LE - Local excited singlet state

^{3}LE - Local excited triplet state

LED – light-emitting diode

LPL - Long-persistent luminescence

LUMO - Lowest unoccupied molecular orbital

mCP - 1,3-Di(9H-carbazol-9-yl)benzene, N,N′-Dicarbazolyl-3,5-benzene

MCS - Multi-channel scaling

MeCN – Acetonitrile

MMA - Methyl methacrylate

OLED - Organic light emitting diode

OLPL - Organic long-persistent luminescence

Pe - Perylene

PF - Prompt fluorescence

PH – Phosphorescence

PhMe – Toluene

PIA – Photoinduced absorption

PL - Photoluminescence

PLQY - Photoluminescence quantum yield

PMMA – Poly(methyl methacrylate)

PMT - Photomultiplier tube

PPT - 2,8-bis(diphenyl-phosphoryl)dibenzo[b,d]thiophene

RTP - Room-temperature phosphorescence

rISC - Reverse intersystem crossing

SCE - Saturated calomel electrode

SiPM - Silicon-photomultiplier

SOC - Spin-orbit coupling

SOP - Spontaneous orientation polarization

TADF - Thermally activated delayed fluorescence

TBPe - 2,5,8,11-tetra-tert-butylperylene

TBRb - 2,8-di-tert-butyl-5,11-bis(4-tertbutylphenyl)-6,12-diphenyltetracene

TCSPC – Time-correlated single photon counting

TDA - Tamm-Dancoff approximation

TDC - Time-to-digital converter

TD-DFT - Time-dependent density functional theory

TGA - Thermal gravimetric analysis

TL - thermoluminescence TL

TMB - N,N,N′,N′-tetramethylbenzidine

TMPD - N,N,N′,N′-Tetramethyl-p-phenylenediamine

TPBi - 2,2',2"-(1,3,5-Benzinetriyl)-tris(1-phenyl-1-H-benzimidazole)

TRPL - Time-resolved photoluminescence

TTA - Triplet-triplet annihilation

TTPA - 9,10-bis[N,N-di-(ptolyl)-amino]anthracene

Chapter 1 Introduction

1.1 Research motivation

Electronic displays have had a huge impact on all aspects of our daily lives because they have dramatically changed our methods for work and leisure activities. This is why the market size of electronic displays is expected to grow to $700 billion by 2022 (1). As the information revolution depends on displays, people are still developing thinner, lighter, more elegant and more efficient displays for the electronic devices (2). Organic light emitting diode (OLED) displays are one of the best commercial displays due to their high refresh rate, high contrast ratio, flexibility, etc. and so they are currently widely used in the latest exclusive mobile phones, gaming monitors and TVs (3). One of the most important components in OLEDs are the light-emitting materials. According to the light-emitting mechanisms, current commercial blue emitters in OLED displays are classified as fluorescent emitters, while the green and red ones are classified as phosphorescent emitters (4). Fluorescent emitters are mainly composed of light atoms (e.g. C, H, O), and consequently fluorescent OLEDs usually have theoretical maximum external quantum efficiency, EQE_{max}, around 5% (5), meaning each 100 electrons injected into a fluorescent OLED can only generate maximum 5 photons that can be emitted from the device. In comparison, phosphorescent emitters have a theoretical EQE_{max} around 20% because of the introduction of heavy metals (e.g. Ir, Pt, Os) and the consequent heavy atom effect in these emitters (6,7). However, these heavy metals are rare and toxic, and so phosphorescent emitters are not sustainable for long-term OLED applications. In 2012, Uoyama *et al.* demonstrated that comparably high EQE_{max} values can also be obtained from emitters composed of light atoms using a mechanism called thermally activated delayed fluorescence (TADF) (8). Since then, many purely organic TADF emitters with EQE_{max} above 20% have been reported (9–12) and the working principle of TADF is extensively studied (13–16).

TADF works through converting the excited-state emitters from non-emissive triplet states to emissive singlet states, which is called reverse intersystem crossing (rISC), and so all the excitons generated in an OLED can be used for light emission (8). The rISC process requires flipping the molecular spins, which was commonly regarded as difficult or forbidden in purely organic molecules. However, the rISC rates in some TADF molecules are much higher than the traditional theory can explain (12), and so new mechanisms were proposed (16) which fit the experimental results much better. This thesis introduces current understanding of the mechanism of TADF and discusses the consequent ideal molecular designs for efficient TADF emitters. An

experimental study of two groups of newly designed TADF emitters were studied for the explorations of high-performance orange and deep-blue TADF emitters.

Besides being used in OLEDs, TADF emitters have also been applied to fluorescence microscopy (17), sensing (18) and catalysts (19). Here, the author demonstrated the first case of applying TADF compounds to the realization of room-temperature organic long-persistent luminescence (OLPL). Long-persistent luminescence (LPL) is a phenomenon that when the excitation source is removed, the materials can still show long-lived afterglow for seconds or even hours (20). Current commercial LPL emitters mainly use inorganic metal oxide, such as $CaAl_2O_4$ or $SrAl_2O_4$, as the hosts with rare metals, Eu, Nd and Dy, as the dopants. They require high fabrication temperatures (> 1000 ^{o}C) (21). In comparison, OLPL emitters use purely organic materials, which dramatically reduces the fabrication temperature (< 300 ^{o}C) and does not require rare metals. The first high performance room-temperature OLPL emitter was reported by Kabe *et al.* in 2017 (22), and they found an organic exciplex emitter having afterglow lasting for thousands of seconds after photoexcitation. Since then, many other exciplex-based OLPL emitters have been published with different colours and afterglow durations (23–25). Here, the author found that exciplex emitters are not necessary for OLPL formations because doping TADF compounds into common organic host materials can also realize OLPL. This new class of OLPL systems has the advantage of enabling wide a range of host materials to be used including materials as simple as Poly(methyl methacrylate) (PMMA). This dramatically increases the rigidity and transparency of the OLPL samples compared with the exciplex-based OLPL emitters which use small molecules as the hosts. Furthermore, multi-colour TADF-compound-based OLPL emitters were also obtained to demonstrate the advantage of this new class of OLPL system. Therefore, combining the flexible design of TADF emitters and the mature PMMA industry, this work opens the 'door' of large-scale, colour tuneable and cost-efficient room-temperature OLPL materials.

Moreover, to get further understanding of this new OLPL system, its light-emitting properties and mechanisms were studied in order to guide further improvements in these new OLPL systems. To realize large-scale (> 1 grams) PMMA-based OLPL sample fabrication, which can enhance the absorption and emission of OLPL samples, the author of this thesis developed a method which makes the final large-scale OLPL products clear and transparent, and the corresponding instrument for the fabrication is easily accessed in lab condition.

1.2 Thesis organization

Chapter **2** introduces the fundamental knowledge of molecular physics those are relevant to the work in this thesis.

Chapter **3** introduces the experimental methods used for the data collections and the working principles of some measurement platforms.

Chapter **4** briefly reviews different classes of OLED emitters according to their light-emitting mechanisms to show the fundamental advantages of TADF emitters. The recent mechanism study of TADF emitters and the ideal molecular designs are also discussed.

Chapter **5** shows the study of two new yellow and orange TADF emitters regarding their photophysical properties and electroluminescence performance in OLEDs.

Chapter **6** presents the study of four new blue TADF emitters comparing with a reference sky-blue TADF emitter.

Chapter **7** introduces the current popular room-temperature long-lived afterglow materials. OLPL is discussed in detail in terms of its advantages and working principles.

Chapter **8** shows the first case of applying TADF compounds to OLPL. The light-emitting properties and the mechanisms of this kind of OLPL emitters were studied. The advantages of this new class of OLPL systems were also demonstrated.

Chapter **9** discussed the importance of large-scale OLPL samples and the difficulties of large-scale PMMA-based OLPL sample fabrication using solution processing and melt-casting. The author also demonstrated how the problems were solved using a new method which only requires the instruments that can be easily accessed in lab conditions.

Chapter **10** summarizes the work in this thesis and the prospects of future improvements of TADF emitters and TADF-compound-based OLPL materials.

1.3 References

1.   Grand View Research. Electronic Display Market Worth $733.7 Billion By 2022 [Internet]. 2020. Available from: https://www.grandviewresearch.com/press-release/global-electronic-display-market

2.   Display Daily. Top Display Technology Trends for 2019 [Internet]. 2020. Available from: https://www.displaydaily.com/article/display-daily/top-display-technology-trends-for-2019

3.   Pioneer. Transparent OLED for Multiple Colors [Internet]. 2020. Available from: https://global.pioneer/en/info/globalnetwork/japan/tohokupioneer/mainbusinesses/oled/lp/?utm_source=gs_x&gclid=EAIaIQobChMIheGI6LDm6gIVw7TtCh0IhwzSEAAYASAAEgLokvD_BwE

4.   Display Daily. A Breakthrough in Blue OLED [Internet]. 2020. Available from: https://www.displaydaily.com/article/display-daily/a-breakthrough-in-blue-oled

5.   Zhao Y, Zhang J, Miao Y, Wei X, Xu H, Wu Y, Wang H, Li T, Xu B. All-fluorescent white organic light-emitting diodes with EQE exceeding theoretical limit of 5% by incorporating a novel yellow fluorophor in co-doping forming blue exciplex. Org Electron. 2020;83(February):105746. Available from: https://doi.org/10.1016/j.orgel.2020.105746

6.   Cho W, Sarada G, Lee H, Song M, Gal Y-S, Lee Y, Jin S-H. Highly efficient, conventional and flexible deep-red phosphorescent OLEDs using ambipolar thiophene/selenophene-phenylquinoline ligand-based Ir(III) complexes. Dye Pigment. 2017;136:390–7. Available from: http://dx.doi.org/10.1016/j.dyepig.2016.08.060

7.   Jiang B, Ning X, Gong S, Jiang N, Zhong C, Lu Z-H, Yang C. Highly efficient red iridium(iii) complexes cyclometalated by 4-phenylthieno[3,2-c]quinoline ligands for phosphorescent OLEDs with external quantum efficiencies over 20%. J Mater Chem C. 2017;5(39):10220–4. Available from: http://xlink.rsc.org/?DOI=C7TC03667A

8.   Uoyama H, Goushi K, Shizu K, Nomura H, Adachi C. Highly efficient organic light-emitting diodes from delayed fluorescence. Nature. 2012;492(7428):234–8. Available from: http://dx.doi.org/10.1038/nature11687

9.   Rajamalli P, Senthilkumar N, Huang P-Y, Ren-Wu C-C, Lin H-W, Cheng C-H. New Molecular Design Concurrently Providing Superior Pure Blue, Thermally Activated Delayed Fluorescence and Optical Out-Coupling Efficiencies. J Am Chem Soc. 2017;139(32):10948–51. Available from: https://pubs.acs.org/doi/10.1021/jacs.7b03848

10.   Kim JU, Park IS, Chan C-Y, Tanaka M, Tsuchiya Y, Nakanotani H, Adachi C. Nanosecond-time-scale delayed fluorescence molecule for deep-blue OLEDs with small efficiency rolloff. Nat Commun. 2020;11(1):1765. Available from: http://dx.doi.org/10.1038/s41467-020-15558-5

11.   Kondo Y, Yoshiura K, Kitera S, Nishi H, Oda S, Gotoh H, Sasada Y, Yanai M, Hatakeyama T. Narrowband deep-blue organic light-emitting diode featuring an organoboron-based emitter. Nat Photonics. 2019;13(10):678–82. Available from: http://dx.doi.org/10.1038/s41566-019-0476-5

12.   dos Santos PL, Ward JS, Congrave DG, Batsanov AS, Eng J, Stacey JE, Penfold TJ, Monkman AP, Bryce MR. Triazatruxene: A Rigid Central Donor Unit for a D-A 3 Thermally Activated Delayed Fluorescence Material Exhibiting Sub-Microsecond Reverse Intersystem Crossing and Unity Quantum Yield via Multiple Singlet-Triplet State Pairs. Adv Sci. 2018;5(6):1700989. Available from: http://doi.wiley.com/10.1002/advs.201700989

13.   Gibson J, Penfold TJ. Nonadiabatic coupling reduces the activation energy in thermally activated delayed fluorescence. Phys Chem Chem Phys. 2017;19(12):8428–34. Available from: http://xlink.rsc.org/?DOI=C7CP00719A

14.   Marian CM. Mechanism of the Triplet-to-Singlet Upconversion in the Assistant Dopant ACRXTN. J Phys Chem C. 2016;120(7):3715–21. Available from: https://pubs.acs.org/doi/10.1021/acs.jpcc.6b00060

15.   Dias FB, Santos J, Graves DR, Data P, Nobuyasu RS, Fox MA, Batsanov AS, Palmeira T, Berberan-Santos MN, Bryce MR, Monkman AP. The Role of Local Triplet Excited States and D-A Relative Orientation in Thermally Activated Delayed Fluorescence: Photophysics and Devices. Adv Sci. 2016;3(12):1600080. Available from: http://doi.wiley.com/10.1002/advs.201600080

16.   Gibson J, Monkman AP, Penfold TJ. The Importance of Vibronic Coupling for Efficient Reverse Intersystem Crossing in Thermally Activated Delayed Fluorescence Molecules. ChemPhysChem. 2016;17(19):2956–61. Available from: http://doi.wiley.com/10.1002/cphc.201600662

17.   Li T, Yang D, Zhai L, Wang S, Zhao B, Fu N, Wang L, Tao Y, Huang W. Thermally Activated

Delayed Fluorescence Organic Dots (TADF Odots) for Time-Resolved and Confocal Fluorescence Imaging in Living Cells and In Vivo. Adv Sci. 2017;4(4):1600166. Available from: http://doi.wiley.com/10.1002/advs.201600166

18.   Ni F, Li N, Zhan L, Yang C. Organic Thermally Activated Delayed Fluorescence Materials for Time-Resolved Luminescence Imaging and Sensing. Adv Opt Mater. 2020;8(14):1902187. Available from: https://onlinelibrary.wiley.com/doi/abs/10.1002/adom.201902187

19.   Bouzrati-Zerelli M, Guillaume N, Goubard F, Bui T-T, Villotte S, Dietlin C, Morlet-Savary F, Gigmes D, Fouassier JP, Dumur F, Lalevée J. A novel class of photoinitiators with a thermally activated delayed fluorescence (TADF) property. New J Chem. 2018;42(10):8261–70. Available from: http://xlink.rsc.org/?DOI=C7NJ04394E

20.   Hölsä J. Persistent luminescence beats the afterglow: 400 Years of persistent luminescence. Electrochem Soc Interface. 2009;18(4):42–5.

21.   Van den Eeckhout K, Smet PF, Poelman D. Persistent Luminescence in Eu2+-Doped Compounds: A Review. Materials (Basel). 2010;3(4):2536–66. Available from: http://www.mdpi.com/1996-1944/3/4/2536

22.   Kabe R, Adachi C. Organic long persistent luminescence. Nature. 2017;550(7676):384–7. Available from: http://www.nature.com/articles/nature24010

23.   Lin Z, Kabe R, Nishimura N, Jinnai K, Adachi C. Organic Long-Persistent Luminescence from a Flexible and Transparent Doped Polymer. Adv Mater. 2018;30(45):1803713. Available from: http://doi.wiley.com/10.1002/adma.201803713

24.   Jinnai K, Kabe R, Adachi C. Wide-Range Tuning and Enhancement of Organic Long-Persistent Luminescence Using Emitter Dopants. Adv Mater. 2018;30(38):1800365. Available from: http://doi.wiley.com/10.1002/adma.201800365

25.   Jinnai K, Nishimura N, Kabe R, Adachi C. Fabrication-method Independence of Organic Long-persistent Luminescence Performance. Chem Lett. 2019;48(3):270–3. Available from: http://www.journal.csj.jp/doi/10.1246/cl.180949

Chapter 2 Introduction of molecular physics

As previously mentioned in Chapter **1**, OLEDs play an important role in electronic displays, which have a huge impact on our lives. The development of OLEDs is driven by developing greater understanding of organic semiconductors and molecular physics. Therefore, this chapter mainly introduces fundamental molecular physics information that is relevant to OLEDs and the research conducted in this thesis.

2.1 Fundamental molecular physics

2.1.1 Schrödinger wave equation and Born-Oppenheimer approximation

Quantum mechanics rules the microscopic world, especially at the atomic and molecular scale. The behaviours of atoms and molecules can be described by Schrödinger equation (1):

$$H\psi = E\psi \qquad (2.1)$$

where

ψ is a wave function which describes the state of a particle

H is Hamiltonian operator

E is the eigenvalue of the operator H

In principle, using this equation can fully compute the properties of an atom, including its electronic, nuclear, and spin configurations, and even the average values of any measurable properties. Furthermore, as a molecule is composed of many atoms, molecular simulations can be achieved by adding up the Schrödinger equations of each atom. However, in spite of the huge advances in computational power, simulations for problems involving more than 3 bodies are still challenging due to increasing complexity. In comparison, a visible-light-emitting molecule, such as anthracene, can easily contain more than 20 atoms, which makes a complete computational simulation using Schrödinger equation very expensive. To validate molecular simulations, approximation methods were proposed to simplify the calculations. For organic molecules, the most important method for determining molecular wave functions and associated energies is Born-Oppenheimer approximation (2,3). In this approximation, the motions of atomic nuclei and electrons in a molecule can be treated separately because the motions of electrons in orbitals are much faster than the nuclear vibrational motions, and so

negatively charged electrons can immediately adjust their distribution to the positive potential provided by the nuclei. Therefore, when making calculations of wave functions, the nuclei was first independently calculated to find the lowest energy configurations, and then treated as 'frozen'. Under these nuclei configurations, the electron wave function was calculated. This method significantly simplifies the calculations and make the calculations of large organic molecules much less expensive.

2.1.2 Molecular bonds, ground state and excited state, HOMO and LUMO

As shown in Figure **2.1a**, when atoms are connected and form a molecule (e.g. an ozone molecule), they generate new molecular bonds and molecular orbitals with different energy levels. Within these molecular orbitals, the most important ones for photophysical studies are bonding orbitals (π), nonbonding orbitals (n) and antibonding orbitals (π*). Among these three orbitals, normally, π orbitals have the lowest energy levels, while π* orbitals have the highest energy levels. The shapes of these molecular orbitals can be calculated using Schrödinger equations, and the electron cloud distribution in these orbitals are presented in Figure **2.1a** with yellow and blue colours showing different phases of the wavefunctions. Similar to the cases in atomic orbitals, electrons in molecular orbitals also follow Pauli Exclusion Principles – one orbital can only contain maximum two electrons with different spins. A stable molecule at ground state is usually neutral, meaning the highest occupied molecular orbital (HOMO) contains two electrons with opposite spins, while the lowest unoccupied molecular orbital (LUMO) is empty.
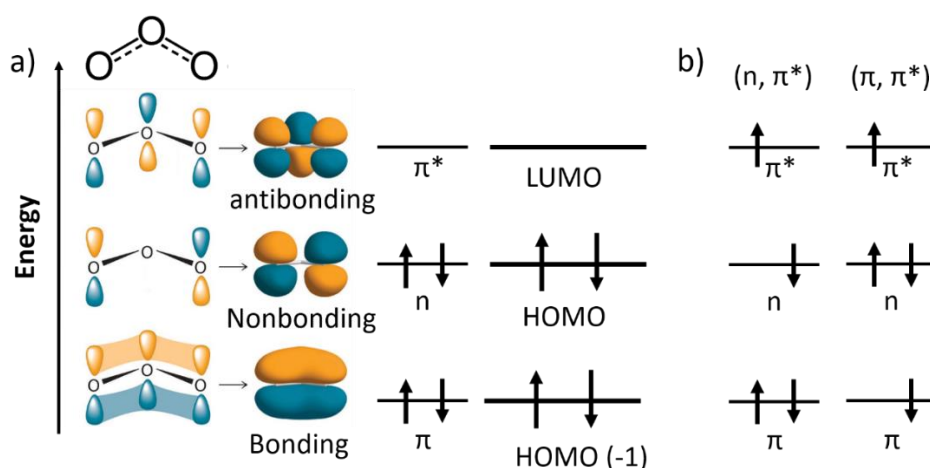
Figure 2.1. a) Schematic diagram of the molecular orbitals of ozone and the energy levels these orbitals. Figure adapted from (4). b) Schematic diagram of (n, π*) and (π, π*) excited states of a molecule.

Electrons in n and π orbitals can be excited to higher molecular orbitals like π* orbitals. Figure **2.1b** shows an example of the electron distributions of (n, π*) and (π, π*) excited states of the ozone molecule, representing the electron transitions between the n and π* orbitals, and the electron transitions between the π and π* orbitals.

2.1.3 Molecular spins, singlets and triplets, fluorescence and phosphorescence

In molecular scope, when the total spin of the electrons in a molecule equals 0, it is said to be in a singlet state. When the total spin of the electrons in a molecule equals 1, it is said to be in a triplet state. As mentioned in the last section, a ground state molecule has 2 electrons with opposite spin orientations staying in its HOMO (Figure **2.2a**). Therefore, the total spin of this ground-state molecule equals 0, and so this molecule is at singlet state. Also, this molecule is at the lowest singlet state, which is marked as S_0. Higher singlet states are marked as S_n with n = 1, 2, 3, …

Compared, when a molecule is at the lowest excited state, there is one electron in the HOMO and the other electron in the LUMO. In this case, these two electrons are allowed to have either the same or different spin directions. When the spins of these two electrons are opposite (Figure **2.2b**), the total spin of the molecule again equals 0 and this molecule is a singlet. This lowest singlet excited state is marked as S_1. When the electron on the LUMO decays to the HOMO and releases a photon, this process is called fluorescence. As the total spin of the molecule is 0 before and after the fluorescence process, this electron transition from LUMO to HOMO is spin allowed and the decay rates are usually high ($10^8 \sim 10^9$ s^{-1}) which corresponds to typical fluorescence lifetimes of 1-10 nanoseconds.

In the other case, as shown in Figure **2.2c**, when these two electrons share the same spin direction (e.g. both electrons have spin of 1/2), the total molecular spin equals 1, which makes this molecule a triplet. The lowest triplet excited state is marked as T_1. If a molecule decays from T_1 to S_0 and emits a photon, this process is called phosphorescence. However, as this process changes the total spin from 1 to 0, which breaks the law of spin conservation, and so this process is forbidden. However, this transition can still happen at a low rate, and so phosphorescence lifetimes of purely organic emitters are typically on the millisecond and second timescales. As the rate of phosphorescence, k_{PH}, is often much lower than the rate of non-radiative decay, k_{nr}, caused by molecular vibrations, most molecules do not show emission from the T_1 state at room

temperature. However, a low temperature (< 150 K) can suppress the vibrations and allows more T_1 molecules to show phosphorescence. Therefore, the phosphorescence spectra of molecules are usually studied at liquid nitrogen temperature (77 K) or even at liquid helium temperature (< 20 K). Similarly, the spin conservation law also applies to light absorption processes. As the ground state molecules are at singlet states, most molecules are pumped to only higher singlet excited states after photoexcitation.
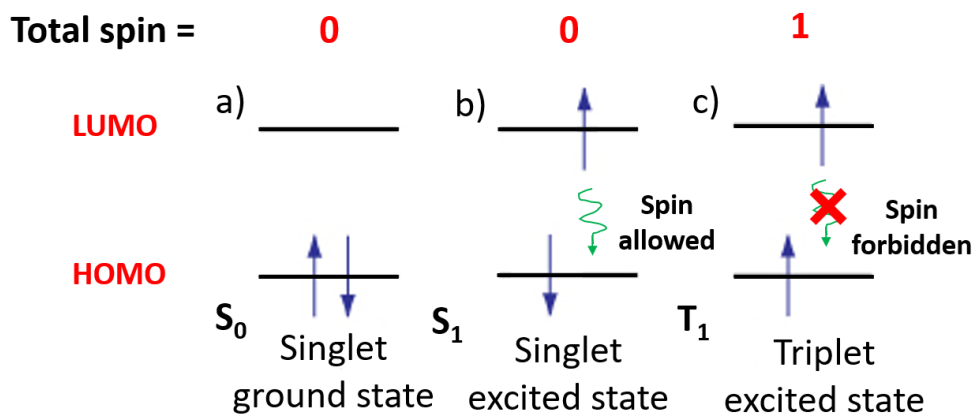
Figure 2.2. Schematic diagram of singlet ground state, the lowest singlet excited state and lowest triplet excited state

2.1.4 Singlet and triplet energy splitting and exchange integration integral

The schematic diagram of the energy levels of the S_0, S_1 and T_1 states in a molecule is shown in Figure **2.3**.
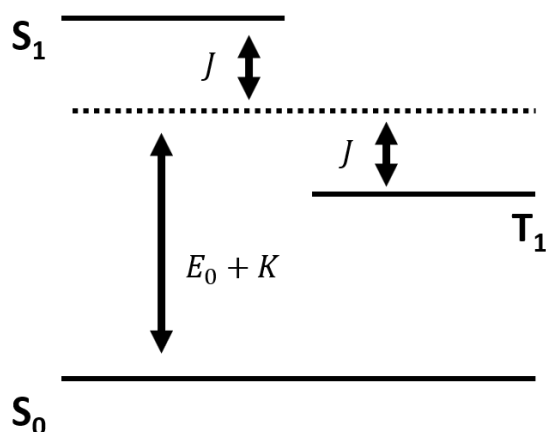
Figure 2.3. schematic diagram of the energy levels of the S_0, S_1 and T_1 states in a molecule

In a molecule, the excited state energy of S_1 and T_1 can be expressed using the following equations:

$$E_S = E_0 + K + J \tag{2.2}$$

$$E_T = E_0 + K - J \tag{2.3}$$

$$J = \iint \psi_H^*(1)\psi_L^*(2)\left(\frac{e^2}{r_1 - r_2}\right)\psi_H(2)\psi_L(1)dr_1 dr_2 \tag{2.4}$$

where,

1 and 2 label the electron 1 and electron 2

E_0 is the zero-order energy of a one-electron orbital derived excited state

K is the fist-order Coulombic correction due to classical electron-electron repulsion

J, also called exchange interaction integral, is the first-order quantum mechanical correction of the electron-electron repulsion energy due to Pauli exclusion principle

$\psi_H(r_1)$ and $\psi_L(r_2)$ are wavefunctions of the HOMO and LUMO

e is the charge of an electron

$r_1 - r_2$ is the distance between the two electrons

Equations **2.2** and **2.3** show that the energy levels of S_1 and T_1 are based on the zero-order excited state energy with the correction of Coulomb repulsion energy, K, and exchange energy, J. As the value of J is the integration between the HOMO and LUMO wavefunctions, it is always positive, and so the singlet energy is always higher than that of the triplet. Furthermore, the energy difference between S_1 and T_1, ΔE_{ST}, can be calculated through $E_S - E_T = 2J$. Therefore, the ΔE_{ST} value can be modulated though controlling the HOMO and LUMO overlaps.

2.1.5 Quantum anharmonic oscillators

When atoms are connected using chemical bonds, the nuclei of these atoms vibrate according to their interactive forces. These vibrations have a huge impact on the electron transitions and the consequent photophysical properties, and so quantum anharmonic oscillator model was proposed to describe the properties of these vibrations, which was found to provide good estimations of real molecular systems. The black solid curve in Figure **2.4** shows a schematic diagram of a quantum anharmonic oscillator which is composed of two atoms with significantly

different atomic weights (e.g. Cl and H). In this model, as shown in Figure **2.4**, when the oscillator is compressed severely, the potential energy dramatically increases, while when the oscillator is elongated severely, it breaks the chemical bonds.
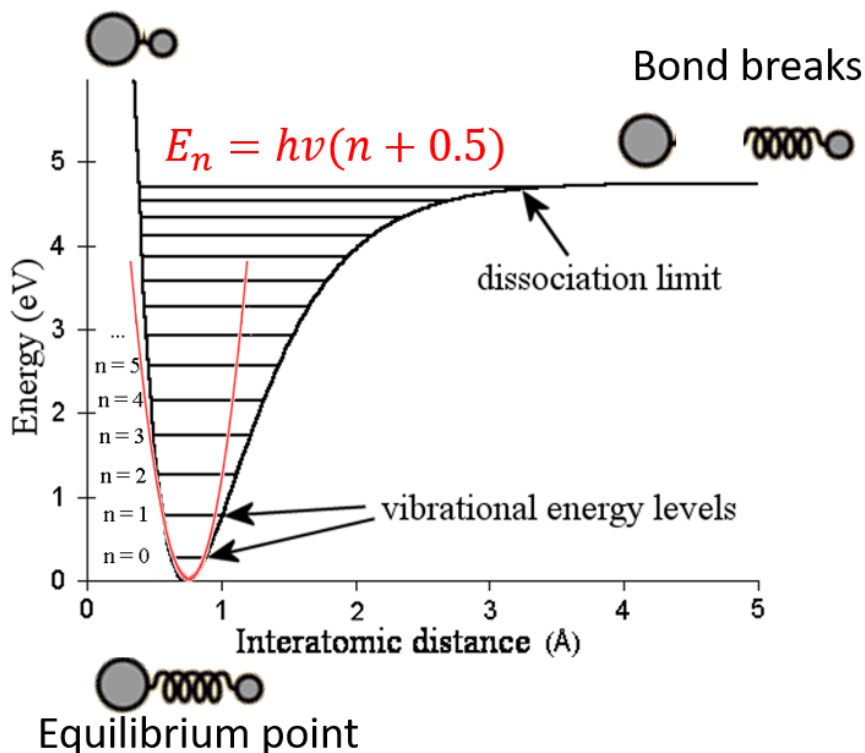
Figure 2.4. Schematic diagram of potential energy curves for a quantum anharmonic oscillator. Figure adapted from (5).

When the distance between the two atoms is close to the equilibrium point, this molecule can be treated as a harmonic oscillator whose potential energy looks like a parabolic curve in the energy diagram, which is presented as the solid red curve in Figure **2.4**. The potential energy of this harmonic oscillator is quantized, which can be expressed by the equation (1):

$$E_n = hv(n + 0.5) \qquad\qquad (2.5)$$

where,

h is the Planck constant

v is oscillation frequency

n is the vibrational quantum number, which can only take n = 0, 1, 2, …

When the value of n is large, the distance between these two atoms is also large that the bond energy between these two atoms decreases. This makes the potential energy smaller than that predicted by Equation **2.5**. Consequently, the energy differences between neighbouring states become smaller at higher vibrational states. Therefore, Equation **2.5** only gives a good energy estimation when the value of n is small.

2.1.6 Vibrational energy relaxation and Kasha's rule

Vibrational energy relaxation describes a process that when a molecule is initially at a higher vibrational state, e.g. $n = 5$ as shown in Figure **2.5a**, this molecule will quickly go through a relaxation to its lowest vibrational state ($n = 0$) on femtosecond timescales, and so most of the electrons in molecules are in the lowest vibrational state ($n = 0$) before further electronic transitions.

As shown in Figure **2.5b**, Kasha's rule (6) says that when a molecule is excited to its higher excited state, S_n, this molecule will quickly decay to its lowest electronic excited state, S_1 or T_1, before further decaying to S_0. As this process also happens on a femtosecond time scale, combining with vibration energy relaxation, both fluorescence and phosphorescence should only originate from the transitions between the lowest vibrational state of S_1 and T_1 to the ground state S_0. Although recent research shows that some rare exceptions to Kasha's rule (7–9), this rule is still valid in nearly all light-emitting materials, including the emitters presented this thesis.

Figure 2.5. a) Schematic diagram of vibrational energy relaxation. b) Schematic diagram of the absorption and emission process of a molecule.

2.1.7 Transitions between states

The transitions between different molecular states are the core of molecular photophysics. Assuming the wavefunction of a molecule before and after the transition can be noted as ψ_1 and ψ_2, the observed rate of this transition, k_{obs}, is given by time-dependent perturbation theory and can be expressed using Fermi's golden rule (10):

$$k_{obs} \sim \rho < \psi_1 | P_{1-2} | \psi_2 >^2 \tag{2.6}$$

where

> P_{1-2} is a mixing operator which makes ψ_2 "look like" ψ_1

> ρ is the number of states of ψ_2 that are of the same energy as ψ_1 and are capable of being mixed with ψ_1

Using this mathematical language, the transitions between states which involve both vibronic coupling and spin-orbit coupling can be described using Equation **2.7** (1):

$$k_{obs} = k_{max}^0 \frac{< \psi_1 | P_{vib} | \psi_2 >^2}{\Delta E_{12}^2} \times \frac{< \psi_1 | P_{soc} | \psi_2 >^2}{\Delta E_{12}^2} \times < \chi_1 | \chi_2 >^2 \tag{2.7}$$

where,

> k_{max}^0 is the maximum possible rate constant, also referred as 'zero-point motions determined rate constant'

> P_{vib} is vibronic coupling operator

> P_{SOC} is spin-orbit coupling operator

> ΔE_{12} is the energy gap between ψ_1 and ψ_2

> χ_1 and χ_2 are vibrational wave functions

Within this equation, k_{obs} is much smaller than k_{max}^0 in most cases because the products of the other terms in this equation are much smaller than 1. The first three terms on the right side of the Equation **2.7** are referred as vibrational coupling factor, spin-orbital coupling factor and vibrational overlap Frank-Condon factors, respectively, which are all important for the transitions in thermally activated delayed fluorescence (TADF) emitters. The mechanisms behind these terms are described in the following sections.

2.1.8 Frank-Condon Principle

The Frank-Condon principle (11) claims the electron transition is more likely to happen between two vibronic states when the vibrational wave functions, χ, of these two states have more significant overlap. The square of the vibrational overlap integral, $< \chi_1 | \chi_2 >^2$, of the two vibrational wave functions before and after the transition is called 'Frank-Condon factor' or 'FC factor'. Figure **2.6** presents the schematic diagram of applying the Frank-Condon principle to a transition between S_1 and S_0. As shown in Figure **2.6a**, the wave function (χ_1) of the $n' = 0$ state in S_1 is almost destructive with the wave function (χ_2) of the $n = 6$ state in S_0, and so the FC factor is almost 0, consequently, the transitions between these two vibrational states are not likely to happen. In comparison, as shown in Figure **2.6b**, half of the wave function of the $n' = 0$ state in S_1 is overlapping constructively with the wave function of the $n = 6$ state in S_0, and so the FC factor is large, and the consequent transitions between these two states are likely to happen.
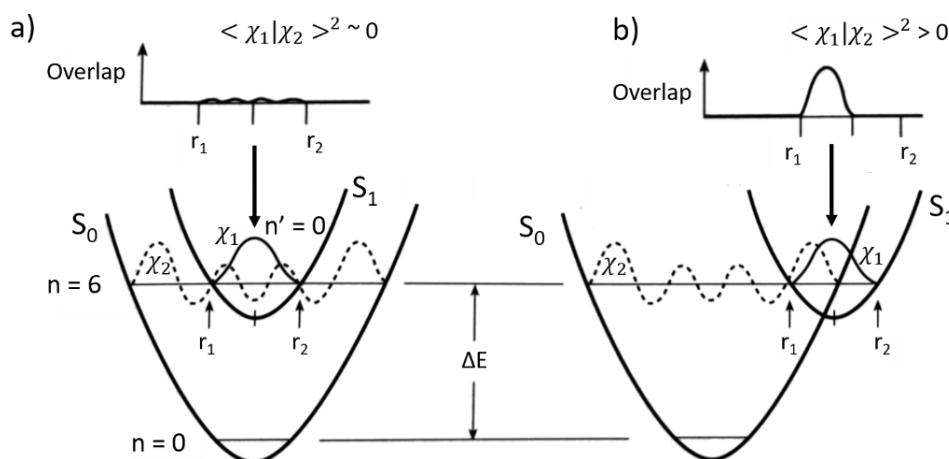
Figure 2.6. a, b) Schematic diagram of situations for poor (left) and good (right) net positive overlap of vibrational wave functions. The value of the integral $< \chi_1 | \chi_2 >^2$ as a function or r is shown at the top of the figure. Figures adapted from (1).

Therefore, according to Frank-Condon principle, the absorption and emission intensity is dependent on the overlaps of the vibrational wave functions before and after the transitions. Figure **2.7** presents an example of applying the Frank-Condon principle to explaining the shape of an absorption spectrum. As shown in Figure **2.7a**, the wave function overlap between the $n = 0$ state in S_0 has significant overlap between the $n' = 4$ state in S_1, and so the transition between these two states have high possibility, and the consequent absorption spectrum (Figure **2.7b**) has an absorption peak originating from this transition. In comparison, the wave function

overlap between the n = 0 state and n' = 1 state is not as good, and the consequent absorption intensity is weak (labelled in Figure **2.7b**).
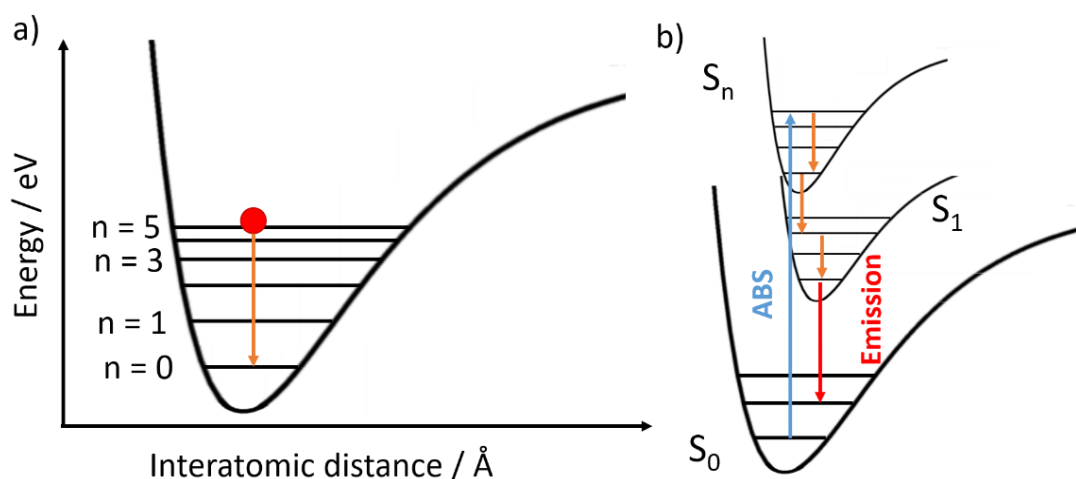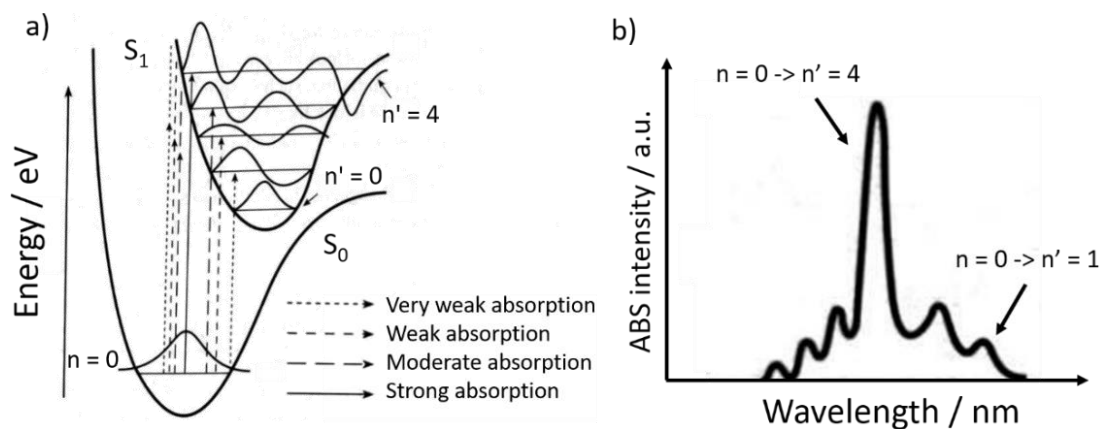

Figure 2.7. a) Schematic diagram of vibrational energy relaxation. b) Schematic diagram of the absorption and emission process of a molecule. Figures adapted from (1).

2.1.9 Vibronic mixing

Mixing of electronic states as the result of vibrations is termed "vibronic mixing" (1). Within this process, molecular-orbital overlaps can be induced by the vibrations, twisting, or bending of the molecules, and so the electrons in the overlapped orbitals can transfer between these orbitals or possess the properties of all these overlapped orbitals and reach a "mixed state".

Figure **2.8a** shows a schematic diagram of the vibronic mixing of p and s orbitals: consider a carbon atom is bound to three other atoms, and this carbon is initially sp^2 hybrid. Therefore, this atom has a pure p orbital which is symmetric above and below the plane, and so the electrons within this orbital should also have the same density above and below the plane. However, when the molecule goes through a bending, the s orbitals from the connection of the other two atoms start to mix with the p orbital below the plane and so this orbital possesses both s and p character and is labelled as sp^n orbital, where n is a measure of the "p character" remaining.
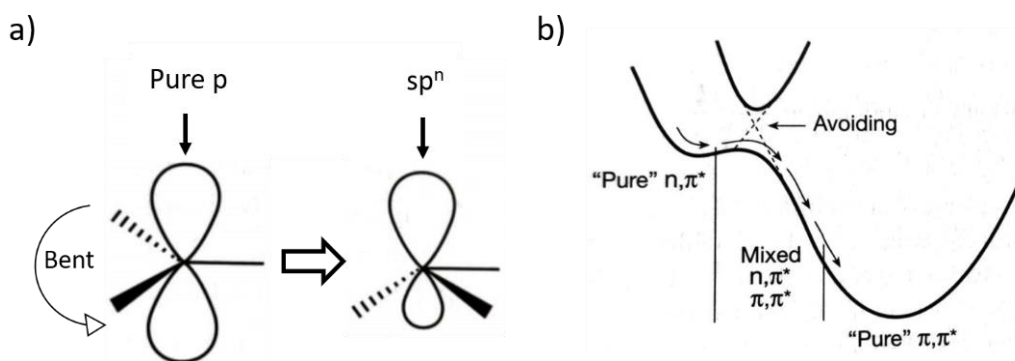
Figure 2.8. a) Schematic diagram of vibronic mixing of p orbital. b) Schematic diagram of vibronic mixing of n, π* and π, π*. Figures adapted from (1).

Vibronic coupling serves as a kind of perturbation for the transition between two excited states close in energy: as shown in Figure **2.8b**, there exists both n, π* and π, π* excited states in a molecule, which are both close in energy and nuclear coordinates. With certain molecular distortion (out-of-plane vibration), the transition between these two states is allowed, and so the original n, π* excited state can be converted into π, π* excited states through the mixed region. The magnitude of this mixing is dependent on the vibronic mixing integral (1):

$$< n, \pi^* | P_{vib} | \pi, \pi^* >$$

(2.8)

2.1.10 Spin-orbit coupling

Spin-orbit coupling (SOC) is the key for transitions between singlets and triplets in TADF emitters, which is further discussed in Chapter **4**. Here, only the mechanism and properties of SOC is introduced. SOC originates from the interaction between the spin magnetic moment, $\boldsymbol{\mu_s}$, and the orbital magnetic moment, $\boldsymbol{\mu_L}$, of an electron, which is explained in detail as follow: Figure **2.9a** shows an electron possessing its quantum mechanical spin with the spin momentum, $\boldsymbol{S}$, pointing up, and this spin can generate a spin magnetic moment in the opposite direction. The relationship between this magnetic moment and the spin can be expressed using Equation **2.9**:

$$\boldsymbol{\mu_s} = -g_e \gamma_e \boldsymbol{S}$$

(2.9)

where

g_e is called the g factor which is a dimensionless constant with the experimental value close to 2

$\gamma_e = e/2m$, which is called magnetogyric ratio. e and m are the charge and mass of the electron

Figure **2.9b** shows an electron orbiting around its positively charged nucleus in the Bohr orbit, and so this electron possesses an angular momentum, L, pointing up. This orbiting behaviour also generates an orbital magnetic moment in the opposite direction, which can be expressed using Equation **2.10**:

$$\boldsymbol{\mu}_L = -\gamma_e \boldsymbol{L} \tag{2.10}$$

Furthermore, Figure **2.9b** is in principle equal to Figure **2.9c** where the electron is treated as fixed, and the electron sees the positively charged nucleus orbiting around it. The orbiting nucleus is equivalent to a coil with a current going through it, which can generate a magnetic field, H, pointing up. Finally, as shown in Figure **2.9d**, this magnetic field can interact with electron's spin magnetic dipole moment and force the electron to precess in the magnetic field at an angular frequency $\boldsymbol{\omega}$. Therefore, the spin momentum, S, and the orbital momentum, L, can exchange their angular momentum using this magnetic interaction. The process of this angular momentum exchange is the core of SOC.
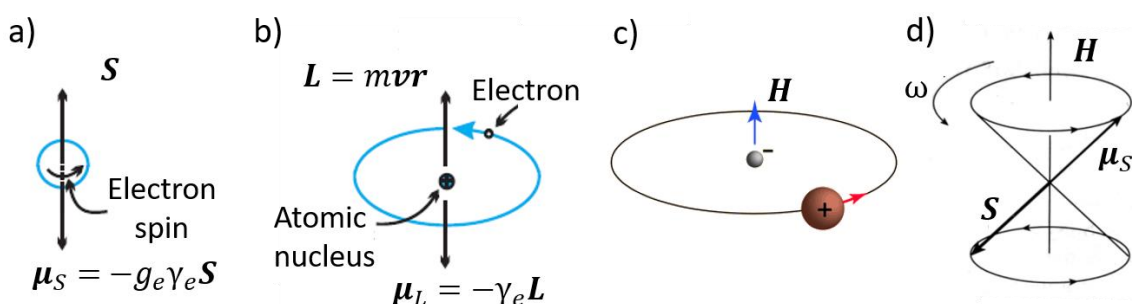
Figure 2.9. a) Schematic diagram of a spinning electron. b) An electron is orbiting around its nucleus. c) An electron sees its nucleus orbiting around it. d) The precession of electron's magnetic moment in a magnetic field. Figures adapted from (1).

Assuming the wave functions of the molecule before and after a SOC is ψ_1 and ψ_2, the magnitude of the SOC, E_{SOC}, can be expressed using the following equations (1):

$$E_{SOC} = < \psi_1 | P_{SOC} | \psi_2 > \tag{2.11}$$

$$P_{SOC} = \xi_{SOC} \boldsymbol{SL} \sim \xi_{SOC} \boldsymbol{\mu}_s \boldsymbol{\mu}_L \tag{2.12}$$

where

ξ_{SOC} is the spin-orbit coupling constant

The value of ξ_{SOC} is related to the nuclear charge, Z, and so heavier atoms can provide a larger ξ_{SOC} and the consequent higher SOC. For hydrogen-like atoms, $\xi_{SOC} \sim Z^4$.

Figure **2.10** shows the ISC of a benzophenone molecule as an example. The S_1, T_1 and T_2 states of benzophenone are (n, π*), (n, π*) and (n, π*) states, respectively, with S_1 and T_2 states energetically close to each other. Within the process of SOC, the electron in carbon's p_x orbit (vertical) jumps to oxygen's p_y orbit (horizontal), and so the orbital of this electron rotates by 90° and generate a change in orbit angular momentum. This angular momentum change forces the electron to flip its spin so as to conserve the total angular momentum in the molecule. Therefore, the initial S_1 state (n, π*) can be converted into the T_2 state (π, π*) through SOC. Considering the T_2 states are vibronically coupled with T_1 states with a high transition rate between them (12), the consequent overall ISC rate from S_1 to T_1 is around ~10^{11} s^{-1}.
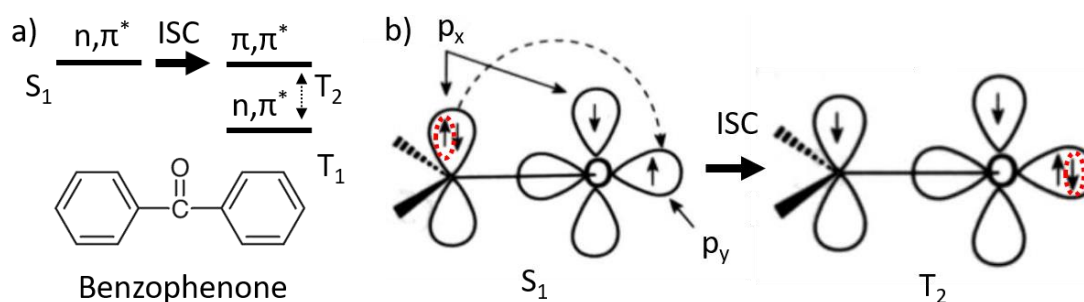
Figure 2.10. a) Molecular structure of benzophenone and the schematic diagram of the energy levels of its S_1, T_1 and T_2 states. b) Schematic diagram of a SOC induced ISC in a benzophenone molecule. Both figures adapted from (1).

Hence, taking the effect of SOC into account, there are also selection rules for ISC, which is known as El-Sayed's rule (13), and the conclusion is summarized as below (1):

Allowed transitions:

$$S_1(n, \pi^*) \rightarrow T_n(\pi, \pi^*); \; S_1(\pi, \pi^*) \rightarrow T_n(n, \pi^*); \; T_1(n, \pi^*) \rightarrow S_0(n^2) \qquad (2.13)$$
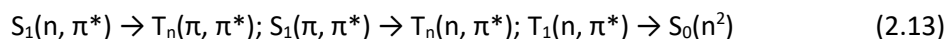
Forbidden transitions:

$$S_1(n, \pi^*) \rightarrow T_n(n, \pi^*); \; S_1(\pi, \pi^*) \rightarrow T_n(\pi, \pi^*); \; T_1(\pi, \pi^*) \rightarrow S_0(\pi^2) \qquad (2.14)$$
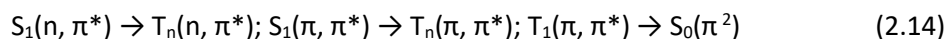
It can be seen that it is necessary to have different types of orbitals before and after the transitions to trigger SOC, so as to allow the electron spin to be flipped. It is because, only in this way, orbitals can be rotated and provide the change in angular momentum.

2.1.11 Jablonski Diagram

Figure **2.11** shows an example of a Jablonski diagram which is usually used to neatly present the important molecular states and transitions inside an emitter. Within Jablonski diagrams, the molecular states are arranged vertically by energy and depicted as solid thick lines with thin grey lines presenting the vibrational states; nonradiative transitions are indicated by squiggly arrows or dashed lines, and radiative transitions are illustrated by straight arrows. Jablonski diagrams simplify the illustrations of the molecular state evolutions in an emitter, which are widely used in this thesis. Also, the common timescales of each transition process are summarized Figure **2.11**.

Process	Timescale [s]
1 Absorption	10^{-15} (fs)
2 Vibrational relaxation	10^{-14}-10^{-12} (fs-ps)
3 Internal Conversion	10^{-12}-10^{-6} (ps-μs)
4 Fluorescence	10^{-9}-10^{-7} (ns)
5 Intersystem Crossing (S→T)	10^{-14}-10^{-6} (fs-μs)
6 Intersystem Crossing (T→S)	10^{-9}-10^{1} (ns-s)
7 Phosphorescence	10^{-6}-10^{-3} (μs-ms)
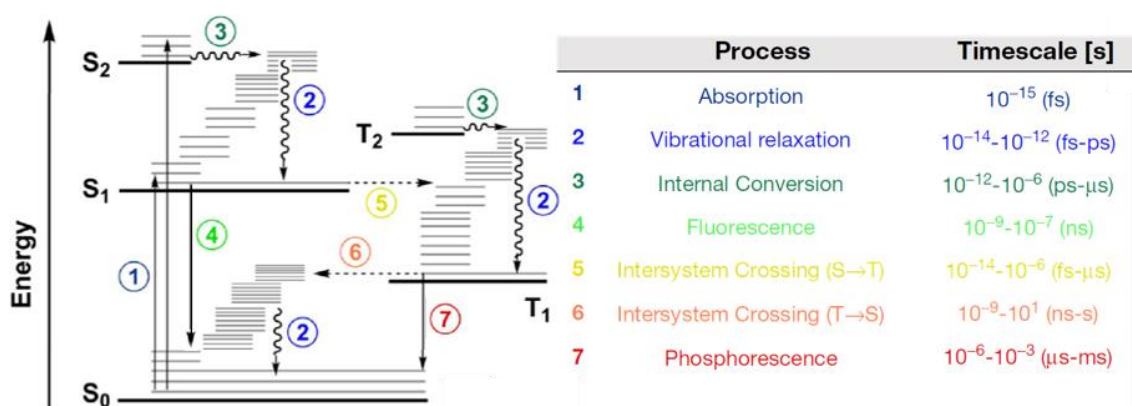
Figure 2.11. Jablonski diagram and the timescales of transitions in an emitter. Figure adapted from (13).

2.2 Intermolecular interactions

2.2.1 Förster resonance energy transfer

Förster resonance energy transfer (FRET) describes an energy transfer process between two light-emitting materials (14). It is widely used in the emission layers of OLEDs as a technique to avoid the aggregation and concentration quenching of the actual emitters so as to maximize the overall light-emitting efficiency. The schematic diagram of its working principle is shown in Figures **2.12a** and **b**: in a film where two different emitters are spatially close to each other (< 10 nm), the donor (host) can transfer its excited-state energy to the acceptor (guest) through a nonradiative process, and so only the acceptor molecules show emission in this system.
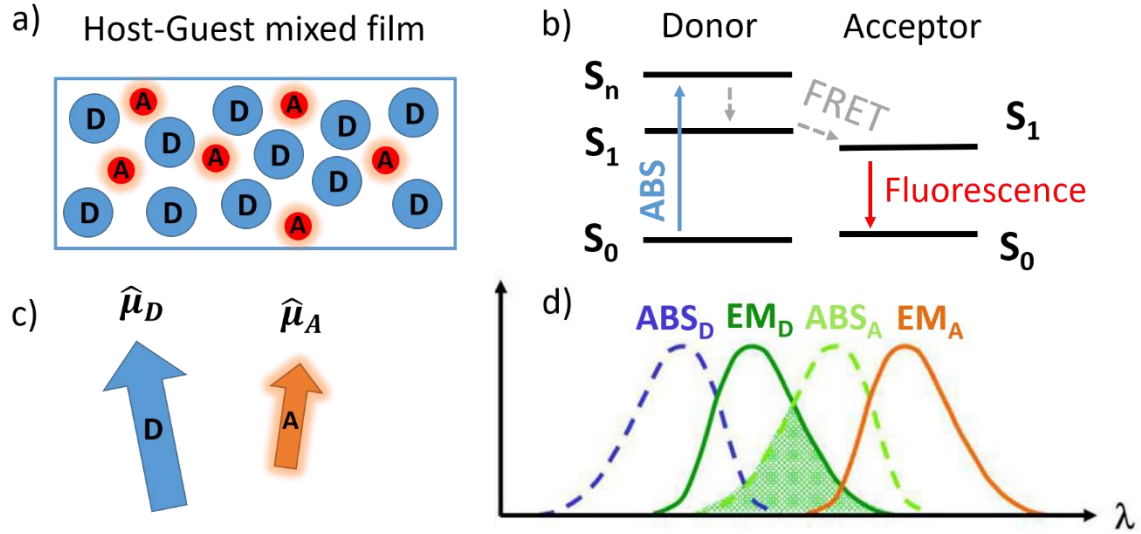
Figure 2.12. a) Schematic diagram of a host-guest mixed film. b) Jablonski diagram of the absorption and emission process in a host-guest matrix. c) The dipole moments of the donor and acceptor molecules. d) the absorption and emission spectra of the donor and the acceptor molecules.

The core of FRET is the dipole-dipole (or multipole-dipole or multipole-multipole) interaction between the donors and the acceptors (Figure **2.12c**), and its efficiency, E_{FRET}, can be affected by many factors which is describe by the following equations (16):

$$E_{FRET} = \frac{1}{1+(r/R_0)^6} \tag{2.15}$$

$$R_0^6 = \frac{2.07}{128\pi^5 N_A} \frac{\kappa^2 Q_D}{n^4} J(\lambda) \tag{2.16}$$

$$J(\lambda) = \int F_D(\lambda)\,\varepsilon_A(\lambda)\lambda^4 d\lambda \tag{2.17}$$

$$\kappa = \hat{\mu}_D \hat{\mu}_A - 3(\hat{\mu}_D \hat{R})(\hat{\mu}_A \hat{R}) \tag{2.18}$$

where

    r is the distance between the donor and the acceptor molecules

    R_0 is the distance at which the energy transfer efficiency is 50%

    Q_D is the photoluminescence quantum yield of the donor itself

    N_A is the Avogadro constant

    n is the reflective index of the film

    J(λ) is the spectral overlap integral, with wavelength, *λ*, as the variable

$F_D(\lambda)$ is the normalized emission spectra of the donor

$\varepsilon_A(\lambda)$ is the molar extinction coefficient of the acceptor

κ is orientation factor

$\hat{\mu}_D$ and $\hat{\mu}_A$ are the dipole moments of the donor and the acceptor

$\hat{R}$ is the normalized inter-fluorophore displacement

It can be seen in Equation **2.15** that E_{FRET} depends on the donor-to-acceptor separation distance with an inverse 6th-power law due to the dipole–dipole coupling mechanism. Also, Equations **2.16**, **2.17** and **2.18** show that a decent overlap between the emission spectrum of the donor and the absorption spectrum of the acceptor (Figure **2.12d**), and a good alignment of their dipole moments (Figure **2.12c**) are also the keys to harvest a high E_{FRET}.

2.2.2 Dexter energy transfer and triplet-triplet annihilation

Dexter energy transfer typically takes place between two molecules within the distance of 10 Å which is almost comparable to the collisional diameter (15). Within this process, these two molecules exchange their electrons based on the spin conservation rule (Wigner rule). Figure **2.13a** shows the process of triplet-triplet annihilation (TTA) which is a special case of Dexter energy transfer: two molecules in triplet states exchange their electrons and generate one molecule in a singlet ground state and the other in a singlet exited state. One of the resulting singlets gain the energy as the total energy of the two triplets (Figure **2.13b**).
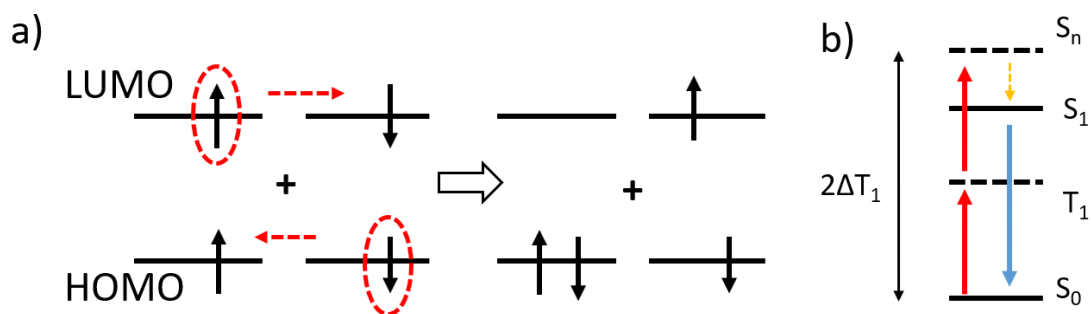
Figure 2.13. a, b) Schematic diagram of TTA in molecular orbital diagram and energy diagram. Figures adapted from (15).

2.2.3 Exciplex, localized excited states and charge transfer states

An exciplex is a heterodimeric species which can be generated in the excited state but dissociate in the ground state (1). Figure **2.14a** shows a schematic diagram of the absorption and emission processes of an exciplex emitter. The formation of an exciplex usually requires a donor molecule with a shallow HOMO and an acceptor molecule with a deep LUMO. During the excitation process, usually, the donor absorbs a photon and an electron is sent from its HOMO to its LUMO, and the resulting excited state is called a localized excited (LE) state as this process happens only inside the donor molecule. As the LUMO of the acceptor is deeper than that of the donor, this electron is transferred from the LUMO of the donor to the LUMO of the acceptor, and so forms an exciplex between these two molecules. This excited state is also called a charge transfer (CT) state. In the emission process, the electron transfers from the LUMO of the acceptor to the HOMO of the donor and emits a photon. The energy diagram of this exciplex is presented in Figure **2.14b**, covering the singlet and triplet states of each LE and CT state. LE_D and LE_A are used to denote the localized excited states of the donor and the acceptor, respectively. Importantly, although each state has different energy levels, the triplet state energy level is always lower than that of the singlet state in the same orbital. The use of CT state is the core of organic solar cells, TADF and OLPL, which are further discussed in the following chapters.
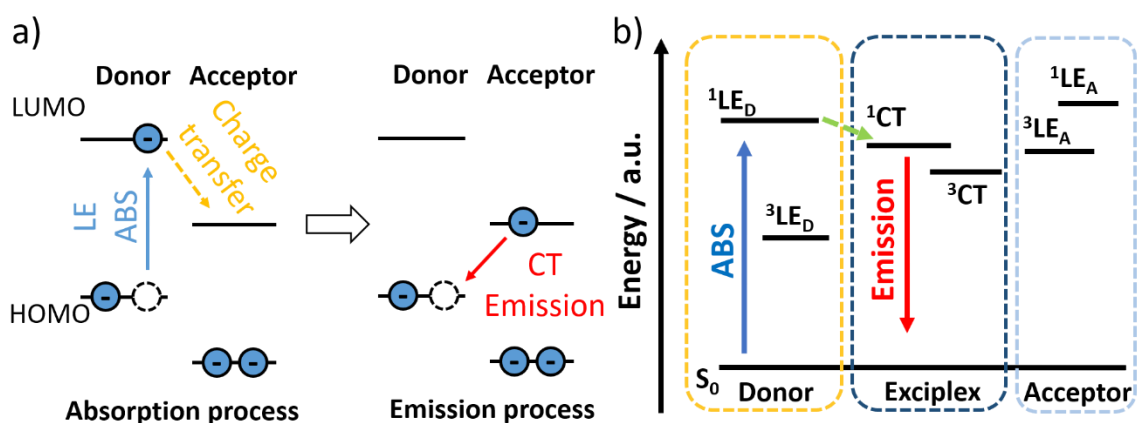
Figure 2.14. a) HOMO and LUMO energy diagram of an exciplex. b) Molecular state energy diagram of an exciplex

2.2.4 Solvatochromism

Solvatochromism describes the phenomenon that when an emitter is dissolved in different solvents, the emission spectrum changes according to the different polarities of the solvents.

Positive solvatochromism corresponds to a bathochromic shift (or red shift) with increasing solvent polarity.

The origin of solvatochromism is the dipole-dipole interaction between the emitter and the solvent molecules. As shown in Figure **2.15a**, a molecule usually has a permanent dipole moment due to the uneven electron distribution over the whole molecule, which can generate electric fields. As shown in Figure **2.15b**, when a ground-state emitter is dissolved in a solvent, as the solvent molecules also have permanent dipole moments, the solvent molecules will align their dipole orientations according to the electrical fields created by this emitter. The dipole moment of the emitter at ground state is labelled as μ_g. As shown in Figure **2.15c**, when the emitter is excited, it goes through a conformation change within femtoseconds, and the dipole moment is also changed. The new dipole moment of the emitter is labelled as μ_e. As the fluorescence lifetime of an emitter (nanoseconds) is much longer than the relaxation lifetime of solvent molecules (picoseconds), the solvent molecules around the emitter can rearrange their dipole moments before the emission process of the emitter, which is shown in Figure **2.15d**. Consequently, the excited state energy of emitter is lowered, and the emission shows red-shift. Also, a higher solvent polarity results in a more significant spectrum shift.

a)	b)	c)	d)
Molecule in gas phase at ground state	Molecule in solution at ground state	Molecule in solution at excited state before solvent relaxation	Molecule in solution at excited state after solvent relaxation
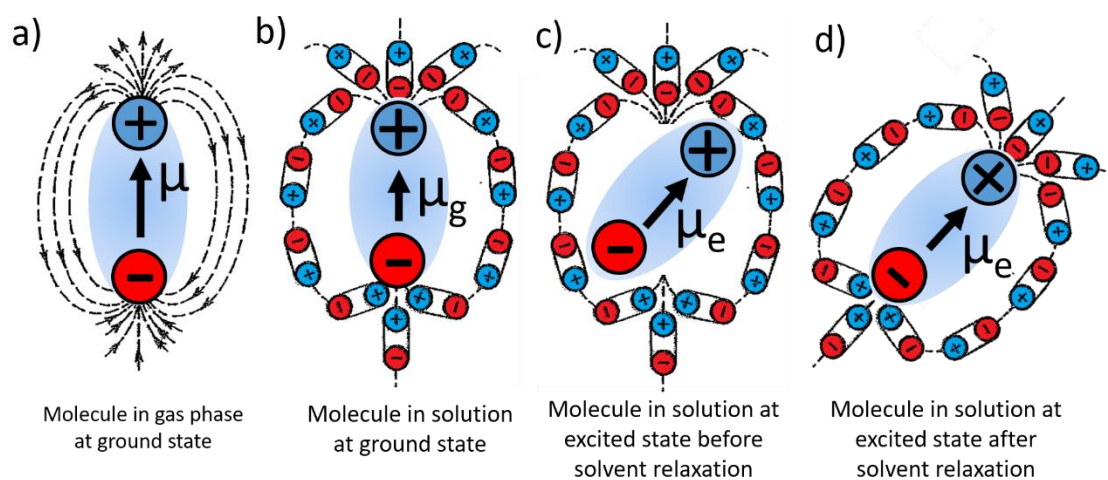
Figure 2.15. Schematic diagram of the mechanism of solvatochromism.

The mechanism of solvatochromism does not only apply to emitters in solutions, but also in the solid state, which is important for the host material selection for TADF emitters. Furthermore, CT states show more significant solvatochromism effects than LE states because the dipole moment of CT states are much larger, and so solvatochromism is also used as a technique to analyse the CT character of an emitter.

2.3 References

1. Nicholas J Turro; V Ramamurthy; Juan C Scaiano. Principles of Molecular Photochemistry: An Introduction. 2009.

2. Born M, Oppenheimer R. Zur Quantentheorie der Molekeln. Ann Phys. 1927;389(20):457–84. Available from: http://doi.wiley.com/10.1002/andp.19273892002

3. Penfold TJ, Gindensperger E, Daniel C, Marian CM. Spin-Vibronic Mechanism for Intersystem Crossing. Chem Rev. 2018;118(15):6975–7025. Available from: https://pubs.acs.org/doi/10.1021/acs.chemrev.7b00617

4. Ernest Z. What are nonbonding molecular orbitals? [Internet]. 2020. Available from: https://socratic.org/questions/what-are-nonbonding-molecular-orbitals%0A

5. Uskoković V. Chemical Reactions As Petite Rendezvous: the Use of Metaphor in Materials Science Education. J Mater Educ. 2014;36(1–2):25–50.

6. Kasha M. Characterization of electronic transitions in complex molecules. Discuss Faraday Soc. 1950;9(c):14. Available from: http://xlink.rsc.org/?DOI=df9500900014

7. Demchenko AP, Tomin VI, Chou P-T. Breaking the Kasha Rule for More Efficient Photochemistry. Chem Rev. 2017;117(21):13353–81. Available from: https://pubs.acs.org/doi/10.1021/acs.chemrev.7b00110

8. Yanagi K, Kataura H. Breaking Kasha's rule. Nat Photonics. 2010;4(4):200–1. Available from: http://www.nature.com/articles/nphoton.2010.77

9. Yushchenko O, Licari G, Mosquera-Vazquez S, Sakai N, Matile S, Vauthey E. Ultrafast Intersystem-Crossing Dynamics and Breakdown of the Kasha–Vavilov's Rule of Naphthalenediimides. J Phys Chem Lett. 2015;6(11):2096–100. Available from: https://pubs.acs.org/doi/10.1021/acs.jpclett.5b00882

10. Fermi E. Nuclear Physics. University of Chicago Press; 1950.

11. Coolidge AS, James HM, Present RD. A Study of the Franck-Condon Principle. J Chem Phys. 1936;4(3):193–211. Available from: http://aip.scitation.org/doi/10.1063/1.1749818

12. Aloïse S, Ruckebusch C, Blanchet L, Réhault J, Buntinx G, Huvenne J-P. The

Benzophenone S 1 (n,π*) → T 1 (n,π*) States Intersystem Crossing Reinvestigated by Ultrafast Absorption Spectroscopy and Multivariate Curve Resolution. J Phys Chem A. 2008;112(2):224–31. Available from: https://pubs.acs.org/doi/10.1021/jp075829f

13.   El-Sayed MA. Spin—Orbit Coupling and the Radiationless Processes in Nitrogen Heterocyclics. J Chem Phys. 1963;38(12):2834–8. Available from: http://aip.scitation.org/doi/10.1063/1.1733610

14.   Steffen A, Hupp B. Design of Efficient Emissive Materials. In: Reference Module in Chemistry, Molecular Sciences and Chemical Engineering. Elsevier; 2019. p. 1–37. Available from: http://dx.doi.org/10.1016/B978-0-12-409547-2.14753-5

15.   Medintz I, Hildebrandt N, editors. FRET – Förster Resonance Energy Transfer [Internet]. Wiley; 2013. Available from: https://onlinelibrary.wiley.com/doi/book/10.1002/9783527656028

16.   SCHAUFELE F, DEMARCO I, DAY RN. FRET Imaging in the Wide-Field Microscope. In: Molecular Imaging. Elsevier; 2005. p. 72–94. Available from: https://www.sciencedirect.com/science/article/pii/B9780195177206500134?via%3Dihub

17.   LibreTexts. Dexter Energy Transfer [Internet]. 2020. Available from: https://chem.libretexts.org/Bookshelves/Physical_and_Theoretical_Chemistry_Textbook_Maps/Supplemental_Modules_(Physical_and_Theoretical_Chemistry)/Fundamentals/Dexter_Energy_Transfer

Chapter 3 Experimental methods

This chapter introduces the experimental methods used in this project, including the protocols for computational simulations, substrate cleaning, film and solution preparations, and photophysical measurements. In addition, I built a setup for time-resolved PL (TRPL) spectrum measurements, which plays an important role in thermally activated delayed fluorescence (TADF) and organic long-persistent luminescence (OLPL) mechanism studies.

Z. Li and C. Si performed the molecular calculations and material synthesis in E. Zysman-Colman's group at the University of St Andrews. Thermal gravimetric analysis (TGA), differential thermal analysis (DTA) and differential scanning calorimetry (DSC) was conducted by the technicians in school of chemistry at the St Andrews. I carried out the photophysical measurements, sample preparation, OLED fabrication and characterisations in I. D. W. Samuel's group at the University of St Andrews. I also built the TRPL spectrum measurement setup by combining the time-gated intensified CCD (iCCD) and the femtosecond laser in I. D. W. Samuel's group. Within this setup A. Ruseckas helped to integrate a third-harmonic crystal to the 1030 nm femtosecond laser to obtain the emission at 343 nm. The TRPL decay measurement setup for OLPL samples in longer time windows (> 1 s) was built by R. Kabe in C. Adachi's group at Kyushu University.

3.1 Computational modelling

Density Functional Theory (DFT) calculations were performed with Gaussian 09 revision D.018 suite (1). Initially the ground state geometry was fully optimized using a DFT methodology employing the PBE0 -functional with the standard Pople 6-31G (d, p) basis set (2). Excited state calculations were performed using Time-Dependent DFT (TD-DFT) and with the Tamm-Dancoff approximation (TDA) (3) using the same functional basis set. This methodology has been shown to provide accurate quantification of ΔE_{ST} in comparison to experiment (4).

3.2 Thermal gravimetric analysis and Differential thermal analysis

Thermal gravimetric analysis (TGA) and Differential thermal analysis (DTA) was performed on a Stanton Redcroft STA-780 instrument. Differential scanning calorimetry (DSC) was performed on a NETZSCH Thermal Analysis DSC 204 F1 Phoenix instrument.

3.3 Electrochemistry measurements

Cyclic voltammetry (CV) and differential pulse voltammetry (DPV) analysis were performed on an Electrochemical Analyzer potentiostat model 620E from CH Instruments. Samples were prepared in acetonitrile (MeCN) solutions, which were degassed by sparging with MeCN-saturated nitrogen gas for 5 minutes prior to measurements. All measurements were performed using 0.1 M tetra-*n*-butylammonium hexafluorophosphate, [*n*Bu$_4$N]PF$_6$, in MeCN. An Ag/Ag$^+$ electrode was used as the reference electrode; a platinum electrode was used as the working electrode and a platinum wire was used as the counter electrode. The redox potentials are reported relative to a saturated calomel electrode (SCE) with a ferrocenium/ferrocene (Fc/Fc$^+$) redox couple as the internal standard (0.38 V vs SCE) (5).

3.4 Substrate cleaning and sample preparation

3.4.1 Substrate cleaning

Glass, quartz, sapphire and tin-doped indium oxide (ITO) substrates were washed by ultrasonication in acetone and then isopropanol for 15 min followed by exposure to oxygen plasma for 3 min to remove all the dust and organics on the sample surfaces. In addition, glass

substrates for OLPL film fabrication were heated up by a heat gun for 30 s before the sample fabrication to remove all the remaining solvents.

3.4.2 Solution sample preparations

All solution samples were prepared in HPLC grade toluene (PhMe), dichloromethane (DCM) or acetonitrile (MeCN) with varying concentrations on the order of 10^{-5} or 10^{-6} M for absorption and emission studies. Degassed solutions were prepared via three freeze-pump-thaw cycles prior to emission analysis using an in-house adapted fluorescence cuvette, itself purchased from Starna Scientific.

3.4.3 Film sample preparations

Solution processed doped thin films were prepared by mixing hosts and guest in organic solvents, followed by spin-coating on quartz or sapphire substrates at a speed of 2000 revolutions per minute for 1 min. Thermally evaporated films were fabricated on quartz or sapphire substrates in the evaporator (Angstrom Engineering, 03123 EVOVAC D00 vacuum deposition system) inside a glovebox.

OLPL films based on small-molecule hosts, such as 2,8-bis(diphenyl-phosphoryl)dibenzo[b,d]thiophene (PPT) and 2,2',2"-(1,3,5-Benzinetriyl)-tris(1-phenyl-1-H-benzimidazole) (TPBi), were fabricated by melt-casting mixed host and guest powders on glass substrates between 250 ^{o}C and 270 ^{o}C, which is similar to the method described in Jinnai *et al*.'s work (6). The OLPL samples using PMMA as the host were fabricated though drop-casting or synthesizing from PMMA's monomer, which is discussed in detail in Chapter **9**.

3.5 Photophysical measurements

3.5.1 Ambient pressure photoemission spectroscopy

Ambient pressure photoemission spectroscopy (APS) measurements were performed using a KP Technology state model. Film samples for the APS measurement were prepared by vacuum deposition of 60 nm organic materials on cleaned ITO substrates. Figure **3.1** shows a schematic diagram of the working principle of the APS setup. During the APS measurement, the samples

were grounded by connecting the ITO to earth so as to avoid charge accumulation. Excitation light from a deuterium lamp was passed through a monochromator and then directed onto the sample surface through a fibre optic cable. Photoelectrons can be extracted from the sample when the incident photon energy exceeds the HOMO energy levels of the materials. These photoelectrons created a cloud of charges which were then collected by a Kelvin Probe tip held at a potential of +70 V. The cube root of the measured photocurrent yield was plotted against incident photon energy, and the HOMO value was estimated by extrapolating the tangent of the curve down to the x axis.
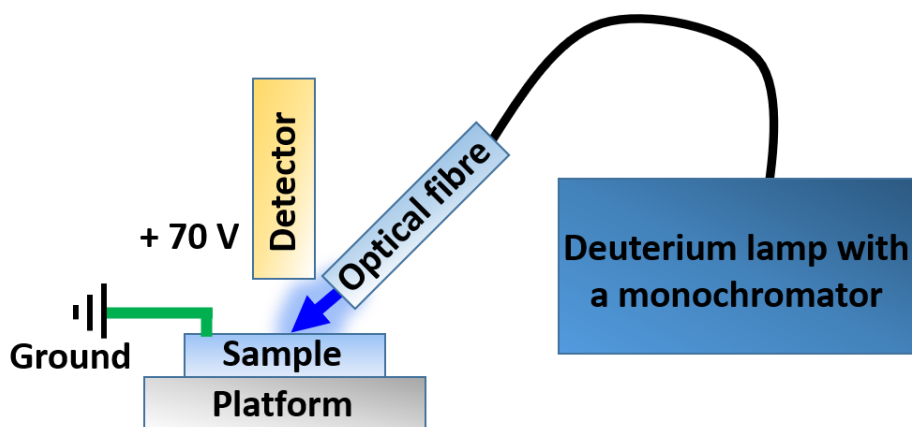
Figure 3.1. Schematic diagram of the working principle of APS.

3.5.2 Photoluminescence quantum yields

Photoluminescence quantum yields (PLQY) for solutions (excited at 340 nm) were determined using the optically dilute method (7). A stock solution with absorbance of ca. 0.353 at 340 nm was prepared and then four dilutions were prepared with dilution factors of 4.25, 5.8, 8 and 15 to obtain solutions with absorbances of ca. 0.083, 0.061, 0.044 and 0.024, respectively. The absorbance calculated by the Beer-Lambert law was found to be proportional to the concentrations of the solutions. For each sample, linearity between absorption and emission intensity was verified using linear regression analysis and additional measurements were acquired until the Pearson regression factor (R^2) for the linear fit of the data set surpassed 0.9. Individual relative quantum yield values were calculated for each solution and the values reported represent the gradient value. The equation $\Phi_s = \Phi_r(A_r/A_s)(I_s/I_r)(n_s/n_r)^2$ was used to calculate the relative quantum yield of each of the sample, where Φ_r is the absolute quantum yield of the reference, n is the refractive index of the solvent, A is the absorbance at the excitation wavelength, and I is the integrated area under the corrected emission curve. The

subscripts *'s'* and *'r'* refer to the sample and reference, respectively. A solution of Rhodamine 6G in ethanol (Φ_r = 94%) was used as the external reference (8).

A Hamamatsu C9920-02 integrating sphere was employed for the PLQY measurements of thin film samples (with 5% of the measurement error). A xenon lamp coupled to a monochromator enabled selective excitations, chosen here to be 340 nm as the excitation wavelength. The output was then fed into the integrating sphere via a fibre, exciting the sample. PL spectra were collected with a multimode fibre and detected with a back-thinned CCD. Then the quantum yields of the films were measured in air and N_2 atmosphere by purging the integrating sphere with flowing N_2 gas.

3.5.3 Steady-state absorption

Steady-state absorption spectra were recorded using an absorption spectrometer (Cary, 300 Bio). Molar absorptivity determination was verified by linear least-squares fit of values obtained from at least five independent solutions at varying concentrations with absorbance ranging from 2.6×10^{-6} to 4.4×10^{-3} M^{-1} cm^{-1}.

3.5.4 Steady-state PL spectra and time-resolved PL decay measurements

The steady-state PL spectra and the TRPL decays measured in time windows shorter than 2 seconds were obtained using a fluorimeter (Edinburgh Instruments, FLS 980). The wavelength axis and the responsivity of its detector has been calibrated by the manufacture. The samples for the steady-state PL spectrum measurements were excited at 340 nm using a xenon lamp, while the samples for the TRPL decay measurements were excited at 375 nm using a picosecond laser (PicoQuant, LDH-D-C-375, FWHM < 40 ps, pulse energy = 58.5 ± 1.2 pJ, peak power = 1.5 ± 0.3 W, laser spot diameter = 0.4 ± 0.1 mm, power density = 11.6 ± 3.7 mW/cm^2) driven by a laser driver (PDL 800-D). Within the TRPL decay measurements in this thesis, short-time range (200 ns – 20 µs) PL decays were measured using the time-correlated single photon counting (TCSPC) mode. Long-time range (10 ms – 2 s) PL decays were measured using the multi-channel scaling (MCS) mode.

TCSPC is usually used as a technique to record fast decays (typically from picosecond to microsecond timescales). A schematic diagram of the mechanism of TCSPC is shown in Figure

3.2. In this setup, the function generator spontaneously sends a reference pulse to the time-to-digital converter (TDC) and another pulse to trigger the laser. The sample is excited by the laser and the sample emission is attenuated to make sure that at most only a single photon can reach and be detected by the photomultiplier tube (PMT). The PMT converts the single photon into electrical signal which is then sent to the TDC to compare the arrival time difference between this electrical signal and that of the reference pulse, and these arrival time differences are recorded for statistics. After many cycles of arrival time difference comparisons, the frequency of each time difference can be obtained and is illustrated in a histogram which reflects the decay kinetics of the sample. It is important to make sure only one photon reaches the PMT in each excitation cycle so as to guarantee the histogram generated by the TDC can represent the sample decays. TCSPC systems are usually designed to register only one photon per excitation cycle. Therefore, if the number of photons arriving in each excitation cycle are typically > 1, the system would only register the first photon, which would lead to an over-representation of early photons in the histogram and make the measured decay lifetimes shorter than the real decay lifetimes. In practice, to maintain single photon statistics, the sampling rate of the PMT was set below 5% of the repetition rate of the reference pulse, and so there will be no photons in most measurement cycles.
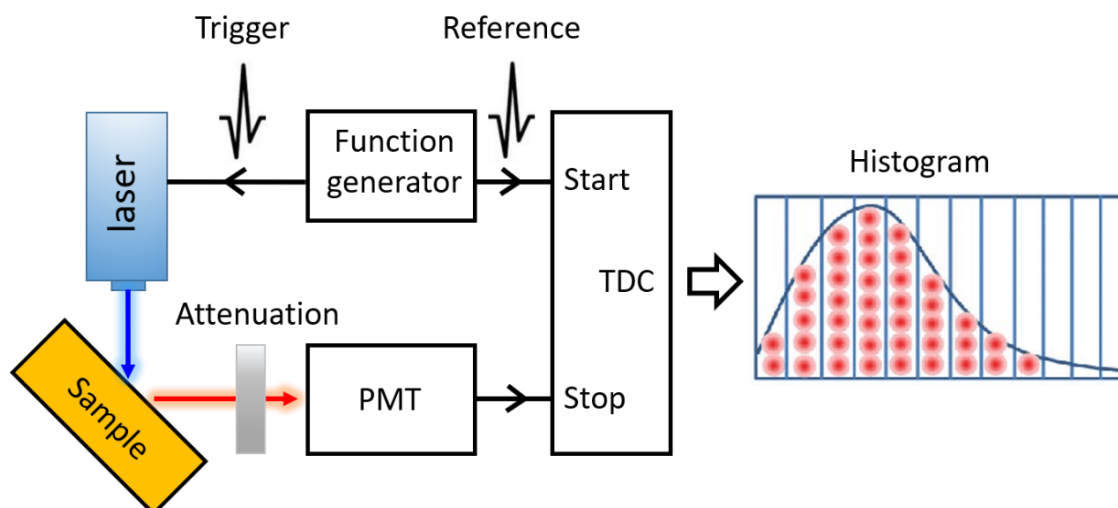
Figure 3.2. Schematic diagram of the working principle of TCSPC.

MCS is a technique used to record relatively slow decays (typically in millisecond and second timescales). The experimental setup of MCS mode is similar to that of TCSPC (Figure **3.2**) with the difference that a shift register is used in MCS instead of the TDC. In addition, the numbers of photons are counted in very different ways in these two modes. In TCSPC mode, the detector

only detects a maximum of one photon in each excitation cycle, while, in MCS mode, the PMT is set to count many photons in each cycle. Figure **3.3** shows a schematic diagram of the working principle of photon counting in MCS mode. The shift register is synchronous to the excitation laser, and the software allocates the detection time length for each time bin in the shift register according to the required measurement time window and the number of detecting channels. For example, assuming the allocated detection duration is 1 ms for each time bin (Figure **3.3**), when a measurement cycle starts, only the first time bin is activated. The PMT counts the number of photons it receives within the first 1 ms and saves this number into the first channel. After the detection duration of the first 1 ms is fulfilled, the detection gate moves to the second time bin, and the PMT again starts to count the number of photons it receives in the second 1 ms, and it saves this number into the second time bin. Therefore, the number of counts in each time bin can reflect the intensity of the sample emission over time.
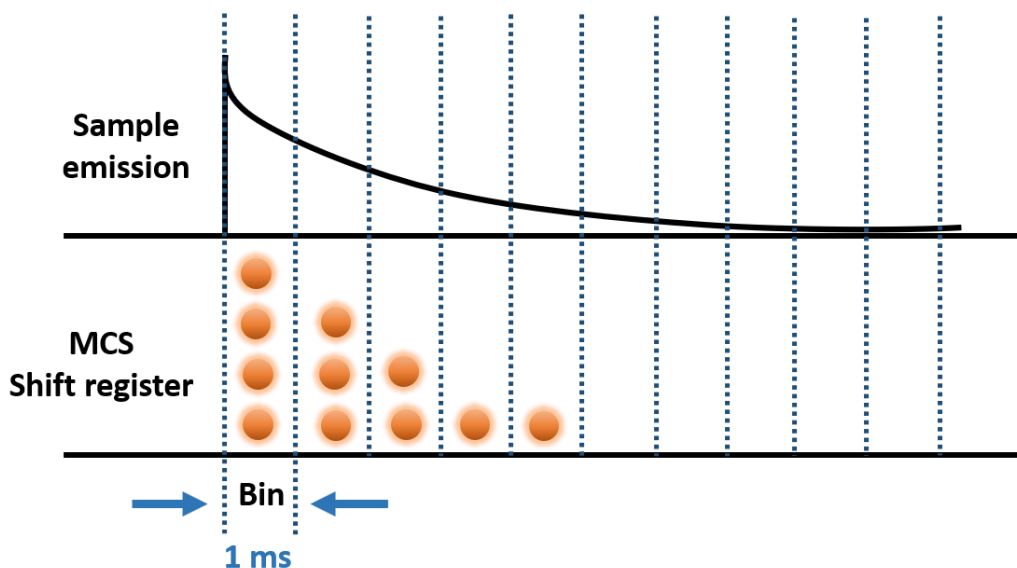
Figure 3.3. Schematic diagram of the working principle of MCS.

Importantly, within each time bin, the minimum time interval between two photon counting is 100 ns. Therefore, the PMT is more easily saturated when detecting the prompt component from samples and distort the PL decay profiles in early time. On the other hand, if the PMT always receives a very small number of photons during the detection, a PL decay measurement may take a long time. To solve this dilemma with appropriate sample emission intensity, the laser is triggered in burst mode in the MCS measurements to adjust the number of photons used for excitation. It is realized by integrating a delay generator (Stanford Research Systems, DG645) between the function generator and the laser driver. A schematic diagram of the working principle of burst mode is shown in Figure **3.4**. When the delay generator receives a pulse signal

from the function generator, it outputs a larger number of pulses according to the setting. In this delay generator, the time interval between each two generated pulses is 100 ns. The output of the delay generator is used as the laser trigger signal, and so more laser pulses can be used for sample excitation in each measurement cycle instead of one. Although this excitation technique distorts the PL decay profiles in nanosecond and microsecond time windows, its effect should be negligible in millisecond and second time windows which are the main focus of MCS measurements. Furthermore, to minimize the decay profile distortion caused by the burst mode, the duration of the entire excitation burst is always set to be shorter than the detection duration of a time bin.
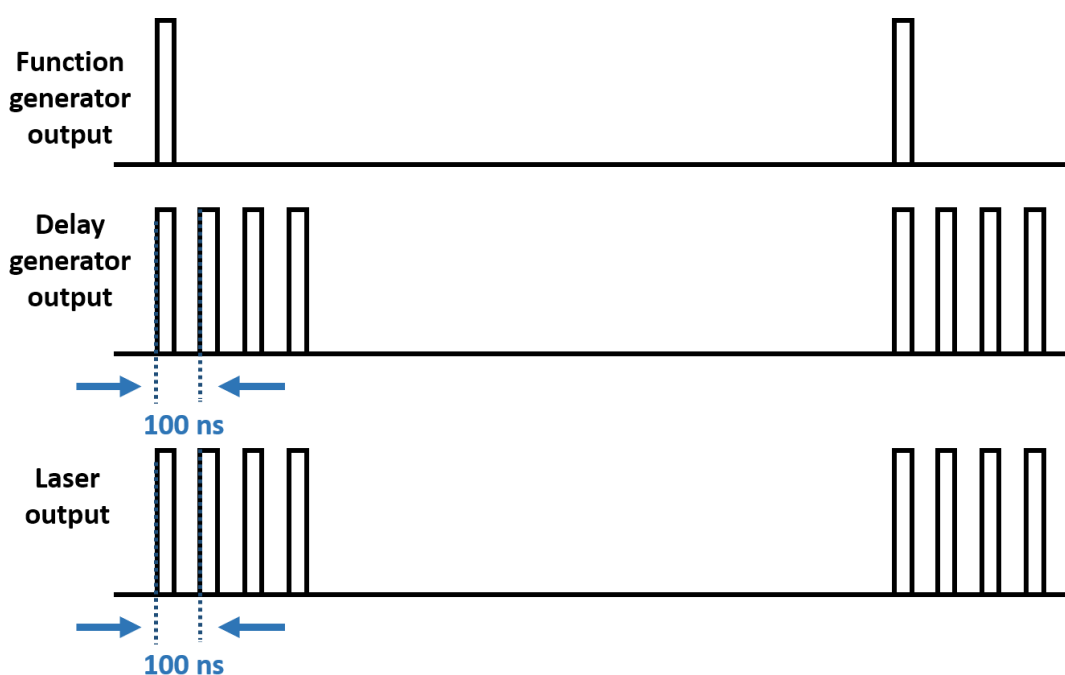
Figure 3.4. Schematic diagram of the working principle of burst mode.

3.5.5 Time-resolved spectroscopy and time-gated intensified CCD

Time-resolved spectroscopy reveals the spectral evolution of a light-emitting system over time. It can separate the emission spectrum of each excited state according to their different light-emitting time windows. Therefore, time-resolved spectroscopy is important for light-emitting material studies especially for TADF emitters which have different light emitting mechanisms over time, namely prompt fluorescence (ps-ns), TADF (µs-ms) and RTP (ms-s). When the author joined the group, there was no experimental setup for the spectrum measurements in microsecond and millisecond time windows for TADF and RTP studies. To achieve the goal, the

author built a setup by combining the time-gated intensified CCD (iCCD, Stanford Computer Optics, 4Picos) and the femtosecond laser (Orpheus-N, model: SP-06-200-PP) in this group. The iCCD has a 1%-to-90% rise time of 30 ps, and the detection time-resolution down to 200 ps. At the same time, the femtosecond laser has a pulse width (FWHM) of 190 fs with its tuneable repetition rate from 100 kHz and 100 Hz. Therefore, this setup provides the capability of measuring the TRPL spectra from 200 ps to 10 ms, which can cover the timescales of most of the light-emitting species in TADF emitters. Furthermore, as TADF materials usually need high energy photon in UV regime for excitation, the 1030 nm light from the femtosecond laser was converted into 343 nm light using a third harmonic crystal. After the wavelength conversion, the 343 nm laser beam has the pulse energy of 488 nJ and peak power of 2.7 MW. Moreover, TADF samples have various forms such as films, liquids and powders. Also, these samples are required to be measured at different temperatures (77 K ~ 300 K). Therefore, the author integrated different sample holders into the setup, which enables the measurement for the samples of all these forms between 77 K to 300 K. The details of this setup are described below:

Figure **3.5a** shows the schematic diagram of this measurement setup, and Figure **3.5b** shows the photo of it. After passing though the optical shutter (when the shutter was open), the 343 nm laser beam was sent to a flipping mirror for the choice of optical path. Optical path **1** was used to excite film samples in the cryostat (as shown in Figure **3.6a**) as it enables the laser excitation from the side of the cryostat and the emission collection from the front of it. Optical path **2** was used to excite solution or powder samples loaded in NMR tubes (as shown in Figure **3.6d**) because this optical path allows both the laser excitation and emission collection from the front. This is important for powder and frozen solution samples because the transparency of them is low, and so exciting and detecting from the same side of the samples can minimize the effect of reabsorption or light scattering. However, optical path **2** cannot take the place of optical path **1** because the quartz windows in the cryostat are not sufficiently large to allow the laser beam to hit on the film samples through optical path **2**. Therefore, both optical paths were integrated in this setup.

After the optical path selection (e.g. optical path **1**), the laser beam was then focused by a lens and guided on the film samples inside the cryostat to increase the excitation intensity (laser spot diameter = 1.2 ± 0.2 mm, power density = 2.3 ± 0.4 MW/cm^2). The sample emissions were collected by a lens set (a telescope) and then sent to a spectrograph (Brucker Optics, Chromex 250is Imaging Spectrograph) for spectrum analysis. The focal lengths of these lenses are 200 mm

(the left one in Figure **3.5a**) and 60 mm (the right one in **Figure 3.5a**), respectively. The 200 mm one was used to fit the numerical aperture of the spectrograph, while the 60 mm one provides a short distance between the lens and the samples so as to maximize the light collection efficiency. A 350 nm long-pass-filter was used before the spectrograph to block the 343 nm excitation light scattered from the samples. On the spectrum detection side, the iCCD was synchronized with the laser and its light detection was controlled by a lab PC.

In the TRPL spectrum measurement process, the wavelength axis of the iCCD was first calibrated using the fluorescent room lights. The background noise from the iCCD and the environmental light were then collected when the optical shutter was closed. Finally, the emission spectra from samples were collected when the optical shutter was open, and the collected emission spectra were then subtracted by the background spectra for corrections.
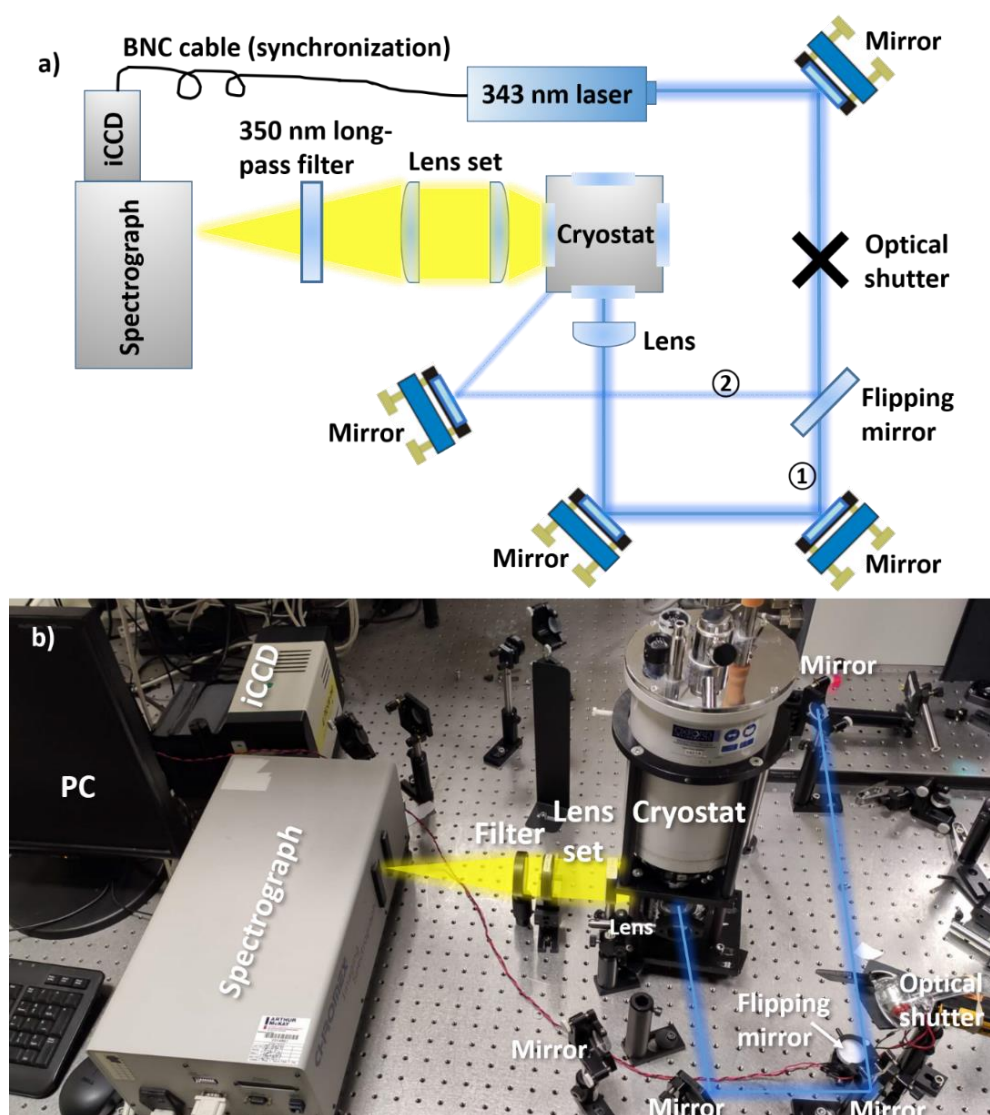
Figure 3.5. a, b) Schematic diagram and photo of the TRPL spectrum measurement setup.

On the sample holder side, there are three different holders for different kinds of samples. Figure **3.6a** shows the photo of a cryostat for film sample measurements. This cryostat conducts the heat from film samples through a copper cold finger whose temperature can be set in the range between 77 K and 300 K, which was controlled by a temperature controller (MercuryiTC, Oxford Instrument). Furthermore, the film samples were fabricated on sapphire substrates to guarantee a good thermal conductivity between the substrate and the organic materials, and so the temperature of the organic materials can be well controlled. Figure **3.6b** shows another cryostat for powder and solution measurements, which uses helium as the exchange gas for heat conduction. Also, the cuvette for loading the solution and powder samples used in this cryostat is shown in Figure **3.6c**. The combination of this cryostat and the long cuvette also enables the solutions and powders to be measured between 77 K and 300 K. Figures **3.6d** and **3.6e** show a suprasil nitrogen dewar flask for holding NMR tubes. This dewar has a double wall glass with vacuum in between, and so liquid nitrogen can be maintained inside for more than 15 min. In addition, this dewar was placed in a 3D printed plastic holder during the measurements (Figure **3.6d**). Liquid and powder samples can be cooled down in NMR tubes when the NMR tubes were soaked in the liquid nitrogen bath. Although this dewar only allows the measurements to be carried out at room temperature and 77 K, it is sufficient for most of TADF materials studied in liquid phase.
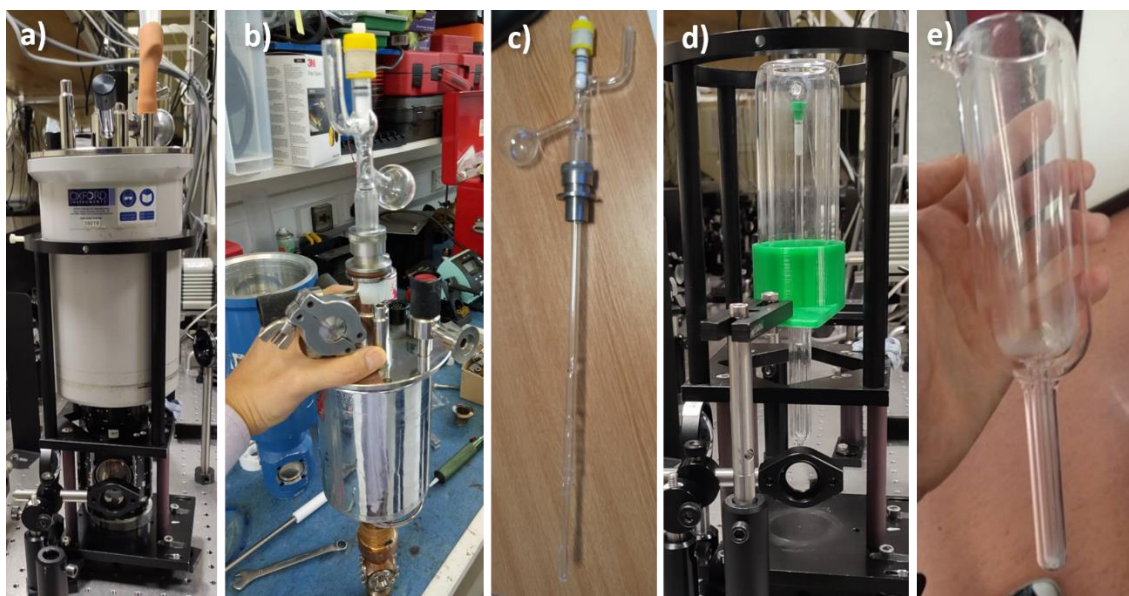
Figure 3.6. Photographs of the three cryostats used. a) Cryostat with cold finger for film samples. b) Cryostat using He exchange gas for solution and powder samples. c) The cuvette used in the cryostat shown in Figure **3.6b**. d, e) Suprasil nitrogen dewar flask for NMR tubes with the 3D printed holder (green).

3.5.6 Measurement of singlet-triplet splitting energy

The singlet-triplet splitting energy, ΔE_{ST}, was estimated by comparing the prompt fluorescence and the delayed phosphorescence spectra obtained at 77 K. Film samples were prepared on sapphire substrates and cooled down to 77 K in the cryostat with a cold finger (Figure **3.6a**). 77 K solution glass samples were prepared by transferring solution into NMR tubes which were subsequently cooled down inside the suprasil nitrogen dewar flask in a liquid nitrogen bath (Figure **3.6d**). Film or frozen solution samples were photoexcited at 343 nm and their emissions were detected by the iCCD. Prompt fluorescence spectra were integrated between 1 ns – 100 ns after photoexcitation. Phosphorescence spectra were integrated between 0.1 – 1 ms after photoexcitation for solution samples and 1-10 ms after photoexcitation for film samples. The energy levels of S_1 and T_1 were determined from the onsets of these fluorescence and phosphorescence spectra.

3.5.7 OLPL spectrum measurement

After the preparation of OLPL films using the method described in Section **3.4.3**, the 1-100 ns and 1-10 ms emission spectra from the 300 K films and 1-10 ms emission spectra from 77 K films were measured by the iCCD setup described in Section **3.5.5**. The 1-3 s and 5-56 s spectra were measured by a fibre coupled CCD spectrograph (Andor, Model Number: DV420-BV), and the excitation source was a 365 nm LED. The responsivity of the CCD has been calibrated using a standard tungsten lamp.

3.5.8 OLPL decay curve measurements

To obtain the TRPL decay profiles of long-lived (> 10 s) but weak (< 1 μW) OLPL (as discussed in Chapter **8** and **9**), a silicon-photomultiplier (SiPM, C13366-1350GA, Hamamatsu photonics) based setup was built at Kyushu university. This SiPM is composed of an array of avalanche photodiodes which can detect optical powers as low as 1 pW at it peck sensitive wavelength of 500 nm. A built-in amplifier converts the number of photons it receives per second into the voltages it outputs. The output voltage is designed to be linear to the incident optical power. Figure **3.7a** shows the schematic diagram of this TRPL decay measurement setup and Figure **3.7b**

shows a photo of it. In this setup, OLPL film samples were placed in a cryostat under vacuum (pressure < 1 × 10^{-4} mbar) for a water and oxygen free environment. A 365 nm LED (M365LP1, Thorlabs) was used as the excitation source, and a fibre coupled spectrometer (QE-Pro, Ocean photonics) was used for emission spectrum detections. The SiPM was connected to a multimeter (34461A, Keysight) for its voltage readings, which was used to determine the OLPL intensity. During the OLPL detection process, samples were excited by the LED continuously for 60 s or longer, and the TRPL decay detections started 1 s after the photoexcitation. The sample rate of the SiPM was around 1 Hz. The excitation and detection were synchronized by a computer.
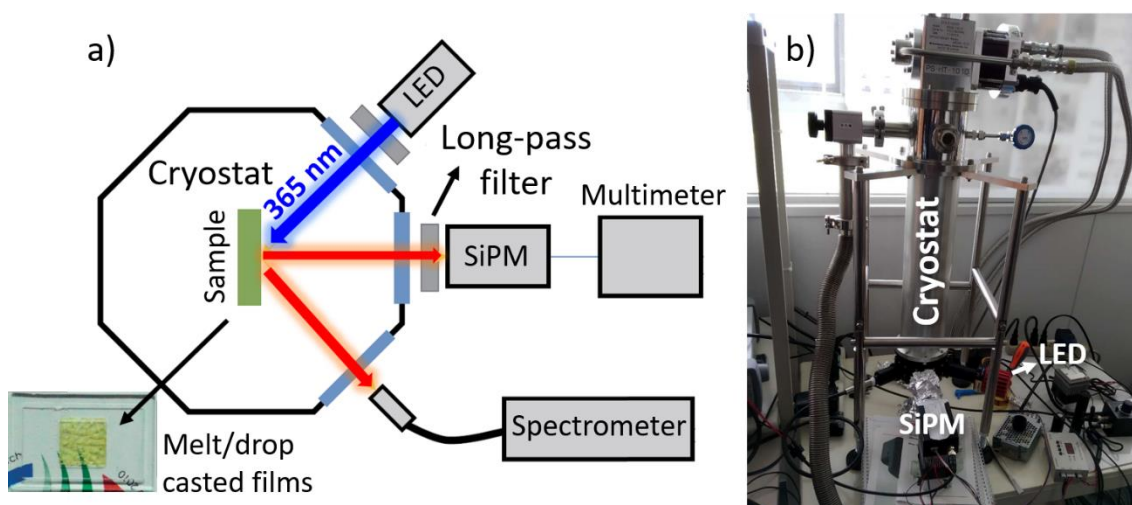
Figure 3.7. a, b) Schematic diagram and the photo of the SiPM-based TRPL decay measurement setup for OLPL samples.

3.6 OLED fabrication and characterisation

OLEDs were fabricated in bottom emitting architecture on ITO (thickness: 900 Å, resistivity: <30 ohms/sq, transmission: >88% at 550nm, from Thin Film Devices). After being cleaned according to the process described in Section **3.4.1**, the substrates were immediately transferred into the Angstrom evaporator inside a glovebox. The chamber of the evaporator is then pumped down to lower than 7 × 10^{-7} mbar for organic material thermal evaporations. After the evaporation, the OLEDs were taken out from the evaporator and encapsulated inside the glovebox with desiccant inside the encapsulation glass for water absorption. The OLED active areas were 2 mm^2 (pixels dimension: 1 mm × 2 mm).

The OLEDs were taken out from the glovebox for current-voltage-luminance characteristics, and the schematic diagram of the characterisation setup is shown in Figure **3.8**. Within the OLED

characterisation processes, voltages were scanned across the OLED using a source meter (Keithley 2400) with the current measured for each applied voltage. The OLED emission intensity was detected by a photodiode whose output current was converted into voltage by a transimpedance amplifier. The output voltage of this amplifier is designed to be linear to the incident optical power, this output voltage was measured by a multimeter (Keithley 2000). The EL emission spectra were collected by an optical fibre connected to the same spectrograph (Andor CCD) used for OLPL spectrum measurements in longer time windows. Combining the EL emission spectra, photodiode voltages and the response function of the photodiode, the total photon numbers emitted from the OLEDs can be estimated when the emission patterns of the OLEDs are assumed to be Lambertian. In addition, the total numbers of the electron injected into the OLEDs can be estimated by the measured current, and so the external quantum efficiency (EQE) of the OLEDs can be calculated by dividing the number of the emitted photons by the number of injected electrons.
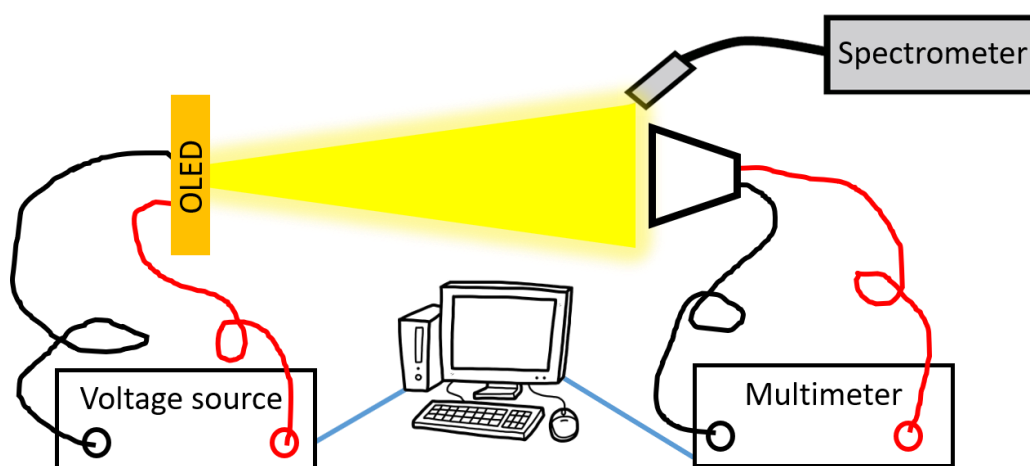
Figure 3.8. Schematic diagram of the OLED characterisation setup.

3.7 References

1.   M. J. Frisch, G. W. Trucks, H. B. Schlegel, G. E. Scuseria, M. A. Robb, J. R. Cheeseman, G. Scalmani, V. Barone, G. A. Petersson, H. Nakatsuji, X. Li, M. Caricato, A. Marenich, J. Bloino, B. G. Janesko, R. Gomperts, B. Mennucci, H. P. Hratchian, J. V. Ort and DJF. Gaussian 09. Wallingford CT: Gaussian Inc.; 2013.

2.   Pople JA, Binkley JS, Seeger R. Theoretical models incorporating electron correlation. Int J Quantum Chem. 2009;10(S10):1–19. Available from:

http://doi.wiley.com/10.1002/qua.560100802

3.   Moral M, Muccioli L, Son W-J, Olivier Y, Sancho-García JC. Theoretical Rationalization of the Singlet–Triplet Gap in OLEDs Materials: Impact of Charge-Transfer Character. J Chem Theory Comput. 2015;11(1):168–77. Available from: https://pubs.acs.org/doi/10.1021/ct500957s

4.   Crosby GA, Demas JN. Measurement of photoluminescence quantum yields. Review. J Phys Chem. 1971;75(8):991–1024. Available from: https://pubs.acs.org/doi/abs/10.1021/j100678a001

5.   Pavlishchuk V V, Addison AW. Conversion constants for redox potentials measured versus different reference electrodes in acetonitrile solutions at 25°C. Inorganica Chim Acta. 2000;298(1):97–102. Available from: https://linkinghub.elsevier.com/retrieve/pii/S0020169399004077

6.   Jinnai K, Kabe R, Adachi C. Wide-Range Tuning and Enhancement of Organic Long-Persistent Luminescence Using Emitter Dopants. Adv Mater. 2018;30(38):1800365. Available from: http://doi.wiley.com/10.1002/adma.201800365

7.   HORIBA. Recording Fluorescence Quantum Yields [Internet]. 2021. Available from: https://www.horiba.com/en_en/applications/materials/material-research/quantum-dots/recording-fluorescence-quantum-yields/

8.   Fischer M, Georges J. Fluorescence quantum yield of rhodamine 6G in ethanol as a function of concentration using thermal lens spectrometry. Chem Phys Lett. 1996;260(1–2):115–8. Available from: https://linkinghub.elsevier.com/retrieve/pii/000926149600838X

Chapter 4 Introduction to Thermally Activated Delayed Fluorescence

Efficient organic emitters are important for the applications of OLEDs. This chapter briefly overviews the four classes of organic emitters people have developed, namely fluorescent emitters, phosphorescent emitters, triplet-triplet annihilation (TTA) emitters and thermally activated delayed fluorescence (TADF) emitters, and especially focuses on the recent mechanism developments in TADF emitters and the consequent ideal molecular designs for them. Also, the challenges of TADF material development are also introduced.

4.1 OLED emitter overviews

There are various ways to harvest light emission from excited states. To date, people have developed four classes of organic emitters, namely fluorescent emitters, phosphorescent emitters, TTA emitters and TADF emitters. Among these emitters, phosphorescent, TTA and TADF emitters were proposed to obtain the emission from triplets which are non-emissive in fluorescent emitters, and so the light-emitting efficiency can be improved. The mechanisms of these four classes of emitters are briefly introduced below to demonstrate the fundamental advantages of TADF emitters:

Figure **4.1a** shows the schematic diagram of the emission process in a fluorescent OLED. When excitons are generated in an OLED, according to spin statics and experimental analysis (1,2), there is around 25 % chance for S_1 formation and 75 % for T_1 formation. The energy splitting between the S_1 and T_1, ΔE_{ST}, is usually large (> 0.6 eV), and the spin-orbit coupling (SOC) is small in the fluorescent emitters which are composed of light atoms (e.g. N, H, C, O. etc.). Therefore, the rates of intersystem crossing (k_{ISC}) and reverse intersystem crossing (k_{rISC}) are usually negligible. Also, the emissive transition between T_1 and S_0 (phosphorescence) is not allowed. Therefore, only the S_1 which accounts for 25 % of all the generated excitons can show emission, which causes a substantial energy waste. Although, fluorescent emitters are not energy-efficient for light emission, they usually have long operation lifetimes, and so they are widely used in commercial blue OLEDs (3).

In comparison, phosphorescent emitters which contain heavy atoms (such as Ir, Pt, Os. etc.) can theoretically make 100% use of all the excitons for light emission (4–6). Figure **4.1b** shows the emission process in a phosphorescent OLED. As has been discussed in Section **2.1.10**, because of the heavy atom effect, the strong SOC makes the transitions between triplets and singlets allowed. The consequent k_{ISC} is so high that all the S_1 excitons are converted into T_1 excitons before they show fluorescence. Therefore, all the excitons decay to S_0 through the phosphorescence channel. Because of their high light-emitting efficiencies, phosphorescent emitters are commercially used in red and green OLEDs (3). However, those commonly used heavy atoms are rare, expensive, and toxic, and so may not be sustainable for long-term and large-scale OLED fabrications.

Figure **4.1c** shows the emission process in a TTA OLED. TTA emitters also do not contain heavy metals, and the core working principle of this class of emitters is converting non-emissive T_1 into S_1 by TTA (7). The mechanism of TTA and Dexter energy transfer has been discussed in Section

2.12.2. Assuming each of two T_1 can be converted into one S_1, TTA emitters can use up to 62.5% of all the generated excitons for light emission, which is a lot more efficient than fluorescent emitters. However, it is still much less efficient than phosphorescent emitters which use all the excitons for light emission.
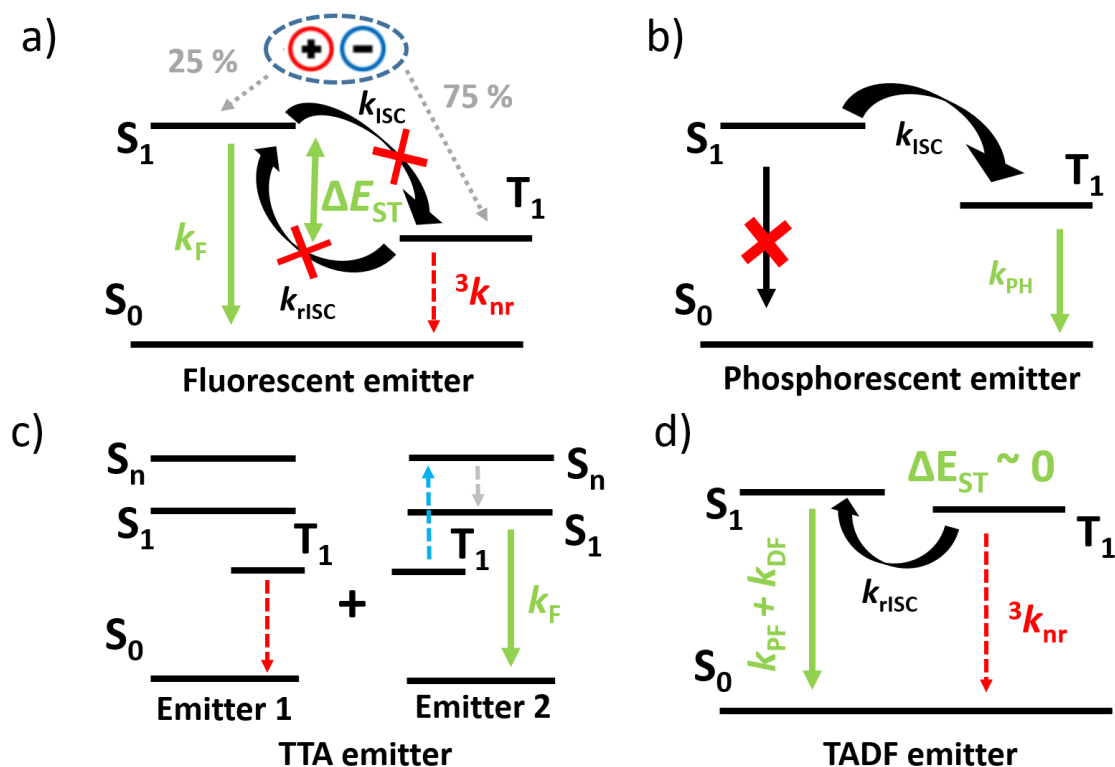
Figure 4.1. a, b, c, d) Schematic diagrams of the emission processes of fluorescent emitters, phosphorescent emitters, TTA emitters and TADF emitters in OLEDs.

TADF materials are widely regarded as the most promising emitters which can take the place of fluorescent emitters and phosphorescent emitters in commercial OLEDs. It is because TADF emitters provide a way of harvesting triplets in organic molecules, without the need for heavy atoms such as Ir and Pt. Figure **4.1d** shows a simplified mechanism diagram of TADF emitters. When the ΔE_{ST} is sufficiently small (< 0.4 eV), the emitters in T_1 states can be converted into S_1 for light emission. Since Uoyama *et al.*'s first report of efficient TADF emitters in 2012 (8), many studies have been carried out to investigate the mechanisms and molecular designs of TADF emitters. Recent models for TADF mechanisms have been improved considerably compared with the one proposed by Uoyama *et al.* which is similar to the schematic diagram shown in Figure **4.1d**. Also, the current understanding of the design strategy of TADF molecules, the molecular states in TADF molecules and the mechanisms of TADF are discussed in the following sections.

4.2 Design strategy for TADF emitters

The key requirement for TADF is to design molecules with small ΔE_{ST} (8). According to Equation **2.4**, the value of ΔE_{ST} is dependent on the overlap of HOMO and LUMO orbitals. Therefore, an effective method to reduce ΔE_{ST} is minimizing this overlap by spatially separating the HOMO and LUMO orbitals. The most common way for TADF emitter designs to achieve this is to connect strong electron-donors and electron-acceptors with their electron clouds decoupled using a bridge. The advantage of this method is that it breaks down the complicated TADF molecular designs into simpler donor and acceptor designs with different techniques for HOMO and LUMO decoupling. The commonly used donors, acceptors and bridges for donor-acceptor (D-A) type TADF emitters are summarized in Figure **4.2a**. Also, Figure **4.2b** shows an example of a TADF emitter, DPTZ-DBTO2, designed using this strategy. Within this molecule, because the donor moiety (phenothiazine) and the acceptor moiety (dibenzothiophenedioxide) are connected with a C-N bond, the dihedral angle between the donor and the acceptor is almost 90° (9), thereby decoupling the HOMO and LUMO. As the HOMO and LUMO overlap is almost 0, the resulting exchange energy, *J*, and ΔE_{ST} are small.
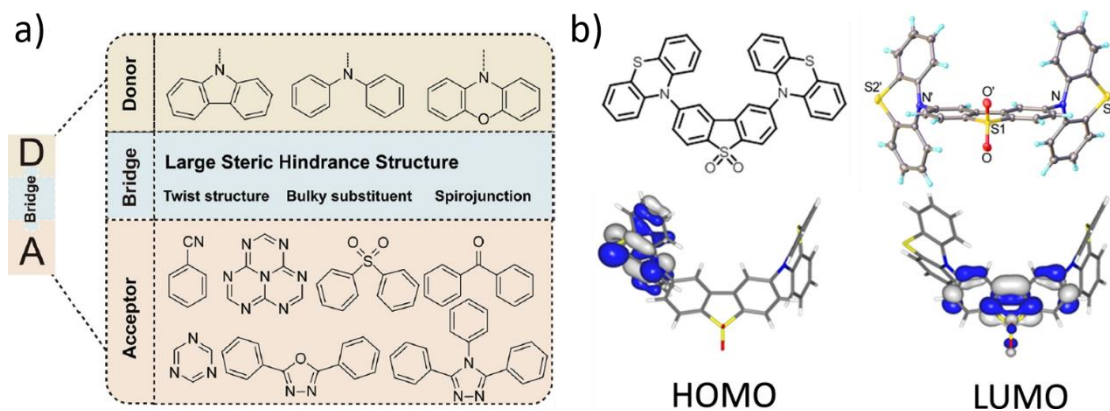
Figure 4.2. a) Schematic diagram of commonly used donors and acceptors for D-A type TADF emitters. b) The molecule structure and the HOMO/LUMO orbitals of a TADF emitter, DPTZ-DBTO2. Figures adapted from (10) and (11).

Figure **4.3a** shows a schematic diagram of the emission process in a TADF compound. Figure **4.3b** shows a schematic diagram of the molecular states in this compound and the transitions among these molecular states. The working principle of TADF compounds is very much like exciplex emitters in which charge transfer state (CT) characters are dominant in the emission process (Figure **4.3a**). However, the major difference between TADF compounds and exciplex

emitters is that CT states also exist in TADF compounds in the ground state. Therefore, as shown in Figure **4.3b**, CT absorptions can also be observed in TADF emitters but not in exciplex emitters. As the HOMO and LUMO are almost decoupled for CT states, the oscillator strengths of CT states are usually weak, and so CT absorptions are also weak. In addition, Figure **4.3b** not only shows the energy diagram of different excited states in a common TADF compound, but also the singlet and triplet states of the individual donor, acceptor and CT state. All these excited states are labelled using S_n or T_n (n = 1, 2, 3, …) according to their spins and energy levels. Normally, in a TADF compound, the S_1 state is charge transfer singlet (^1CT) state and the T_1 state is localised excited triplet state (^3LE_A) state from the acceptor moiety. In addition, the energy gap between the localised excited singlet state (^1LE) and ^3LE in individual donor or acceptor are always much larger than that between the ^1CT and charge transfer triplet state (^3CT) because the HOMO and LUMO overlap of LE states are much larger than that of CT states. Consequently, even a small energy gap is reached between the ^1CT and ^3CT states in a TADF compound, the total ΔE_{ST} of this emitter can still be large because the energy level of the ^3LE_A state can be much lower than that of the ^1CT state, which is schematically shown in Figure **4.3b**.
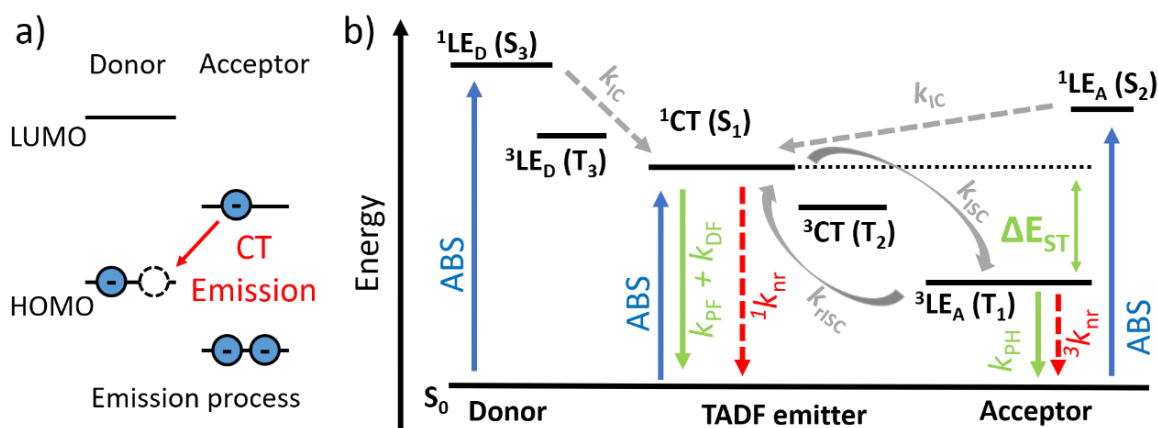
Figure 4.3. a) Schematic diagram of the emission process of donor-acceptor type TADF emitters. b) Energy diagram of the excited states of this TADF emitter.

Within the photophysical studies of this kind of TADF emitters (Figure **4.3b**), the photon absorption can happen both in LE and CT states in photoexcitation process. Following that, the emitters at higher singlet excited states (S_2 or higher) quickly decay to the ^1CT state according to Kasha's rule (Section **2.1.6**), and so fluorescence only takes place in the ^1CT state when the prompt fluorescence rate, k_{PF}, is much larger than the singlet nonradiative rate, $^1k_{nr}$, and k_{ISC}. Some ^1CT excitons can be converted into triplet excitons (^3LE) by intersystem crossing (ISC). After that, if the k_{rISC} is much higher than both the triplet nonradiative decay rate, $^3k_{nr}$, and

phosphorescence rate, k_{PH}, the ^{3}LE states (again because of Kasha's rule, all the triplets are assumed to be staying at T_1 states before further transitions) can be converted back into ^{1}CT state and show delayed fluorescence, which is the core of TADF.

For efficient TADF emitter designs, It is ideal to have high k_{rISC} (> 10^6 s^{-1}) (12) and low k_{nr} ($^1k_{nr}$ < 10^5 s^{-1}, $^3k_{nr}$ < 10^2 s^{-1}) (12,13). Also, as ground state oxygen is also a triplet state, delayed fluorescence of a TADF emitter can be easily quenched by oxygen. Therefore, comparing the PLQY difference or the changes in TRPL decay curves of the emitters with and without oxygen is usually used as a quick tool to check if TADF is operating in these emitters. Vice versa, TADF emitters can also be used for oxygen sensing because of this property.

As the definition of ΔE_{ST} is the energy splitting between the S_1 and T_1 of an emitter, an experimental way for ΔE_{ST} determinations is measuring difference between the energy levels of the S_1 and T_1. S_1 and T_1 energy levels can be calculated by the onsets of the fluorescence and phosphorescence spectra of an emitter (e.g. Figure **5.4**). Because of the simplicity of this method, it was used as the only way for ΔE_{ST} determinations in this thesis. However, according to Boltzmann distribution, k_{rISC} can also be expressed using Equation **4.1** (14):

$$k_{rISC} = A exp(^{-E_a}/_{k_B T}) \tag{4.1}$$

where

      A is pre-exponential factor

      E_a is the activation energy for the rISC process

      k_B is the Boltzmann constant

      T is temperature

In this equation, when the temperature is fixed, k_{rISC} is governed by the activation energy E_a. The value of E_a can be experimentally determined by fitting the k_{rISC} values obtained at different temperatures. Importantly, in the same TADF emitters, the values of ΔE_{ST} are usually many times larger than those of E_a (15–17), which indicates that the rISC processes is more complicated than the direct transitions from T_1 to S_1. Therefore, more detailed rISC mechanism studies were carried out and people found the higher triplet states, especially T_2, are also playing important roles in rISC processes, which is further discussed in the next section.

4.3 Mechanism of reverse intersystem crossing in TADF emitters

The rISC process requires to overcome the difficulties of flipping molecular spins without breaking the angular momentum conservation law, which usually requires the operation of spin-orbit coupling (SOC) in the emitters. However, SOC was traditionally regarded to be weak in purely organic molecules because of the lack of heavy metals and the consequent heavy atom effects. To reveal the mechanism of the high rISC rates observed in TADF emitters, people studied how the triplet states contribute to the rISC process. A schematic diagram of the molecular transitions in a TADF emitter is presented in Figure **4.4** which is a simplified diagram of Figure **4.3b**.
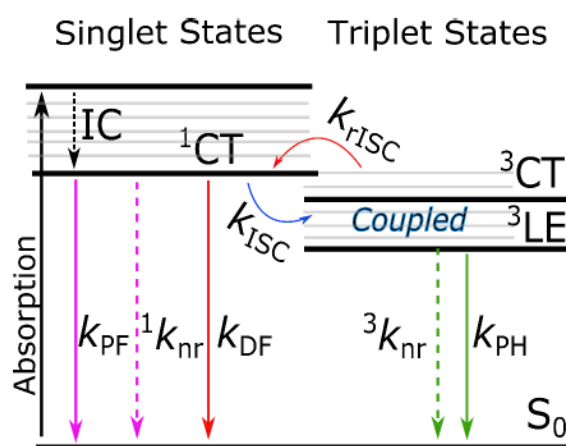
Figure 4.4. a) Schematic diagram of the molecular state transitions in a TADF emitter. Figure adapted from (18).

As has been discussed in Section **2.1.10**, transitions between singlets and triplets are forbidden via SOC when there is no orbital change in the transition processes. This is because SOC is not allowed if there is no orbit-angular-momentum change to compensate the spin-angular-momentum change to conserve the total angular momentum. For the same reason, transitions between ^3CT and ^1CT that are driven by SOC are not allowed, which can be noted as $\langle ^1CT|H_{SOC}|^3CT\rangle$ = 0 (19). In principle, ^3CT and ^1CT can still interact through hyperfine coupling (HFC) in which the nuclear provides the spin-angular-momentum change for the transitions between these two states. However, the typical energy for HFC is in between 1 µeV ~ 20 µeV (19) which is much smaller than typical energy difference between ^3CT and ^1CT (> 10 meV), and so transitions between ^3CT and ^1CT is unlikely to be responsible for efficient rISC in TADF emitters. Therefore, the ^3LE states seem to be the choice for the interaction between ^1CT because the transition from LE orbital to CT orbital can provide the orbit-angular-momentum changes. Nevertheless, in 2015, Chen *et al.* (20) used Fermi's Golden Rule to calculate the transition rate

between ^{1}CT and ^{3}LE, and they concluded that direct SOC between these two states was too small in purely organic TADF emitters to explain the experimental high k_{rISC} (> 10^6 s^{-1}) in them. Similar results were also obtained by Marian *et al*. (21) using multi-reference quantum chemistry methods. Therefore, to give a plausible explanation, both Chen *et al*. and Marian proposed that the mixing of ^{3}LE and ^{3}CT state through nonadiabatic vibronic coupling is the key for realizing efficient rISC. Within a nonadiabatic vibronic coupling, the radiationless transitions happen in pico- to femtosecond timescales, which is in the comparable timescales of nuclear vibrations, and so the Born-Oppenheimer approximation breaks down in this situation, which makes the computational simulations difficult (22). Probably due to this reason, Chen *et al*. and Marian did not give an explicit calculation of this process. To solve this problem, in 2016 and 2017, Gibson *et al*. (14,23) used model quantum dynamic simulations with their Hamiltonian consisting of the most important electronic and vibrational degrees of freedom to study the rISC process without Born-Oppenheimer effects. They found the nonadiabatic mixing of ^{3}LE and ^{3}CT states can be calculated using first order perturbation theory:

$$k_{rIC} = \frac{2\pi}{\hbar} \left| \left\langle \psi\,_{^3LE} \left| \hat{H}_{vib} \right| \psi\,_{^3CT} \right\rangle \right|^2 \delta \left(E\,_{^3CT} - E\,_{^3LE} \right) \qquad (4.2)$$

where

ħ is the Planck constant h/2π

$\psi\,_{^3CT}$ and $\psi\,_{^3LE}$ are the wavefunctions of ^{3}CT and ^{3}LE states

$E\,_{^3CT}$ and $E\,_{^3LE}$ are energy levels of ^{3}CT and ^{3}LE states

$\hat{H}_{vib}$ is vibronic coupling operator which mix ^{3}CT states and ^{3}LE states

$\delta(x)$ is Dirac delta function

It can be seen from Equation **4.2** that the conversion rate between ^{3}CT and ^{3}LE is dependent on both the size of the nonadiabatic vibronic coupling operator, $\hat{H}_{vib}$, and the energy gap between these two states. This conversion is efficient when the ^{3}LE and ^{3}CT states are almost degenerate with good vibrational overlap, so that the Dirac delta function reaches 1. In this case, the nonadiabatic vibronic coupling mixes its ^{3}LE and ^{3}CT states on a timescale much faster than rISC and so an equilibrium is quickly formed between them. However, Gibson *et al.* also found that the critical role of the nonadiabatic vibronic coupling between ^{3}LE and ^{3}CT for the rISC process from ^{3}LE to ^{1}CT cannot be described within a first order perturbation theory approach. After

adapting Henry and Siebrand's work (24), they proposed that second-order perturbation theory can describe this process with the equation of:

$$k_{rISC} = \frac{2\pi}{\hbar} \left| \frac{\langle \psi\,_{^1CT} | \hat{H}_{SOC} | \psi\,_{^3LE} \rangle \langle \psi\,_{^3LE} | \hat{H}_{vib} | \psi\,_{^3CT} \rangle}{E\,_{^3CT} - E\,_{^3LE}} \right|^2 \delta \left(E\,_{^1CT} - E\,_{^3LE} \right) \tag{4.3}$$

where,

$\hat{H}_{SOC}$ is SOC operator which mix ^{3}LE states and ^{1}CT states

$\psi\,_{^1CT}$ is the wavefunctions of ^{1}CT states

$E\,_{^1CT}$ is the energy levels of ^{1}CT states

Subsequently, as shown in Equation **4.3**, the conversion from ^{3}CT to ^{1}CT is via the intermediate state ^{3}LE. Combining Equations **4.2** and **4.3**, it can be seen that small energy gaps among all the ^{1}CT, ^{3}CT and ^{3}LE are important for harvesting an efficient rISC. Therefore, Gibson *et al.* (14) proposed that when ^{3}CT and ^{3}LE are energically close to each other, the energy level distribution presented in Figure **4.5b** is more ideal for highly efficient rISC compared with the common energy level distributions in current TADF emitters (Figure **4.5a** or Figure **4.3b**). It is because the almost degenerate ^{1}CT and ^{3}LE states in Figure **4.5b** can maximize the Dirac delta function in Equation **4.3** and increase k_{rISC}.
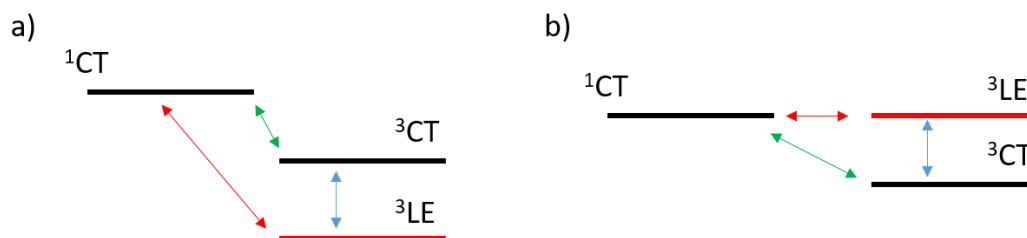
Figure 4.5. a, b) Schematic energy level distributions of current common TADF emitters and ideal TADF emitters.

Gibson *et al.*'s conclusion has a fairly good agreement with experimental results. In 2018, dos Santos *et al.* (25) designed a TADF emitter, TAT-3DBTO$_2$, which has the ΔE_{ST} value of 0.03 eV between the ^{1}CT state and the ^{3}LE state (the ^{3}LE state is the T_1 of the emitter in solid state). Because the energy level of the ^{3}CT state must be lower than that of the ^{1}CT state, the energy level of the ^{3}CT state is expected to be in between those of the ^{1}CT and ^{3}LE states, which makes all these three states energetically close to each other. Consequently, a k_{rISC} of 1.5×10^7 s^{-1} was obtained in the emitter, which corresponds to the delayed-emission lifetime, τ_{DF}, of 103.9 ns,

which is even shorter than the decay lifetimes of many well-known Ir-based phosphorescent emitters such as Ir(ppy)$_3$ (τ_{PH} = 0.65 µs) (26), FIrpic (τ_{PH} = 1.21 µs), Ir(ppy)$_2$(acac) (τ_{PH} = 0.16 µs) and Ir(MDQ)$_2$(acac) (τ_{PH} = 1.31 µs) (27). Similarly, in 2020, Kim *et al*. (15) demonstrated that their TADF emitter, TMCz-BO, showing a small ΔE_{ST} value of 20 meV between the ^{1}CT state and the ^{3}CT state (the ^{3}CT state is the T$_1$ of the emitter in solid state). Also, they found the energy level of the ^{3}LE state is only 70 meV above the ^{3}CT state. Therefore, this emitter shows τ_{DF} of 750 ns, which is also one of the shortest delayed-emission lifetimes people have obtained in TADF emitters. In summary, both the computational and the experimental results show the importance of aligning the energy levels of all the ^{1}CT, ^{3}CT and ^{3}LE states, which is the key for harvesting high k_{rISC} and short delayed-emission lifetimes in TADF emitters.

4.4 The challenges of TADF

4.4.1 Efficiency roll-off

Efficiency roll-off describes the phenomenon that the light-emitting efficiency of an OLED reduces with increasing driving current or luminance. Figure **4.6** shows an example of the efficiency roll-off of two OLEDs. This efficiency reduction is mainly caused by the introduction of quenching mechanisms (e.g. TTA, singlet-triplet annihilation, singlet-polaron annihilation. etc.) when the exciton density is high (28). Among these quenching mechanisms, TTA is the most common origin of the efficiency roll-off in TADF OLEDs because T$_1$ lifetimes of most TADF emitters are long (> 10 µs), which leads to triplets to build up and cause the subsequent TTA (the mechanism of TTA has been discussed in Section **2.12.2**).
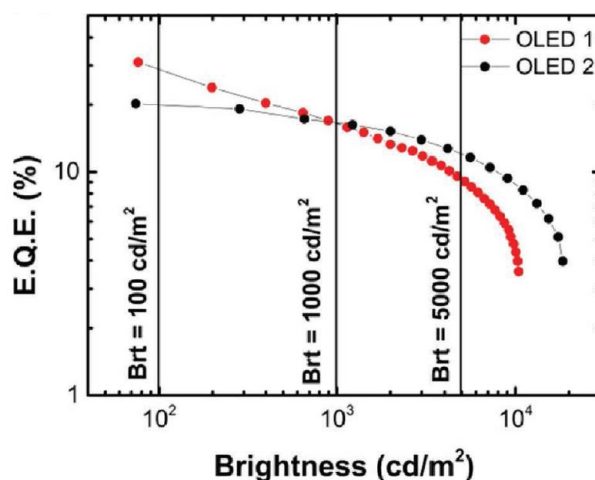
Figure 4.6. Example of efficiency roll-off in OLED. Figure adapted from (25).

An effective way to reduce TTA is increasing k_{rISC} to suppress the triplet populations without losing excitons. For example, the two TADF emitters with high k_{rISC}, as discussed in the last section, namely TAT-3DBTO$_2$ and TMCz-BO, both have EQE values of 20.2% at 100 cd/m^2, and drop only slightly to 16.6% and 17.4%, respectively, at 1000 cd/m^2. Furthermore, in 2018 and 2019, Zhang *et al.* (29) and Wu *et al.* (30) reported two TADF emitters, namely 32alCTRZ and (*R*)-OBN-Cz, having EQE > 20% at 10000 cd/m^2. However, the majority of TADF emitters still possess significant efficiency roll-off because of the low k_{rISC} caused by improper excited-state energy level alignments. For example, in 2016, Ren *et al.* (31) synthesised an emitter, Copo 1, which shows EQE of 20.1% at low current density (0.01 mA/cm^2) and low brightness (~ 1 cd/m^2). However, the EQE dropped to 5.3% at 100 cd/m^2, because its ΔE_{ST} is as large as 0.35 eV. Also, in 2020, Zou *et al*. reported a TADF molecule, 2PhCz2CzBn, which has EQE of 26.6% and 11.7% at 1 cd/m^2 and 1000 cd/m^2, respectively (32), and its ΔE_{ST} is around 0.17 eV . It can be later seen in Chapters **5** and **6** that efficiency roll-off is also a significant problem in the OLEDs fabricated in this work, which is also caused by the large ΔE_{ST} values.

Table 4.1. Examples of TADF emitters with small and large efficiency roll-off

Emitter	ΔE_{ST}[a] / eV	EQE$_{1 cd/m2}$[e] / %	EQE$_{0.01 mA/cm2}$[f] / %	EQE$_{100 cd/m2}$[g] / %	EQE$_{1000 cd/m2}$[h] / %	EQE$_{10000 cd/m2}$[i] / %
TAT-3DBTO$_2$	0.03[b]	-	-	20.2	16.6	8.8
TMCz-BO	0.01[b]	-	20.7	20.2	17.4	-
32alCTRZ	0.15[c]	-	-	-	~ 25	24.8
(*R*)-OBN-Cz	0.04[c]	-	-	~ 29	31.7	~ 29
Copo 1	0.35[b]	20.1	~ 10	5.3	~ 1	-
2PhCz2CzBn	0.17[d]	26.6	-	17.2	11.7	~ 7

[a]$\Delta E_{ST} = S_1 - T_1$. [b, c, d]$\Delta E_{ST}$ determined in solid films, in solutions and by simulations. [e, f, g, h, i]EQE measured at 1 cd/m^2, 0.01 mA/cm^2, 100 cd/m^2, 1000 cd/m^2 and 10000 cd/m^2.

4.4.2 High performance red and blue TADF emitters

According to the National Television System Committee (NTSC) standard, the red, green, and blue emissions of a display should have CIE coordinates of (0.63, 0.34), (0.31, 0.60) and (0.16, 0.07), respectively, so as to display all the required colours on TVs. At the same time, the light-emitting efficiency of OLEDs should be maximized to reduce power consumptions. As both the emission colours and efficiency are mainly dependent on the properties of the emitters, hundreds of new organic materials are synthesized and studied every year to find the best ones

to meet these criteria (33–35). So far, green TADF emitters have reached high EL efficiency (EQE > 20% @ 10000 cd/m^2) (29,30) and reasonable long device-operation lifetimes (LT$_{50}$ > 650 h @ 5000 cd/m^2) (36). However, the performance of red and blue TADF emitters are still far from satisfactory.

Red TADF materials mainly suffer from low light-emitting efficiency at longer emission wavelengths (> 620 nm). It is caused by the small band gaps between S$_1$ (or T$_1$) and S$_0$ in red emitters, which makes the higher vibrational levels of S$_0$ have more overlaps with S$_1$ (or T$_1$), and so molecules at S$_1$ (or T$_1$) can more easily decay to S$_0$ through the vibration channels. Therefore, supressing molecular vibrations by using rigid and planner structures is commonly used as the design strategy for red TADF emitters. Although many highly efficient (EQE > 15% @ 1000 cd/m^2) orange TADF emitters (λ_{EL} < 610 nm) have been reported (37–39), there are only three successful examples of red TADF emitters which have EQE$_{max}$ > 20% with emission peak above 620 nm at low brightness (< 100 cd/m^2) (40–42). However, none of them has EQE > 5% @ 1000 cd/m^2 (40), which is inefficient for display applications.

On the blue TADF emitter side, although there are many emitters having high efficiency (EQE > 15% @ 1000 cd/m^2) (32,43–45), they mainly show sky-blue emissions (CIE$_x$ > 0.20 or CIE$_y$ > 0.20) instead of the deep-blue emissions which can meet the colour requirement for commercial displays. In comparison, deep-blue TADF emitters which have CIE coordinates of (CIE$_x$ < 0.15 or CIE$_y$ < 0.15) with high efficiency are very few (46,47).

Therefore, Chapters **5** and **6** of this thesis aimed to design new red and blue TADF emitters to explore the molecular designs of efficient red and blue TADF emitters.

4.5 References

1. Brown AR, Pichler K, Greenham NC, Bradley DDC, Friend RH, Holmes AB. Optical spectroscopy of triplet excitons and charged excitations in poly(p-phenylenevinylene) light-emitting diodes. Chem Phys Lett. 1993;210(1–3):61–6. Available from: https://linkinghub.elsevier.com/retrieve/pii/000926149389100V

2. Segal M, Baldo MA, Holmes RJ, Forrest SR, Soos ZG. Excitonic singlet-triplet ratios in molecular and polymeric organic materials. Phys Rev B. 2003;68(7):075211. Available from: https://link.aps.org/doi/10.1103/PhysRevB.68.075211

3.	Display Daily. A Breakingthrough in Blue OLED [Internet]. Available from: https://www.displaydaily.com/article/display-daily/a-breakthrough-in-blue-oled

4.	Adachi C, Baldo MA, Thompson ME, Forrest SR. Nearly 100% internal phosphorescence efficiency in an organic light-emitting device. J Appl Phys. 2001;90(10):5048–51. Available from: http://aip.scitation.org/doi/10.1063/1.1409582

5.	Fleetham T, Li G, Li J. Phosphorescent Pt(II) and Pd(II) Complexes for Efficient, High-Color-Quality, and Stable OLEDs. Adv Mater. 2017;29(5):1601861. Available from: http://doi.wiley.com/10.1002/adma.201601861

6.	Endo A, Suzuki K, Yoshihara T, Tobita S, Yahiro M, Adachi C. Measurement of photoluminescence efficiency of Ir(III) phenylpyridine derivatives in solution and solid-state films. Chem Phys Lett. 2008;460(1–3):155–7. Available from: https://linkinghub.elsevier.com/retrieve/pii/S0009261408007446

7.	Kondakov DY. Triplet–triplet annihilation in highly efficient fluorescent organic light-emitting diodes: current state and future outlook. Philos Trans R Soc A Math Phys Eng Sci. 2015;373(2044):20140321. Available from: https://royalsocietypublishing.org/doi/10.1098/rsta.2014.0321

8.	Uoyama H, Goushi K, Shizu K, Nomura H, Adachi C. Highly efficient organic light-emitting diodes from delayed fluorescence. Nature. 2012;492(7428):234–8. Available from: http://dx.doi.org/10.1038/nature11687

9.	Dias FB, Pollock S, Hedley G, Pålsson L-O, Monkman A, Perepichka II, Perepichka IF, Tavasli M, Bryce MR. Intramolecular Charge Transfer Assisted by Conformational Changes in the Excited State of Fluorene-dibenzothiophene- S,S -dioxide Co-oligomers. J Phys Chem B. 2006;110(39):19329–39. Available from: https://pubs.acs.org/doi/10.1021/jp0643653

10.	Tao Y, Yuan K, Chen T, Xu P, Li H, Chen R, Zheng C, Zhang L, Huang W. Thermally Activated Delayed Fluorescence Materials Towards the Breakthrough of Organoelectronics. Adv Mater. 2014;26(47):7931–58. Available from: http://doi.wiley.com/10.1002/adma.201402532

11.	Monkman A. Photophysics of Thermally Activated Delayed Fluorescence. In: Highly Efficient OLEDs. Weinheim, Germany: Wiley-VCH Verlag GmbH & Co. KGaA; 2018. p.

425–63. Available from: http://doi.wiley.com/10.1002/9783527691722.ch12

12.   Wada Y, Nakagawa H, Matsumoto S, Wakisaka Y, Kaji H. Organic light emitters exhibiting very fast reverse intersystem crossing. Nat Photonics. 2020;14(10):643–9. Available from: http://dx.doi.org/10.1038/s41566-020-0667-0

13.   Masui K, Nakanotani H, Adachi C. Analysis of exciton annihilation in high-efficiency sky-blue organic light-emitting diodes with thermally activated delayed fluorescence. Org Electron. 2013;14(11):2721–6. Available from: http://dx.doi.org/10.1016/j.orgel.2013.07.010

14.   Gibson J, Penfold TJ. Nonadiabatic coupling reduces the activation energy in thermally activated delayed fluorescence. Phys Chem Chem Phys. 2017;19(12):8428–34. Available from: http://xlink.rsc.org/?DOI=C7CP00719A

15.   Kim JU, Park IS, Chan C-Y, Tanaka M, Tsuchiya Y, Nakanotani H, Adachi C. Nanosecond-time-scale delayed fluorescence molecule for deep-blue OLEDs with small efficiency rolloff. Nat Commun. 2020;11(1):1765. Available from: http://dx.doi.org/10.1038/s41467-020-15558-5

16.   Noda H, Nakanotani H, Adachi C. Excited state engineering for efficient reverse intersystem crossing. Sci Adv. 2018;4(6):eaao6910. Available from: https://advances.sciencemag.org/lookup/doi/10.1126/sciadv.aao6910

17.   Santos PL, Ward JS, Data P, Batsanov AS, Bryce MR, Dias FB, Monkman AP. Engineering the singlet–triplet energy splitting in a TADF molecule. J Mater Chem C. 2016;4(17):3815–24. Available from: http://xlink.rsc.org/?DOI=C5TC03849A

18.   dos Santos, Lays P. The Study of Thermally Activated Delayed Fluorescence Mechanism in Mono and Bimolecular Systems. 2018.

19.   Dias FB, Santos J, Graves DR, Data P, Nobuyasu RS, Fox MA, Batsanov AS, Palmeira T, Berberan-Santos MN, Bryce MR, Monkman AP. The Role of Local Triplet Excited States and D-A Relative Orientation in Thermally Activated Delayed Fluorescence: Photophysics and Devices. Adv Sci. 2016;3(12):1600080. Available from: http://doi.wiley.com/10.1002/advs.201600080

20.   Chen X-K, Zhang S-F, Fan J-X, Ren A-M. Nature of Highly Efficient Thermally Activated Delayed Fluorescence in Organic Light-Emitting Diode Emitters: Nonadiabatic Effect

between Excited States. J Phys Chem C. 2015;119(18):9728–33. Available from: https://pubs.acs.org/doi/10.1021/acs.jpcc.5b00276

21. Marian CM. Mechanism of the Triplet-to-Singlet Upconversion in the Assistant Dopant ACRXTN. J Phys Chem C. 2016;120(7):3715–21. Available from: https://pubs.acs.org/doi/10.1021/acs.jpcc.6b00060

22. Penfold TJ, Gindensperger E, Daniel C, Marian CM. Spin-Vibronic Mechanism for Intersystem Crossing. Chem Rev. 2018;118(15):6975–7025. Available from: https://pubs.acs.org/doi/10.1021/acs.chemrev.7b00617

23. Gibson J, Monkman AP, Penfold TJ. The Importance of Vibronic Coupling for Efficient Reverse Intersystem Crossing in Thermally Activated Delayed Fluorescence Molecules. ChemPhysChem. 2016;17(19):2956–61. Available from: http://doi.wiley.com/10.1002/cphc.201600662

24. Henry BR, Siebrand W. Spin–Orbit Coupling in Aromatic Hydrocarbons. Analysis of Nonradiative Transitions between Singlet and Triplet States in Benzene and Naphthalene. J Chem Phys. 1971;54(3):1072–85. Available from: http://aip.scitation.org/doi/10.1063/1.1674940

25. dos Santos PL, Ward JS, Congrave DG, Batsanov AS, Eng J, Stacey JE, Penfold TJ, Monkman AP, Bryce MR. Triazatruxene: A Rigid Central Donor Unit for a D-A 3 Thermally Activated Delayed Fluorescence Material Exhibiting Sub-Microsecond Reverse Intersystem Crossing and Unity Quantum Yield via Multiple Singlet-Triplet State Pairs. Adv Sci. 2018;5(6):1700989. Available from: http://doi.wiley.com/10.1002/advs.201700989

26. Tsuboi T, Aljaroudi N. Photoluminescence lifetime of Ir(ppy)3 used for organic light emitting diodes. IEICE Electron Express. 2004;1(10):281–6. Available from: http://joi.jlc.jst.go.jp/JST.JSTAGE/elex/1.281?from=CrossRef

27. Zhu X-D, Zhang Y-L, Yuan Y, Zheng Q, Yu Y-J, Li Y, Jiang Z-Q, Liao L-S. Incorporating a tercarbazole donor in a spiro-type host material for efficient RGB phosphorescent organic light-emitting diodes. J Mater Chem C. 2019;7(22):6714–20. Available from: http://dx.doi.org/10.1039/C9TC01426H

28. Murawski C, Leo K, Gather MC. Efficiency Roll-Off in Organic Light-Emitting Diodes. Adv

Mater. 2013;25(47):6801–27. Available from:
http://doi.wiley.com/10.1002/adma.201301603

29. Zhang D, Song X, Cai M, Kaji H, Duan L. Versatile Indolocarbazole-Isomer Derivatives as Highly Emissive Emitters and Ideal Hosts for Thermally Activated Delayed Fluorescent OLEDs with Alleviated Efficiency Roll-Off. Adv Mater. 2018;30(7):1705406. Available from: http://doi.wiley.com/10.1002/adma.201705406

30. Wu Z, Han H, Yan Z, Luo X, Wang Y, Zheng Y, Zuo J, Pan Y. Chiral Octahydro-Binaphthol Compound-Based Thermally Activated Delayed Fluorescence Materials for Circularly Polarized Electroluminescence with Superior EQE of 32.6% and Extremely Low Efficiency Roll-Off. Adv Mater. 2019;31(28):1900524. Available from: https://onlinelibrary.wiley.com/doi/abs/10.1002/adma.201900524

31. Ren Z, Nobuyasu RS, Dias FB, Monkman AP, Yan S, Bryce MR. Pendant Homopolymer and Copolymers as Solution-Processable Thermally Activated Delayed Fluorescence Materials for Organic Light-Emitting Diodes. Macromolecules. 2016;49(15):5452–60. Available from: https://pubs.acs.org/doi/10.1021/acs.macromol.6b01216

32. Zou S, Xie F, Xie M, Li Y, Cheng T, Zhang X, Lee C, Tang J. High-Performance Nondoped Blue Delayed Fluorescence Organic Light-Emitting Diodes Featuring Low Driving Voltage and High Brightness. Adv Sci. 2020;7(3):1902508. Available from: https://onlinelibrary.wiley.com/doi/abs/10.1002/advs.201902508

33. Wong MY, Zysman-Colman E. Purely Organic Thermally Activated Delayed Fluorescence Materials for Organic Light-Emitting Diodes. Adv Mater. 2017;29(22):1605444. Available from: http://doi.wiley.com/10.1002/adma.201605444

34. Huang T, Jiang W, Duan L. Recent progress in solution processable TADF materials for organic light-emitting diodes. J Mater Chem C. 2018;6(21):5577–96. Available from: http://xlink.rsc.org/?DOI=C8TC01139G

35. Teng J-M, Chen Y-F, Wang C-F. Materials Chemistry C. J Mater Chem C. 2020;1(207890):3777. Available from: http://ncesr.unl.edu/wordpress/wp-content/uploads/2010/07/Synthesis-of-high-quality-inverse-opals-J-Mater-Chem-C-article.pdf

36. Cui L-S, Ruan S-B, Bencheikh F, Nagata R, Zhang L, Inada K, Nakanotani H, Liao L-S,

Adachi C. Long-lived efficient delayed fluorescence organic light-emitting diodes using n-type hosts. Nat Commun. 2017;8(1):2250. Available from: http://dx.doi.org/10.1038/s41467-017-02419-x

37. Zeng W, Lai H-Y, Lee W-K, Jiao M, Shiu Y-J, Zhong C, Gong S, Zhou T, Xie G, Sarma M, Wong K-T, Wu C-C, Yang C. Achieving Nearly 30% External Quantum Efficiency for Orange-Red Organic Light Emitting Diodes by Employing Thermally Activated Delayed Fluorescence Emitters Composed of 1,8-Naphthalimide-Acridine Hybrids. Adv Mater. 2018;30(5):1704961. Available from: http://doi.wiley.com/10.1002/adma.201704961

38. Chen J-X, Tao W-W, Xiao Y-F, Wang K, Zhang M, Fan X-C, Chen W-C, Yu J, Li S, Geng F-X, Zhang X-H, Lee C-S. Efficient Orange-Red Thermally Activated Delayed Fluorescence Emitters Feasible for Both Thermal Evaporation and Solution Process. ACS Appl Mater Interfaces. 2019;11(32):29086–93. Available from: https://pubs.acs.org/doi/10.1021/acsami.9b08729

39. Chen J-X, Wang K, Zheng C-J, Zhang M, Shi Y-Z, Tao S-L, Lin H, Liu W, Tao W-W, Ou X-M, Zhang X-H. Red Organic Light-Emitting Diode with External Quantum Efficiency beyond 20% Based on a Novel Thermally Activated Delayed Fluorescence Emitter. Adv Sci. 2018;5(9):1800436. Available from: http://doi.wiley.com/10.1002/advs.201800436

40. Chen J, Tao W, Chen W, Xiao Y, Wang K, Cao C, Yu J, Li S, Geng F, Adachi C, Lee C, Zhang X. Red/Near-Infrared Thermally Activated Delayed Fluorescence OLEDs with Near 100 % Internal Quantum Efficiency. Angew Chemie Int Ed. 2019;58(41):14660–5. Available from: https://onlinelibrary.wiley.com/doi/abs/10.1002/anie.201906575

41. Zhang Y, Ran Q, Wang Q, Liu Y, Hänisch C, Reineke S, Fan J, Liao L. High-Efficiency Red Organic Light-Emitting Diodes with External Quantum Efficiency Close to 30% Based on a Novel Thermally Activated Delayed Fluorescence Emitter. Adv Mater. 2019;31(42):1902368. Available from: https://onlinelibrary.wiley.com/doi/abs/10.1002/adma.201902368

42. Zeng W, Zhou T, Ning W, Zhong C, He J, Gong S, Xie G, Yang C. Realizing 22.5% External Quantum Efficiency for Solution-Processed Thermally Activated Delayed-Fluorescence OLEDs with Red Emission at 622 nm via a Synergistic Strategy of Molecular Engineering and Host Selection. Adv Mater. 2019;31(33):1901404. Available from: https://onlinelibrary.wiley.com/doi/abs/10.1002/adma.201901404

43.   Ahn DH, Kim SW, Lee H, Ko IJ, Karthik D, Lee JY, Kwon JH. Highly efficient blue thermally activated delayed fluorescence emitters based on symmetrical and rigid oxygen-bridged boron acceptors. Nat Photonics. 2019;13(8):540–6. Available from: http://dx.doi.org/10.1038/s41566-019-0415-5

44.   Hung M, Tsai K, Sharma S, Wu J, Chen S. Acridan-Grafted Poly(biphenyl germanium) with High Triplet Energy, Low Polarizability, and an External Heavy-Atom Effect for Highly Efficient Sky-Blue TADF Electroluminescence. Angew Chemie Int Ed. 2019;58(33):11317–23. Available from: https://onlinelibrary.wiley.com/doi/abs/10.1002/anie.201904433

45.   Zhang D, Cai M, Bin Z, Zhang Y, Zhang D, Duan L. Highly efficient blue thermally activated delayed fluorescent OLEDs with record-low driving voltages utilizing high triplet energy hosts with small singlet–triplet splittings. Chem Sci. 2016;7(5):3355–63. Available from: http://xlink.rsc.org/?DOI=C5SC04755B

46.   Kondo Y, Yoshiura K, Kitera S, Nishi H, Oda S, Gotoh H, Sasada Y, Yanai M, Hatakeyama T. Narrowband deep-blue organic light-emitting diode featuring an organoboron-based emitter. Nat Photonics. 2019;13(10):678–82. Available from: http://dx.doi.org/10.1038/s41566-019-0476-5

47.   Zhang D, Song X, Gillett AJ, Drummond BH, Jones STE, Li G, He H, Cai M, Credgington D, Duan L. Efficient and Stable Deep-Blue Fluorescent Organic Light-Emitting Diodes Employing a Sensitizer with Fast Triplet Upconversion. Adv Mater. 2020;32(19):1908355. Available from: https://onlinelibrary.wiley.com/doi/abs/10.1002/adma.201908355

Chapter 5 New Orange and Yellow Thermally Activated Delayed Fluorescence Emitters

Two new orange and yellow thermally activated delayed fluorescence (TADF) emitters, namely **DMAcPhAP** and **CzPhAP,** were synthesized and studied. These two emitters are featured with a rigid electron accepting group acenaphtho[1,2-b]pyrazine-8,9-dicarbonitrile (**AP**). Calculations and photophysics were first carried out to study their TADF properties. Then, OLED devices were fabricated based on these two emitters to test their EL performance. These OLED devices show EQE_{max} of 13.0% and 11.1% at the luminance around 1 cd/m^2 with peak positions of 604 nm and 570 nm and CIE coordinates of (0.54, 0.45) and (0.47, 0.51). The effect of accumulated charges was also observed in **CzPhAP** doped films and devices, which has an impact on its photophysical properties and device efficiency roll-off.
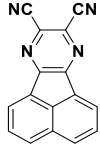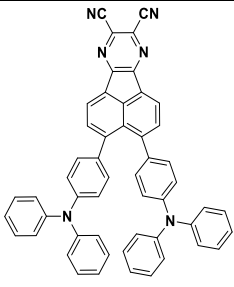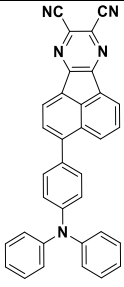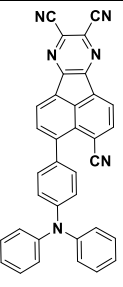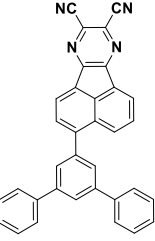
The chapter is partially adapted from a published paper (Li W, Li Z, Si C, Wong MY, Jinnai K, Gupta AK, Kabe R, Adachi C, Huang W, Zysman‐Colman E, Samuel ID. Organic Long‐Persistent Luminescence from a Thermally Activated Delayed Fluorescence Compound. Advanced Materials. 2020, 32, 2003911). It is a collaborative work between I. D. W. Samuel's group and E. Zysman-Colman's group at the University of St Andrews. In this chapter, the studied TADF emitters were firstly design and the synthesized by M. Y. Wong from Zysman-Colman's group. After the first bath of emitters were finished, Z. Li from Zysman-Colman's group synthesized the second batch of the same emitters. He also performed the TD-DFT calculations (computational modelling), CV measurements and solvatochromism PL spectrum measurements. C. Si from Zysman-Colman's group synthesized the third batch of the same emitters. He also synthesized the bare **AP** molecules. I performed the APS measurements, time-resolved PL (TRPL) decay measurements, TRPL spectra measurements, OLED device fabrication and device characterisation.

5.1 Introduction

To explore the molecular design of new red TADF emitters, in this work, two donor-acceptor (D-A) type TADF molecules using **AP** as the strong electron-acceptor group were synthesized and studied. The molecular structure of **AP** is shown in Table **5.1**. Although the first **AP**-based TADF emitter was reported by Yuan *et al.* in 2017 (1), M. Y. Wong in Eli's group also independently designed and synthesised two **AP**-based TADF emitters in 2016 (2). However, the study of these two emitters was finished in 2019, and many other **AP**-based TADF emitters had been published before the completion of this work. Considering the relatively lower performance (poorer colour gamut and lower efficiency) of these two emitters compared with the reported ones, these two emitters were not published as bare TADF emitters but with their OLPL properties. However, this chapter only focuses on discussing the TADF properties of these two emitters, and the OLPL properties are discussed in Chapter **8**.

Because of the high rigidity and strong electron-accepting strength of **AP**, OLEDs using **AP**-based emitters generally show high device efficiency in red and near-infrared regions, which is summarized in Table **5.1**. Within this table, both EQE_{max} and the EQE at 100 cd/m^2 are included to show the maximum EQEs and the EQE values at practical brightness. The EQEs at 1 mA/cm^2 are also employed where the EQEs at 100 cd/m^2 cannot be found in their reports. In 2017 and 2018, Yuan *et al*. (1,3) first synthesized and applied **AP** to a two donor – one acceptor (D2-A) type TADF emitter, named 3,4-bis(4-(diphenylamino)phenyl)acenaphtho[1,2-b]pyrazine-8,9-dicarbonitrile (APDC-DTPA). APDC-DTPA consists of two triphenylamine (TPA) donors linked at the 3 and 8 positions to the **AP** core. The OLEDs based on APDC-DTPA have EQE_{max} of 9.7% at 696 nm ($EQE_{1mA/cm2} \approx 5$ %) and 12.3% at 668 nm ($EQE_{1mA/cm2} \approx 5.9$ %) at different emitter doping concentrations. In 2019, Xue *et al*. reported a related D-A compound, TPAAP, with a single TPA as the donor (4). The TPAAP-based OLED reached EQE_{max} of 5.1% at 765 nm ($EQE_{1mA/cm2} \approx 3.5$ %). In the same year, Congreve *et al*. showed that elaboration of the AP core with a nitrile unit at the 3-position leads to a compound, CAT-1, with significant red-shift of the emission to 950 nm with a photoluminescence quantum yield, Φ_{PL}, of 0.18% (5). However, no OLED was fabricated using CAT-1 because of its low PLQY. In 2020, Hu *et al*. demonstrated that connecting two phenyl groups to the AP core resulted in a molecule APDC-tPh which can be used as the acceptor in an exciplex emitter (6). The OLED using this exciplex as the emission layer has EL peak of 704 nm with EQE_{max} of 1.3% ($EQE_{1mA/cm2} = 1.2$ %).

Table 5.1. Molecular structures and properties of **AP**, APDC-DPTA, TPAAP, CAT-1 and APDC-tPh

Molecule	AP	APDC-DPTA	TPAAP	CAT-1	APDC-tPh
Structure					
$\lambda_{Emission}$ (nm)	-	696	765	950	704
PLQY[a] (%)	-	63	20.3	0.2	9
EQE$_{max}$[b] (%)	-	9.7	5.1	-	1.3
EQE$_{100\,cd/m2}$[c] (%)	-	-	-	-	0.1
EQE$_{1\,mA/cm2}$[d] (%)	-	~5.0	~3.5	-	~1.2

[a]Solid state doped films measured in nitrogen atmosphere. [b]Maximum EQE @ above 1 cd/m^2. [c]EQE @ 100 cd/m^2. [d]EQE @ 1 mA/cm^2

Here, 9,9-dimethyl-9,10-dihydroacridine (DMAc) and carbazole (Cz) were selected as the donors connected to the **AP** core with a phenyl group as the bridges, and the brief synthetic route of these two emitters, **DMAcPhAP** and **CzPhAP**, are presented in Scheme **5.1**. The phenyl bridge between the donors and the acceptors can red-shift the emission without decreasing PLQY, which was demonstrated by Zhang *et al.* in 2014 (7). Moreover, DMAc was selected because its strong electron-donating strength which can further red-shift the emission. Also, DMAc can provide a large dihedral angle between the donor and acceptor moieties so as to minimize the overlap of the HOMO and LUMO. In comparison, Cz has a weaker electron-donating strength, but its rigidity brings the advantage of less vibrational loss. Therefore, both donors were employed in the molecular designs for performance comparison.
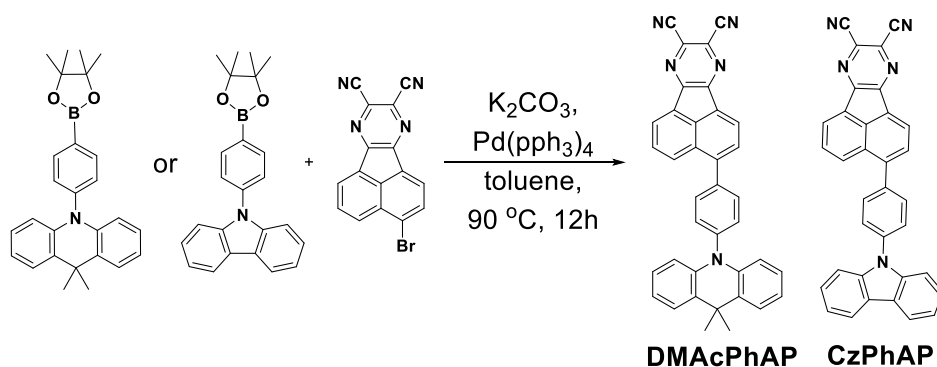
Scheme 5.1. Brief synthetic routes and chemical structures of **DMAcPhAP** and **CzPhAP**.

5.2 Molecular design and calculations

To estimate the properties of these two emitters, density functional theoretical (DFT) and time-dependent density functional (TDDFT) calculations were performed in gas phase with Pbe1pbe/6-31G (d,p) set as presented in Figure **5.1**. Furthermore, their S_1 and T_1 energy levels were determined at the excited states using Tamm-Dancoff approximation. All the calculation results are summarized in Table **5.2**. It can be seen that the calculated LUMO values of these two emitters are comparable because they share the same acceptor. In comparison, their calculated HOMO values are more than 0.5 eV away owing to the very different electron donating strengths of the two donors. The consequent smaller HOMO and LUMO energy gap, ΔE, of **DMAcPhAP** results in redder emission compared with that of **CzPhAP**. Also, **DMAcPhAP** has much small singlet-triplet energy splitting, ΔE_{ST}, value (0.0016 eV) compared with that of **CzPhAP** (0.18 eV) because **DMAcPhAP** has much larger dihedral angle between the donor and the acceptor moieties. However, as the price of the small ΔE_{ST}, the oscillator strength, f, of **DMAcPhAP** is also small (0.0002) because the large dihedral angle decouples its HOMO and LUMO, which may lead to a lower PLQY. Compared, the oscillator strength of **CzPhAP** is much larger (0.1560). As both of them show ΔE_{ST} values < 0.2 eV, which is sufficient for harvesting TADF, emitters were synthesized according to these designs.
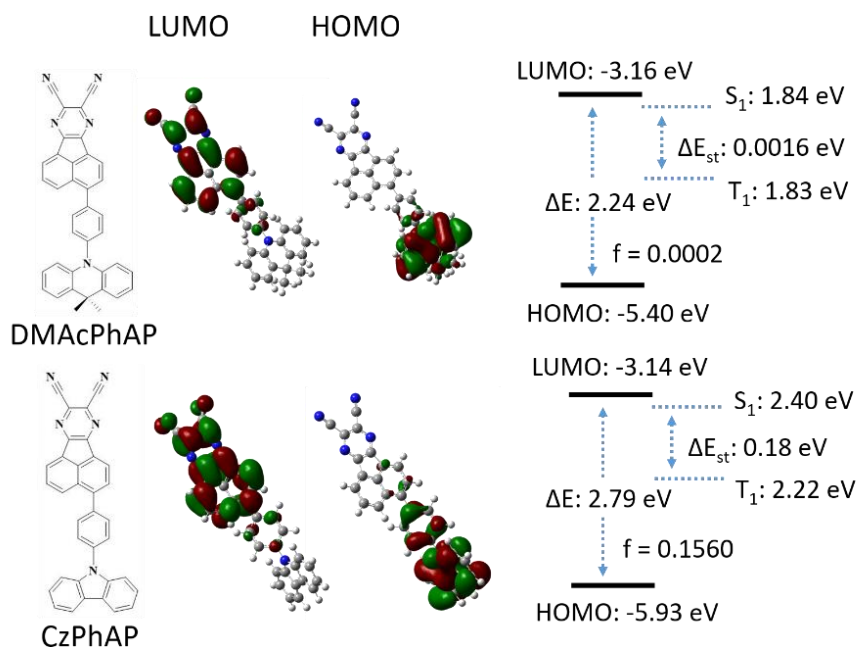
Figure 5.1. Molecular structures and calculation results of **DMAcPhAP** and **CzPhAP**. DFT determined electron density distribution and energy levels of the HOMO and LUMO, TDDFT determined energies of the S_1 and T_1 states of these two molecules in gas phase.

Table 5.2. Summary of the calculated HOMO/LUMO values, S_1/T_1/ΔE_{ST} energies and oscillator strength values of **DMAcPhAP** and **CzPhAP** in gas phase.

Compound	HOMO[a] /eV	LUMO[a] /eV	ΔE /eV	S_1[b] /eV	T_1[b] /eV	ΔE_{ST}[c] /eV	f[b]
DMAcPhAP	-5.40	-3.16	2.24	1.84	1.83	0.0016	0.0002
CzPhAP	-5.93	-3.14	2.79	2.40	2.22	0.18	0.1560

[a]Calculated through DFT. [b]Calculated through TD-DFT. The calculations were performed in gas phase with Pbe1pbe/6-31G (d,p) set. [c]$\Delta E_{ST} = S_1 - T_1$

5.3 Experimental HOMO and LUMO determination

After the material synthesis and purification, experimental HOMO and LUMO energy level determinations were carried out. Figure **5.2a** shows their cyclic voltammetry (CV, solid lines) and differential pulse voltammetry (DPV, dashed lines) traces measured in acetonitrile (MeCN). The reduction of **CzPhAP** wave was found to be reversible while the oxidation wave was irreversible as the carbazole radical cation is known to be electrochemically unstable and subsequently can undergo dimerization (8,9). The oxidation and reduction potential obtained from the DPV are 0.93 V and -0.87 V for **DMAcPhAP**, while 1.33 V and -0.86 V for **CzPhAP**, which corresponds to the HOMO and LUMO energies of -5.32 eV and -3.52 eV for **DMAcPhAP**, while -5.75 eV and -3.65 eV for **CzPhAP**, respectively. For comparison, ambient pressure photoemission spectroscopy (APS) was performed on the neat films of **DMAcPhAP** and **CzPhAP** and gave HOMO values of -5.47 eV and -5.76 eV (Figure **5.2 b, c**), which aligns with the DPV-determined levels.
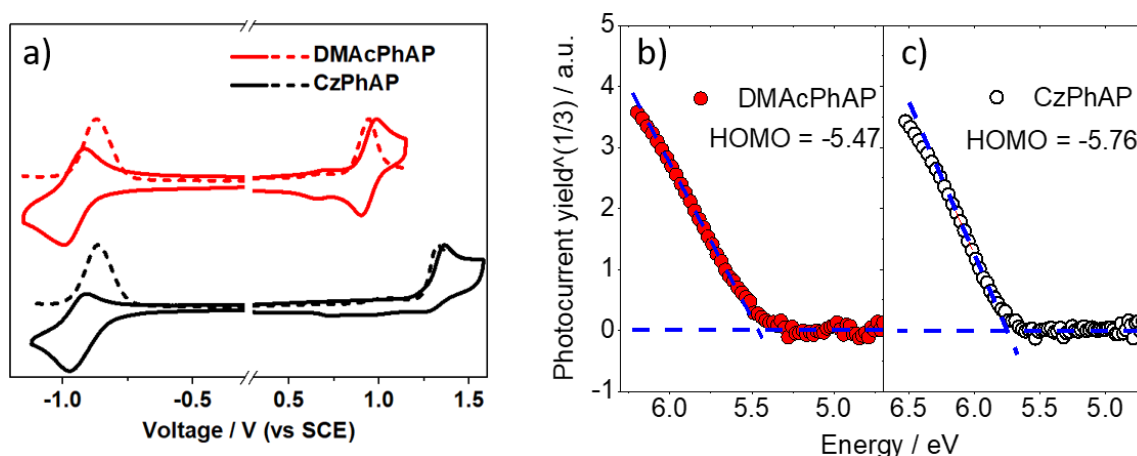
Figure 5.2. a) CV (solid lines) and DPV (dashed lines) measurements of **DMAcPhAP** and **CzPhAP** in MeCN, (Fc/Fc+ are 0.41 V and 0.38 V (10) for **DMAcPhAP** and **CzPhAP**, respectively in the measurement, and the scan rate was 100 mV s^{-1}). b, c) APS measurement results of neat **DMAcPhAP** and **CzPhAP** films.

A comparison of the HOMO, LUMO and band gap values obtained through different methods is shown in Table **5.3**. In the 'APS' column, the band gap values, Δ*E*, were determined from the onsets of their PL spectra in toluene (Figure **5.3**), while the LUMO values were obtained through adding the Δ*E* values to their corresponding HOMO values. It can be seen in Table **5.3** that the HOMO energy values of **DMAcPhAP** obtained from different methods are almost similar. But the LUMO energy value of **DMAcPhAP** obtained from CV is much deeper than those obtained from the other two methods. Similar phenomenon can also be observed in the data of **CzPhAP**. The optical gaps determined from the onsets of the normalized emission spectra in toluene, are 2.30 eV and 2.63 eV, respectively, which are close to the calculated values (2.24 eV and 2.79 eV), but are much larger than those obtained through CV (1.8 eV and 2.10 eV). The different Δ*E* values determined by CV and optical bandgaps may come from the different measurement environments: CV was carried out in DCM but the optical gap was estimated in toluene. As CT states are sensitive to the polarities of the environments, the optical gaps determined by onsets of CT emissions vary according to the measurement conditions.

Table 5.3. Summary of the HOMO, LUMO and the band gap values of **DMAcPhAP** and **CzPhAP** obtained through calculations, CV and APS.

Method	Calculation[a]			CV[b]			APS[c]		
Compound	HOMO /eV	LUMO /eV	Δ*E* /eV	HOMO /eV	LUMO /eV	Δ*E* /eV	HOMO /eV	LUMO /eV	Δ*E* /eV
DMAcPhAP	-5.40	-3.16	2.24	-5.32	-3.52	1.80	-5.47	-3.24	2.23
CzPhAP	-5.93	-3.14	2.79	-5.75	-3.65	2.10	-5.76	-3.19	2.57

[a]Calculated through DFT. [b]HOMO and LUMO values were obtained from CV measurements. Δ*E* = LUMO – HOMO. The CV measurements of **DMAcPhAP** and **CzPhAP** were carried out in DCM with 0.1 M [nBu4N]PF6 as the supporting electrolyte and Fc/Fc+ (vs Ag/Ag+, 0.412 for **DMAcPhAP** and 0.38 V for **CzPhAP**) as the internal reference. [c]Δ*E* was obtained from the onsets of steady-state PL spectra of **DMAcPhAP** and **CzPhAP** in toluene. HOMO was obtained from the APS measurement. LUMO = HOMO + Δ*E*.

5.4 Photophysics in solution

The steady-state absorption spectra of these two emitters in toluene are presented in Figure **5.3**. Both **DMAcPhAP** and **CzPhAP** show CT absorption characters in solution: there are broad and structureless low-energy absorption bands at 455 nm and 425 nm, respectively. Also, the height of the CT absorption band of **DMAcPhAP** is lower than that of the **CzPhAP**, indicating **DMAcPhAP**

has a much lower oscillator strength, which aligns with the prediction of the calculation (f = 0.0002 vs f = 0.1560).

For the steady-state solvatochromism PL study, the emission spectra of **CzPhAP** spectra are generally broad and featureless, and positive solvatochromism is observed: its PL spectrum keeps red-shifting with more polar solvents. This suggests the CT characteristic dominants the PL of **CzPhAP**. However, the solvatochromism behaviour of **DMAcPhAP** is uncommon: although its steady-state PL spectra in hexane, toluene and chloroform show positive solvatochromism, the emission spectrum in chloroform shows two peaks: one at 518 nm and the other at around 800 nm. Furthermore, when it is dissolved in DCM which is the most polar among these solvents, the emission peak goes back to the same peak position as that of hexane which is the least polar among these solvents. Consequently, there could be some interactions between **DMAcPhAP** and the solvents (chloroform and DCM), which changes the emission properties. However, the main focus was to explore OLEDs which are solid state devices, and so this was not explored further.
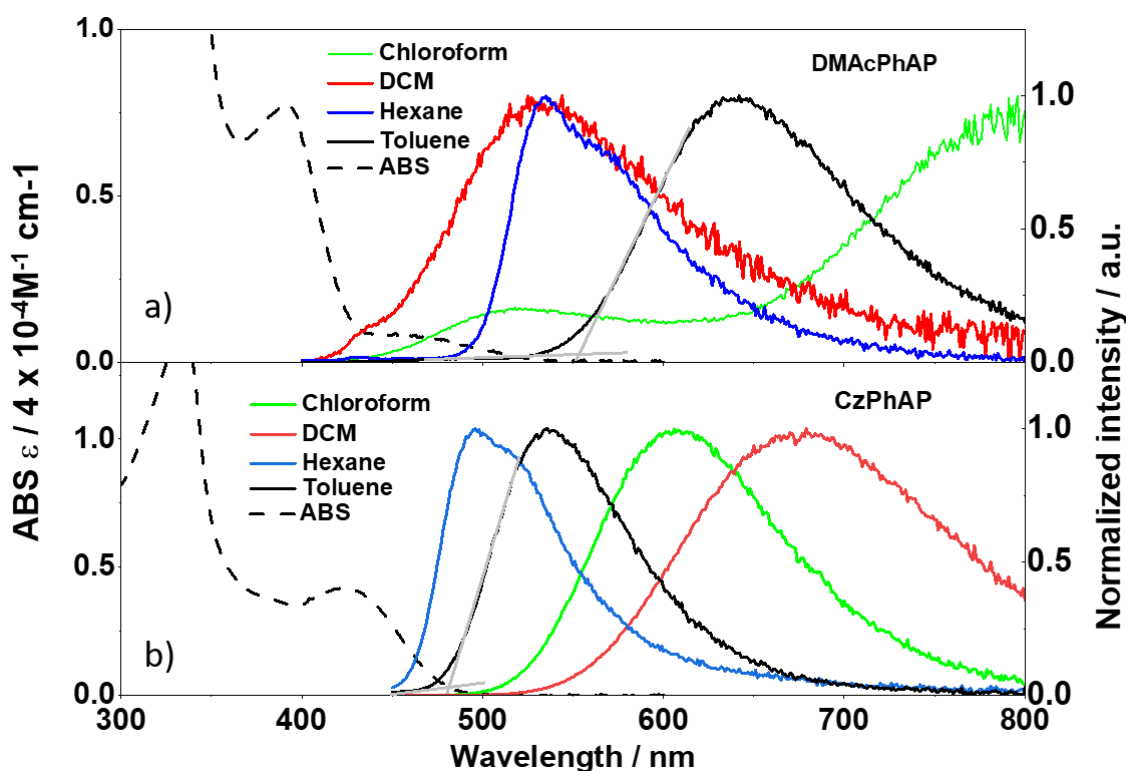
Figure 5.3. a, b) Absorption spectrum in toluene and steady-state solvatochromism PL spectra of **DMAcPhAP** and **CzPhAP** (λ_{exc} = 340 nm)

Singlet and triplet properties of these two emitters and the T_1 of their acceptor, **AP**, were then studied through the TRPL spectra measured in flash cooled 77 K toluene glass (more details

about the measurement setup can be seen in Sections **3.5.5** and **3.5.6**). As shown in Figure **5.4**, the prompt fluorescence spectra and delayed phosphorescence spectra were taken from 1-100 ns and 0.1-1 ms after photoexcitation, respectively. The S_1 and T_1 values were determined from the onsets of these spectra. The ΔE_{ST} values were calculated from the energy level differences between the S_1 and T_1. It can be seen in Figure **5.4** that **DMAcPhAP** and **CzPhAP** have similar phosphorescence spectra, indicating the T_1 of these two emitters are both provided by the acceptor **AP**. However, the onset of the phosphorescence spectrum of bare **AP** has higher energy than those of the phosphorescence spectra of **DMAcPhAP** and **CzPhAP**, which is probably due to the fact that the **AP** groups in **DMAcPhAP** and **CzPhAP** are slightly conjugated with the phenyl bridges as shown in the DFT calculations (Figure **5.1**), which lowers the excited state energy of the **AP** groups. The ΔE_{ST} values of **DMAcPhAP** and **CzPhAP** are 0.25 eV and 0.47 eV in toluene, respectively, which are much larger than those predicted by the DFT calculations.
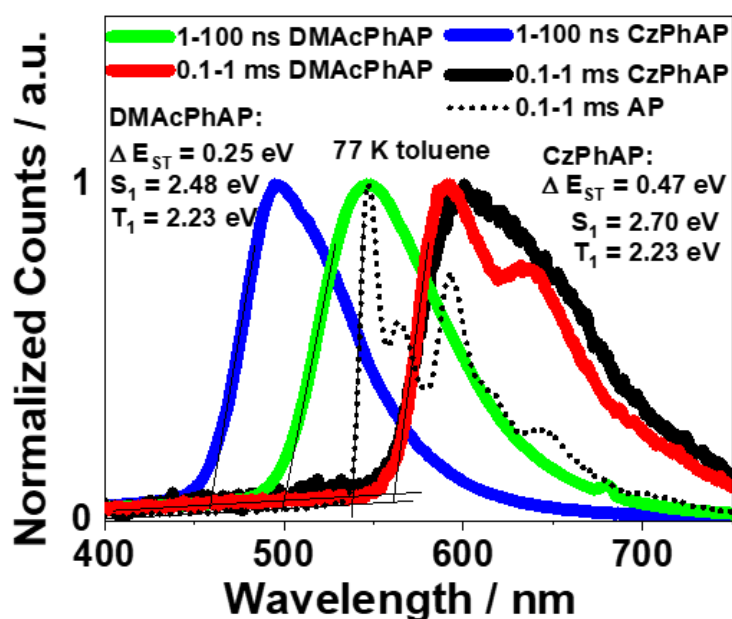
Figure 5.4. Prompt fluorescence of phosphorescence spectra of **DMAcPhAP**, **CzPhAP** and **AP** measured in 77 K toluene glass. (Femtosecond laser, λ_{exc} = 343 nm)

Figure **5.5** shows the TRPL decay of **CzPhAP** measured in toluene. Because of its large ΔE_{ST}, no delayed emission was seen in the degassed toluene. However, emission quenching was still observed in the prompt component in the aerated toluene as it can be seen that the PL decay of **CzPhAP** is slightly quicker in the aerated toluene. This quenching is also reflected in the difference in the PLQY values measured in toluene: 84% when degassed and 75% when aerated. These suggest the S_1 state of **CzPhAP** can also be quenched by air. The PLQY of **DMAcPhAP** was 29% for the degassed solution and 14% for the aerated solution. The much higher PLQY of

CzPhAP may come from its higher oscillator strength, or from its lower vibrational losses because of the rigid carbazole moiety, or a combination of both. The solution-state photophysical data is summarized in Table **5.4**.
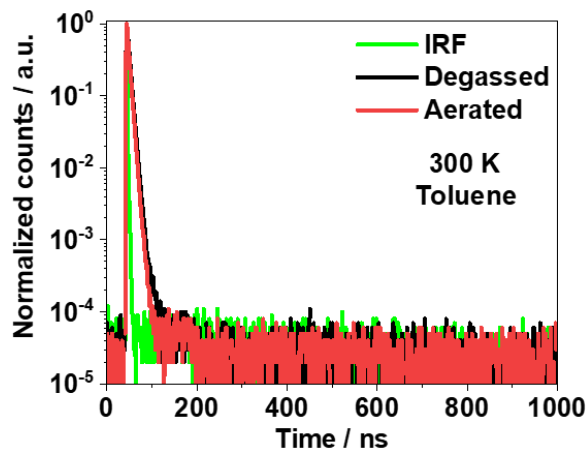
Figure 5.5. TRPL decays of **CzPhAP** measured in degassed and aerated toluene at 300 K. (λ_{exc} = 378 nm)

Table 5.4. Summary of the S_1/T_1/ΔE_{ST} energies and PLQYs of **DMAcPhAP** and **CzPhAP** in toluene.

Compound	λ_{abs}[a] /nm	λ_{PL}[a] /nm	S_1[b] /eV	T_1[b] /eV	ΔE_{ST} /eV	Φ_{PL}[c] /%
DMAcPhAP	455	640	2.48	2.23	0.25	29(14)
CzPhAP	425	536	2.70	2.23	0.47	84(75)

[a]Maximum of the CT steady-state absorption and emission band measured in toluene with solution concentration 10^{-5} mol/L at room temperature. [b]Determined from the onset values of the spectrum measured between 1-100 ns and 0.1-1 ms after photoexcitation in flash cooled 77 K toluene glass (λ_{ext} = 343 nm). [c]Φ_{PL} values were determined by the relative method. The quinine sulfate solution in 0.5M H_2SO_4 (aq) (Φ_{PL}: 54.6%) (11) was used as the external reference for **DMAcPhAP**. At the same time, Rhodamine 6G in ethanol (Φ_r = 94%) (12) was used as the external reference for **CzPhAP**.

5.5 Photophysics in the solid state

PLQY measurements were then carried out on the doped thin films of these two emitters. **DMAcPhAP** and **CzPhAP** were first doped in poly(methyl methacrylate) (PMMA) with various doping concentrations. Figures **5.6a** and **b** show the PLQY and PL peaks of these doped PMMA films measured in nitrogen atmosphere by an integrating sphere. It can be seen that their PLQY keeps decreasing but the λ_{PL} keeps increasing with the increasing doping concentration. Similar phenomena have also been observed by Yuan *el al*. (1) and Xue *et al.* (4). To explain this

phenomenon, Xue *et al*. carried out computational simulations, and proposed J-aggregation as the mechanism here: as the acceptor, **AP**, is rigid and planar, the higher doping concentrations contribute to more significant molecular aggregations, which red-shifts the PL and causes concentration quenching. Here, to obtain a higher PL/EL efficiency, doping concentrations of 3 wt% and 6 wt% were chosen for further PLQY measurements in other hosts. Lower doping concentrations (< 3 wt%) were found to introduce insufficient FRET between the host and the guest, as so were not used. Figure **5.6c** shows the PLQYs of these **DMAcPhAP** and **CzPhAP** doped films measured in air and nitrogen. The PLQYs of the 3% **DMAcPhAP**:TPBi and 6wt% **CzPhAP**:PPT films are 54.4% and 56.2% in a nitrogen atmosphere and 35.3% and 49.1% in air, which are the highest among these films. Therefore, these two films were selected for further photophysical study and were used as the EML for OLED devices. Both films show small Φ_{PL} enhancement in nitrogen atmosphere, indicating a small triplet contribution which is caused by their large ΔE_{ST} values. The steady-state PL spectra of these two films measured under vacuum are shown in Figure **5.7a**, and their peak positions are 605 nm and 580 nm, respectively.

Figure 5.6. a, b) PLQYs and PL maximum of **DMAcPhAP** and **CzPhAP** doped in PMMA films measured in nitrogen atmosphere. The doping concentrations v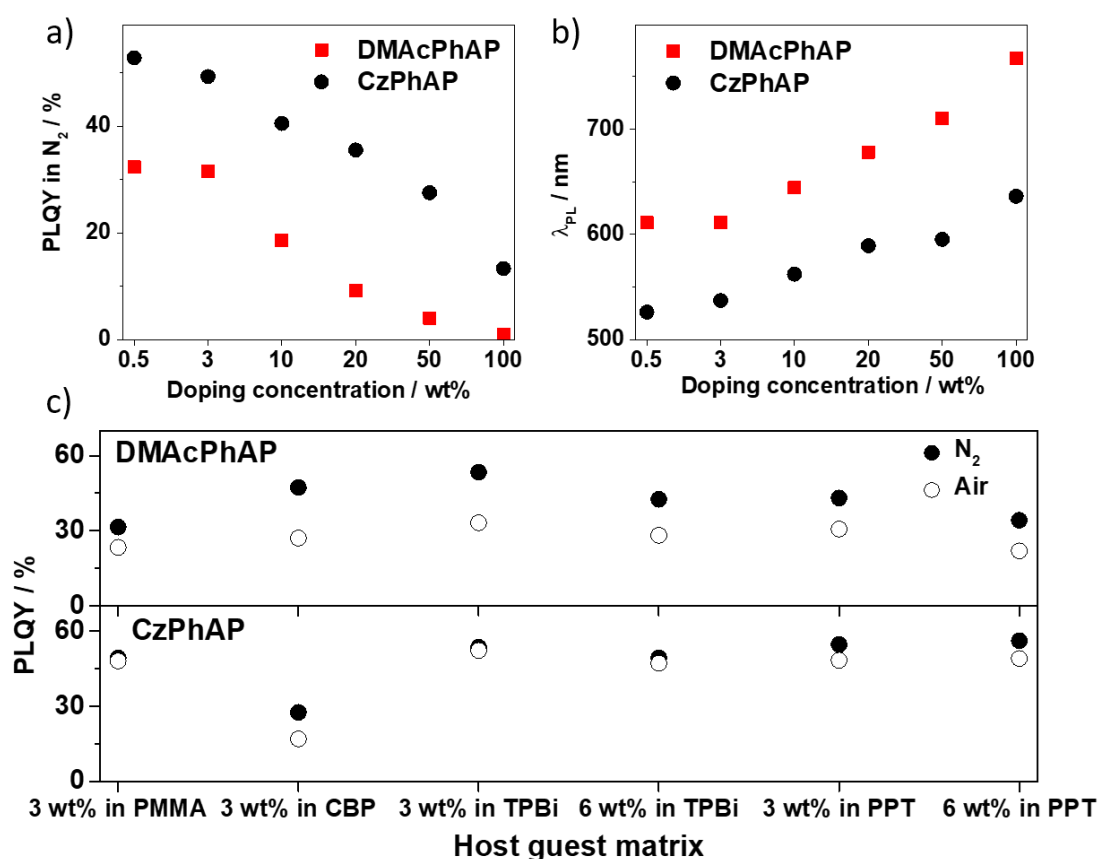ary from 0.5 wt% to 100 wt%. c) PLQYs of **DMAcPhAP** and **CzPhAP** doped in different host materials with different doping concentrations. (λ_{exc} = 340 nm)

To experimentally determine the ΔE_{ST} values of these two films, TRPL spectra were measured at 77 K. As shown in Figure **5.7b**, the fluorescence spectra were taken 1-100 ns after photoexcitation, while the phosphorescence spectra were taken 1-10 ms after photoexcitation. It is noteworthy in the measurement results of **CzPhAP** that, in the 1-10 ms spectrum (black line), there is a shoulder at 578 nm which has the same position as that of the peak of the 1-100 ns spectrum (blue line), which is marked by a blue dashed line. As the 1-100 ns spectrum originates from the S_1 state of **CzPhAP**, the shoulder in the 1-10 ms spectrum should also come from the S_1 state. The generation of the S_1 state at 77 K in the 1-10 ms time windows comes from photo-induced charges instead of TADF, which is further discussed in Chapter **8**. Therefore, the onset value of the phosphorescence spectrum of **CzPhAP** was taken from extrapolating the curve from the main peak rather than this shoulder, and so its ΔE_{ST} value was calculated to be 0.24 eV. The 3wt% **DMAcPhAP**:TPBi film show higher onset values both in the fluorescence and phosphorescence spectra compared with the 6wt% **CzPhAP**:PPT film, and its ΔE_{ST} was calculated to be 0.34 eV, which is much larger than that of **CzPhAP**. The effect of the ΔE_{ST} difference can be seen in their different delayed fluorescence PL decay rate: Figure **5.7c** shows the TRPL decay of these two films measured in a 60 ms time window under vacuum at 300 K. The delayed fluorescence component of **DMAcPhAP** decays a bit slower than that of **CzPhAP**. Also, compared with other highly efficient TADF emitters (13,14), both of these two emitters have large ΔE_{ST} values (> 0.2 eV) and long decay durations (ms), and so they are likely to show significant efficiency roll-off in OLEDs. For the decay kinetics, both films show multi-exponential features in their delayed components. The average lifetimes of the delayed components of these two films were calculated using the equation $\tau_{avg} = \Sigma A_i \tau_i^2 / A_i \tau_i$, where A_i is the pre-exponential factor for lifetime τ_i. The calculated average lifetimes are 4.7 ms and 4.2 ms for **DMAcPhAP** and **CzPhAP**, respectively. To study the properties of their prompt emissions, the TRPL decay curves of these two films were measured at 300 K in a 400 ns time window both under vacuum and in air. As shown in Figure **5.7d**, the prompt components are not oxygen sensitive as the decay curves measured in vacuum overlap perfectly with those measured in air. The average lifetimes of the prompt components of these two films were calculated to be 37.1 ns and 20.5 ns for **DMAcPhAP** and **CzPhAP**, respectively.
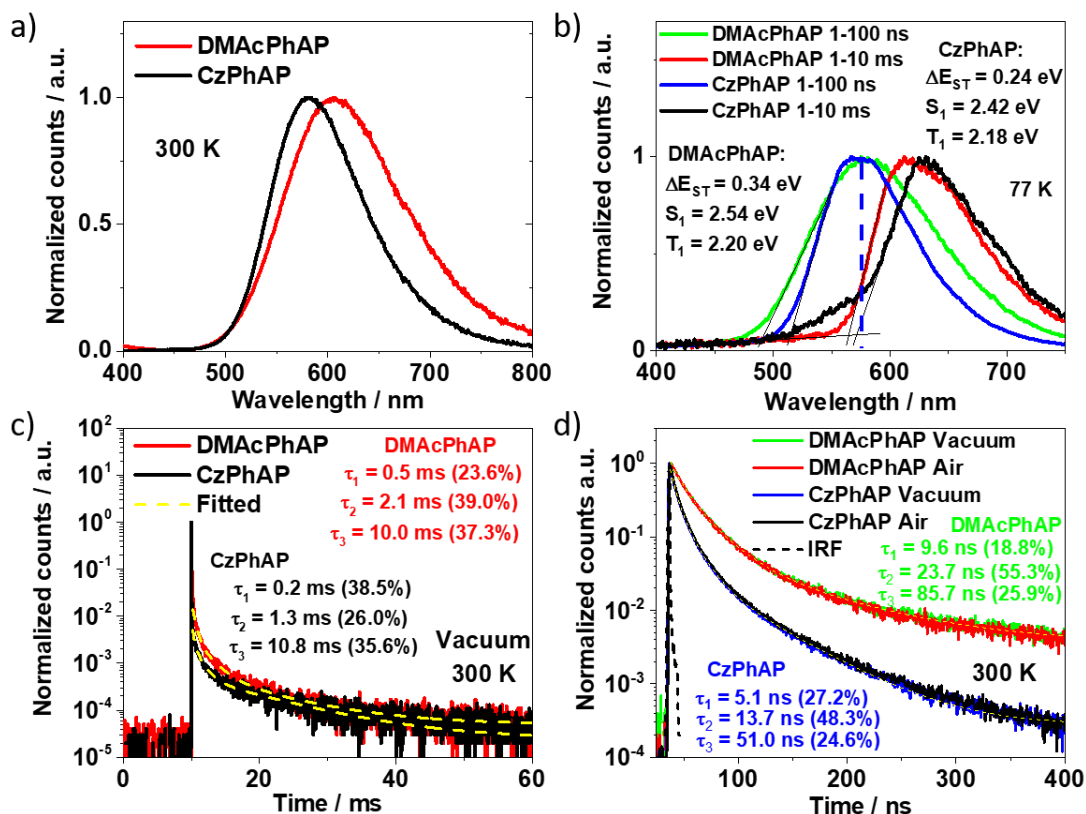
Figure 5.7. a) Steady-state PL spectra of the 3wt% **DMAcPhAP**:TPBi and 6wt% **CzPhAP**:PPT films at 300 K. b) ΔE_{ST}s of these two films measured at 77 K. Prompt fluorescence and delayed phosphorescence spectra were taken 1-100 ns and 1-10 ms after photoexcitation, respectively . c, d) TRPL decay measurement of these two films at 300 K in 60 ms and 400 ns time windows.

To make sure TADF is still operating in these two films in spite of their large ΔE_{ST} values, temperature dependent TRPL decay measurements were carried on these films with the detection wavelength fixed at 600 nm. As shown in Figure **5.8c**, the delayed emission of **CzPhAP** is gradually quenched by a lower temperature, indicating TADF is contributing to the emission of **CzPhAP** at 300 K. The TRPL decay of **DMAcPhAP** (Figure **5.8a**) does not show as much temperature dependence as that of **CzPhAP**. Although this implies TADF is playing a smaller role in **DMAcPhAP**, its PLQY enhancement in nitrogen (from 35.5% to 54.4%) is still larger than that of **CzPhAP** (from 49.1% to 56.2%). This may be due to the higher oscillator strength of **CzPhAP**, which leads to a faster singlet decay, and so fewer triplets were generated during the photoexcitation process in the **CzPhAP** film in the PLQY measurement, consequently, fewer triplets were quenched by oxygen. The higher oscillator strength of **CzPhAP** can also be reflected from its shorter prompt decay lifetime of 20.5 ns compared with that of **DMAcPhAP** (37.1 ns).

Figures **5.8b** and **d** show the temperature dependent steady-state PL spectra of the 3wt% **DMAcPhAP**:TPBi and 6wt% **CzPhAP**:PPT films. The shapes of the spectra almost do not change over different temperatures, implying prompt fluorescence is always dominant regardless the temperature differences, and the phosphorescence intensity is always weak, even at 100 K.

All the solid state photophysical properties of these two films are summarized in Table **5.5**.
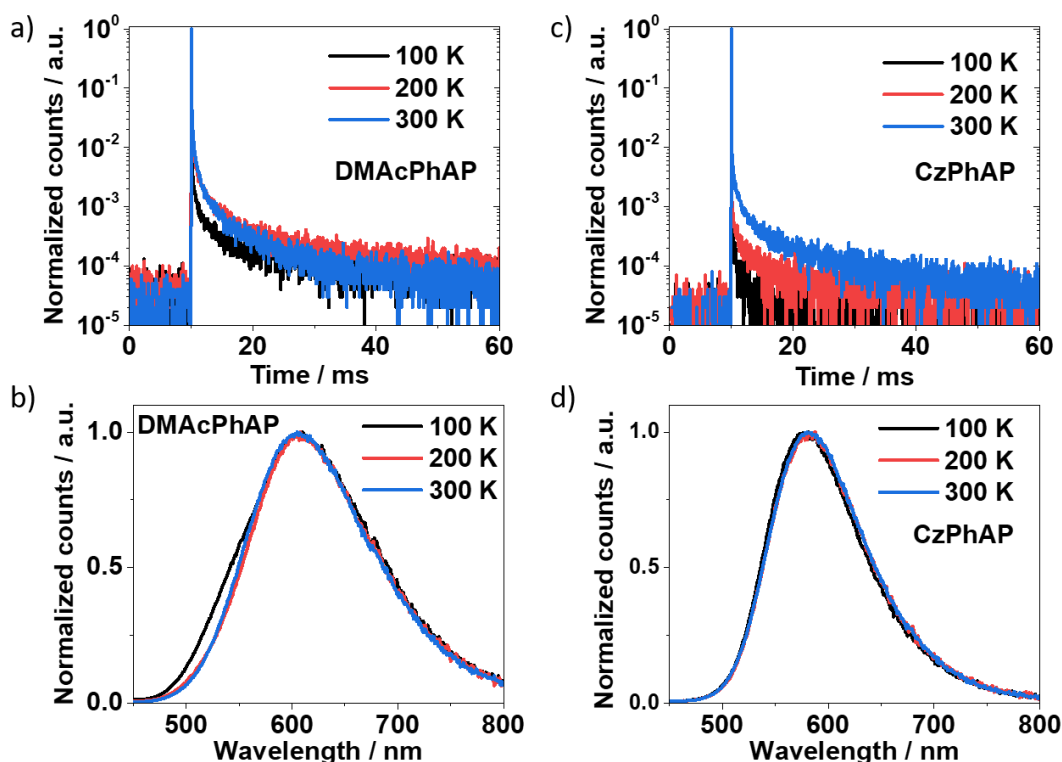
Figure 5.8. Temperature-dependent PL decay curves and steady-state PL spectra of the 3 wt**%** **DMAcPhAP**:TPBi and 6 wt% **CzPhAP:PPT** films measured at 100 K, 200 K and 300 K (λ_{exc} = 378 nm)

Table 5.5. Summary of the photophysical properties of the 3wt% **DMAcPhAP**:TPBi and 6wt% **CzPhAP**:PPT film

Film	λ_{PL}[a] /nm	Φ_{PL}[b] /%	S_1[c] /eV	T_1[c] /eV	ΔE_{ST} /eV	τ_{PF} /ns	τ_d /ms
3 wt% **DMAcPhAP**:TPBi	605	54.4 (35.3)	2.54	2.20	0.34	37.1	4.7
6 wt% **CzPhAP**:PPT	580	56.2 (49.1)	2.42	2.18	0.24	20.5	4.2

[a]Emission maximum is taken from the steady-state PL spectra measured under vacuum at room temperature (λ_{ext} = 340 nm). [b]Values determined using an integrating sphere under nitrogen atmosphere and (in air), (λ_{ext} = 340 nm). [c]Determined from the onset values of the spectra measured between 1-100 ns and 1-10 ms after photoexcitation at 77 K (λ_{ext} = 343 nm).

5.6 Device fabrication

Finally, the EL properties of these two films were studied in OLEDs. Multilayer OLEDs were fabricated through thermal evaporation using the following device stack: indium tin oxide (ITO)/ molybdenum trioxide (MoO$_3$, 3 nm)/ N,N-bis(1-naphthyl)-N,N′ -diphenyl-1,1′ -biphenyl- 4,4′ -diamine (NPB, 55 nm)/ 1,3-di(9H-carbazol-9-yl)benzene (mCP, 10 nm)/EML (20 nm)/PPT (10 nm)/ 1,3,5-tris(3-pyridyl-3phenyl)benzene (TmPyPB, 45 nm)/lithium fluoride (LiF, 1 nm)/Al (100 nm)). The device architecture and the energy levels of all the materials used in the devices are shown in Figure **5.9a**. mCP and PPT were used as the electron and hole blocking layers due to their shallow LUMO and deep HOMO with high T$_1$ energy (2.9 eV and 3.1 eV) which will not quench the triplets in the EMLs.
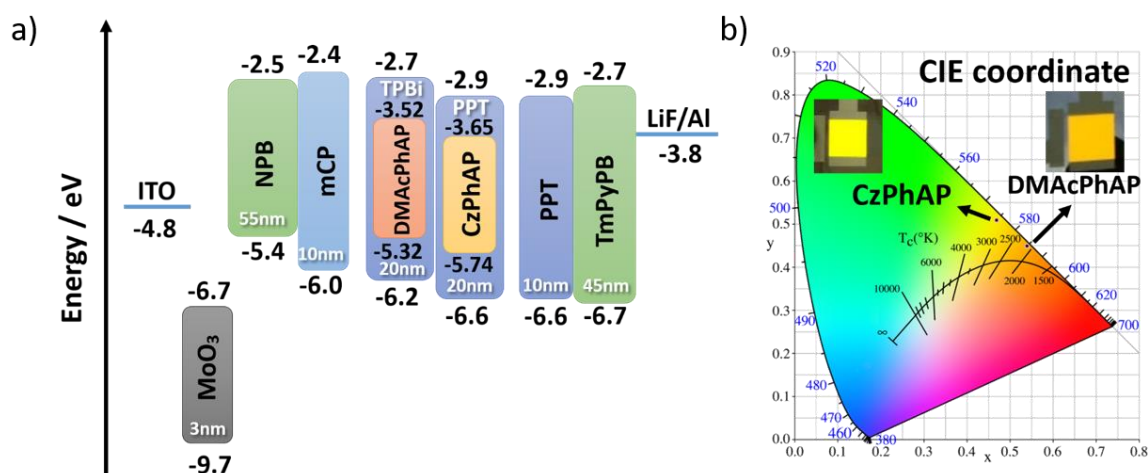
Figure 5.9. a) Schematic of the **DMAcPhAP** and **CzPhAP** OLED device architectures showing the energy level and thickness of each layer. b) CIE coordinates and photos of the OLED devices in operation.

As shown in Figure **5.10a**, both **DMAcPhAP** and **CzPhAP** devices show broad and structureless emission spectra with wide FWHM of 128 nm and 98 nm and peak positions of 605 nm and 570 nm. Figure **5.9b** shows the OLEDs devices in operation with their emission colours described by the CIE coordinates of (0.54, 0.45) and (0.47, 0.51). Combining the facts that their EL colours are orange and yellow, and their EL spectra are wide, these two emitters are consequently not suitable for display applications, but can be used for white light purposes.
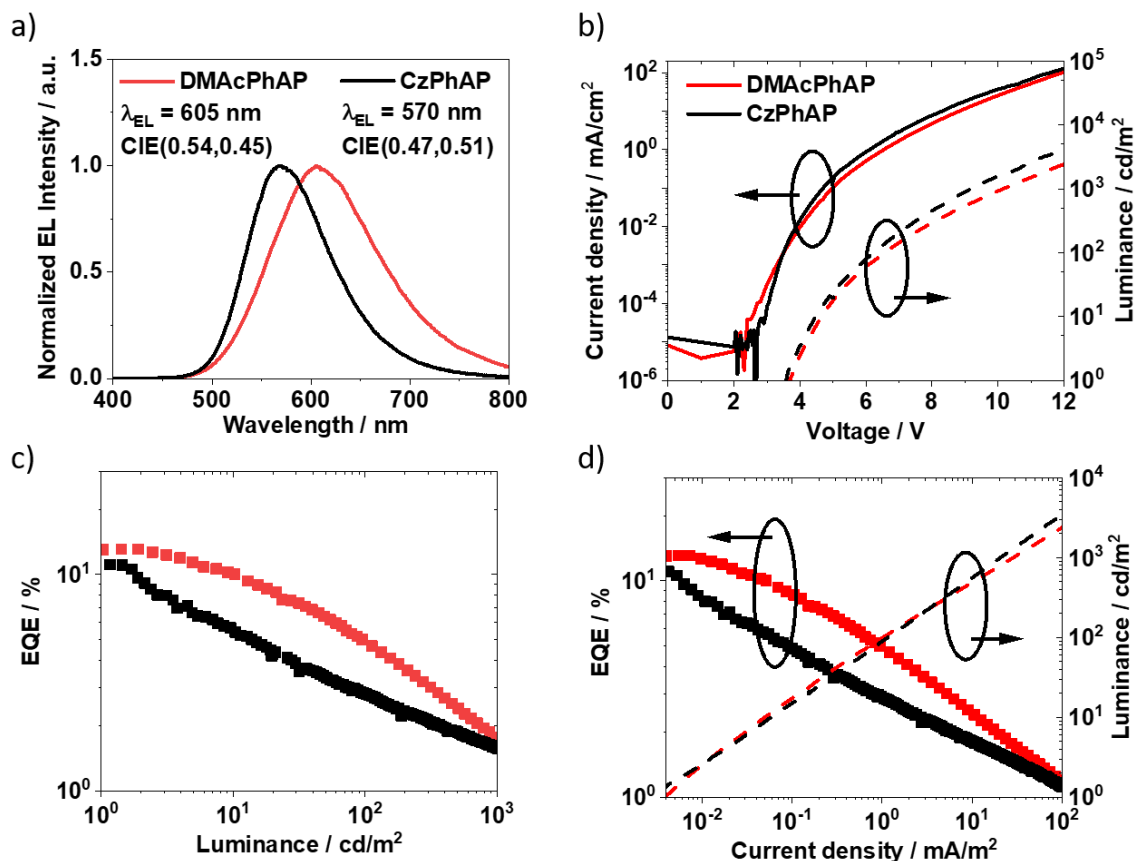
Figure 5.10. a) The electroluminescent spectrum of these OLEDs, red for **DMAcPhAP** and black for **CzPhAP**. b) Current density-voltage curves and luminance-voltage curves of the OLEDs. c) EQE-luminance curves of the OLEDs. d) EQE-current density curves and luminance-current density curves of the OLEDs.

The EL performance of these two emitters is shown in Figures **5.10a-d**. The luminance-voltage curves (Figure **5.10b**) show that both two devices have relatively high turn-on voltages (3.7 V and 3.6 V) for orange and yellow emitters at 1 cd/m^2. The EQE$_{max}$ of these two emitters are 13.0 % and 11.1 % which are far beyond the theoretical EQE$_{max}$ of fluorescent emitters (5%), again demonstrating that TADF is still operating in these two devices regardless their larger ΔE_{ST}s. However, these large ΔE_{ST}s also contribute to significant efficiency roll-off as the EQE values drop to 4.7 % and 2.8 % at 100 cd/m^2, and 1.8% and 1.6% at 1000 cd/m^2.

In the device efficiency roll-off study, a strange phenomenon is found: at 100 cd/m^2, the **DMAcPhAP** device has less efficiency roll-off (calculated from EQE/EQE$_{max}$) compared with that of the **CzPhAP** device (35.81% vs 25.25%). However, at 1000 cd/m^2, the efficiency roll-off of these two devices become comparable (13.57% vs 14.25%). Furthermore, **DMAcPhAP** has a larger ΔE_{ST} than **CzPhAP** (0.34 eV vs 0.24 eV), which should have led to a constantly more

significant efficiency roll-off in the **DMAcPhAP** device, but it did not. Taking into account the observation of singlet emission of **CzPhAP** at 77 K (Figure **5.7b**) which is caused by photo-induced charges, the more significant roll-off in the **CzPhAP** device at 100 cd/m^2 is probably due to singlet-polaron quenching. The effect of polaron and photo-induced charges in the 6 wt% **CzPhAP**:PPT film is further discussed in Chapter **8**.

All the device performance data are summarized in Table **5.6**.

Table 5.6. Summary of the **DMAcPhAP** and **CzPhAP** OLED device performance

Emitter	λ_{EL} /nm	FWHM /nm	V_{on}[a] /V	EQE$_{max}$; EQE$_{100}$; EQE$_{1000}$[b] /%	PE$_{max}$; PE$_{100}$[c] /lm/W	CE$_{max}$; CE$_{100}$[d] /lm/A	CIE /(x, y)
DMAcPhAP	605	128	3.7	13.04; 4.67; 1.77	22.08; 4.82	34.06; 8.60	(0.54, 0.45)
CzPhAP	570	98	3.6	11.09; 2.8; 1.58	29.72; 4.32	26.01; 9.98	(0.47, 0.51)

[a]Defined as the lowest operating voltage at the luminance of >1 cd/m^2. [b]Maximum EQE above 1 cd/m^2; EQE at 100 cd/m^2; and at 1000 cd/m^2. [c]Maximum power efficiency above 1 cd/m^2; power efficiency at 100 cd/m^2. [d]Maximum current efficiency above 1 cd/m^2; current efficiency at 100 cd/m^2;

5.7 Conclusion

Here, we designed two D-A type TADF emitters **DMAcPhAP** and **CzPhAP** using **AP** as the rigid and strong electron-accepting unit, and using DMAc and Cz as the electron-donating unites. Although both **DMAcPhAP** and **CzPhAP** have large ΔE_{ST}s (0.34 eV and 0.24 eV), they still show many TADF properties such as PLQY enhancement in nitrogen atmosphere, delayed fluorescence lasting for milliseconds at room temperature and OLED EQE$_{max}$ values are far above 5%. The corresponding devices have EL emission peaks of 605 nm and 570 nm with CIE coordinates of (0.54, 0.45) and (0.47, 0.51) and FWHM values of 128 nm and 98 nm, which are not sufficiently red or narrow to be used for OLED displays. However, applications might be found in white light devices. During our molecular property study, evidence was found that charges (polaron) are affecting the PL and EL properties of **CzPhAP** in solid state, which is reflected in its phosphorescence spectrum measured at 77 K (Figure **5.7b**), and may also contribute to the efficiency roll-off of the OLED device (Figure **5.10c**). A further study of the charges (polaron) in the **CzPhAP** doped films is discussed in Chapter **8**.

5.8 References

1.   Yuan Y, Hu Y, Zhang Y-X, Lin J-D, Wang Y-K, Jiang Z-Q, Liao L-S, Lee S-T. Over 10% EQE Near-Infrared Electroluminescence Based on a Thermally Activated Delayed Fluorescence Emitter. Adv Funct Mater. 2017;27(26):1700986. Available from: http://doi.wiley.com/10.1002/adfm.201700986

2.   Wong MY. Creating novel thermally activated delayed fluorescence (TADF) emitters for light-emitting electrochemical cells (LEECs) and organic light-emitting diodes (OLEDs) applications and their structure-property relationship [Internet]. University of St Andrews; 2017. Available from: http://hdl.handle.net/10023/12975

3.   Hu Y, Yu Y, Yuan Y, Jiang Z, Liao L. Exciplex-Based Organic Light-Emitting Diodes with Near-Infrared Emission. Adv Opt Mater. 2020;8(7):1901917. Available from: https://onlinelibrary.wiley.com/doi/abs/10.1002/adom.201901917

4.   Xue J, Liang Q, Wang R, Hou J, Li W, Peng Q, Shuai Z, Qiao J. Highly Efficient Thermally Activated Delayed Fluorescence via J-Aggregates with Strong Intermolecular Charge Transfer. Adv Mater. 2019;31(28):1808242. Available from: https://pubs.acs.org/doi/10.1021/jacs.9b09323

5.   Congrave DG, Drummond BH, Conaghan PJ, Francis H, Jones STE, Grey CP, Greenham NC, Credgington D, Bronstein H. A Simple Molecular Design Strategy for Delayed Fluorescence toward 1000 nm. J Am Chem Soc. 2019;141(46):18390–4. Available from: https://pubs.acs.org/doi/10.1021/jacs.9b09323

6.   Hu Y, Yuan Y, Shi Y-L, Li D, Jiang Z-Q, Liao L-S. Efficient Near-Infrared Emission by Adjusting the Guest-Host Interactions in Thermally Activated Delayed Fluorescence Organic Light-Emitting Diodes. Adv Funct Mater. 2018;28(32):1802597. Available from: http://doi.wiley.com/10.1002/adfm.201802597

7.   Zhang Q, Kuwabara H, Potscavage WJ, Huang S, Hatae Y, Shibata T, Adachi C. Anthraquinone-Based Intramolecular Charge-Transfer Compounds: Computational Molecular Design, Thermally Activated Delayed Fluorescence, and Highly Efficient Red Electroluminescence. J Am Chem Soc. 2014;136(52):18070–81. Available from: https://pubs.acs.org/doi/10.1021/ja510144h

8.   Fukushima T, Yamamoto J, Fukuchi M, Hirata S, Jung HH, Hirata O, Shibano Y, Adachi C,

Kaji H. Material degradation of liquid organic semiconductors analyzed by nuclear magnetic resonance spectroscopy. AIP Adv. 2015;5(8):087124. Available from: http://dx.doi.org/10.1063/1.4928515

9.   Tomkeviciene A, Grazulevicius J V., Volyniuk D, Jankauskas V, Sini G. Structure–properties relationship of carbazole and fluorene hybrid trimers: experimental and theoretical approaches. Phys Chem Chem Phys. 2014;16(27):13932. Available from: http://xlink.rsc.org/?DOI=c4cp00302k

10.   Pavlishchuk V V, Addison AW. Conversion constants for redox potentials measured versus different reference electrodes in acetonitrile solutions at 25°C. Inorganica Chim Acta. 2000;298(1):97–102. Available from: https://linkinghub.elsevier.com/retrieve/pii/S0020169399004077

11.   Melhuish WH. QUANTUM EFFICIENCIES OF FLUORESCENCE OF ORGANIC SUBSTANCES: EFFECT OF SOLVENT AND CONCENTRATION OF THE FLUORESCENT SOLUTE 1. J Phys Chem. 1961;65(2):229–35. Available from: https://pubs.acs.org/doi/abs/10.1021/j100820a009

12.   Fischer M, Georges J. Fluorescence quantum yield of rhodamine 6G in ethanol as a function of concentration using thermal lens spectrometry. Chem Phys Lett. 1996;260(1–2):115–8. Available from: https://linkinghub.elsevier.com/retrieve/pii/000926149600838X

13.   dos Santos PL, Ward JS, Congrave DG, Batsanov AS, Eng J, Stacey JE, Penfold TJ, Monkman AP, Bryce MR. Triazatruxene: A Rigid Central Donor Unit for a D-A 3 Thermally Activated Delayed Fluorescence Material Exhibiting Sub-Microsecond Reverse Intersystem Crossing and Unity Quantum Yield via Multiple Singlet-Triplet State Pairs. Adv Sci. 2018;5(6):1700989. Available from: http://doi.wiley.com/10.1002/advs.201700989

14.   Uoyama H, Goushi K, Shizu K, Nomura H, Adachi C. Highly efficient organic light-emitting diodes from delayed fluorescence. Nature. 2012;492(7428):234–8. Available from: http://dx.doi.org/10.1038/nature11687

Chapter 6 New Blue Thermally Activated Delayed Fluorescence Emitters

This work focuses on developing new deep-blue thermally activated delayed fluorescence (TADF) OLED materials by modifying a previously reported efficient sky-blue TADF emitter, **2CzIPN**, to makes its emission deeper blue. This was achieved by replacing its strong acceptor (cyano group) with weak acceptors (1,3,4-oxadiazole derivatives). One of the new emitters, *i*-**2CzOXDMe**, has an EL emission maximum of 452 nm with the CIE coordinates of (0.17, 0.17), which shows a decent blue-shift compared with reference emitter, **2CzIPN**, which has an EL emission maximum of 477 nm and CIE coordinates of (0.18, 0.30), demonstrating the validity of this strategy. In addition, the EQE_{max} of this new emitter is 11.8%, which is comparable with that of **2CzIPN** (15.0%). However, the EQE of *i*-**2CzOXDMe** drops to 1.3% at 100 cd/cm^2, which is much lower than that of **2CzIPN** (7.0%). This is caused by the low T_1 energy levels of the 1,3,4-oxadiazole groups which lead to large ΔE_{ST}s and the consequent severe efficiency roll-off.

This chapter is adapted from a published paper (Li Z, Li W, Keum C, Archer E, Zhao B, Slawin AM, Huang W, Gather MC, Samuel ID, Zysman-Colman E. 1, 3, 4-Oxadiazole-based Deep Blue Thermally Activated Delayed Fluorescence Emitters for Organic Light Emitting Diodes. The Journal of Physical Chemistry C. 2019;123(40):24772-85). It is a collaborative work between I. D. W. Samuel's group and E. Zysman-Colman's group at the University of St Andrews. In this chapter, Z. Li from, Zysman-Colman's group performed the molecular design and synthesis. He also performed the TD-DFT calculations, CV measurement and solvatochromism PL spectrum measurements. I performed the APS measurement, all the photophysics in solid state films, OLED device fabrication and device characterisations.

6.1 Molecular design and computation

Blue emitters are important for OLED displays as blue is one of the three primary colours. As has been discussed in Section **4.4.2**, current blue TADF OLEDs have not met the industry criteria in terms of the light-emitting efficiency and emission colour, which requires to be further developed. In the history of blue TADF emitter studies, Uoyama *et al*. proposed the first sky-blue TADF emitter, 2CzPN (Figure **6.1a**), in 2012 (1). Their 2CzPN based OLED shows EQE_{max} of 8% ($EQE_{1mA/cm2} \approx 3.1\%$) with emission peak at 477 nm. Later, the isomer of 2CzPN, **2CzIPN** (also referred as DCzIPN, Figure **6.1b**), was synthesized and studied by Cho *et al.* in 2015 (2). Compared with 2CzPN which has donors and acceptors connected in ortho-position, **2CzIPN** has donors and acceptors connected in meta-position, which leads to weaker coupling between them and blue-shift the emission spectrum. Their **2CzIPN**-based OLED indeed showed a blue-shifted emission peak to 462 nm with CIE coordinates of (0.17, 0.19), and the EQE_{max} was also enhanced to 16.4% ($EQE_{100 cd/m2} \approx 15.2\%$).

To further blue-shift the emission by modifying **2CzIPN**, in this work, the strong electron-acceptors, cyano groups, in **2CzIPN** were replaced by much weaker electron-acceptors, the derivatives of 1,3,4-oxadiazole groups. The molecular structure of 1,3,4-oxadiazole is shown in Figure **6.1c** and the new emitters are shown in Scheme **6.1**. The shallower LUMO provided by the 1,3,4-oxadiazole derivatives can enlarge the HOMO-LUMO band gap of the materials, and consequently increase the emitted photon energy.
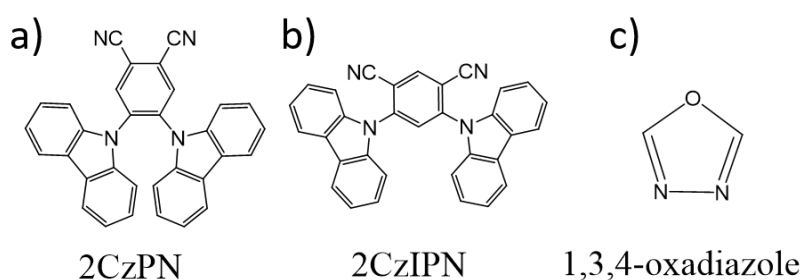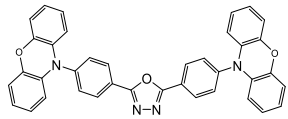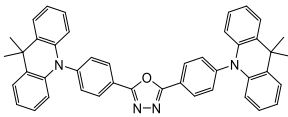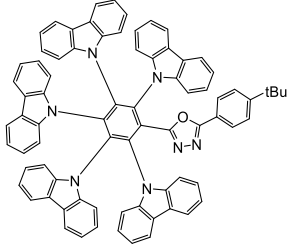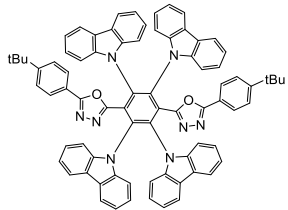
Figure 6.1. a, b, c) Molecular structures of 2CzPN, 2CzIPN and 1,3,4-oxadiazole

1,3,4-oxadiazole and its derivatives have also been previously used for highly efficient OLEDs, which are summarized in Table **6.1**. In 2013, Lee *et al.* (3) reported a green TADF emitter, 2PXZ-OXD, which employed 2,5-diphenyl-1,3,4-oxadiazole as the acceptor and two phenoxazine as the donors. The OLEDs showed EQE_{max} of 14.9% ($EQE_{1 mA/cm2} \approx 8.0\%$) with the emission peak at 517 nm and CIE coordinates of (0.25, 0.45). In 2019, Tan *et al.* (4) replaced its phenoxazine groups by DMAc groups, and got a bluer TADF emitter, BAcOX, which showed EQE_{max} of 22.3%

(EQE$_{100 \text{ cd/m2}}$ ≈ 7.0%) with the emission peak at 476 nm and CIE coordinates of (0.16, 0.24). In 2018, Cooper *et al.* (5) reported a sky-blue TADF emitter, named 2,3,4,5,6CzDPO, which used 2-(pentafluorophenyl)-5phenyl-1,3,4-oxadiazole as the acceptor and 5 carbazole groups as the donors. Its OLEDs showed EQE$_{max}$ of 24.4% (EQE$_{100 \text{ cd/m2}}$ ≈ 18.0%) with the emission peak at 490 nm and CIE coordinates of (0.16, 0.29). Recently, in late 2019, Zhang *et al.* (6) further modified 2,3,4,5,6CzDPO by replacing one of the carbazole by another 2-(pentafluorophenyl)-5phenyl-1,3,4-oxadiazole acceptor, and got a green TADF emitter: TCZPBOX. The OLED showed EQE$_{max}$ of 27.9% (EQE$_{100 \text{ cd/m2}}$ ≈ 26.2%) with emission peak at 527 nm and CIE coordinates of (0.34, 0.58).

Table 6.1. Molecular structures and properties of 2PXZ-OXD, BAcOX, 2,3,4,5,6CzDPO, TCZPBOX

Molecule	Structure	$\lambda_{Emission}$[a] / nm	CIE (x,y)	EQE$_{max}$[b] / %	EQE$_{100 \text{ cd/m2}}$[c] / %	EQE$_{1 \text{ mA/cm2}}$[d] / %
2PXZ-OXD		517	0.25, 0.45	14.9	-	~8.0
BAcOX		476	0.16, 0.24	22.3	~7.0	~7.1
2,3,4,5,6CzDPO		490	0.16, 0.29	24.4	~18.0	-
TCZPBOX		527	0.34, 0.58	27.9	26.2	-

[a]Emission maximum of the molecules. [b]Maximum EQE above 1 cd/m^2. [c]EQE @ 100 cd/m^2. [d]EQE @ 1 mA/cm^2.

In this work, the effect of different 1,3,4-oxadiazole derivatives was explored by connecting them to different substituents, namely methyl group (Me), phenyl group (Ph), trifluorotoluene group (CF$_3$Ph) and anisole group (MeOPh). Therefore, four new TADF emitters were synthesized and denoted as *i-2CzdOXDMe*, *i-2CzdOXDPh*, *i-2CzdOXD4CF$_3$Ph*, and *i-2CzdOXD4MeOPh*. Their

molecular structures and the schematic diagram of their synthetic routes are shown in Scheme **6.1**.
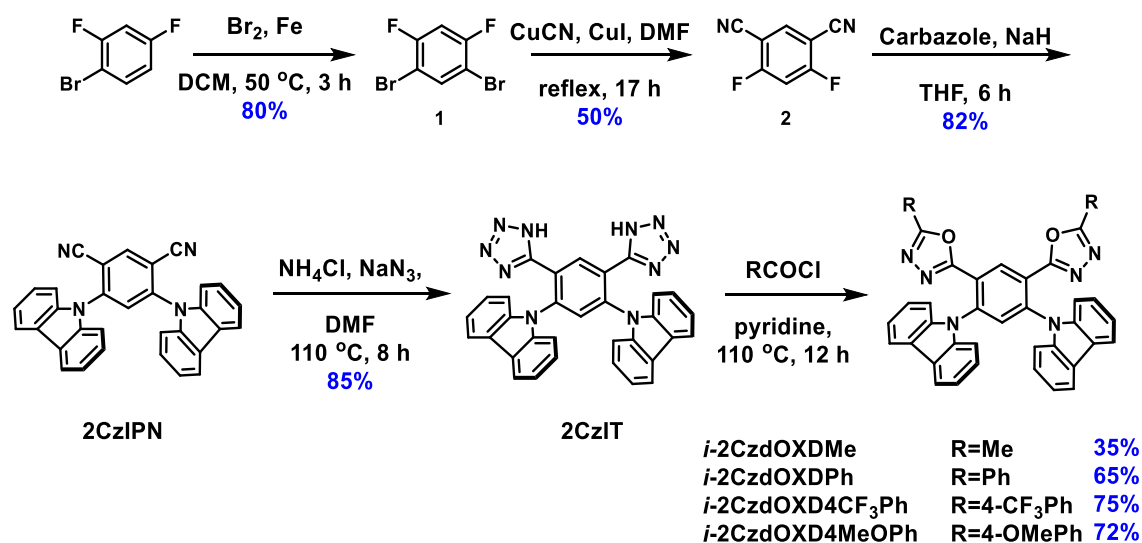
Scheme 6.1. Synthetic routes of **2CzIPN**, *i*-**2CzdOXDMe**, *i*-**2CzdOXDPh**, *i*-**2CzdOXD4CF₃Ph**, and *i*-**2CzdOXD4MeOPh**. Figure adapted from (7).

To estimate the properties of these emitters, DFT and TDDFT calculations in the gas phase with PBE0 functional and the Pople 6-31G (d,p) basis set were performed on all the emitters including the reference molecule, **2CzIPN**. Also, the Tamm-Dancoff approximation (TDA) was used as a variant of TD-DFT. The calculation results are shown in Figure **6.2** and summarized in Table **6.2**. It can be seen that all the LUMO levels of the new emitters become shallower compared with the reference emitter because of the introduction of the 1,3,4-oxadiazole derivatives as the acceptor, which is in line with the purpose of the design. However, apart from **2CzdOXD4MeOPh**, the rest of the emitters have similar S_1 energy levels. It was found that when the LUMO becomes shallower in the new emitters, the HOMO values shift in the same direction almost by the same amount, which cancels the effect of the shift of the LUMO energy. For the TADF properties, all the molecules show small HOMO and LUMO overlap. Consequently, the small ΔE_{ST} values of 0.24 eV, 0.23 eV, 0.25 eV, 0.23 eV and 0.39 eV are obtained for **2CzIPN**, *i*-**2CzdOXDMe**, *i*-**2CzdOXDPh**, *i*-**2CzdOXD4CF₃Ph**, and *i*-**2CzdOXD4MeOPh**, respectively. All their oscillator strengths (*f*) are reasonably large (0.11-0.15) among TADF emitters, which is expected to lead to high PLQYs.
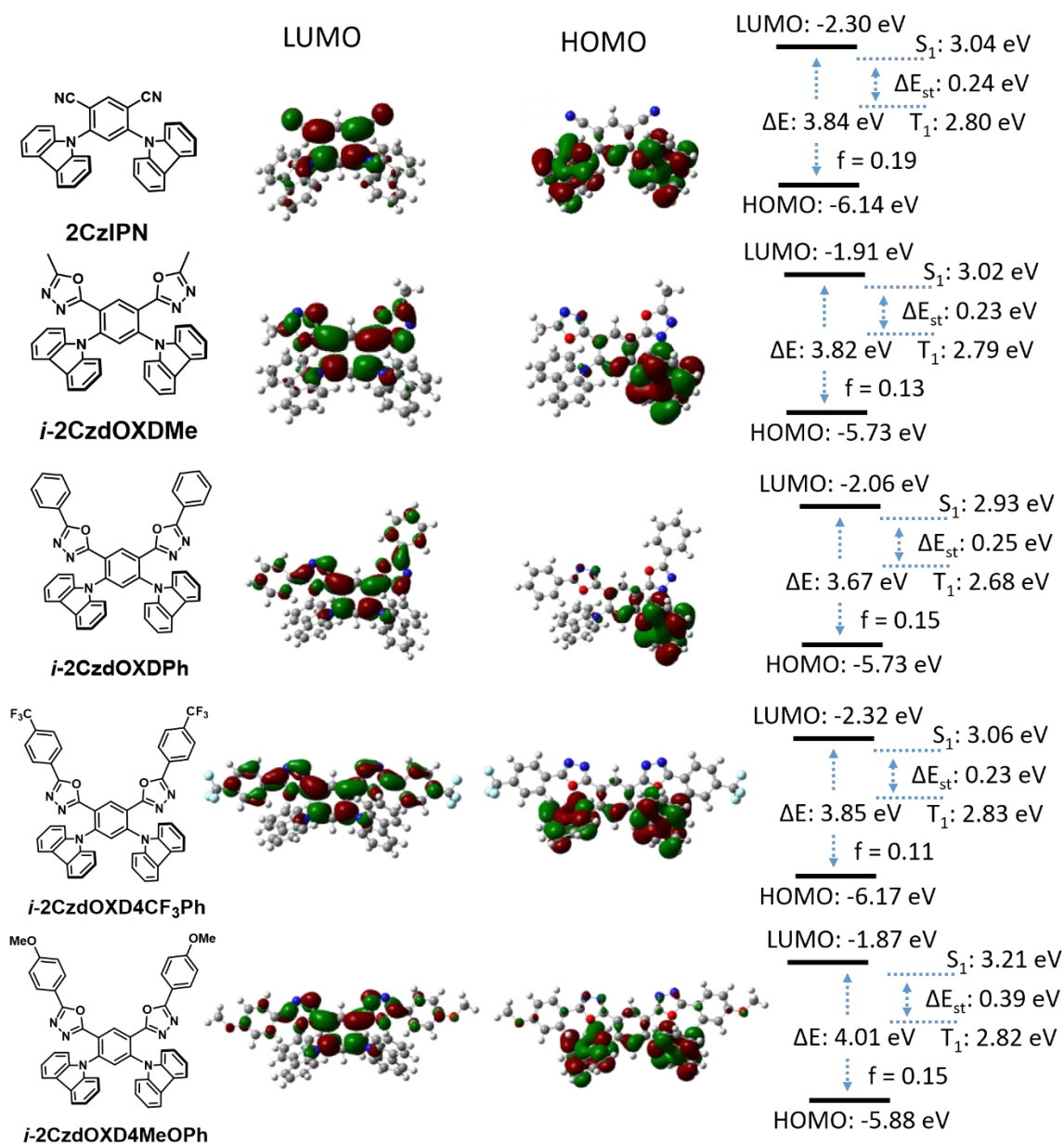
Figure 6.2. Molecular structures and calculation results of **2CzIPN, *i*-2CzdOXDMe, *i*-2CzdOXDPh, *i*-2CzdOXD4CF₃Ph,** and ***i*-2CzdOXD4MeOPh.** DFT determined electron density distribution and energies of the HOMO and LUMO, TDDFT determined energies of the S_1 and T_1 states of these two molecules in gas phase.

Table 6.2. Summary of the calculated HOMO/LUMO values, $S_1/T_1/\Delta E_{ST}$ energies levels and oscillator strength values of **2CzIPN, *i*-2CzOXDMe, *i*-2CzOXDPh, *i*-2CzOXD3CF₃Ph** and ***i*-2CzdOXD4MeOPh** in gas phase.

Compound	HOMO[a] /eV	LUMO[a] /eV	ΔE /eV	S_1[b] /eV	T_1[b] /eV	ΔE_{ST}[c] /eV	f[b]
2CzIPN	-6.14	-2.30	3.84	3.04	2.80	0.24	0.19
***i*-2CzdOXDMe**	-5.73	-1.91	3.82	3.02	2.79	0.23	0.13
***i*-2CzdOXDPh**	-5.73	-2.06	3.67	2.93	2.68	0.25	0.15
***i*-2CzdOXD4CF₃Ph**	-6.17	-2.32	3.85	3.06	2.83	0.23	0.11
***i*-2CzdOXD4MeOPh**	-5.88	-1.87	4.01	3.21	2.82	0.39	0.15

[a]Calculated by DFT. [b]Calculated by TD-DFT. The calculations were performed in gas phase with Pbe1pbe/6-31G (d,p) set. [c]$\Delta E_{ST} = S_1 - T_1$

6.2 Experimental HOMO and LUMO energy level determination

As shown in Figure **6.3**, the HOMO and LUMO energy levels of these molecules were measured using cyclic voltammetry (CV, solid line) and differential pulse voltammetry (DPV, dashed line) in MeCN. Because of the use of carbazole, all the five emitters show irreversible oxidation waves, which is assigned to the dimerization of carbazole (8,9). The HOMO and LUMO energy levels were determined from the onsets of the oxidation and reduction potential. The HOMO values were found to be -5.84 eV, -5.75 eV, -5.71 eV, -5.72 eV and -5.70 eV, respectively, for **2CzIPN, *i*-2CzOXDMe, *i*-2CzOXDPh, *i*-2CzOXD4CF₃Ph** and ***i*-2CzdOXD4MeOPh**, and the LUMO values were found to be -2.96 eV, -2.77 eV, -2.85 eV, -2.93 eV and -2.78 eV. For comparison, the HOMO energy levels were also measured using APS (Figure **6.4**), which were determined from the onsets of the cubic root of the photoemission yield of their neat films. The corresponding HOMO values are -5.98 eV, -5.77 eV, -5.75 eV, -5.71 eV, and -5.78 eV which are close to the CV measurement results.
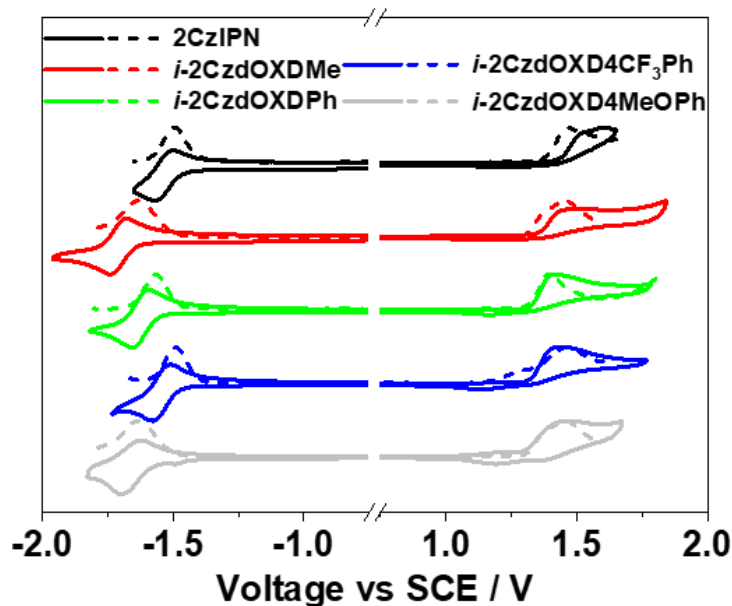
Figure 6.3. CV (solid) and DPV (dashed) traces for all these emitters in degassed MeCN under nitrogen with 0.1 M [nBu4N]PF6 as the supporting electrolyte and using Fc/Fc+ as the internal standard. Scan rate = 100 mV/s.
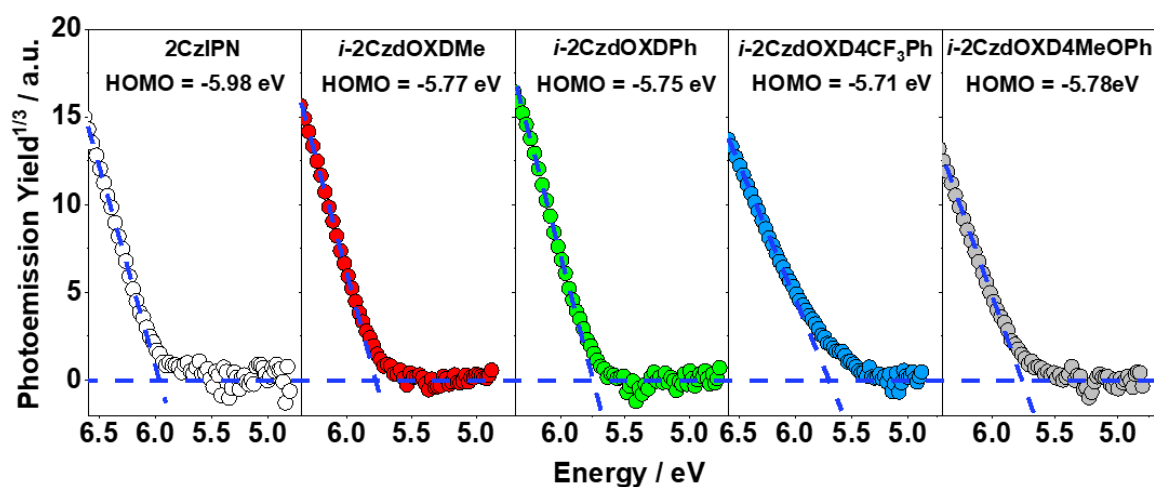
Figure 6.4. APS measurement of the neat **2CzIPN, *i*-2CzOXDMe, *i*-2CzOXDPh, *i*-2CzOXD3CF3Ph** and ***i*-2CzdOXD3MeOPh** films.

Table **6.3** shows the comparison of the HOMO, LUMO and band gap values (Δ*E*) obtained through different measurement methods. In the 'APS' column, the values of Δ*E* were determined from the onsets of their steady-state PL spectra measured in toluene (Figure **6.6**). The LUMO values were obtained through adding these Δ*E* values to the corresponding HOMO values determined by APS. It can be seen that the calculated LUMO values are more than 0.5 eV off from those obtained by CV, such as the LUMO values of ***i*-2CzdOXDPh** (-2.06 eV vs -2.85 eV)

and the LUMO values of *i*-**2CzdOXD4MeOPh** (-1.87 eV vs -2.78 eV). In comparison, CV and APS results usually show a good agreement, especially for the HOMO and LUMO values of the reference emitter, **2CzIPN**.

Table 6.3. Summary of the HOMO, LUMO and the band gap values of **2CzIPN, *i*-2CzOXDMe, *i*-2CzOXDPh, *i*-2CzOXD4CF₃Ph** and ***i*-2CzdOXD4MeOPh** obtained by calculations, CV and APS.

Method	Calculation[a]			CV[b]			APS[c]		
Compound	HOMO /eV	LUMO /eV	ΔE /eV	HOMO /eV	LUMO /eV	ΔE /eV	HOMO /eV	LUMO /eV	ΔE /eV
2CzIPN	-6.14	-2.30	3.84	-5.84	-2.96	2.88	-5.98	-2.98	3.00
***i*-2CzdOXDMe**	-5.73	-1.91	3.82	-5.75	-2.77	2.98	-5.77	-2.65	3.12
***i*-2CzdOXDPh**	-5.73	-2.06	3.67	-5.71	-2.85	2.86	-5.75	-2.63	3.12
***i*-2CzdOXD4CF₃Ph**	-6.17	-2.32	3.85	-5.72	-2.93	2.79	-5.71	-2.67	3.04
***i*-2CzdOXD4MeOPh**	-5.88	-1.87	4.01	-5.70	-2.78	2.92	-5.78	-2.60	3.18

[a]Calculated through DFT (Figure **6.2**). [b]HOMO and LUMO values were obtained from CV measurements. ΔE = LUMO - HOMO. [c]ΔEs were obtained from the onsets of steady-state PL spectra of these emitters in toluene (Figure **6.6**). HOMO values were measured using APS. LUMO = HOMO + ΔE.

6.3 Thermal analysis

After material synthesis, thermogravimetric analysis (TGA) and differential scanning calorimetry (DSC) were carried out in nitrogen atmosphere to study the thermal stability of these emitters. As shown in Figure **6.5a**, all of ***i*-2CzOXDMe, *i*-2CzOXDPh, *i*-2CzOXD4CF₃Ph** and ***i*-2CzdOXD3MeOPh** show high decomposition temperatures (T_d, defined as the temperature of 5% weight loss) of 379 °C, 400 °C, 402 °C, and 402 °C. However, as shown in the DSC study (Figure **6.5b**), their glass transition temperature, T_g, cannot easily be found from the measured curves as all curves are almost flat below 270 °C. Nevertheless, the clear endothermic peaks show that the melting points of these emitters are 298 °C, 294 °C, 325 °C and 270 °C, respectively. Most importantly, the thermal analysis results indicate that these materials are sufficiently thermal stable for vacuum depositions which were later used for their film sample and OLED fabrications.
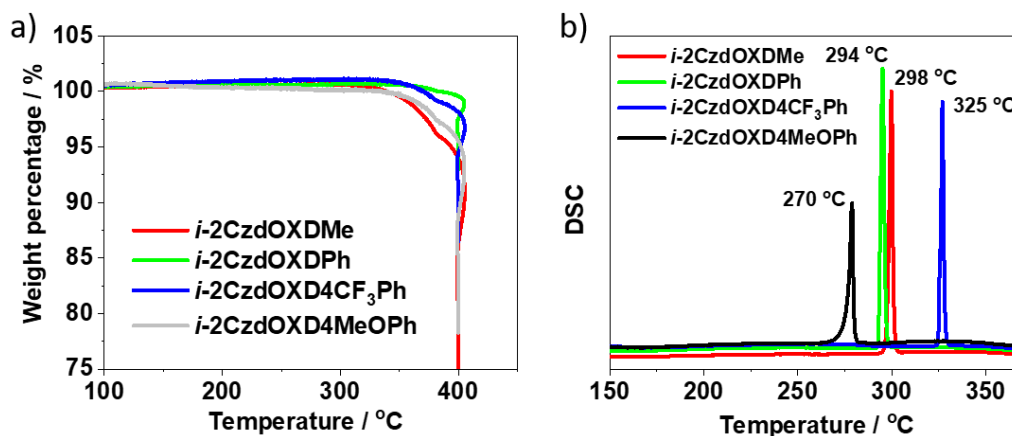
Figure 6.5. a, b) TGA and DSC of *i-2CzOXDMe*, *i-2CzOXDPh*, *i-2CzOXD4CF₃Ph* and *i-2CzdOXD4MeOPh*.

6.4 Photophysics in solution

The steady-state absorption and PL spectra of these emitters were measured in toluene (Figure **6.6**). It can be seen that all these emitters show CT absorption and emission characters. The low-energy CT absorption bands are broad and structureless, with absorption maximum, λ_{abs}, at 374 nm, 359 nm, 370 nm, 376 nm and 371 nm for **2CzIPN, *i-2CzOXDMe*, *i-2CzOXDPh*, *i-2CzOXD4CF₃Ph*** and ***i-2CzdOXD4MeOPh***. The emission maximum, λ_{PL}, of these spectra are 454 nm, 444 nm, 439 nm, 456 nm and 428 nm, respectively. Therefore, although the calculation predicts that all these emitters have almost the same S_1 state energy levels (Figure **6.2**), the experimental results show that all the new 1,3,4-oxadiazole based emitters have obvious blue-shifted steady-state PL spectra compared with that of the reference material, **2CzIPN**. Therefore, the strategy of replacing the cyano group with 1,3,4-oxadiazole derivatives is an effective way to tune emission towards the blue region of the spectrum.
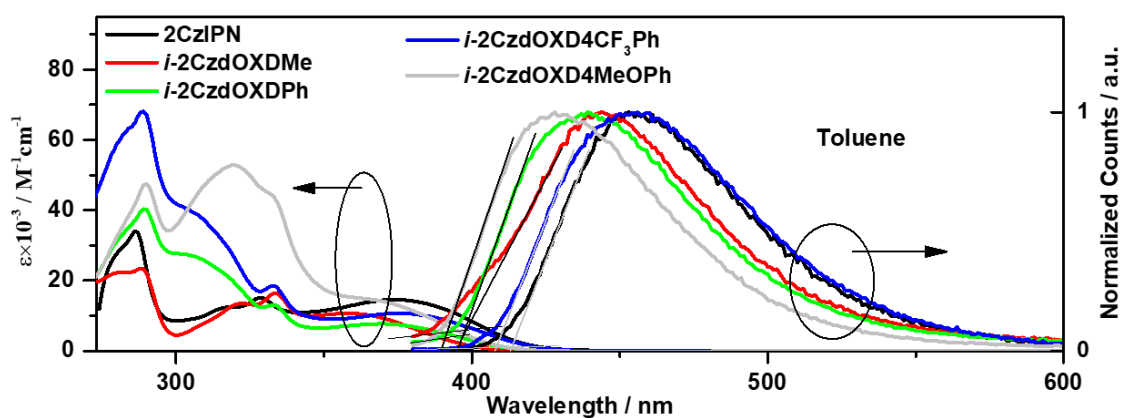
Figure 6.6. Steady-state absorption and PL spectra of **2CzIPN**, *i-2CzOXDMe*, *i-2CzOXDPh*, *i-2CzOXD4CF₃Ph* and *i-2CzdOXD4MeOPh* in toluene.

For further CT character studies, as shown in Figure **6.7**, solvatochromism PL spectra of the new TADF emitters were measured using four solvents with different polarities, namely ethyl acetate, chloroform, dichloromethane and acetonitrile. All the four new emitters show broad, structureless and positive solvatochromism in these solvents (the spectra have more red-shift in the solvents with higher polarity), proving that the CT character is dominant in their emissions.
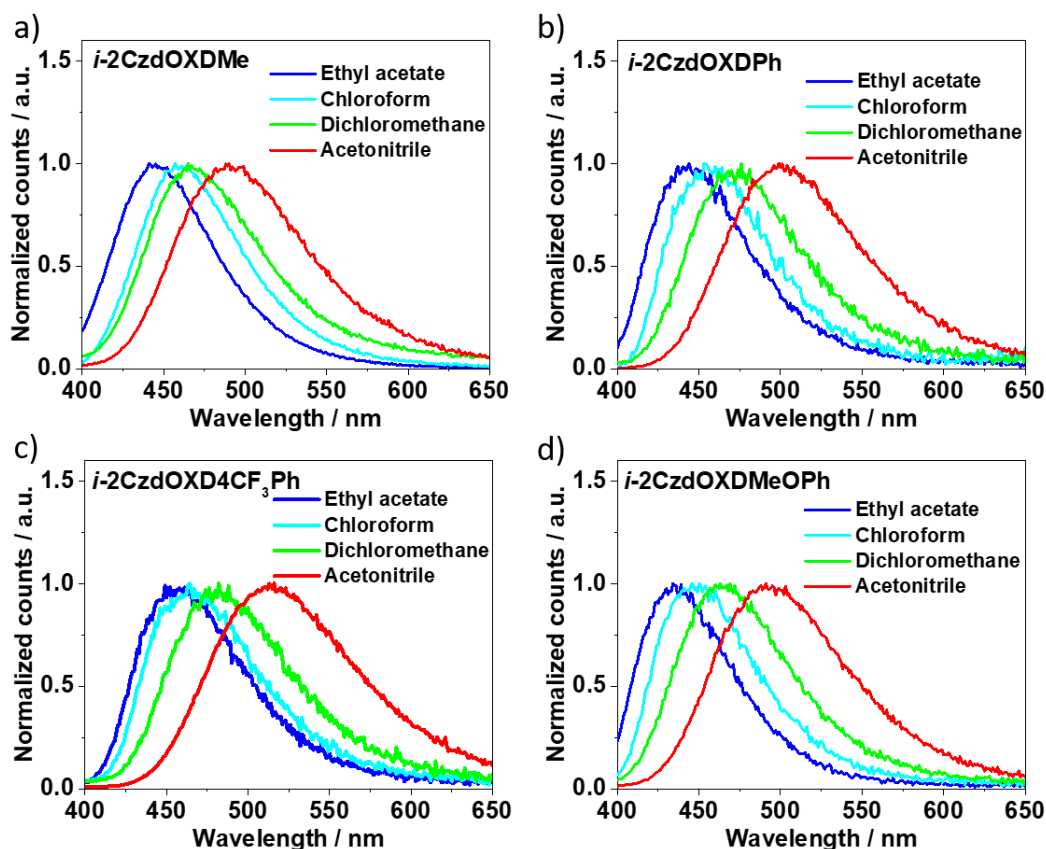
Figure 6.7. Solvatochromism study of *i*-**2CzOXDMe, *i*-2CzOXDPh, *i*-2CzOXD4CF₃Ph** and *i*-**2CzdOXD4MeOPh** in Ethyl acetate, chloroform, dichloromethane and acetonitrile.

The S_1 and T_1 energy levels of these emitters in solution were determined from the onsets of the prompt fluorescence spectra (1-100 ns time window) and phosphorescence spectra (1-10 ms time window) measured at 77 K in flash cooled toluene glass (10^{-5} mol/L) and the results are presented in Figures **6.8a-e** (experimental method: Sections **3.5.5** and **3.5.6**). Apart from *i*-**2CzOXDMe**, the rest emitters show similar S_1 energy levels around 3.15 eV. Although *i*-**2CzOXDMe** has the highest S_1 state energy (3.30 eV), its steady-state PL in toluene is still not as blue as those of *i*-**2CzOXDPh** and *i*-**2CzdOXD4MeOPh** (Figure **6.6**). Also, because of the low T_1 energy levels (around 2.60 eV) of the 1,3,4-oxadiazole based emitters, all the new emitters show much larger ΔE_{ST} values (> 0.50 eV) than that of **2CzIPN** (0.27 eV). The TRPL decays of these emitters measured in degassed toluene is shown in Figure **6.8f**. As the result of the much smaller

ΔE_{ST}, only **2CzIPN** shows TADF. This is in line with the PLQY values measured in toluene that there is almost no difference between the values measured in the degassed and aerated toluene for the new emitters: the PLQYs measured in degassed toluene for ***i*-2CzOXDMe, *i*-2CzOXDPh, *i*-2CzOXD4CF₃Ph** and ***i*-2CzdOXD4MeOPh** are 6.8%, 10.1%, 9.5% and 13.3% respectively, and the PLQYs measured in aerated toluene are 6.9%, 9.9%, 8.8% and 13.1%.

Furthermore, as shown in Figures **6.8a-e**, all the prompt fluorescence spectra are broad and structureless, but the phosphorescence spectra are structured, indicating the S_1 states of these emitters are CT states, while the T_1 states are LE states which are not sensitive to environmental polarities. All the photophysical measurement results are summarized in Table **6.4**.
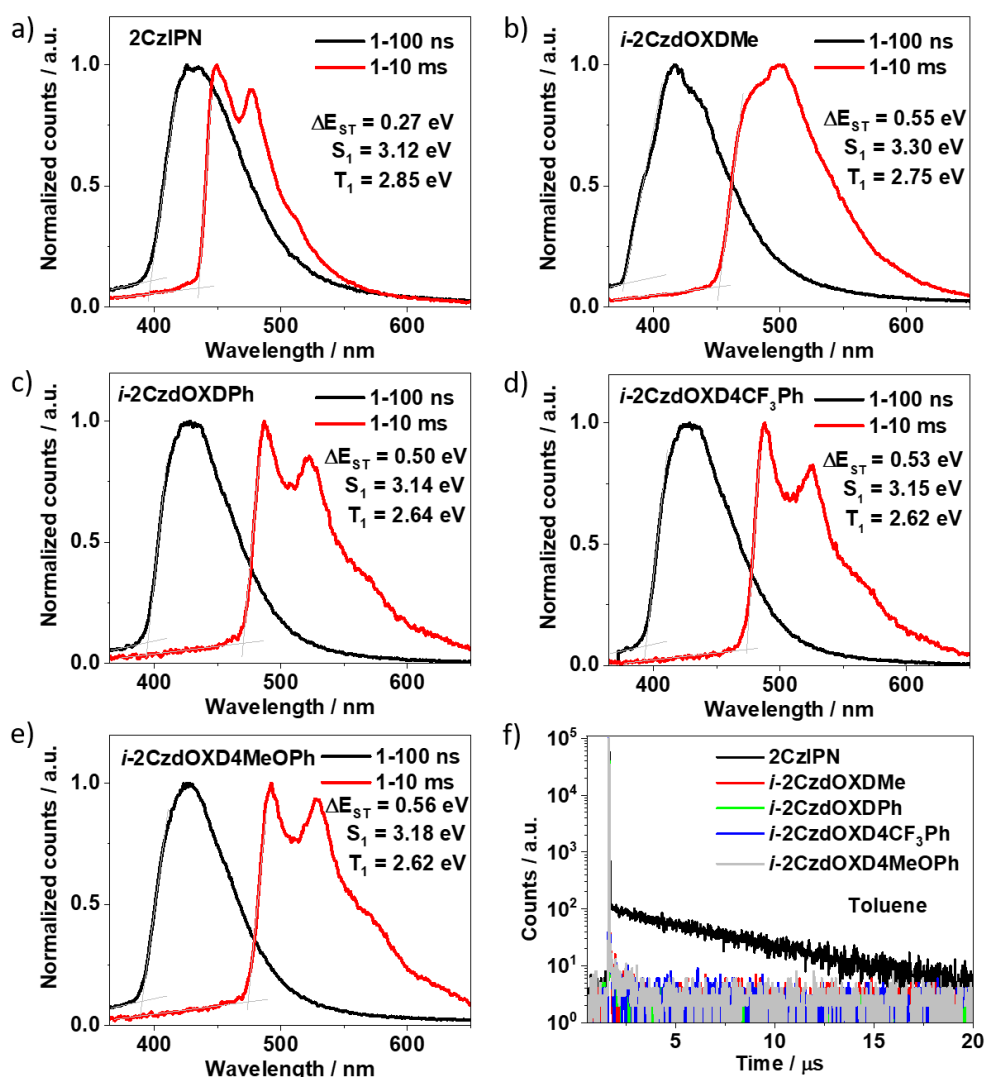
Figure 6.8. a-e) TRPL spectra of **2CzIPN**, ***i*-2CzOXDMe, *i*-2CzOXDPh, *i*-2CzOXD4CF₃Ph** and ***i*-2CzdOXD4MeOPh** measured in 77 K toluene glass. The prompt fluorescence and phosphorescence were taken in the 1-100 ns and 1-10 ms time windows, respective. (λ_{exc} = 343 nm). f) TRPL decay curves of these emitters measured in degassed toluene at room temperature (λ_{exc} = 378 nm).

Table 6.4. Summary of the decomposition temperature of **2CzIPN**, *i*-**2CzOXDMe,** *i*-**2CzOXDPh,** *i*-**2CzOXD4CF₃Ph** and *i*-**2CzdOXD4MeOPh**, and their $S_1/T_1/\Delta E_{ST}$ energy and PLQYs measured in toluene.

| Compound	T_d[a]	λ_{abs}[b]	λ_{PL}[b]	S_1[c]	T_1[c]	ΔE_{ST}	Φ_{PL}[d]	τ_{PF}[e]
	/°C	/nm	/nm	/eV	/eV	/eV	/%	/ns
2CzIPN	-	374	454	3.12	2.85	0.27	-	9.0
i-**2CzdOXDMe**	397	359	444	3.30	2.75	0.55	6.8 (6.9)	6.5
i-**2CzdOXDPh**	400	370	439	3.14	2.64	0.50	10.1 (9.9)	4.9
i-**2CzdOXD4CF₃Ph**	402	376	456	3.15	2.62	0.53	9.5 (8.8)	5.1
i-**2CzdOXD4MeOPh**	402	371	428	3.18	2.62	0.56	13.3 (13.1)	5.1

[a]Decomposition temperatures obtained from TGA. [b]Maximum of the CT steady-state absorption and emission band measured in toluene with the concentration of 10^{-3} mol/L at room temperature. [c]Determined from the onset values of the spectrum measured between 1-100 ns and 1-10 ms after photoexcitation in flash cooled 77 K toluene glass (λ_{ext} = 343 nm). [d]PLQY values were determined by the relative method. The quinine sulfate solution in 0.5M H_2SO_4 (aq) (Φ_{PL}: 54.6%) (10) was used as the reference. [e]Averaged prompt ~~fluorescence~~ lifetimes of these emitters measured in degassed toluene at room temperature. (calculated using the equation $\tau_{avg} = \Sigma A_i \tau_i^2 / A_i \tau_i$, where A_i is the pre-exponential factor for lifetime τ_i).

6.5 Photophysics in the solid state

The photophysical properties of these emitters were next studied in the solid state. A range of host materials was used to explore which would give the highest PLQY. Therefore, 10wt% **2CzIPN**, *i*-**2CzOXDMe,** *i*-**2CzOXDPh,** *i*-**2CzOXD4CF₃Ph** and *i*-**2CzdOXD4MeOPh** doped in Bis[2-(diphenylphosphino)phenyl]ether oxide (DPEPO), 2,8-bis(diphenyl-phosphoryl)dibenzo[b,d]thiophene (PPT), 1,3-Di(9H-carbazol-9-yl)benzene, N,N′-Dicarbazolyl-3,5-benzene (mCP), 9-(4-tert-Butylphenyl)-3,6-bis(triphenylsilyl)-9H-carbazole (CzSi) and poly(methyl methacrylate) (PMMA) films were fabricated though solution processing and their absolute PLQYs were measured using an integrating sphere. The results are summarized in Table **6.5**. It can be seen that, among all the hosts, DPEPO gives the highest PLQYs and the largest Φ_{PL} enhancement in nitrogen atmosphere: the PLQY values of the DPEPO films increased from 68.3%, 19.3%, 19.7%, 24.3% and 18.6% in air to 81.8%, 59.0%, 58.1%, 69.8% and 35.4% in nitrogen. This is probably because all the 1,3,4-oxadiazole-based emitters show large ΔE_{ST} values between their charge transfer singlet states (^{1}CT) and localized excited triplet states (^{3}LE) as shown in Figures

6.8a-e. Therefore, the high polarity of DPEPO can help to lower the ^{1}CT energy levels, and so the ΔE_{ST}s were decreased and the efficiency of TADF was increased (as discussed in Sections **4.2** and **4.3**). Therefore, these DPEPO films were used for further solid state photophysical study and OLED fabrication.
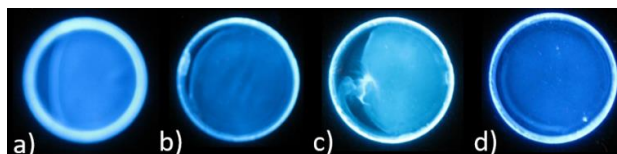
Figure 6.9. a-d) Photographs of 10 wt% *i*-**2CzOXDMe**/*i*-**2CzOXDPh**/*i*-**2CzOXD4CF₃Ph**/*i*-**2CzdOXD4MeOPh**:PPT films under UV excitation. (λ_{ext} = 365 nm).

Table 6.5. PLQYs of the 10 wt% doped films using DPEPO, PPT, mCP, CzSi and PMMA as the hosts.

Compound/Host[a]	DPEPO	PPT	mCP	CzSi	PMMA
2CzIPN	81.8 (68.3)	-	70.7 (57.3)	-	-
i-**2CzdOXDMe**	59.0 (19.3)	36.8 (17.5)	16.3 (14.7)	32.0 (11.0)	37.7 (17.4)
i-**2CzdOXDPh**	58.1 (19.7)	45.7 (18.0)	27.1 (16.0)	38.1 (19.3)	41.3 (19.5)
i-**2CzdOXD4CF₃Ph**	69.8 (24.3)	58.8 (24.4)	43.4 (18.5)	43.6 (13.1)	51.7 (20.2)
i-**2CzdOXD4MeOPh**	35.4 (18.6)	37.3 (20.2)	22.9 (18.5)	20.2 (12.7)	27.6 (17.5)

[a]Absolute PLQY values measured in nitrogen atmosphere (in air) using an integrating sphere. (λ_{ext} = 380 nm)

To analyse the change of ΔE_{ST} in the solid state, the fluorescence and phosphorescence spectra of these DPEPO films were measured at 77 K to compare with those measured in toluene (Figure **6.8a-e**), and the results are presented in Figure **6.10a**. The fluorescence and phosphorescence spectra were taken between 1-100 ns and 0.5-1 ms after photoexcitation, respectively, and the S_1 and T_1 energy levels were determined from the onsets of these spectra. It can be seen that the ΔE_{ST}s are much smaller in DPEPO (0.1 eV, 0.31 eV, 0.31 eV, 0.32 eV and 0.44 eV) compared with in toluene (0.27 eV, 0.55 eV, 0.50 eV, 0.53 eV and 0.56 eV), which explains the operation of TADF in the DPEPO films. In addition, *i*-**2CzOXDMe** and *i*-**2CzdOXD4MeOPh** show the highest S_1 state energy (both are 3.07 eV), indicating the bluest emission from these two emitters. *i*-**2CzdOXD4MeOPh** and *i*-**2CzOXD4CF₃Ph** also show 0.2 eV higher S_1 energy levels than that of **2CzIPN**, and so all the new emitters are bluer than the reference one in the solid state. However, among these emitters, all the 1,3,4-oxadiazole-based emitters show much larger ΔE_{ST} values (>

0.3 eV) than that of **2CzIPN** (0.1 eV), indicating longer T_1 lifetimes and more significant efficiency roll-off in the consequent new emitter-based OLEDs. It is noteworthy that the 0.5-1 ms spectrum of the ***i*-2CzdOXD4MeOPh**:DPEPO film again shows a shoulder that has the same peak position as that of its 1-100 ns spectrum, which is similar to the **CzPhAP** case as shown in Chapter **5** (Figure **5.7b**). This shoulder also comes from the singlet emissions that were generated from photo-induced charges, which is further discussed in Chapter **8**.
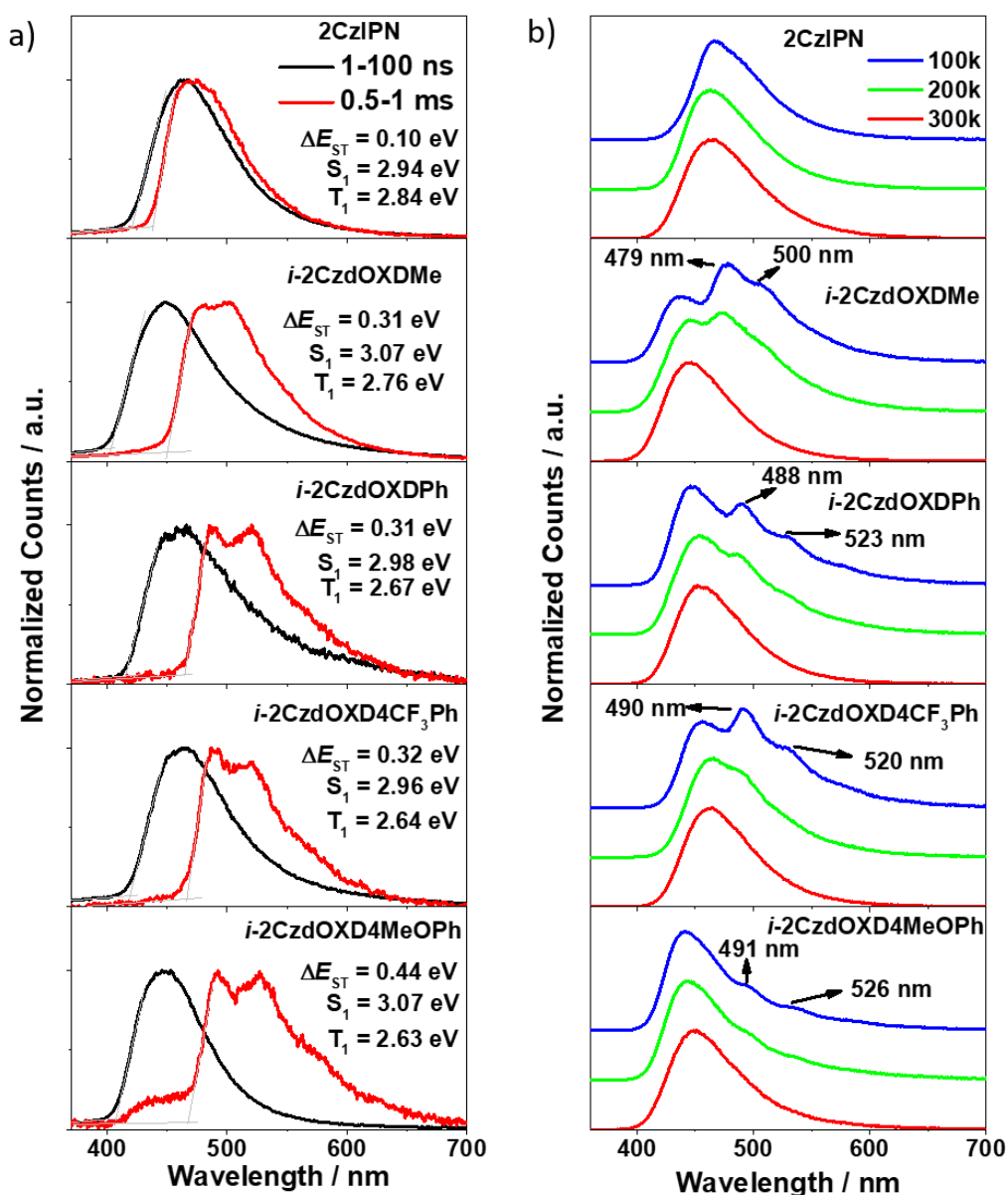
Figure 6.10. a) ΔE_{ST} measurement of the 77 K 10wt% **2CzIPN/*i*-2CzOXDMe/*i*-2CzOXDPh/*i*-2CzOXD4CF₃Ph/*i*-2CzdOXD4MeOPh**:DPEPO films. Prompt fluorescence and phosphorescence spectra were taken 1-100 ns and 0.5-1 ms after photoexcitation, respectively. The onsets of these spectra were used for S_1 and T_1 energy level determinations. (λ_{ext} = 343 nm). b) The steady-state PL spectra of these films measured at 100 K, 200 K and 300 K. (λ_{ext} = 340 nm).

Figure **6.10b** shows the steady-state PL spectra of these films measured at 100 K, 200 K and 300 K using a xenon lamp as the excitation source (λ_{ext} = 340 nm). It can be seen that all the 1,3,4-oxadiazole emitters have multiple peaks/shoulders in their 100 K spectra, and the wavelengths of the low-energy peaks/shoulders are labelled in these graphs. The wavelengths of the labelled peaks/shoulders perfectly match those of the corresponding phosphorescence peaks measured at 77 K in the 0.5-1 s time window as presented in Figure **6.10a**, indicating the labelled peaks/shoulders come from the phosphorescence of these emitters. Furthermore, Figure **6.10b** shows that the intensities of these labelled phosphorescence peaks are at comparable height as those of their fluorescence peaks in *i*-**CzdOXDMe**, *i*-**CzdOXDPh**, *i*-**CzdOXD4F₃Ph**, demonstrating the phosphorescence emissions from these films are strong at 100 K. In comparison, the phosphorescence peak of **2CzIPN** is hard to be distinguished in its 100 K steady-state PL spectrum because its ΔE_{ST} is small. Also, its phosphorescence spectrum is similar to its fluorescence spectrum.

Figure **6.11a** shows the steady-state PL spectra comparison of these films measured at 300 K. These spectra have the emission maximum of 464 nm, 445 nm, 454 nm, 464 nm and 450 nm with FWHM of 74 nm, 68 nm, 68 nm, 70 nm and 71 nm, respectively. The emission from the *i*-**2CzOXDMe**:DPEPO film is the bluest among the rest, which is different from the situation in toluene (Figure **6.6**) where *i*-**2CzdOXD4MeOPh** shows the bluest emission. This may be due to their different ^{1}CT energy shifts in DPEPO.
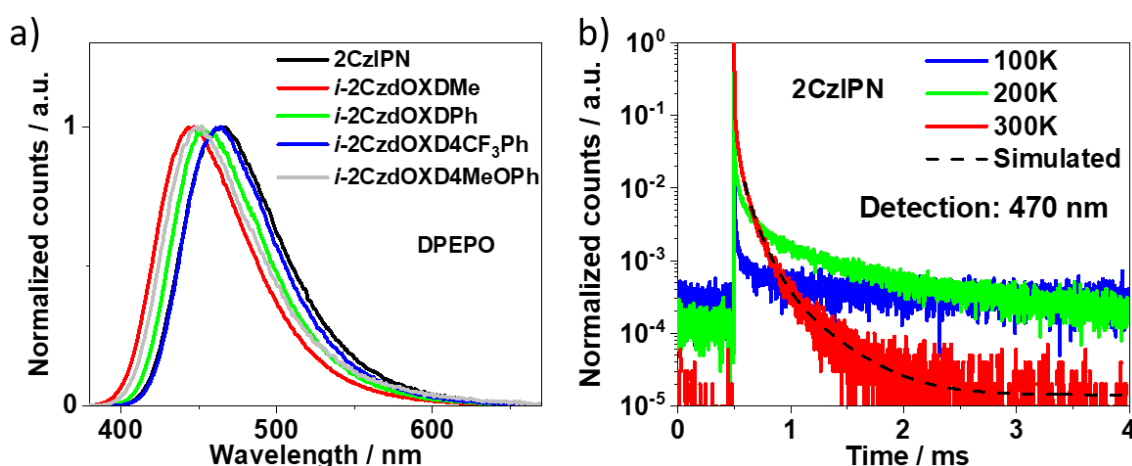

Figure 6.11. a) 300 K steady-state PL spectra of the 10wt% **2CzIPN/*i*-2CzOXDMe/*i*-2CzOXDPh/*i*-2CzOXD4CF₃Ph/*i*-2CzdOXD4MeOPh**:DPEPO films under vacuum. Temperature dependent TRPL decays of the **2CzIPN**:DPEPO film measured at 100 K, 200 K and 300 K with the detection wavelength of 470 nm.

Temperature dependent TRPL decay measurements were carried to further investigate the operation of TADF in these emitters, and the results are presented in Figures **6.11b**, **6.12a** and **6.12b**. Figure **6.11b** shows that the **2CzIPN** film has a relatively short PL decay duration around 1.5 ms at 300 K, which is due to it having the smallest ΔE_{ST}. The delayed emission of **2CzIPN** at 300 K was fitted 100 μs after photoexcitation using a three-exponential-decay model, and the consequent lifetimes of the delayed emission are τ_1 = 40.5 μs (21.16%), τ_2 = 101.9 μs (60.55%), τ_3 = 332.2 μs (18.29%), respectively. The simulated fitted curve is shown as a black dashed line in Figure **6.11b**. The average lifetime of the delayed emission measured at 300 K is 131 μs (calculated using the equation $\tau_{avg} = \Sigma A_i \tau_i^2 / A_i \tau_i$).

The temperature dependent TRPL decay measurements of the new emitters are more complicated because of their large ΔE_{ST}s. It can be seen in Figure **6.12a** that when the detection wavelength was set to 460 nm which is close to the 300 K steady-state PL maximum of these emitters (Figure **6.11a**), almost no long-lived emission could be observed at 100 K. It is because 460 nm is at the edge of their phosphorescence spectra (Figure **6.10a**), and so the phosphorescence emission cannot be detected in this measurement condition even at low temperature. Instead, as shown in Figure **6.12b**, when the detection wavelength was set to 495 nm which is around the emission maximum of their phosphorescence spectra, the TRPL decay of the phosphorescence was detected. Therefore, care needs to be taken when selecting the detection wavelength for temperature dependent TRPL decay measurements for the emitters with large ΔE_{ST} because some detection wavelengths will miss the phosphorescence. It can be seen in Figures **6.12a** and **6.12b** that, when the temperature was decreased, the TADF contributions in these films decreased but the phosphorescence contributions increased. Therefore, it can be concluded that TADF is operating in all these films.

It can be seen in Figure **6.12b** that all the 1,3,4-oxadiazole-based emitters have much longer delayed emission durations, compared with that of **2CzIPN** (Figure **6.11b**), which last for more than 400 ms at 300 K. However, these delayed emissions cannot be meaningfully fitted to a sum of exponentials because the TADF and organic long-persistent luminescence (OLPL) overlap. OLPL decay follows a power law, which originates from charge recombination. The OLPL process is also happening in these 1,3,4-oxadiazole-emitters doped films, and is discussed further in Chapters **7** and **8**. Therefore, the delayed emission lifetimes of the 1,3,4-oxadiazole-based emitters were not calculated.
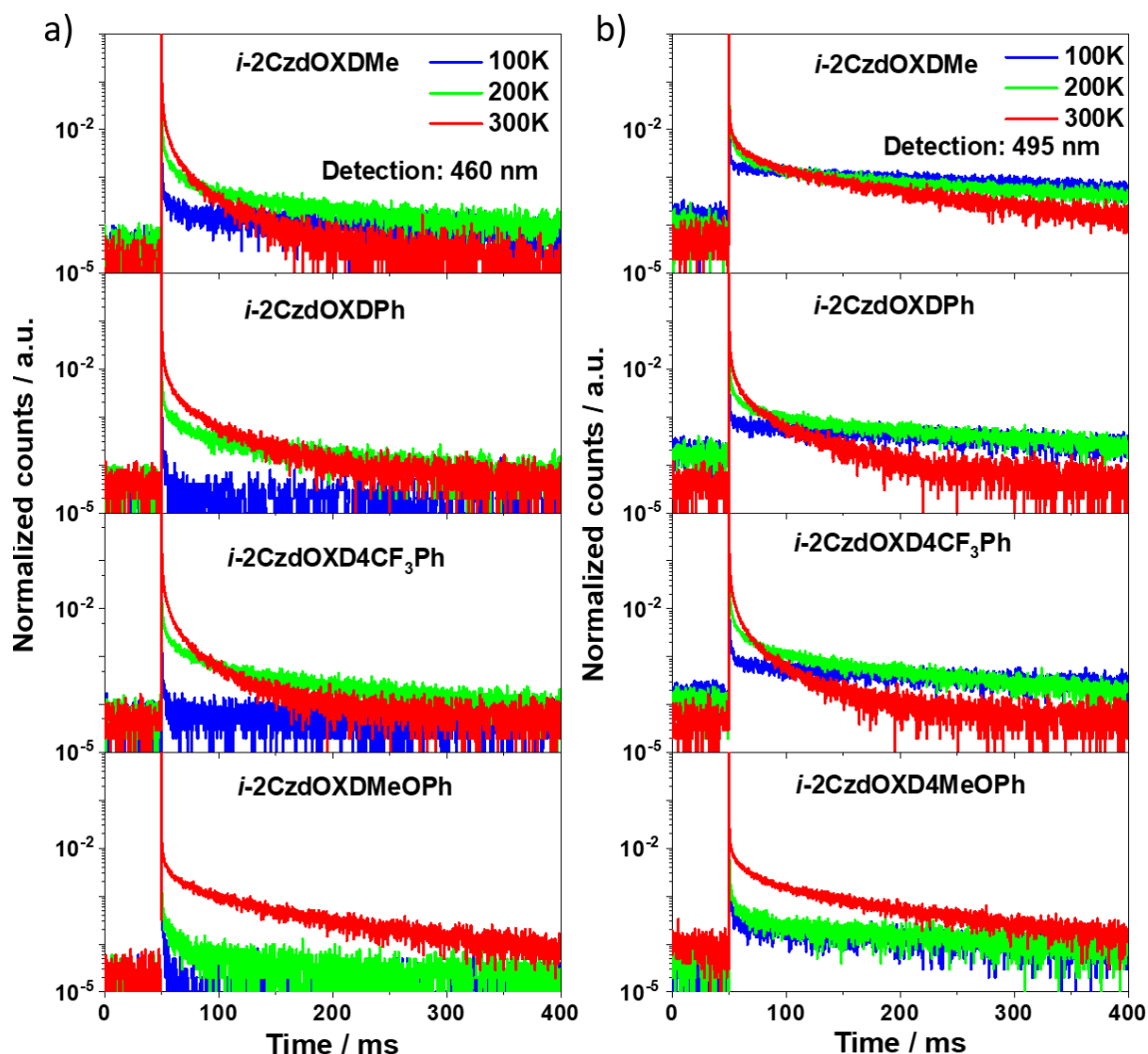
Figure 6.12. a, b) Temperature dependent TRPL decays of the 1,3,4-oxadiazole-based emitters doped in DPEPO measured at 100 K, 200 K and 300 K with the detection wavelengths of 460 nm and 495 nm.

Although a quantitative analysis of delayed emission was not performed, a qualitative comparison of delayed emission comparison of these new emitters is shown in Figure **6.13a**. The **i-2CzdOXD4MeOPh**:DPEPO film shows the longest PL decay duration at 300 K, which is probably due to its largest ΔE_{ST} (0.47 eV) among these emitters. Figure **6.13b** shows the decay curves of their prompt fluorescence measured in the 200 ns time window. All the prompt components show double exponential decays with average lifetimes of 13.6 ns, 8.2 ns, 8.4 ns, 9.1 ns and 7.3 ns, respectively (calculated using the equation $\tau_{avg} = \Sigma A_i \tau_i^2 / A_i \tau_i$). All the solid state photophysics data are summarized in Table **6.6**.
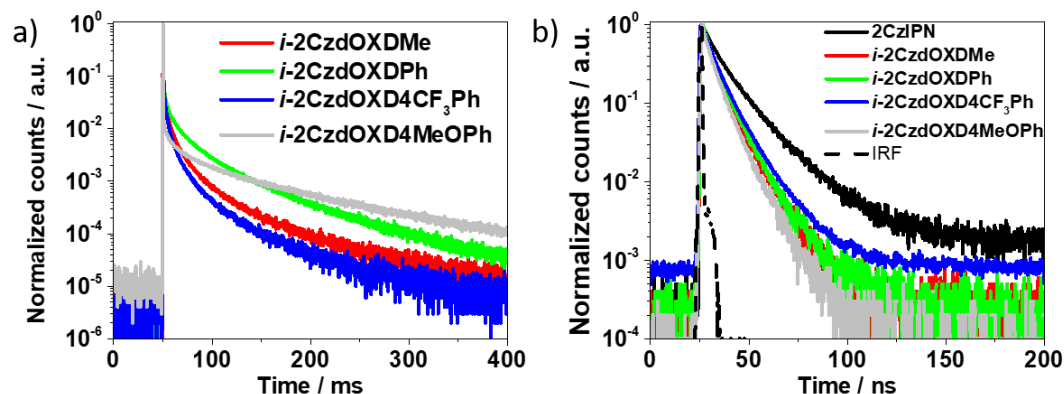
Figure 6.13. a, b) TRPL decay comparison of the 300 K 10wt% **2CzIPN/*i*-2CzOXDMe/*i*-2CzOXDPh/*i*-2CzOXD4CF₃Ph/*i*-2CzdOXD4MeOPh**:DPEPO films measured under vacuum in the 400 ms and 200 ns time windows.

Table 6.6. Summary of the photophysical properties of the 10wt% **2CzIPN/*i*-2CzOXDMe/*i*-2CzOXDPh/*i*-2CzOXD4CF₃Ph/*i*-2CzdOXD4MeOPh**:DPEPO films.

Compound	λ_{PL}[a] /nm	FWHM /nm	S_1[b] /eV	T_1[b] /eV	ΔE_{ST} /eV	τ_{PF}[c] /ns
2CzIPN	464	74	2.94	2.84	0.10	13.60
***i*-2CzdOXDMe**	445	68	3.07	2.76	0.31	8.17
***i*-2CzdOXDPh**	454	68	2.98	2.67	0.37	8.38
***i*-2CzdOXD4CF₃Ph**	464	70	2.96	2.64	0.32	9.07
***i*-2CzdOXD4MeOPh**	450	71	3.07	2.63	0.44	7.25

[a]Emission maximum are taken from the steady-state PL spectra measured under vacuum at room temperature (λ_{ext} = 340 nm). [b]Determined from the onset values of the spectra measured between 1-100 ns and 0.5-1 ms after photoexcitation at 77 K (λ_{ext} = 343 nm). [c]Calculated using the equation $\tau_{avg} = \Sigma A_i \tau_i^2 / A_i \tau_i$, where A_i is the pre-exponential factor for lifetime τ_i.

6.6 Device fabrication

OLED devices were fabricated by thermal evaporation to study the EL properties of these emitters. The device architectures with the energy level and thickness of each layer are shown in Figure **6.14**. NPB and TCTA were used as the HTL, and TPBi was used as the ETL. mCP and DPEPO played the role of EBL and HBL, respectively, because of their shallow LUMO and deep HOMO with high T₁ energies. The EMLs were 20 nm thick 10wt% **2CzIPN/*i*-2CzOXDMe/*i*-

2CzOXDPh/*i*-2CzOXD4CF₃Ph/*i*-2CzdOXD4MeOPh:DPEPO films. The photos of these devices in operation are shown in Figure **6.14b** with their CIE coordinates of (0.18, 0.30), (0.17, 0.17), (0.15, 0.16), (0.18, 0.28) and (0.17, 0.17) as presented in Figure **6.14c**. It can be seen in the CIE coordinate (Figure **6.14c**) that all the 1,3,4-oxadiazole-based emitters show bluer emissions than the reference emitter **2CzIPN**, suggesting the success of replacing the cyano groups with the 1,3,4-oxadiazole groups to blueshift the emissions. Although their CIE coordinates values are still far from the 'standard blue' proposed by National Television System Committee (NTSC) with CIE coordinates of (0.16, 0.07), the *i*-2CzOXDMe and *i*-2CzdOXD4MeOPh devices are already among the bluest TADF OLEDs that have been reported.
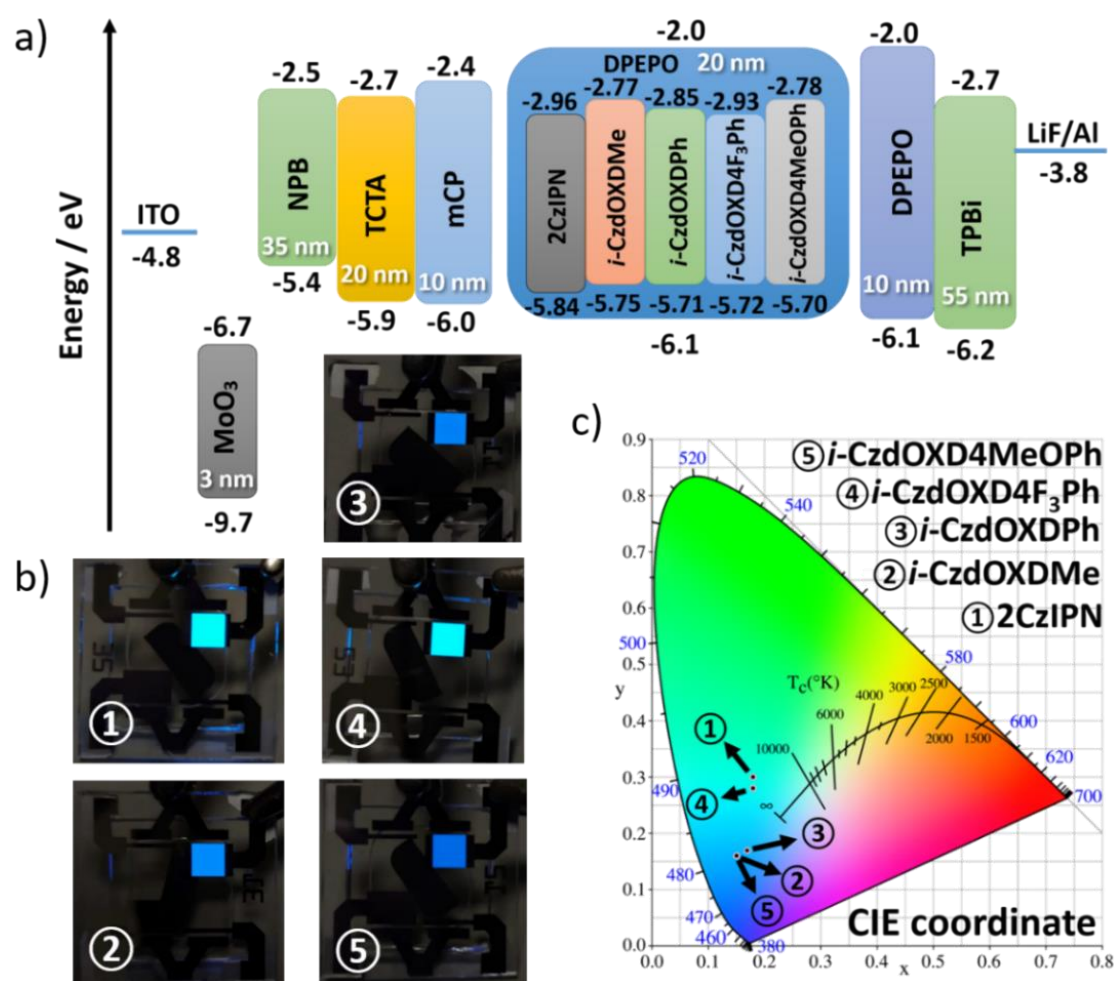
Figure 6.14. a) Schematic diagram of the OLED device architectures with the energy level and thickness of each layer. b) OLED devices in operation. c) CIE coordinate of the emissions of these OLEDs.

The device performance is shown in Figure **6.15**. Figure **6.15a** presents the EL spectra of all these devices. These spectra have emission maximum of 477 nm, 452 nm, 460 nm, 472 nm and 452 nm with FWHMs of 89 nm, 85 nm, 84 nm, 88 nm and 78 nm, respectively. All the 1,3,4-

oxadiazole-based emitters show shorter peak wavelengths and narrower FWHMs than those of the reference emitter, which contribute to bluer colours. As shown in Figure **6.15b**, the turn-on voltages of all these devices are similar (around 4.4 V), which may be due to their similar S_1 energy levels and identical device architectures. However, because the 1,3,4-oxadiazole-based emitters have much larger ΔE_{ST}, they show more significant efficiency roll-off at high brightness. As shown in Figure **6.15c**, these devices have EQE_{max} of 15.0%, 11.8%, 7.0%, 12.3% and 4.8% at around 1 cd/m^2, while the EQE values drop to 7.0%, 1.3%, 1.3%, 2.6% and 1.3% at around 100 cd/m^2. It is noteworthy that the EQE_{max} of **i-2CzdOXD4MeOPh** is only 4.8% which is similar to the theoretical limit of the EQE_{max} of fluorescent emitters. This suggests TADF is not making much contribution to the emission, which is in line with it having the largest ΔE_{ST} among these emitters. All the device performance data are summarized in Table **6.7**.
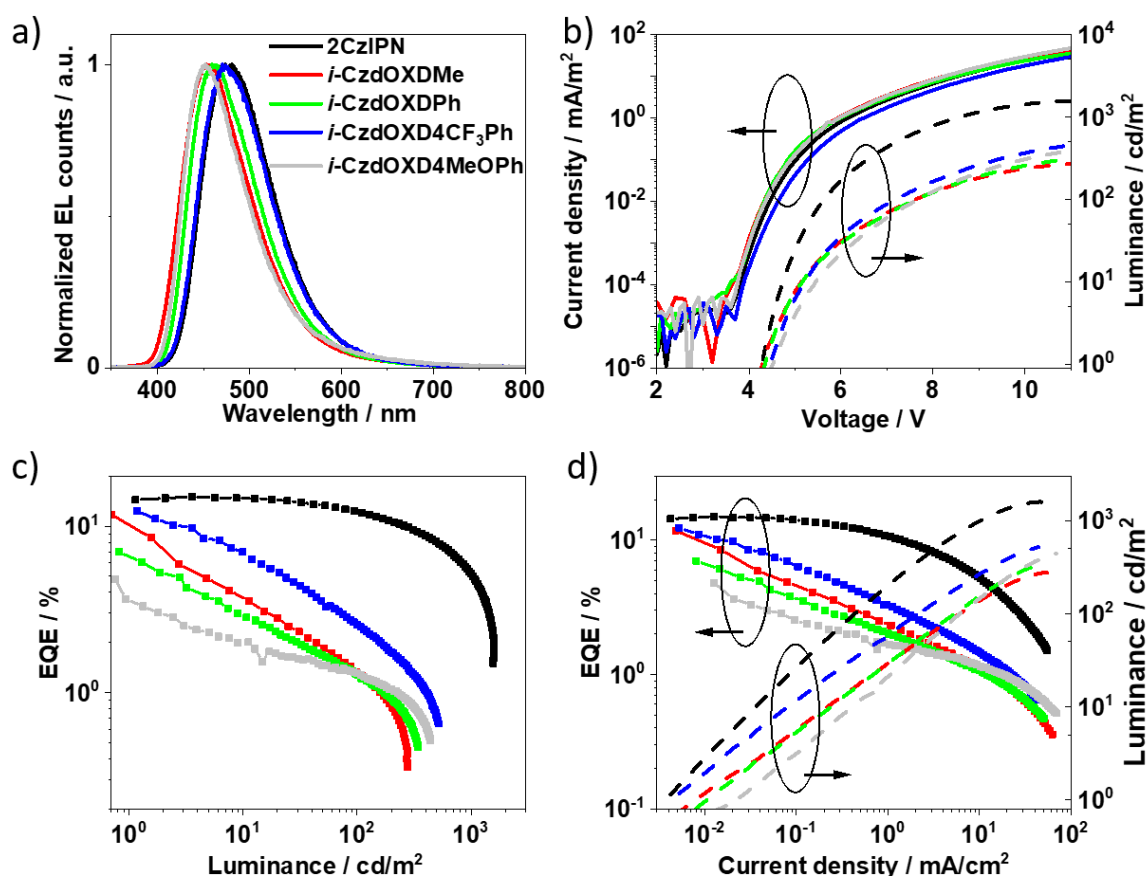
Figure 6.15. a) Electroluminescence spectra of oxadiazole based OLEDs. b) Current density-voltage curves and luminance-voltage curves of these OLEDs. c) EQE-luminance curves of the OLEDs. d) EQE-current density curves and luminance-current density curves of the OLEDs.

Emitter	λ_{EL} /nm	FWHM /nm	V_{on}[a] /V	EQE_{max}; EQE_{100}[b] /%	PE_{max}; PE_{100}[c] /lm/W	CIE / (x, y)
2CzIPN	477	89	4.3	15.0; 7.0	19.76; 12.49	(0.18, 0.30)
***i*-2CzdOXDMe**	452	85	4.3	11.8; 1.3	10.88; 0.68	(0.17, 0.17)
***i*-2CzdOXDPh**	460	84	4.3	7.0; 1.3	7.39; 0.77	(0.15, 0.16)
***i*-2CzdOXD4CF₃Ph**	472	88	4.5	12.3; 2.6	15.57; 2.02	(0.18, 0.28)
***i*-2CzdOXD4MeOPh**	452	78	4.5	4.8; 1.3	3.18; 0.67	(0.17, 0.17)

Table 6.7. Summary of the OLED device performance

[a]Defined as the lowest operating voltage at a luminance of >1 cd/m^2. [b]Maximum EQE above 1 cd/m^2; EQE at 100 cd/m^2; and at 1000 cd/m^2. [c]Maximum power efficiency above 1 cd/m^2; power efficiency at 100 cd/m^2.

6.7 Conclusion

This chapter presents the study of four new blue TADF emitters whose designs are based on the strategy of replacing the cyano group in the sky-blue TADF emitter, **2CzIPN**, by 1,3,4-oxadiazole derivatives, and so to reduce the electron-accepting strength of the acceptors and increase the HOMO-LUMO band gaps. The consequent 1,3,4-oxadiazole-emitter-based OLEDs show shorter EL emission maximum wavelengths and narrower FWHMs compared with the **2CzIPN** device, demonstrating this design strategy is an effective way to blue-shift the emission of TADF emitters. Especially, compared with **2CzIPN** which has EQE_{max} of 15.0% with CIE coordinates of (0.18, 0.30), the emitter ***i*-2CzdOXDMe** has EQE_{max} of 11.8% and CIE coordinates of (0.17, 0.17), which is significantly bluer than **2CzIPN** without much loss of the maximum EQE.

However, the employment of 1,3,4-oxadiazole derivatives misaligned the T_1 energy and dramatically increased the ΔE_{ST} (from 0.10 eV to above 0.30 eV), and so the efficiency roll-off is severe in the new-emitter-based OLEDs. The EQE values of ***i*-2CzOXDMe/*i*-2CzOXDPh/*i*-2CzOXD4CF₃Ph/*i*-2CzdOXD4MeOPh** drop to 1.3%, 1.3%, 2.6% and 1.3% at 100 cd/m^2, which is not useful for practical applications. Therefore, for further improvement of this design strategy, care needs to be taken to keep ΔE_{ST} small when tuning emission.

Although the 1,3,4-oxadiazole based emitter have large ΔE_{ST}s, there are several experimental proofs of the operation of TADF in these emitters, such as the existence of the delayed emissions

lasting for hundreds of milliseconds in the ***i*-2CzOXDMe/*i*-2CzOXDPh/*i*-2CzOXD4CF₃Ph/*i*-2CzdOXD4MeOPh**:DPEPO films at 300 K, and these delayed emissions can be quenched at 100 K. Furthermore, the EQE_{max} of these devices are 11.8%, 7.0% and 12.3%, respectively, demonstrating TADF is contributing to the light emission. The EQE_{max} of ***i*-2CzdOXD4MeOPh** is only 4.8% which is close to the theoretical EQE_{max} of fluorescent emitters. This may be due to its largest ΔE_{ST} (0.44 eV) which decreases the contribution of TADF in it.

Finally, there is evidence of the existence of photo-induced charges in the ***i*-2CzdOXD4MeOPh**:DPEPO film as singlet emission was observed in the 0.5-1 ms time window at 77 K (Figure **6.10a**). More relevant details are discussed in Chapter **8** to show the important role that photo-induced charges are playing in TADF emitter doped films.

6.8 References

1. Uoyama H, Goushi K, Shizu K, Nomura H, Adachi C. Highly efficient organic light-emitting diodes from delayed fluorescence. Nature. 2012;492(7428):234–8. Available from: http://www.ncbi.nlm.nih.gov/pubmed/23235877

2. Cho YJ, Yook KS, Lee JY. Cool and warm hybrid white organic light-emitting diode with blue delayed fluorescent emitter both as blue emitter and triplet host. Sci Rep. 2015;5(1):7859. Available from: http://www.nature.com/articles/srep07859

3. Lee J, Shizu K, Tanaka H, Nomura H, Yasuda T, Adachi C. Oxadiazole- and triazole-based highly-efficient thermally activated delayed fluorescence emitters for organic light-emitting diodes. J Mater Chem C. 2013;1(30):4599. Available from: http://xlink.rsc.org/?DOI=c3tc30699b

4. Tan Y, Rui B, Li J, Zhao Z, Liu Z, Bian Z, Huang C. Blue thermally activated delayed fluorescence emitters based on a constructing strategy with diversed donors and oxadiazole acceptor and their efficient electroluminescent devices. Opt Mater (Amst). 2019;94(May):103–12. Available from: https://doi.org/10.1016/j.optmat.2019.05.040

5. Cooper MW, Zhang X, Zhang Y, Jeon SO, Lee H, Kim S, Fuentes-Hernandez C, Barlow S, Kippelen B, Marder SR. Effect of the Number and Substitution Pattern of Carbazole Donors on the Singlet and Triplet State Energies in a Series of Carbazole-Oxadiazole Derivatives Exhibiting Thermally Activated Delayed Fluorescence. Chem Mater.

2018;30(18):6389–99. Available from:
https://pubs.acs.org/doi/10.1021/acs.chemmater.8b02632

6.   Zhang X, Cooper MW, Zhang Y, Fuentes-Hernandez C, Barlow S, Marder SR, Kippelen B.
        Host-Free Yellow-Green Organic Light-Emitting Diodes with External Quantum
        Efficiency over 20% Based on a Compound Exhibiting Thermally Activated Delayed
        Fluorescence. ACS Appl Mater Interfaces. 2019;11(13):12693–8. Available from:
        https://pubs.acs.org/doi/10.1021/acsami.8b18798

7.   Li Z, Li W, Keum C, Archer E, Zhao B, Slawin AMZ, Huang W, Gather MC, Samuel IDW,
        Zysman-Colman E. 1,3,4-Oxadiazole-based Deep Blue Thermally Activated Delayed
        Fluorescence Emitters for Organic Light Emitting Diodes. J Phys Chem C.
        2019;123(40):24772–85. Available from:
        https://pubs.acs.org/doi/10.1021/acs.jpcc.9b08479

8.   Tomkeviciene A, Grazulevicius J V., Volyniuk D, Jankauskas V, Sini G. Structure–
        properties relationship of carbazole and fluorene hybrid trimers: experimental and
        theoretical approaches. Phys Chem Chem Phys. 2014;16(27):13932. Available from:
        http://xlink.rsc.org/?DOI=c4cp00302k

9.   Fukushima T, Yamamoto J, Fukuchi M, Hirata S, Jung HH, Hirata O, Shibano Y, Adachi C,
        Kaji H. Material degradation of liquid organic semiconductors analyzed by nuclear
        magnetic resonance spectroscopy. AIP Adv. 2015;5(8):087124. Available from:
        http://dx.doi.org/10.1063/1.4928515

10.   Melhuish WH. QUANTUM EFFICIENCIES OF FLUORESCENCE OF ORGANIC SUBSTANCES:
        EFFECT OF SOLVENT AND CONCENTRATION OF THE FLUORESCENT SOLUTE 1. J Phys
        Chem. 1961;65(2):229–35. Available from:
        https://pubs.acs.org/doi/abs/10.1021/j100820a009

Chapter 7 Organic Room-Temperature Afterglow Material Overview

Ultra-long afterglow materials have a wide range of applications. Currently, they are mainly used for glow-in-dark toys, safety signs and indoor decorations. People are still developing cheaper but more efficient ultra-long afterglow materials for illumination. In this chapter, an overview was done on the popular methods people are using to make room-temperature ultra-long afterglow materials, especially the technique called organic long-persistent luminescence (OLPL) which recently again started to attract people's attention. Furthermore, the theory of OLPL is introduced, especially focusing on the studies of its photo-induced charge separation and recombination processes.

7.1 Room-temperature afterglow material overview

7.1.1 Inorganic long-persistent luminescence materials

Room-temperature ultra-long afterglow materials are those which show long-lived emission lasting for seconds to even hours after the excitation source is removed. Current commercial high performance long-live afterglow emitters are mainly inorganic long-persistent luminescent (LPL) materials, which are based on $CaAl_2O_4$ or $SrAl_2O_4$ using Eu, Nd and Dy as dopants (1,2). These kinds of materials have afterglow duration lasting for more than 10 hours, and only require weak indoor lights as the excitation source. Figures **7.1a** and **b** show examples of these kinds of emitters for applications as glow-in-dark safety signs and toys.
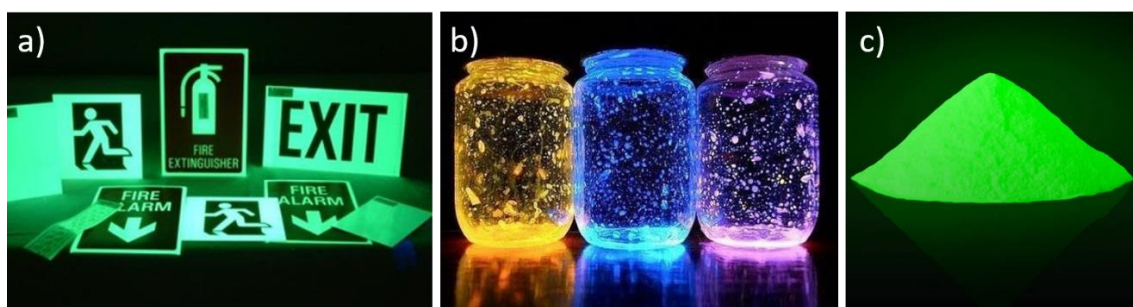
Figure 7.1. a, b) Examples of applying inorganic LPL materials to glow-in-dark safety signs and toys. (Pictures adapted from (3) and (4)) c) An example of an inorganic LPL material powder (Picture adapted from (5))

Although the detailed mechanism of LPL is not fully understood, people generally agree that this ultra-long afterglow comes from the recombination of photo-induced charges (6). Figure **7.2** shows a simplified schematic diagrams of one of the proposed mechanisms (7). In a $SrAl_2O_4$ crystal (Figure **7.2a**), the oxygen vacancies in the lattice play the role of electron traps. The processes of photo-induced charge generation and recombination are shown in the energy diagram presented in Figure **7.2b**: during the photoexcitation process, electrons from the 4f orbitals of the dopants, Eu^{2+} ions, are firstly promoted to their 5d orbitals, which creates Eu^{3+} ions. As the 5d orbital of Eu^{3+} ions have similar energy level to that of the conduction band (CB) of $SrAl_2O_4$, the electrons in this 5d orbital can hop into the CB of $SrAl_2O_4$ and diffuse into the electron traps which have the energy level of V_O. After the excitation source is turned off, the electrons can be released from the traps through thermal energy and go back the CB of $SrAl_2O_4$. They finally return to the 5d orbitals of the Eu^{3+} ions and emit light through recombining with these ions.
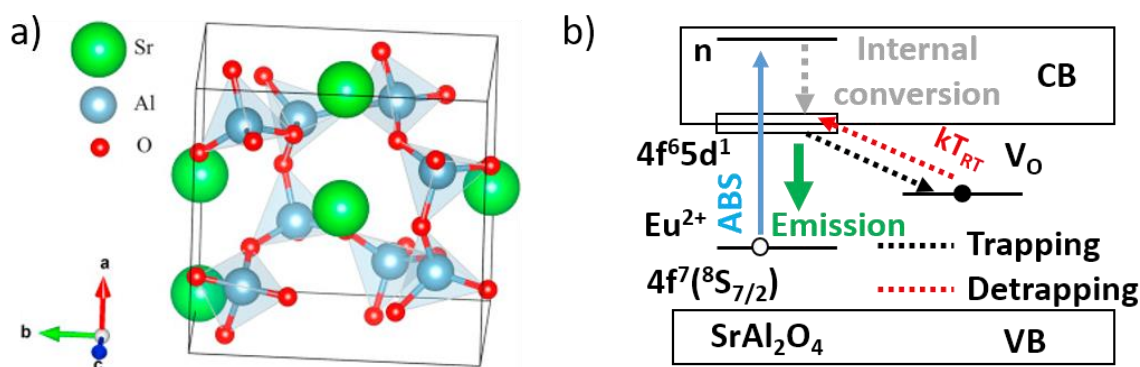
Figure 7.2. a) Schematic diagram of a $SrAl_2O_4$ crystal. Picture adapted from (8). b) Schematic diagram of the mechanism of LPL. Picture adapted from (7).

7.1.2 Room-temperature phosphorescence materials

Although the afterglow duration of inorganic LPL emitters is long, the fabrication of them requires high temperatures (> 1000 °C) and rare metals (1). Besides, the applications of it require mixing of ground powders with organic solvents, and the final product cannot be clear and transparent, which can be seen in Figure **7.1**. In comparison, purely organic long afterglow materials have many advantages, including much lower fabrication temperatures (at room temperature for solution process or crystallisation, and < 300 °C (9) for melt-casting. etc.) and only require sustainable elements such as carbon, hydrogen and nitrogen. So far, there are two main branches of organic room-temperature long-lived afterglow materials, namely room-temperature phosphorescence (RTP) and OLPL materials.

RTP emitters are recently heavily studied (10–14) and their long emission lifetimes come from the slow emissive transition from T_1 to S_0 because of the weak spin-orbit coupling between these two states. The key technique to make a good RTP emitter is suppressing molecular vibrations so as to minimize non-radiative losses. So far, many methods have been proposed for this purpose, and the easiest one among these methods is using rigid and planar molecules without connections to vibrating side-chains. Figure **7.3a** shows the structure of coronene, as an example, which is composed of 6 benzene rings and forms a rigid planar structure. This simple structure enables coronene to have a phosphorescence lifetime, τ_{PH}, around 6 s when doped at 0.02 wt% into poly(methyl methacrylate) (PMMA) (15). A further step for vibrational loss suppression is replacing hydrogen by deuterium because heavier atoms can reduce the molecular vibrations. Therefore, a deuterated coronene doped in PMMA film can reach a τ_{PH} around 23 s (15) which is the longest-lived RTP so far. Crystallization is another effective way of suppressing molecular

vibrations. In 2010, Yuan *et al.* found that some molecules start to show RTP with τ_{PH} around 4.8 ms when they are crystalized (11). Similar to crystallization, molecular packing such as π-π stacking and H-aggregation can also supress non-radiative decay. In 2018, Yang *et al.* reported π-π stacked emitters, CS-F, can reach a τ_{PH} around 410 ms (Figure **7.3b**) (13). In 2014, An *et al.* found the H-aggregated molecules, DECzT, realized a τ_{PH} around 1.35 s (Figure **7.3c**) (16).
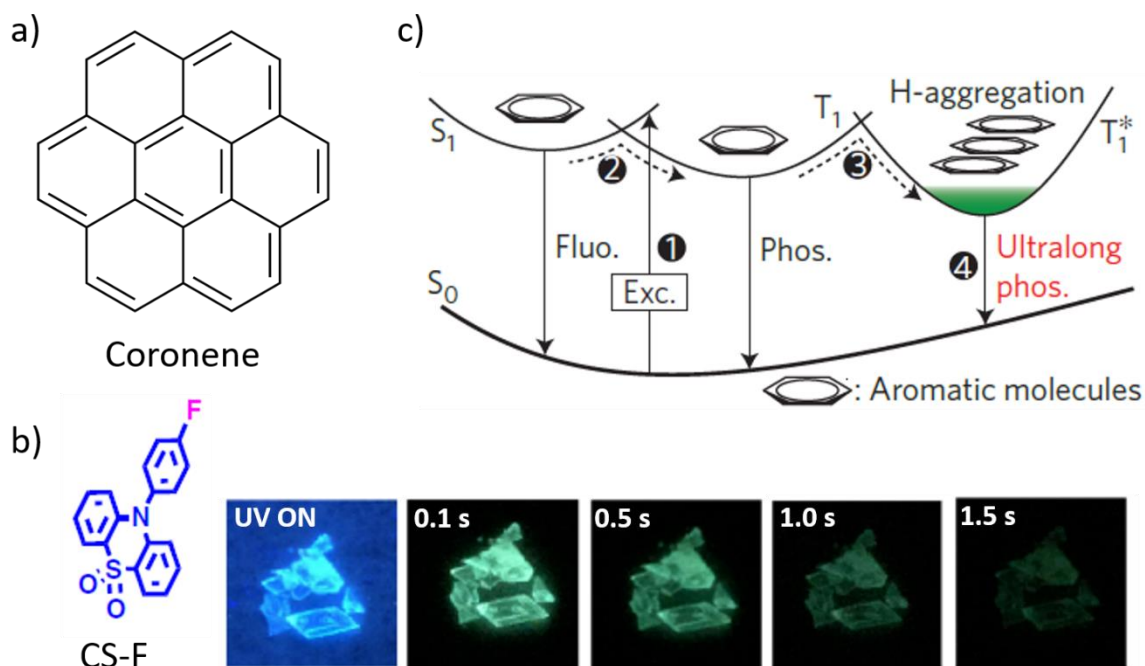
Figure 7.3. a) Molecular structure of Coronene. b) Schematic diagram of H-aggregation. Picture adapted from (13). c) Photos of CS-F's afterglow. Picture adapted from (16).

7.1.3 Organic long-persistent luminescence materials

Although RTP emitters do not require high fabrication temperature and are mostly metal free, they usually need to be crystallised, which is still difficult for large scale sample fabrication, and the morphology requirement limits its application. Most importantly, the longest phosphorescence lifetime is only around 23 s, which is far from satisfactory for illumination applications. OLPL emitters have the advantage of longer afterglow duration, whilst retaining the simplicity of all organic composition.

Many details about the mechanism of OLPL remains unknown, however, the core of OLPL is similar to that of LPL, which is photo-induced charges and electron traps. A schematic diagram of the mechanism of OLPL is shown in Figure **7.4**. Compared with the inorganic $SrAl_2O_4$ lattice which have a continuous CB that is electronically conductive, electrons need to hop from one

molecule to another in OLPL systems. In the photo-induced charge generation process, an OLPL system is exposed to an excitation source so that electrons are ionized from the emitters. These ionized electrons are ejected into the solid surrounding media. As the positively charged radicals are much larger and heavier than the electrons, they are assumed to be unmoved. This process leads to a charge separated state and the electrons are trapped in the electron traps in the OLPL system, even though the nature of the electron traps is still not clearly understood. After the excitation source is switched off, the ejected electrons in the solid media slowly recombine with the emitter radicals and form excitons which decay and emit photons. As this recombination process can take a long time, the afterglow from OLPL systems can last for hours. However, Figure **7.4** only describes an over simplified OLPL mechanism. There were many studies focused on the detailed mechanisms of the charge separation and recombination process. However, a satisfying conclusion still yet to be made, as is discussed in the next section.
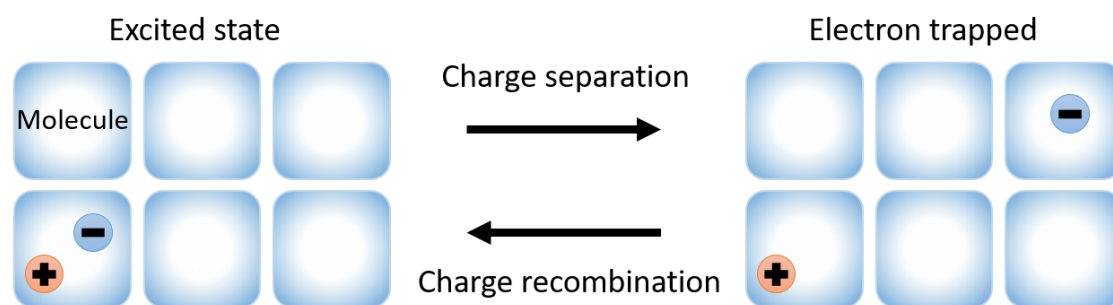
Figure 7.4. Schematic diagram of the OLPL mechanism. Picture adapted from (9).

People started to notice the importance of the photo-induced charges in organic materials around 1940s (17–19). They also found extraordinarily long afterglow duration can be obtained from organic materials when they take the advantage of photo-induced charges. Earlier studies of OLPL usually required liquid helium temperature (20 K) or liquid nitrogen/air temperature (77/88 K). For example, in 1952, Debye and Edwards (20) found many organic solutions can have afterglow duration longer than 1000 s at liquid nitrogen temperature, as shown in Figure **7.5a**. These solutions include phenol in aqueous alkali, *p*-toluidine in methanol and tyrosine in aqueous alkali. At that time, OLPL was called long-lifetime phosphorescence so as to distinguish from normal (or true) phosphorescence. Later, OLPL was also called isothermal luminescence (ITL) because these ultra-long PL decay curves were measured at a fixed temperature (21). ITL was used to distinguish from another photo-induced charge related phenomenon called thermoluminescence (TL) (22). In a TL measurement, samples are excited at low temperature (e.g. 20 K), and the emission from the sample is measured during the sample warming up process

with the excitation source off. During the warming up process, the trapped electrons will be released and recombine with the positively charged radicals and form excitons.

For solid-state OLPL system investigations, in 1980, Hama *et al.* (21) reported a frozen poly(ethylene terephthalate) (PET) film (Figure **7.5b**) which has afterglow duration lasting for thousands of minutes at 77 K. They also studied how the different excitation conditions are changing the OLPL decay rates. For further OLPL materials exploration, in 1997, Ohkita *et al.* observed 10,000 s afterglow duration from a N,N,N′,N′-tetramethylbenzidine (TMB) doped in poly(n-butyl methacrylate) PnBMA film at 20 K (23). In the same work, they also reported that a perylene (Pe) doped in PnBMA film can have afterglow duration longer than 1000 s below 200 K (Figure **7.5c**). However, the decay duration dropped to around 200 s when the temperature was increased to 300 K. Nevertheless, this was the first reported OLPL system that operated at 300 K. In these reports, although the afterglow durations of these OLPL systems are in the order of thousands of seconds, the low-temperature requirement significantly limits their applications. Therefore, it was not as popular as its counterpart—RTP emitters between 2000 and 2017.
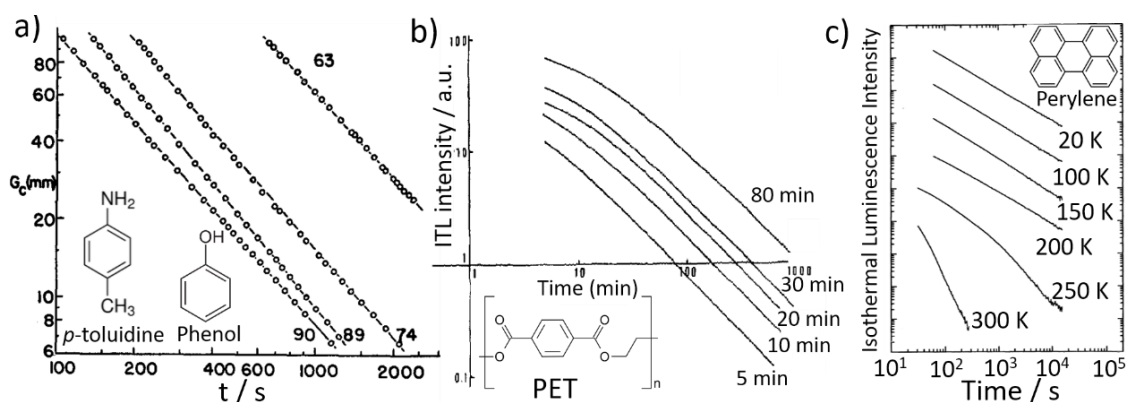
Figure 7.5. a) OLPL decay curves of different 77 K solutions. 63: phenol in aqueous alkali; 74: *p*-toluidine in methanol; 89: *p*-toluidine in mixed solvent (20% methanol and 80% glycerol); 90: tyrosine in aqueous alkali. (Excitation source: high pressure mercury vapour arc). b) OLPL decay curves of 77 K PET film with different excitation duration. (Excitation source: γ-ray. Dose: 25 krad/h). c) OLPL decay curves of a Pe:PnBMA film at different temperatures. (Excitation source: 308 nm laser. Pulse energy and intensity: 3 mJ/cm^2). These figures are adapted from (20), (21) and (23).

OLPL started to attract people's attention again in 2017, as Kabe *et al*. found that much longer OLPL can be realized at room temperature (24). They demonstrated that doping 1 mol% TMB in PPT resulted in an exciplex emitter whose afterglow duration is more than one hour (Figure **7.6a**). To further enhance the afterglow performance, in 2018, the same group found another exciplex emitter, 1 mol% m-MTDATA: PPT (25), which can reach a twofold longer afterglow duration

compared with the original TMB:PPT film. Furthermore, to realize multi-colour OLPL, this group doped different fluorescent chromophores, namely 2,5,8,11-tetra-tert-butylperylene (TBPe), 9,10-bis[N,N-di-(ptolyl)-amino]anthracene (TTPA), 2,8-di-tert-butyl-5,11-bis(4-tertbutylphenyl)-6,12-diphenyltetracene (TBRb), 4-(dicyanomethylene)-2-methyl6-julolidyl-9-enyl-4H-pyran (DCM2) and tetraphenyldibenzoperiflanthene (DBP), into the TMB:PPT system (9). Taking advantage of the FRET between the TMB:PPT exciplex and the chromophores, they managed to obtain OLPL colours from sky-blue to red and even warm white (Figure **7.6b**). Moreover, to lower the cost of room-temperature OLPL materials, they replaced the expensive small molecule, PPT, with an inexpensive n-type polymer, PBPO, and also obtained OLPL which lasted for 7 min (26). Compared with brittle PPT, PBPO is mechanically stronger, which also allows folding and twisting, and so PBPO can expand the range of applications of OLPL (Figure **7.6c**).

Figure 7.6. a) OLPL decay curve of a 1 mol% TMB:PPT film. b) Molecular structure of PBPO and photos of the OLPL from the 1 mol% TMB:PBPO film. c) Photos of multi-colour OLPL. These figures are adapted from (24), (26) and (9). (Excitation source: 340 nm LED)
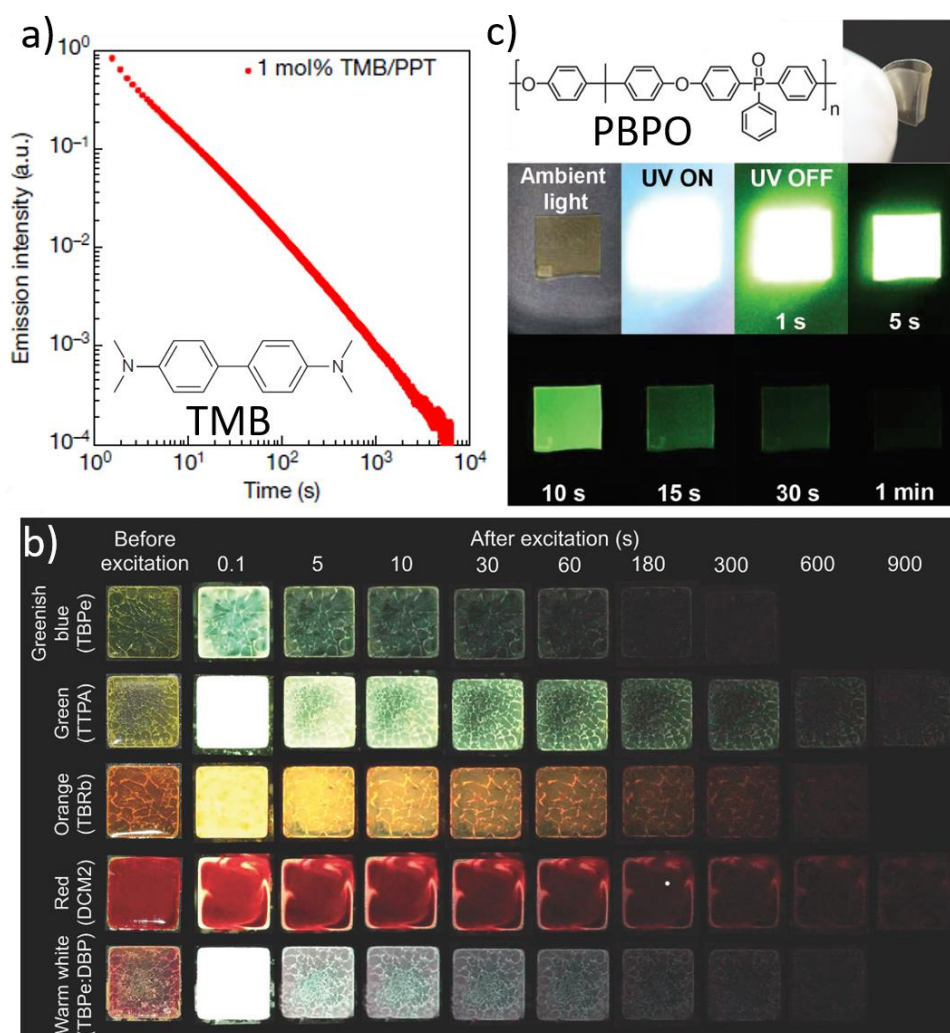
7.2 OLPL mechanism overview

This section gives an overview of the mechanism studies of OLPL, including the charge separation and recombination process in OLPL systems.

7.2.1 Charge separation process in OLPL systems

As photo-induced charges are the origin of OLPL, people have tried different methods to ionize organic molecules to obtain them. In the development of the field, things also happened in the other way around: OLPL was first observed in some experiments, and then people tried to explain how the photo-charges were generated in those systems. In this section, we briefly review the light sources people used to create photo-induced charges and how the ionized electrons are trapped. To expand the application of OLPL, photo-induced charges should be easily created by common light sources such as indoor room lights, the sun and light torches. However, organic molecules usually have HOMO values deeper than -5 eV, which requires high energy photons to ionize organic molecules, and these photons are difficult to access in daily life. Therefore, people developed different methods to overcome this problem, as discussed below.

7.2.1.1 Charge separation through ionisation radiation, deep UV radiation and high energy electron-beam

The most straightforward way to ionize organic molecules is using high-energy photons or electrons which are energetic enough to excite the electrons from their HOMOs to vacuum, as shown in Figure **7.7a**. In 1974, Serpi *et al.* (27) used X-rays generated from Cu targets (30 kV) to ionize urea and thiourea to study their OLPL decays (schematic diagram of X-ray generation is shown in Figure **7.7b**: the Cu target was bombarded by high energy electrons and emitted X-rays). In 1980, Hama *et al.* (21) used γ-rays generated from ^{60}Co decay to ionize a polymer, PET (schematic diagram of γ-ray generation is shown in Figure **7.7c**: ^{60}Co decays and emits γ-rays). In 1981, Miller *et al.* used high energy electron beams (15 MeV) to ionize TMPD molecules (28). These excitation sources were applied in early OLPL studies, but were later unused because of the dangers of ionising radiation. Also, the ionising radiation sources, such as ^{60}Co, are expensive

and difficult to store, which limits the research and applications of OLPL. Therefore, people were seeking for less energetic excitation source for organic molecule ionisation.
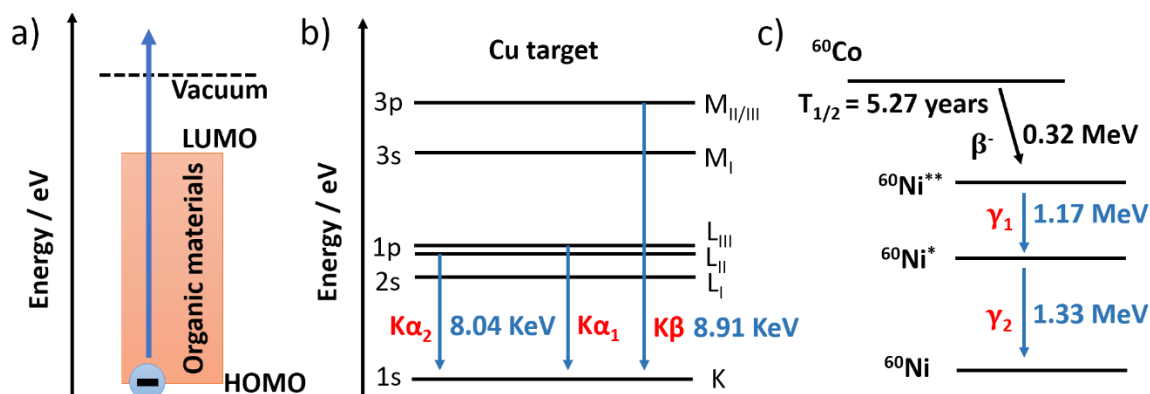
Figure 7.7. a) Schematic diagram of ionizing organic materials using high energy photons or electrons. b) Schematic diagrams of X-rays and γ-rays generation.

7.2.1.2 Multi-photon ionisation (successive two-photon ionisation and two-photon absorption)

Compared with using ionisation radiation or high energy electrons, multi-photon ionisation is an effective way to ionize organic molecules using lower-energy photons. Within this mechanism, successive two-photon ionisation is the most commonly used method: as shown in Figure **7.8a**, if the S_1 or T_1 lifetime of an organic molecule is sufficiently long, this organic molecule at the excited state can absorb another photon before it decays to the ground state, and so this molecule can be ionized. Therefore, two low energy photons in the visible light range (e.g. 400 nm, 3.1 eV) can ionize a common organic molecule (e.g. HOMO = -5 eV).
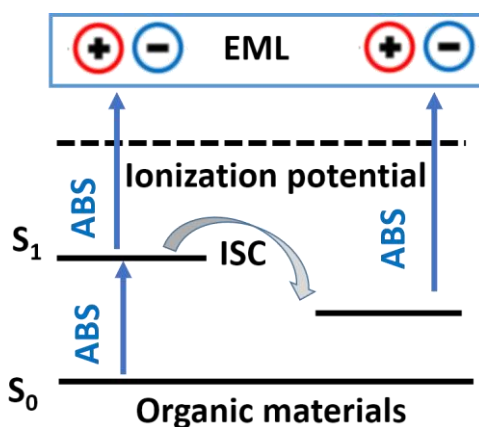
Figure 7.8. Schematic diagram of successive two-photon ionisation

Early multiple-photon ionisation studies of organic molecules were carried out on anthracene single crystals and liquid benzene (29,30) in 1968 and 1982. The first successive two-photon ionisation on OLPL molecules was carried out by Braun *et al.* in 1981 (31). They used a nitrogen laser pumped dye laser (λ: 370 nm, repetition rates: 5 Hz, intensity: 10^{23} photons/cm^{2}s) to excite the N,N,N′,N′-Tetramethyl-p-phenylenediamine (TMPD) molecules dissolved in hydrocarbon solution, and they found the TMPD molecules were ionized mainly through a two-photon process. Successive two-photon ionisation in solid-state OLPL systems was first reported by Tsuchida *et al.* in 1988 (32). They found using either a XeF excimer laser (λ: 308 nm, FWHM: 17 ns, pulse energy: 60 mJ) or a focused xenon lamp to excite a 77 K TMPD:PMMA film (doping concentration: 1.2×10^{-4} mol/d^3) could generate wurster's blue colour in the film, indicating TMPD$^+$ radicals were generated after the photoexcitation. Moreover, in 1992, they extended this experiment further (33) and studied the properties of the successive two-photon ionisation process. They concluded that, when the total excitation energy is higher than required for ionisation, the exceeding energy becomes electrons' kinetic energy. Therefore, higher energy photons eject electrons further away from the parent TMPD$^+$ radicals after ionisation, which can extend the duration of the subsequent charge recombination process.

In summary, successive two-photon ionisation uses much lower energy photons for organic molecules ionisation compared with using ionisation radiation and high energy electron beams. Although high energy photons are not required, highly intense excitation sources are needed to build up the excited state molecules. Moreover, the organic materials need to have sufficiently long-lived S_1 or T_1 state to absorb a second photon, which does not apply to all molecules.

7.2.1.3 CT exciton dissociations

CT exciton dissociation is the core of organic solar cells. A brief mechanism description of organic solar cells follows: as shown in Figure **7.9**, the active layer in an organic solar cell is usually a blend of 50:50 mol% of donor and acceptor molecules. When the donor molecules are excited (process **1**), the electrons will be transferred from the HOMO of the donor to its empty LUMO, which correspondingly leaves holes in the HOMO. These excited-state electrons will automatically transfer to the deeper LUMO of the acceptor LUMO (process **2**), and so the electrons and holes are separated on different molecules, which completes the photo-induced charge-separation process. As it is a one-photon process, CT exciton dissociation can be triggered at low excitation intensity and has a high charge-separation efficiency. This mechanism

was also used in Kabe *et al.*'s (24) room-temperature OLPL emitters (Figure **7.6a**). In Kabe's experiment, a 340 nm LED was selected to directly excite the host, PPT, which consists of 99 mol% of the film. As shown in Figure **7.9b**, in the excitation process, electrons transfer from the HOMO of PPT its LUMO (process **i**) and leave holes on the HOMO. These holes are spontaneously filled up by the electron from the HOMO of TMB (process **ii**), which generates TMB$^+$ radicals. At the same time, the electrons on the LUMO of PPT can hop to the LUMOs of neighbouring PPT molecules, and so the electrons are separated further apart from the parent TMB$^+$ radicals. In the emission process, as shown in Figure **7.9c**, the electrons on the LUMOs of PPT keep hopping until they meet the TMB$^+$ radicals, which generates new CT excitons, leading to exciplex emission.
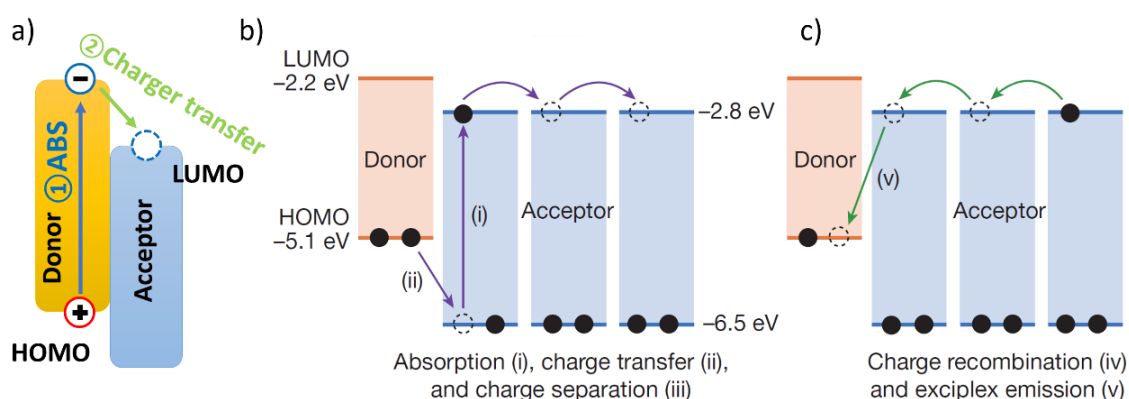
Figure 7.9. a) Schematic diagram of the charge separation process in the active layer of an organic solar cell. b, c) Schematic diagram of the charge separation and recombination processes in Kabe's 1 mol% TMB:PPT film. Figure b and c are adapted from (24).

To collect further evidence to prove that photo-induced charges are generated through CT exciton dissociation in exciplex-based OLPL emitters, the same group designed another experiment in which they compare the afterglow durations of different emitters with different CT state populations (34). To control these populations, three different donors were doped in PPT to build different thermally activated delayed fluorescence (TADF) exciplex emitters with different ΔE_{ST}s. As shown in Figure **7.10a**, different ΔE_{ST} values lead to different k_{rISC}, and so a smaller ΔE_{ST} enables more ^{3}LE excitons to be converted into CT excitons (the related mechanism has been discussed in Sections **4.2** and **4.3**). The corresponding OLPL decay curves of these exciplex emitters are shown in Figure **7.10b**. It can be seen that the smaller the ΔE_{ST} values, the longer the OLPL durations, indicating larger CT exciton populations lead to more photo-induced charges. This is consistent with the mechanism of CT exciton dissociation for photo-induced charge generation.
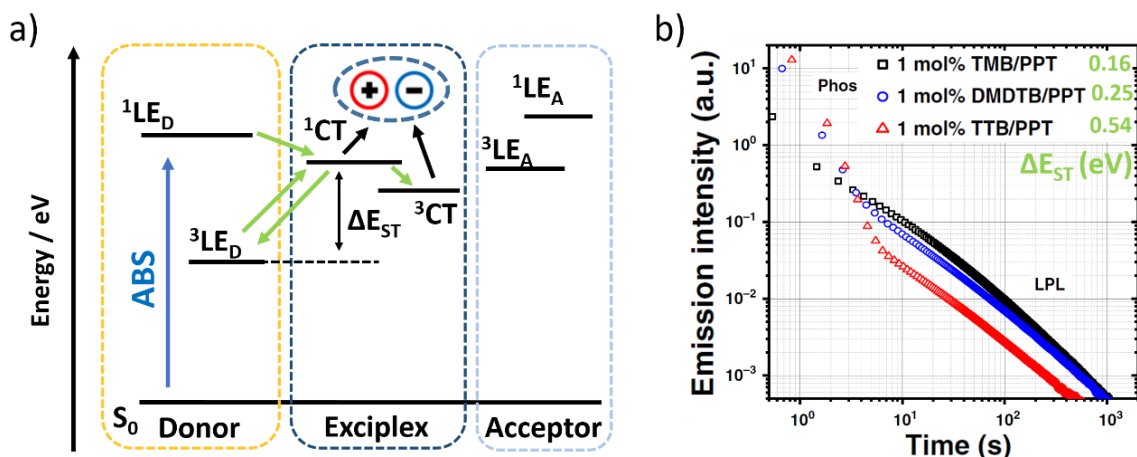
Figure 7.10. a) Schematic diagram of an exciplex-based TADF OLPL emitter. The charge separates from the ^1CT and ^3CT states. b) PL decay curve of the different exciplex emitters used by Kabe's group. Figure a) and b) are adapted from (34).

In summary, charge separation through CT exciton dissociation has the advantage of high charge generation efficiency. It can be triggered even at low excitation intensity as it is a one-photon process.

7.2.1.4 Spontaneous orientation polarization

In 2019, Yamanaka *et al.* (35) demonstrated that photo-induced charges were generated in the emission layers (EMLs, 4CzIPN:CBP and TPA-DCPP:CBP) of their TADF OLEDs when the OLEDs were exposed to a 470 nm LED. That was the first time people reported photo-induced charges generated from TADF compounds. To explain the origin of the photo-induced charge separation in the EML, they proposed spontaneous orientation polarization (SOP) as the mechanism. The normal CT exciton dissociation model used in Kabe *et al.*'s (24,34) experiment cannot be applied here because no exciplex was formed between the host and the guest molecules: as shown in Figure **7.11a**, the HOMOs of the emitters are shallower than that of the host and the LUMOs of the emitters are deeper than that of the host, making the condition unpreferable for exciplex formations. The mechanism of SOP is described as follow: as shown in Figure **7.11b**, in an EML, the permanent dipole moment of the TADF emitters can create a static electrical field. Although the dipole orientations of the emitters are random, these dipole moments can still create electrical fields in a small region. When the TADF emitters are excited to CT states, CT excitons can dissociate into electron and hole pairs with the help of these electrical fields.
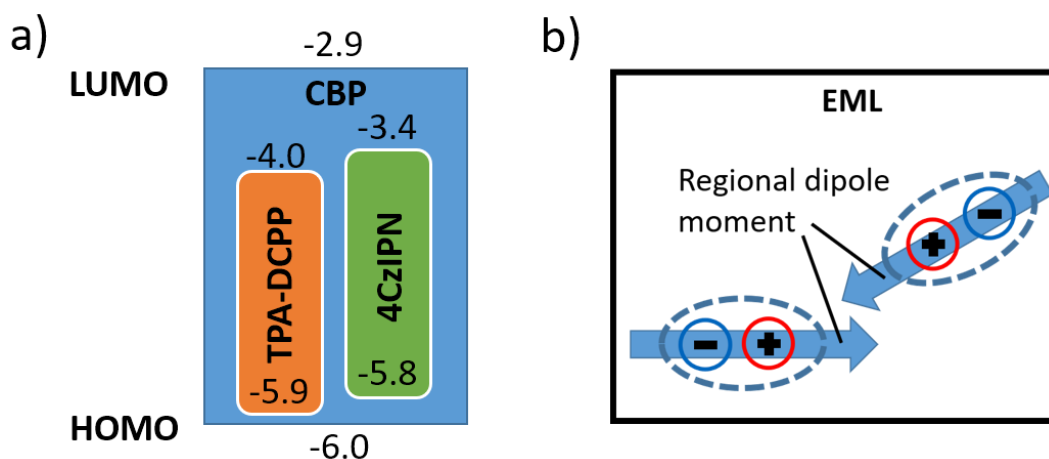
Figure 7.11. a) HOMO and LUMO energy diagram of TPA-DCPP, 4CzIPN and CBP. b) Schematic diagram of SOP.

In Yamanaka *et al.'s* experiment, although they have solidly proved the existence of photo-induced charges in their EML because these charges have response to external voltage, their mechanism explanation of SOP requires further experimental proof and analysis. Furthermore, the afterglow duration in their system was only a few miliseconds, which is far less than those of other OLPL materials.

7.2.2 Charge recombination process in the OLPL system

Compared with RTP emitters whose emission decay curves are exponential, the PL decays of OLPL follow power laws (e.g. Figure **7.6a**). As OLPL is from charge recombinations, it indicates the charge-recombination rates also follow power laws. However, the origin behind this power law recombination rate is still not completely understood. To reveal the mechanism behind it, people proposed many models to describe the microscopic image of how the electrons meet the positively charged radicals. The most important models include electron diffusion, continuous-time random walk (CTRW) and electron tunnelling. In the following sections, the details of these models and the problem of each model are discussed.

7.2.2.1 Electron diffusion model:

The very first charge recombination model, also called electron diffusion model, for OLPL was proposed by Debye and Edwards in 1952 (20). In this model, the positively charged emitter radicals are treated as electron sinks with many photo-induced electrons around them after

photoexcitation. The emitter radicals are normally much larger and heavier than the electrons, and so they are considered to be firmly held by the solid media and cannot move. At the same time, the ejected electrons are assumed to be able to diffuse in the solid media. Also, it does not require energy for the recombination process between the emitter radicals and the diffusing electrons. Therefore, a prediction from this model is that the charge recombination rate is doping concentration dependent: it takes a longer time for the electrons to meet the emitter radicals in a more dilute doped solid media, and so the OLPL decays become longer as well. However, in an infinitely diluted case, the recombination rate should not be infinitely slow, but should converge to a constant. Although Debye and Edwards proposed this physical image for the charge-recombination process, they did not manage to fully derive an expression for the charge recombination rate. Therefore, they combined an empirical OLPL decay rate equation with their experimental results to analyse their prediction about the effect of doping concentrations on the charge-recombination rates. Also, they predicted that the m value in the empirical equation equals -1 when the doping concentration is infinitely low. The expression of this empirical equation is shown below:

$$I(t) = k \cdot t^m \tag{7.1}$$

where

  I is the OLPL intensity

  k is a constant which varies for each measurement

  t is time

  m is an exponent

It was found Equation **7.1** fitted their experimental OLPL decay curves well. The experimental data were collected through measuring the TRPL decays of several 77 K solutions with various emitter concentrations (Figure **7.5a**). After fitting the OLPL decay curves, they found the value of m in Equation **7.1** dropped from -1.13 to -1.00 when the phosphors concentration was decreased from 0.34 mol/L to 0.00068 mol/L. The ultra-low phosphor concentration of 0.00068 mol/L is close to infinitely dilute. Therefore, the measured m = -1 in this case aligns with their prediction. Consequently, the power law decay rate described by Equation **7.1** with m = -1 was called Debye-Edwards law by Hamill in 1979 (36).

Although Equation **7.1** fits Debye and Edwards' experimental results, it can be seen that this equation breaks down when the variable t approaches 0, because the initial intensity, I_0, becomes infinite in this case, which cannot be physically true. In addition, the integration of the intensity in Equation **7.1** is not normalized, which can result in an unreal infinite number of charges. It was not an issue for Debye and Edwards because they started the TRPL decay measurement around 100 seconds after the photoexcitation. But this problem cannot be ignored for initial state study of the system around time zero.

As an improvement of Debye and Edwards' model, in 1972, Abell and Mozumder (37) got an intensity decay equation from strict mathematical derivation. However, the new equation is far more complex and looks completely different from Equation **7.1**. In Abell and Mozumder's paper, they assume that there is no Coulomb effect between the radical sinks and the diffusing electrons. In other words, radicals and electrons are treated as electronically neutral. They claimed that this assumption is reasonable when the microscopic dielectric relaxation is very fast, so that coulombic perturbation on the electron diffusion is not strong. In this model, they got the equation for the recombination rate as:

$$R(\tau) = \frac{2a^3\pi^{0.5}}{\tau^{1.5}} \int_0^\infty x exp(-\frac{x^2}{4r})F_0(x)dx \qquad (7.2)$$

where:

$$x = r/a - 1$$

$$\tau = Dt/a^2\tau$$

$$F(x,0) = F_0(x) = (x+1)n_0(r)$$

$$n(r,0) = n_0(r)$$

In the equations above, the definitions of the symbols follow:

a is the radius of the electron sink: there is no electrons beyond this radius

r is the distance from the centre of the sink to the volume unit

D is the diffusion constant of electrons

n is the number of electrons per small volume unit

In addition, the afterglow intensity should be proportional to the charge recombination rate:

$$I(t) \propto R(\tau) \tag{7.3}$$

Consequently, combining Equation **7.2** and **7.3**, when $t \rightarrow \infty$, $I(t) \propto t^{-1.5}$. Based on these calculations, Abell and Mozumder claimed that no matter what the electron distribution is like at $t = 0$, the value of m always goes to -1.5 at longer time scale. Although some experimental results show the value of m varies from -1 to -1.2, which do not match their theory, Abell and Mozumder claimed that those values were measured in the intermediate states of the decays, and the value of m would finally go to -1.5 with a sufficiently long time. Moreover, they claimed that m = -1.5 is only correct when the charge recombination is mainly because of the electron diffusion rather than other processes such as electron tunnel.

7.2.2.2 Continuous-time random walk model

Continuous-time random walk model (CTRW) model was first applied to inorganic semiconductor lattice in 1965 by Montroll and Weiss (38). In this model, they assumed that the electrons diffuse through hopping to the nearest-neighbour lattice point, which occurs at random time intervals. In that study, they derived and studied a random-walk generation function which can describe the properties of random walks. Based on this function, in 1975, Scher and Montroll (39) derived a hopping time distribution function which describes the average time required by an electron walker to go from a given lattice point to another preassigned point. Later, in 1977, Hamill and Funabashi (40) applied both of the random-walk generation function and hopping time distribution function to solve the OLPL decay rate, and they concluded that, in a longer time scale, the emission intensity can be expressed as follow:

$$I(t) \propto t^{\alpha-1} \tag{7.4}$$

where:

α is a constant and $0 < \alpha < 1$

It can be found that the value of m is in the range from -1 to 0 in the CTRW model. Importantly, Equation **7.4** is an asymptotic expression, and I_0 again approaches to infinity when t approaches to 0. Also, an integration of Equation **7.4** from $t = 0$ to $t \rightarrow \infty$ lead to an ionic species divergence. Therefore, Equation **7.4** still cannot describe the whole decay process of OLPL.

7.2.2.3 Electron tunnelling model

In 1971, Kieffer *et al*. (41) found that the OLPL decay rate in the rigid solution of methyl-cyclohexane is independent of temperature ranging from 4 K to 77K, which also indicates a temperature independent charge recombination mechanism. Therefore, in 1975, Tachiya and Mozumder (42) explained this phenomenon by proposing a model in which the electrons recombine with the emitter radicals through electron tunnelling. They also assumed that the initial electron density decreases exponentially against the distance from the emitter radicals. These assumptions allow them to strictly derive an emission decay rate:

$$I(t) = (\alpha v a/b)\Gamma(1 + a/b)N_0(vt)^{-(1+a/b)} \tag{7.5}$$

where:

α is constant, which is the ratio between the emission intensity and the number of recombined charges

v is the frequency factor which is of the order of 10^{15}/s

a is a parameter which is of the order of 1 Å

b is a parameter which is of the order of 50 Å

$\Gamma(x)$ is Gamma function with $x = (1 + a/b)$

N_0 is the number of electrons at t = 0

Therefore, inserting a = 1 Å and b = 50 Å, the value of m in this equation equals -1.02 which is very close to the experimental values obtained by Debye and Edwards (20). Although Equation **7.5** was analytically derived from the initial assumption, insufficient experiments have been done to analyse the validity of this equation.

7.2.2.4 Empirical approach

Compared with the analytical equations derived above, there is an empirical OLPL decay equation which shows more simplicity and elegance, and it is the most widely used one for OLPL studies (21,43,44). The expression of this equation follows:

$$I(t) = I_0(1 + \alpha t)^m \tag{7.6}$$

where:

I_0 is the initial light emission

α is a parameter

This equation is similar to Equation **7.1**, but with the improvement of solving the problem of the infinite intensity at t = 0. Furthermore, to make sure the total ionic species is convergent, the value of m should be < -1. This can be simply proved by integrating Equation **7.6** from t = 0 to t → ∞, which is presented below:

$$\int_0^{+\infty} I(t)dt = \int_0^{+\infty} I_0(1+\alpha t)^m dt \tag{7.7}$$

$$\int_0^{+\infty} I(t)dt = \frac{I_0}{\alpha} \int_0^{+\infty} (1+\alpha t)^m d(1+\alpha t) \tag{7.8}$$

$$\int_0^{+\infty} I(t)dt = \frac{I_0}{\alpha(m+1)} (1+\alpha t)^{m+1} |_{t\,=\,0}^{t\,=\,+\infty} \tag{7.9}$$

$$\int_0^{+\infty} I(t)dt = \frac{I_0}{\alpha(m+1)} \{[1+\alpha \cdot (+\infty)]^{m+1} - (1+\alpha \cdot 0)^{m+1}\} \tag{7.10}$$

Apparently, the prerequisite to make Equation **7.10** convergent is that m < -1, and the Equation **7.10** becomes:

$$\int_0^{+\infty} I(t)dt = -\frac{I_0}{\alpha(m+1)} \tag{7.11}$$

Therefore, if the Equation **7.6** can correctly describe OLPL decays, the total amount of generated ionic species can be estimated by inserting the fitting parameters of I_0, α and m. However, it was found extracting the values of these parameters are not easy because, in an OLPL decay measurement, only the tails of the decay can be measured (> 1s), and so the estimation of initial intensity around t = 0 is inaccurate. Moreover, the value of I_0 has a significant effect to the final results. Therefore, combing the fact that the validity of Equation **7.6** has not been fully analysed and the difficulties of estimating I_0, the estimation of total amount of the generated ionic species was not carried out in this thesis.

The rudiment of this Equation **7.6** was first proposed by Burton and Funabashi in 1969 (45) and it was improved to its final state by Boustead *et al.* in 1972 (22) as they found this equation best fits their experimental results. Furthermore, in 1980 and 1983, Hama *et al.* (21,43) studied how the parameters m, I_0 and α in this equation are affected by the experimental conditions. They used γ-rays from ⁶⁰Co to ionize PET at 13 K with various irradiation durations and doses. After

the excitation source was removed, the TRPL decays of the samples were recorded by a PMT and the decay curves were fitted using Equation **7.6**. They found that the parameter m, I_0 and α have following relationships with the excitation conditions:

$$m = -(1 + a/R) \tag{7.12}$$

$$I_0 = bRT^{1/4} \tag{7.13}$$

$$\alpha = c \cdot R \cdot T^{-1/2} \tag{7.14}$$

where:

a, b and c are constants

R is irritation dose rate

T is excitation duration

Although Equation **7.6** is empirical, which lacks fundamental physics models, many people applied this equation to their OLPL studies because they found this equation best fits their experimental results. Within these studies, most people still assume that electron tunnelling is the main charge recombination mechanism because there is no temperature dependence in their OLPL decay slope at low temperatures (< 200 K) (21,23,43).

7.3 Conclusion

This chapter introduced the three main classes of materials people used to realize room-temperature long-lived afterglow, namely inorganic LPL, RTP and OLPL materials. LPL materials have the advantage the longest afterglow duration (> 10 h) and have already been commercialized for the applications as glow-in-dark toys, decorations and safety signs, etc. However, organic materials have the advantages of lower fabrication temperature and rare metal free, which can be potentially cheaper and more sustainable. Although RTP materials also possess these advantages, they have the significant disadvantages of high morphology requirements (packing or crystallization) and short afterglow durations (τ_{PH} < 23 s), which limits their applications. In comparison, OLPL materials possess all the advantages described above, namely low fabrication temperature, rare metal free, no morphology requirement and long afterglow durations (> 1 h). Therefore, OLPL materials are one of the most promising next generation afterglow materials.

OLPL originates from photo-induced charge generation and the subsequent charge recombination. To generate photo-induced charges, people developed many methods such as ionisation irradiation (X-rays, γ-rays), multiphoton-ionisation, CT exciton dissociations, and SOP. Within these techniques, multiphoton-ionisation and CT exciton dissociation are most widely used because of the easy access to the required excitation sources (xenon lamps, lasers and LEDs). On the other hand, to explain the origin of different OLPL decay rates, people proposed many models to explain the different rates of charge-recombination. The most important models among these are electron diffusion, CTRW and electron tunnelling. The values of the decay slopes, *m*, predicted by these three models are in the ranges of (-1, -1.5], (0, -1) and around -1, respectively. However, the expressions for the OLPL decays derived from these models are all very complicated. Furthermore, the validity of these models requires further analysis and more experimental proofs. Therefore, people generally do not use those expressions but an empirical equation (Equation **7.6**) to analyse their experimental results. Although this equation describes OLPL decays well in long time windows (> 5 s), its validity in short time windows (< 1 s) still has not been studied much. It is because many other emission dominant the short time windows, namely prompt fluorescence, TADF and RTP. Therefore, the extraction of the pure OLPL decays in short time scales is still difficult, and so the expression of charge-recombination process still requires further studies.

7.4 References

1. Matsuzawa T. A New Long Phosphorescent Phosphor with High Brightness, SrAl[sub 2]O[sub 4]:Eu[sup 2+],Dy[sup 3+]. J Electrochem Soc. 1996;143(8):2670. Available from: https://iopscience.iop.org/article/10.1149/1.1837067

2. Lin Y, Zhang Z, Tang Z, Zhang J, Zheng Z, Lu X. The characterization and mechanism of long afterglow in alkaline earth aluminates phosphors co-doped by Eu2O3 and Dy2O3. Mater Chem Phys. 2001;70(2):156–9. Available from: https://linkinghub.elsevier.com/retrieve/pii/S0254058400005009

3. Alibaba. No Title [Internet]. 2020. Available from: https://www.alibaba.com/product-detail/glow-In-The-Dark-Exit-Signs_163036554.html%0A

4. Pinterest. No Title. 2020; Available from: https://www.pinterest.co.uk/pin/441634307182602027/

5.   Special FX Creative. No Title [Internet]. Available from: https://www.sfxc.co.uk/products/glow-in-the-dark-pigments%0A

6.   Van den Eeckhout K, Smet PF, Poelman D. Persistent Luminescence in Eu2+-Doped Compounds: A Review. Materials (Basel). 2010;3(4):2536–66. Available from: http://www.mdpi.com/1996-1944/3/4/2536

7.   Clabau F, Rocquefelte X, Jobic S, Deniard P, Whangbo M-H, Garcia A, Le Mercier T. Mechanism of Phosphorescence Appropriate for the Long-Lasting Phosphors Eu 2+ - Doped SrAl 2 O 4 with Codopants Dy 3+ and B 3+. Chem Mater. 2005;17(15):3904–12. Available from: https://pubs.acs.org/doi/10.1021/cm050763r

8.   Tai Y, Zheng G, Wang H, Bai J. Broadband down-conversion based near infrared quantum cutting in Eu2+–Yb3+ co-doped SrAl2O4 for crystalline silicon solar cells. J Solid State Chem. 2015;226:250–4. Available from: http://dx.doi.org/10.1016/j.jssc.2015.02.020

9.   Jinnai K, Kabe R, Adachi C. Wide-Range Tuning and Enhancement of Organic Long-Persistent Luminescence Using Emitter Dopants. Adv Mater. 2018;30(38):1800365. Available from: http://doi.wiley.com/10.1002/adma.201800365

10.   Jia W, Wang Q, Shi H, An Z, Huang W. Manipulating the Ultralong Organic Phosphorescence of Small Molecular Crystals. Chem – A Eur J. 2020;26(20):4437–48. Available from: https://onlinelibrary.wiley.com/doi/abs/10.1002/chem.201904500

11.   Wang C-R, Gong Y-Y, Yuan W-Z, Zhang Y-M. Crystallization-induced phosphorescence of pure organic luminogens. Chinese Chem Lett. 2016;27(8):1184–92. Available from: https://linkinghub.elsevier.com/retrieve/pii/S1001841716301498

12.   Kabe R, Notsuka N, Yoshida K, Adachi C. Afterglow Organic Light-Emitting Diode. Adv Mater. 2016;28(4):655–60. Available from: http://doi.wiley.com/10.1002/adma.201504321

13.   Yang J, Zhen X, Wang B, Gao X, Ren Z, Wang J, Xie Y, Li J, Peng Q, Pu K, Li Z. The influence of the molecular packing on the room temperature phosphorescence of purely organic luminogens. Nat Commun. 2018;9(1):840. Available from: http://dx.doi.org/10.1038/s41467-018-03236-6

14.   Xu S, Chen R, Zheng C, Huang W. Excited State Modulation for Organic Afterglow:

Materials and Applications. Adv Mater. 2016;28(45):9920–40. Available from: http://doi.wiley.com/10.1002/adma.201602604

15. Kropp JL, Dawson WR. Radiationless deactivation of triplet coronene in plastics. J Phys Chem. 1967;71(13):4499–506. Available from: https://pubs.acs.org/doi/abs/10.1021/j100872a054

16. An Z, Zheng C, Tao Y, Chen R, Shi H, Chen T, Wang Z, Li H, Deng R, Liu X, Huang W. Stabilizing triplet excited states for ultralong organic phosphorescence. Nat Mater. 2015;14(7):685–90. Available from: http://www.nature.com/articles/nmat4259

17. Warren P. Phosphorescence and electron traps - I. The study of trap distributions. Proc R Soc London Ser A Math Phys Sci. 1945;184(999):365–89. Available from: https://royalsocietypublishing.org/doi/10.1098/rspa.1945.0024

18. Lewis GN, Lipkin D, Magel TT. Reversible Photochemical Processes in Rigid Media. A Study of the Phosphorescent State. J Am Chem Soc. 1941;63(11):3005–18. Available from: https://pubs.acs.org/doi/abs/10.1021/ja01856a043

19. Lewis GN, Lipkin D. Reversible Photochemical Processes in Rigid Media: The Dissociation of Organic Molecules into Radicals and Ions. J Am Chem Soc. 1942;64(12):2801–8. Available from: https://pubs.acs.org/doi/abs/10.1021/ja01264a025

20. Debye P, Edwards JO. Long-Lifetime Phosphorescence and the Diffusion Process. J Chem Phys. 1952;20(2):236–9. Available from: http://aip.scitation.org/doi/10.1063/1.1700385

21. Hama Y, Kimura Y, Tsumura M, Omi N. Studies on the recombination of cation—electron pairs by long-range tunneling, as studied by ITL measurement in irradiated polymers. Chem Phys. 1980;53(1–2):115–22. Available from: https://linkinghub.elsevier.com/retrieve/pii/0301010480870595

22. Boustead I, George TJ. A preliminary study of thermoluminescence in polypropylene. J Polym Sci Part A-2 Polym Phys. 1972;10(10):2101–5. Available from: http://doi.wiley.com/10.1002/pol.1972.180101022

23. Ohkita H, Sakai W, Tsuchida A, Yamamoto M. Charge Recombination via Electron Tunneling after Two-Photon Ionization of Dopant Chromophore in Poly(butyl

methacrylate) Film at 20 K. Bull Chem Soc Jpn. 1997;70(11):2665–70. Available from: http://www.journal.csj.jp/doi/10.1246/bcsj.70.2665

24. Kabe R, Adachi C. Organic long persistent luminescence. Nature. 2017;550(7676):384–7. Available from: http://www.nature.com/articles/nature24010

25. Jinnai K, Nishimura N, Kabe R, Adachi C. Fabrication-method Independence of Organic Long-persistent Luminescence Performance. Chem Lett. 2019;48(3):270–3. Available from: http://www.journal.csj.jp/doi/10.1246/cl.180949

26. Lin Z, Kabe R, Nishimura N, Jinnai K, Adachi C. Organic Long-Persistent Luminescence from a Flexible and Transparent Doped Polymer. Adv Mater. 2018;30(45):1803713. Available from: http://doi.wiley.com/10.1002/adma.201803713

27. Serpi PM, Rucci A, Serpi A. Thermoluminescence and isothermal decay of luminescence in x-irradiated urea and thiourea. J Lumin. 1975;9(6):488–501. Available from: https://linkinghub.elsevier.com/retrieve/pii/0022231375900630

28. Miller JR, Beitz J V. Long range transfer of positive charge between dopant molecules in a rigid glassy matrix. J Chem Phys. 1981;74(12):6746–56. Available from: http://aip.scitation.org/doi/10.1063/1.441078

29. Strome FC. Direct, Two-Photon Photocarrier Generation in Anthracene. Phys Rev Lett. 1968;20(1):3–5. Available from: https://link.aps.org/doi/10.1103/PhysRevLett.20.3

30. Schwarz FP, Mautner M. Photoionization of liquid benzene: Fluorescence and electron scavenger quenching between 1900 and 1150 Å. Chem Phys Lett. 1982;85(2):239–44.

31. Braun CL, Scott TW, Albrecht AC. Multiphoton ionization of N,N,N'.N'-tetramethyl-p-phenylenediamine: the condensed-phase two-photon ionization spectrum. Chem Phys Lett. 1981;84(2):248–52. Available from: https://linkinghub.elsevier.com/retrieve/pii/0009261481803375

32. Tsuchida A, Nakano M, Yoshida M, Yamamoto M, Wada Y. Long-lived cation radical formation of aromatic amines in poly(methyl methacrylate) matrix at room temperature by two-photon excitation. Polym Bull. 1988;20(3):297–304. Available from: http://link.springer.com/10.1007/BF00261984

33. Tsuchida A, Sakai W, Nakano M, Yamamoto M. Electron capture of dopants in two-

photonic ionization in a poly(methyl methacrylate) solid. J Phys Chem. 1992;96(22):8855–8. Available from: https://pubs.acs.org/doi/abs/10.1021/j100201a032

34. Lin Z, Kabe R, Wang K, Adachi C. Influence of energy gap between charge-transfer and locally excited states on organic long persistence luminescence. Nat Commun. 2020;11(1):191. Available from: http://dx.doi.org/10.1038/s41467-019-14035-y

35. Yamanaka T, Nakanotani H, Adachi C. Slow recombination of spontaneously dissociated organic fluorophore excitons. Nat Commun. 2019;10(1):5748. Available from: http://dx.doi.org/10.1038/s41467-019-13736-8

36. Hamill WH. Debye–Edwards electron recombination kinetics. J Chem Phys. 1979;71(1):140–2. Available from: http://aip.scitation.org/doi/10.1063/1.438113

37. Abell GC, Mozumder A. Application of Diffusion Model for Recombination of Isolated Pairs in Condensed Media. J Chem Phys. 1972;56(8):4079–85. Available from: http://aip.scitation.org/doi/10.1063/1.1677818

38. Montroll EW, Weiss GH. Random Walks on Lattices. II. J Math Phys. 1965;6(2):167–81. Available from: http://aip.scitation.org/doi/10.1063/1.1704269

39. Scher H, Montroll EW. Anomalous transit-time dispersion in amorphous solids. Phys Rev B. 1975;12(6):2455–77. Available from: https://link.aps.org/doi/10.1103/PhysRevB.12.2455

40. Hamill WH, Funabashi K. Kinetics of electron trapping reactions in amorphous solids; a non-Gaussian diffusion model. Intergovernmental Panel on Climate Change, editor. Phys Rev B. 1977;16(12):5523–7. Available from: https://www.cambridge.org/core/product/identifier/CBO9781107415324A009/type/book_part

41. Kieffer F, Meyer C, Rigaut J. Is isothermal deferred luminescence in organic glasses due to electron tunnelling? Chem Phys Lett. 1971;11(3):359–61. Available from: https://linkinghub.elsevier.com/retrieve/pii/0009261471805079

42. Tachiya M, Mozumder A. Kinetics of geminate-ion recombination by electron tunnelling. Chem Phys Lett. 1975;34(1):77–9. Available from: https://linkinghub.elsevier.com/retrieve/pii/0009261475802041

43.   Hama Y, Gouda K. Initial distribution and tunneling recombination of cation-electron pairs in irradiated rigid materials as studied by ITL measurement. Radiat Phys Chem. 1983;21(1–2):185–90. Available from: https://linkinghub.elsevier.com/retrieve/pii/0146572483901450

44.   Ohkita H, Sakai W, Tsuchida A, Yamamoto M. Charge Recombination via Electron Tunneling after Two-Photon Ionization of Dopant Chromophore in Poly(butyl methacrylate) Film at 20 K. Bull Chem Soc Jpn. 1997;70(11):2665–70. Available from: http://www.journal.csj.jp/doi/10.1246/bcsj.70.2665

45.   Burton M, Funabashi K. Luminescence in High-Energy-Irradiated Alkanes at Low Temperature. Mol Cryst. 1969;9(1):153–81. Available from: http://www.tandfonline.com/doi/abs/10.1080/15421406908082737

Chapter 8 Organic Long-Persistent Luminescence from Thermally Activated Delayed Fluorescence Compounds

Current room-temperature organic long-persistent luminescence (OLPL) materials are mainly based on exciplex emitters. This chapter presents the first case of applying thermally activated delayed fluorescence (TADF) compounds to OLPL and demonstrates that exciplex formation is not necessary for harvesting room-temperature OLPL. This enables a wide range of host materials, such as 2,8-bis(diphenyl-phosphoryl)dibenzo[b,d]thiophene (PPT), 2,2',2"-(1,3,5-Benzinetriyl)-tris(1-phenyl-1-H-benzimidazole) (TPBi) and poly(methyl methacrylate) (PMMA), for OLPL emitters. Compared with current exciplex-based OLPL emitters which uses 99 mol% of expensive and brittle small molecule, PPT, as the host, PMMA is more easily moulded and more rigid, and so enables a wide range of applications. Furthermore, the time-resolved PL (TRPL) spectrum study of the new OLPL emitters in this work shows that S_1 can still be continuously generated in the phosphorescence measurement time window at 77 K because of the recombination of the photo-induced charges. Therefore, care needs to be taken when using the onset of a delayed emission spectrum collected at low temperature (e.g. 77 K) to determine the T_1 energy level of a TADF emitter. Moreover, the photo-induced charge separation mechanism in this new OLPL emitter was studied and discussed, and successive two-photon ionisation was assigned to be the most likely mechanism. At the end of this chapter, deep-blue OLPL materials are presented to demonstrate the wide application of this strategy to obtain multi-colour OLPL.

8.1 Introduction

As has been discussed in Chapter **7**, OLPL is currently one of the most promising methods to realize room-temperature long-lived afterglow using purely organic materials. An important advantage of organic materials over inorganic ones (1) is that they do not need rare metals or high fabrication temperatures, which makes them more easily fabricated, more sustainable and potentially cheaper. At the same time, an advantage of OLPL over RTP (2) is that OLPL materials do not have morphology requirements, and have much longer afterglow duration (thousands of seconds). Although OLPL materials have been heavily studied between 1950s and 1990s (3–5), as has been discussed in Chapter **7**, those studies were mainly carried out at 77 K or even 20 K because OLPL was found to be mainly working at low temperatures and the longest room-temperature OLPL reported before 2017 only lasts for around 200 s (4). The turning point came in 2017, when Kabe *et al*.(6) found that a exciplex emitter can realize room-temperature OLPL lasting for more than an hour. However, this kind of exciplex emitters is still rare: so far, fewer than 10 combinations of exciplex-based OLPL emitters have been reported (7–10). Also, almost all of them require 99 mol% of expensive and brittle material, PPT, as the host, which limits its application. Furthermore, it is difficult to have a large band gap in exciplex emitters. Therefore, it is almost impossible to obtain deep-blue emission from this approach to OLPL.

My work shows an alternative approach in which exciplex is not needed. Within this approach, doping some TADF compounds into common hosts like PPT, TPBi and PMMA can also realize room-temperature OLPL with the afterglow duration comparable to that of exciplex emitters. This finding is significant because it combines the advantages of TADF emitters which are flexible in design, and the advantages of PMMA whose manufacture is mature. This combination makes a purely organic, colour tuneable and low-cost OLPL materials possible, which would massively expand the range of applications. One more feature of TADF-compound-based OLPL materials is that it is much easier to realize deep-blue afterglow compared with exciplex-based OLPL materials because deep-blue emission is more easily obtained from a TADF compound, which is also demonstrated in this work.

To understand the properties of this new OLPL system, a range of PL measurements were performed on the **CzPhAP** doped OLPL films. The TADF properties of **CzPhAP** has been discussed in detail in Chapter **5**. Within these PL measurements in this chapter, the TRPL decay curves contain the information of the afterglow durations and the PL decay rates of this kind of OLPL materials. Furthermore, the PL decay rates also imply the mechanism of charge recombination.

The TRPL spectrum measurements help to identify the excited states that are responsible for the emission in each time window, which further disclose the emission properties of this OLPL materials. In addition, the excitation intensity dependence and photoinduced absorption measurements were used to investigate the mechanism of the charge separation process of this new OLPL system. The experimental results indicate that successive two-photon absorption is the most likely mechanism. Therefore, both OLPL properties and OLPL mechanisms were systematically and comprehensively investigated.

Finally, deep-blue OLPL materials using the 1,3,4-oxadiazole emitters studied in Chapter **6** were presented. It demonstrates that multi-colour OLPL can be easily obtained in this way, and this strategy can be easily adapted to other TADF emitters.

8.2 History of the discovery of TADF-compound-based OLPL emitters

The discovery of TADF-compound-based OLPL emitters comes from the photophysical study of **CzPhAP**. As has been discussed in Chapter **5**, **CzPhAP** was originally designed to be published as a common TADF emitter with the newly designed acceptor **AP**. However, during the study of **CzPhAP** between 2017 and 2018, many other **AP**-based TADF emitters which have better OLED performance were published (11–15). Therefore, **CzPhAP** lost it novelty as a bare TADF emitter. However, the author of this thesis found that **CzPhAP** possesses an unusual long-lived delayed emission in the TRPL decay study: spin-coated **CzPhAP**:CBP/mCP/TPBi/PMMA films (~ 100 nm) have delayed emission lasting for more than 1 s under vacuum, which is longer than those of many RTP materials. Furthermore, this delayed emission duration and the decay curve slopes were found to be dependent on excitation duration, indicating not only TADF or RTP is contributing to the delayed emission. To further investigate this delayed emission, much thicker films (~ 1 mm) were fabricated to increase the delayed emission intensity. It was observed by eye that the consequent samples have afterglow duration lasting for dozens of minutes after the samples were excited by a 365 nm LED. As the fluorimeter (Section **3.5.4**) has a detection time window limit of 4 s which is not long enough to measure this long-lived afterglow, the author started to collaborate with Prof. Ryota Kabe at Kyushu University for their OLPL detection setup (Section **3.5.8**). Prof. Kabe and his PhD student Mr. Kazuya Jinnai helped the author with the TRPL decay measurement of the **CzPhAP** doped films. We also discussed the origin of this long-lived emission, which is photo-induced charge separation and recombination. The whole **CzPhAP**-based OLPL study finished in late 2019. However, some related work was published by

Yamanaka *et al.* in late 2019 (16). They reported that photo-induced charges were found in their TADF compound doped films. Fortunately, they only focused on proving the existence of photo-induced charges, and the afterglow duration of their films were only a few milliseconds. Therefore, **CzPhAP-**based OLPL materials are still the first reported TADF-compound-based OLPL materials that have afterglow duration of seconds or more.

8.3 OLPL study of CzPhAP

8.3.1 TRPL decay and TRPL spectrum

As has been discussed in the last section, the OLPL study of **CzPhAP** started from the observation of its unusual long-lived delayed emission in the TRPL decay study. Furthermore, the PL decay rates and decay durations were found to be dependent on the photoexcitation durations. Figure **8.1a** shows the TRPL decay curves of a spin-coated 6 wt% **CzPhAP**:PPT film (thickness ~ 100 nm) measured under vacuum at room temperature using different numbers of excitation shots. The excitation source was a pulsed 378 nm picosecond laser running in burst mode with a pulse duration around 200 ps, and a time interval between each shot of 100 ns (Section **3.5.4**). It can be seen in the normalized TRPL decay curves that the larger the number of excitation shots (or the longer the excitation duration), the longer the PL decays last for. Furthermore, the slopes of the decay curves are different for different numbers of excitation shots, indicating the emission process is more complicated than typical TADF or RTP because the shapes of the normalized decay curves of these two processes do not change with varying excitation durations. Also, simple decay of a single species would be monoexponential. Therefore, it indicates additional processes are involved in the PL decay of the film. Similar phenomenon was also observed by Yamanaka *et al.* (16) in late 2019 that they could extend the PL decay duration of their TADF emitter doped film from around 0.5 ms to more than 2 ms by increasing the excitation duration from 10 µs to 500 µs. Furthermore, when this doped film was used as the EML of an OLED after photoexcitation, an emission spike will appear in the PL decay curve when an external voltage which is much lower than the turn-on voltage was applied to the OLED, indicating some electrons and holes in the EML were forced to recombine. This is a solid proof of the existence of photo-induced charges in the EML after photoexcitation. However, Yamanaka *et al.* only observed emission lasting around 2 ms and did not report a long-lived afterglow. In contrast, long-lived delayed emission (> 1 s) was observed in many **CzPhAP** doped films using PPT, 4,4′-Bis(N-carbazolyl)-1,1′-biphenyl (CBP), 1,3-Di(9H-carbazol-9-yl)benzene, N,N′-Dicarbazolyl-

3,5-benzene (mCP), TPBi or even PMMA as the host. Figure **8.1b** shows that all the 10wt% **CzPhAP** doped in PPT, TPBi and PMMA films have decay durations lasting for more than 1 seconds with 10,000 excitation shots (around 2 µs of excitation duration spread over 1 ms).
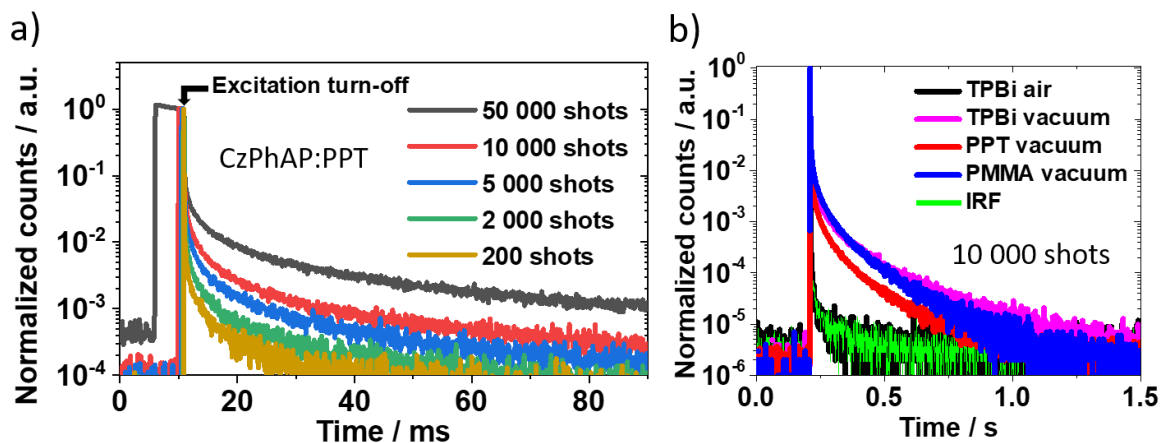
a)

b)

Figure 8.1. a) TRPL decay curve of the 6 wt% **CzPhAP**:PPT film with different numbers of excitation shots. (Excitation source: 378 nm picosecond laser). b) TRPL decay of 6 wt% **CzPhAP**:PPT and 10 wt% **CzPhAP**:TPBi/PMMA films measured in air and under vacuum with 10,000 excitation shots. Figures adapted from (17).

To further investigate the long-lived emission from **CzPhAP**, much thicker (~ 1 mm) amorphous films were fabricated using PPT, TPBi and PMMA as the hosts. The molecular structures and HOMO-LUMO energy diagram are shown in Figure **8.2a** and **b**. The HOMO of **CzPhAP** is shallower than those of these hosts, while the LUMO of **CzPhAP** is deeper than all these hosts, so that it is unlikely to have exciplex formation between the host and guest. The 0.5 wt% **CzPhAP**:PPT/TPBi were fabricated through melt-casting of mixed host-guest powder on glass substrates at 250 °C in the same manner as described by Kabe *et al.* (6). The 0.5 wt% **CzPhAP**:PMMA film was fabricated by polymerizing methyl methacrylate as described in Chapter **9** (section **9.3**). Thicker films were used to increase the absorption and emission, and so to enhance the signal for emission detection. The doping concentration was reduced to 0.5 wt% because Kabe *et al*. (6) had proven that a lower doping concentration is better for longer OLPL durations. However, too low a doping concentration will result in insufficient FRET and introduce host emission. Therefore, 0.5 wt% was chosen as the doping concentration of these thick films. For the measurement of the long-lived and weak afterglow from the samples, a silicon photomultiplier (Section **3.5.8**) was used as the detector. Furthermore, the PL decays were measured 1 second after the photoexcitation, so that only the afterglow was detected. In addition, for the photoexcitation, a 365 nm LED was used to continuously excite the sample for 60 s (for the PPT

and TPBi films) or 1000 s (for the PMMA film) before the PL decay measurement to extend the afterglow durations. Figure **8.2c** shows the photos of the afterglow of the 0.5 wt% **CzPhAP**:PPT/TPBi/PMMA films. It can be seen that all these films show long-lived afterglow.
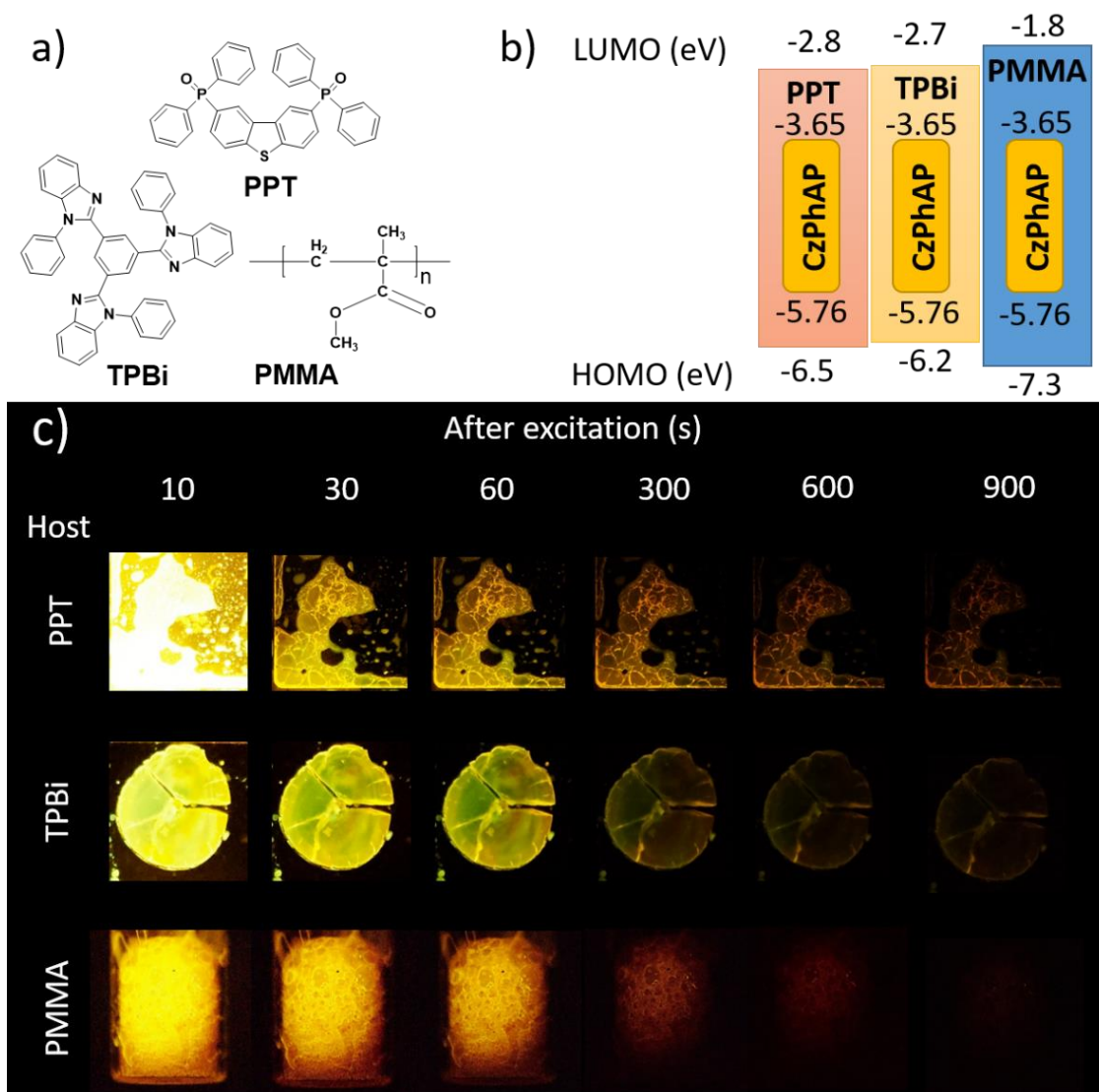
Figure 8.2. a) Molecular structures of PPT, TPB and PMMA. b) HOMO and LUMO energy diagram of PPT, TPBi, PMMA and **CzPhAP**. The values of HOMO and LUMO for PPT, TPBi and PMMA are from (6), (18) and (19), respectively. c) OLPL pictures of the 0.5 wt% **CzPhAP**:PPT/TPBi/PMMA films taken under vacuum. (λ_{ext} = 365 nm) Figures adapted from (17).

To study the afterglow properties, their TRPL decay curves were measured under vacuum at room temperature, and the results are shown in Figure **8.3a**. Both the **CzPhAP** doped in PPT and TPBi films show emission duration over 1000 s which is comparable with that of the state-of-the-art room-temperature exciplex OLPL emitters (6). Importantly, we observed this

phenomenon from a donor-acceptor type TADF compound doped films instead of exciplex emitters. Compared with the **CzPhAP**:PPT/TPBi films, the afterglow duration of the **CzPhAP**:PMMA film is shorter (around 400 s). Furthermore, in the TRPL decay rate analysis, as shown in Figure **8.3a**, the decay curves of the **CzPhAP**:PPT/TPBi films start to follow power laws around 5 seconds after photoexcitation, whereas, that of the **CzPhAP**:PMMA film starts to follow power laws around 7 seconds after photoexcitation. As has been discussed in Chapter **7**, power law decays were attributed to the emission from photo-induced charge separation and the consequent charge recombination. This suggests the mechanism of the long-lived afterglow in our systems is also OLPL, which is similar to that of previously reported OLPL materials (6). Furthermore, as shown in Figure **8.3a**, linear fittings of the power law components of these films in log-log scale result in slope values of -0.98, -1 and -0.55 for the **CzPhAP**:PPT/TPBi/PMMA films, respectively. These differences among different films suggest that the OLPL properties are dependent on the host materials.

The different slope values of the decays indicate the photo-induced charges recombine at different rates, which has been studied in between early 1950s and late 1990s (Chapter **7**). Although these studies were mainly carried out at low temperature (< 200 K), the physics models used for the decay rate explanations are also applicable to room-temperature OLPL. As has been discussed in Chapter **7**, the most important physics models that have been proposed include the electron diffusion model, the CTRW model and the electron tunnelling model. These models predict decay slope values in the range of [-1.5, -1], [-1, 0), and close to -1, respectively. Our measured slopes for all 3 hosts are compatible with the model of CTRW. As all models can explain a slope of -1, our results in PPT and TPBi hosts could also be explained by the other models. However, the main focus of our work is to demonstrate room-temperature OLPL can be realized in TADF emitter doped films, and that it has similar afterglow duration to exciplex-based OLPL emitters.
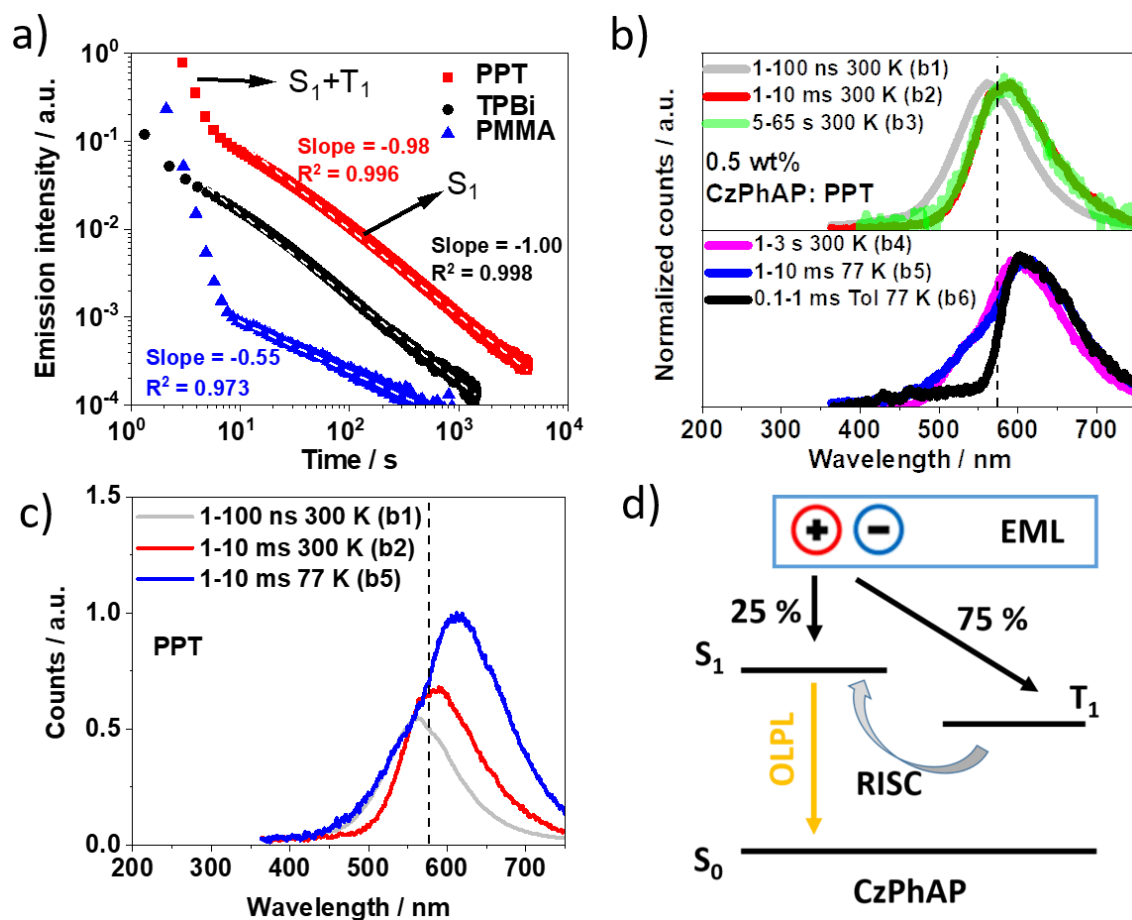
Figure 8.3. a) TRPL decay curves of the 0.5 wt% **CzPhAP**:PPT/TPBi/PMMA films measured under vacuum at room temperature. (λ_{exc} = 365 nm, the excitation intensities and durations for these films are: 23.20 mW/cm^2, 60 s; 7.30 mW/cm^2, 60s; 23.20 mW/cm^2, 1000 s, respectively). The dashed white lines are the linear fits of the power law components of these decays. b) TRPL spectra of the 0.5 wt% **CzPhAP**:PPT film and **CzPhAP** in toluene (λ_{exc} = 343 nm). c) Comparison among the spectra **b1**, **b2** and **b5** to illustrate that the spectrum **b5** is composed of spectra **b1** and **b2**. d) Schematic diagram of charge recombination and OLPL process in the 0.5 wt% **CzPhAP**:PPT film. Figures adapted from (17).

In addition to the TRPL decay analysis, it can be seen in Figure **8.3a** that all the films show two decay regimes with different decay rates. For the PPT and TPBi films, one regime is between 1-5 s, and the other is after 5 s; For the PMMA films, one regime is between 1-7 s and the other is after 7 s. To investigate the origin of these two regimes, TRPL spectra of these films were collected under vacuum in different time windows so as to identify the emitting species in each time window. Figure **8.3b** shows the TRPL spectra of the 0.5 wt% **CzPhAP**:PPT film. Figure **8.3b** (top) compares the spectra of the 0.5 wt% **CzPhAP**:PPT film collected in the time window of 1-100 ns, 1-10 ms and 1-3 s at 300 K, labelled as **b1**, **b2** and **b3**, respectively. Spectrum **b1** is broad and structureless, which is the prompt S$_1$ emission from **CzPhAP**. Compared with spectrum **b1**,

spectrum **b2** shows a modest red-shift. According to the measurement time window (1-10 ms), spectrum **b2** is from the TADF of **CzPhAP**, which also comes from the S_1 state. This red-shift is commonly observed in TADF films because of the conformation relaxation of the emitters or the polarity changes of the hosts (20). Spectrum **b3** shows a perfect overlap with spectrum **b2**, indicating spectrum **b3** also comes from the S_1 state. Therefore, the afterglow in the second decay regime (5 s after the excitation) should all come from the S_1 state, which is labelled in Figure **8.3a**. This is understandable because OLPL comes from charge recombination. As shown in Figure **8.3d**, within the charge recombination process, there is 25% chance for S_1 formation and 75% chance for T_1 formation. As TADF is operating in the 300 K 0.5 wt% **CzPhAP**:PPT film, the generated triplets can be converted into singlet through the TADF channel, and so only S_1 emission can be observed in the power law decay regime.

Figure **8.3b** (bottom) compares the spectra of the 0.5 wt% **CzPhAP**:PPT film collected in the 1-3 s time window at 300 K and 1-10 ms at 77 K. The 0.1-1 ms spectrum of **CzPhAP** in 77 K toluene glass is also used for comparison, and these three spectra are labelled as **b4**, **b5** and **b6**, respectively. Spectra **b4** and **b5** have similar profiles, implying similar species are contributing to both emissions regardless of the huge temperature and time window differences. In addition, spectrum **b5** shows a peak at 608 nm and a shoulder at 584 nm, which suggests more than one species are emitting. To understand these emitting species, spectra **b5** and **b6** were compared. Spectrum **b6** is the phosphorescence spectrum of **CzPhAP** collected in 77 K toluene glass, and so it can be assumed to be purely from the T_1 of **CzPhAP**. In addition, it can be seen on the right side of the black dashed line in Figure **8.3b** (bottom) that the lower energy component (peak at 608 nm) of spectrum **b5** and **b6** show a perfect overlap. Therefore, it can be concluded that the 608 nm peak of spectrum **b5** is from the T_1 emission, while the shoulder of spectrum **b5** at 584 nm was found to come from the S_1 of **CzPhAP**: Figure **8.3c** shows a comparison among spectra **b1**, **b2** and **b5**. It can be seen on the left side of the black dashed line that the higher energy component of spectrum **b5** is composed of spectra **b1** and **b2**. As both of spectra **b1** and **b2** come from S_1, S_1 emission is also contributing to spectrum **b5**. Therefore, spectrum **b5** contains contributions from both S_1 and T_1 emission.

Importantly, spectrum **b5** was measured at 77 K in the 1-10 ms time window. Singlets were unlikely to come from rISC because of the large ΔE_{ST} value of **CzPhAP** in PPT (0.24 eV) and the low temperature. Instead, singlet generation was assigned to photo-induced charge generation and the subsequent charge recombination. The choice of this mechanism is based on the fact

that photo-induced charges have been demonstrated to play an important role in the **CzPhAP** doped films. Furthermore, people have done many studies on photo-induced charges at low temperature (< 200 K) (21). Within this mechanism, there is 25% chance for the singlet exciton formation, and so the S_1 emission can still be seen in the phosphorescence time window. Therefore, charge recombination is most likely to be responsible for the singlet generation here. This phenomenon has also been mentioned in Chapter **5** (Figure **5.7b**) that we found a singlet emission shoulder can be seen in the delayed emission spectrum of the 77 K 6wt% **CzPhAP**:PPT film. Therefore, through this spectrum analysis, it can be concluded that care needs to be taken when the onset of a 77 K delayed emission spectrum is used to determine the T_1 energy level of a TADF emitter. This is because singlet excitons can also be generated through charge recombination in the phosphorescence measurement time window, so that the consequent 'phosphorescence spectrum' may contain both S_1 and T_1 emission.

Furthermore, as shown in Figure **8.3b** (bottom), spectra **b4** and **b5** have similar shapes. Therefore, spectrum **b4** should also contain both S_1 and T_1 emission. So that the emission from the 300 K 0.5 wt% **CzPhAP**:PPT film in the 1-5 s time window has both the S_1 and T_1 contributions, as labelled in Figure **8.3a**. Hence, at 300 K, the OLPL decay measured 1 s after excitation can be considered as a combination of RTP and OLPL. The general PL decay expressions of RTP, OLPL and the combination of them are presented below:

$$I(t)_{PH} = I_p e^{-t/\tau_{PH}} \tag{8.1}$$

$$I(t)_{OLPL} = I_0 (1 + \alpha t)^m \tag{8.2}$$

$$I(t) = I(t)_{PH} + I(t)_{OLPL} \tag{8.3}$$

where:

I_p is the initial intensity of the phosphorescence

τ_{PH} is phosphorescence lifetime

I_0 is the initial intensity of the OLPL

α is a parameter

m is a parameter

To describe the OLPL decay rate, the empirical expression (Equation **8.2**) was used as people found it can best fit their experimental data (4) (as been discussed in Chapter **7**). In order to find

if Equation **8.3** can describe the TRPL decay of the 0.5 wt% **CzPhAP**:PPT film shown in Figure **8.3a**, a fitting was carried out, and the result is presented in Figure **8.4a**. The simulated curve of Equation **8.3** almost completely fits the experimental data (R^2 = 0.99995) with the fitting parameters of I_p = 19.02, τ_{PH} = 0.87 s, I_0 = 0.22, α = 0.19 and m = -1.01 for the PPT film. It needs to be highlighted that although the slope value, m, equals -1.01 in this more serious decay curve fit, this value is close enough to that obtained through a rough tail fit as shown in Figure **8.4a**. Therefore, both fitting methods should be acceptable. Although Equation **8.3** shows a good fitting with the experimental data, may not be valid to accurately describe the real decay because some discrepancy was found between the simulated results and the experimental data: in Figure **8.4a**, the dashed black and green curves are the simulated resulted obtained from Equations **8.1** and **8.2** with the fitted parameters above. If these two dashed lines can really describe the emission intensity of the RTP and OLPL, respectively, then it can be predicted from the Figure **8.4a** that, in the 1-3 s time window, the RTP intensity should be more than 10 times stronger than that of the OLPL. However, it can be seen from spectrum **b4** in Figure **8.3b** (bottom) that the intensity of the 584 nm shoulder is almost half of the intensity of the 608 nm peak, indicating the OLPL intensity is half of that of the RTP in the 1-3 s time window. This conflicts with the prediction from Equation **8.1** and **8.2**. Therefore, it indicates Equation **8.3** could describe the decay rate in longer time windows, but may not operate in short time windows.

Furthermore, combining the prompt fluorescence, TADF, RTP and OLPL, the whole TRPL decay process of a TADF-emitter-based OLPL material is expected to have the decay profile shown in Figure **8.5b**. There four light-emitting mechanisms should be dominant in different time windows. This figure is adapted from Lin *et al.*'s (8) work on their TADF-exciplex-based OLPL emitter. However, due to the large intensity difference between the prompt fluorescence and LPL (> 6 orders of magnitude), the experimental measurement of this whole decay curve is difficult.
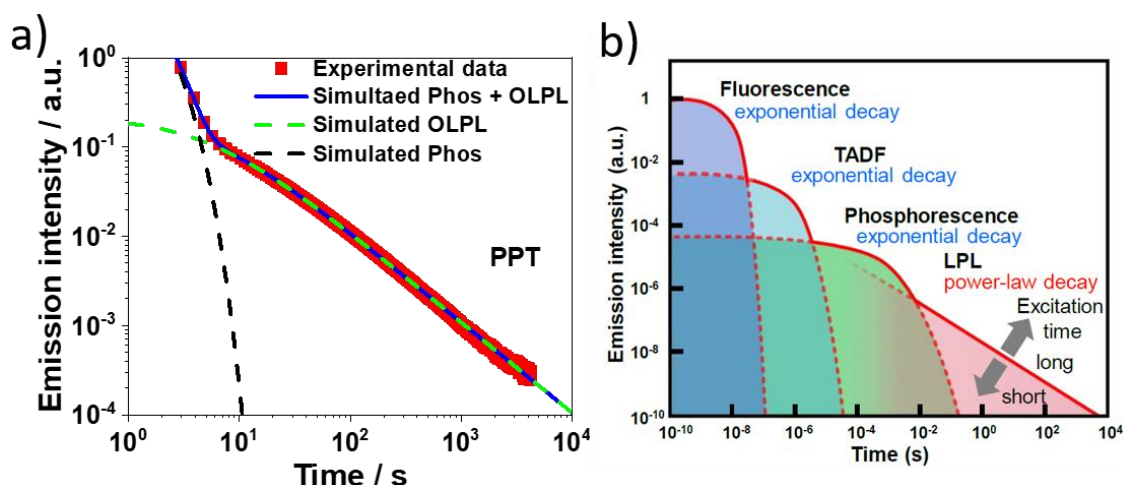
Figure 8.4. a) OLPL decay fitting of the 0.5 wt% **CzPhAP**:PPT film. b) Schematic diagram of the whole TRPL decay process of a TADF-emitter-based OLPL material. Figure b is adapted from (8).

Figure **8.5** shows that the spectral evolution behaviour of the 0.5 wt% **CzPhAP**:TPBi film is similar to that of the 0.5 wt% **CzPhAP**:PPT film. At the same time, Equation **8.3** can also very well fit the decay curve of the TPBi film (R^2 = 0.99999) with fitting parameters of I_p = 17.53, τ_{PH} = 0.42 s, I_0 = 0.15, α = 0.73 and m = -1.04.

Figure 8.5. a) TRPL spectra of the 0.5 wt% **CzPhAP**:TPBi film and **CzPhAP** in toluene (λ_{exc} = 343 nm). b) OLPL decay fitting of the 0.5 wt% **CzPhAP**:TPBi film.

However, the spectral evolution of the 0.5 wt% **CzPhAP**:PMMA film at 77 K is different from those of the PPT and TPBi films. As presented in Figure **8.6a** (bottom), spectrum **d5** overlap perfectly with spectrum **d6**, indicating spectrum **d5** is almost completely from T_1 without much contribution from S_1. This suggests the charge recombination rate in the PMMA film is so low at 77 K that only a small number of singlets are generated in the 1-10 ms time window, and so the phosphorescence dominates the shape of spectrum **d5**. Therefore, the onset of the 1-10 ms

spectrum measured from the 77 K PMMA film is perfectly fine for the T_1 energy level determination.

At 300 K, the spectral evolution behaviour of the PMMA film is similar with those observed in the PPT and TPBi films. As shown in Figure **8.6a** (right), the higher energy component of spectrum **d4** (on the left side of the dashed line) again can be treated as the superposition of spectra **d1** and **d2** which are both from S_1. Also, as shown in **8.6a** (bottom), the lower energy component of spectrum **d4** overlap perfectly with spectrum **d6**, indicating T_1 emission is a component of spectrum **d4**. As spectrum **d4** was measured in the 1-3 s time window, it suggests the emission in the first TRPL decay regime (1-7 s) contains both of S_1 and T_1 emission. However, at 300 K, the spectrum in the second decay regime (> 7 s) cannot be obtained. It is because the low emission intensity from the film after 7 s is out of the measurement range of the spectrometer. In addition, as shown in Figure **8.6b**, the decay curve of the PMMA film can also be fitted by the Equation **8.3** (R^2 = 0.99981) with fitting parameters of I_p = 7.36, τ_{PH} = 0.61 s, I_0 = 0.0055, α = 2.60 and m = -0.56. The spectral evolution behaviours of these three films are also in line with those of Lin *et al.*'s observation (8).
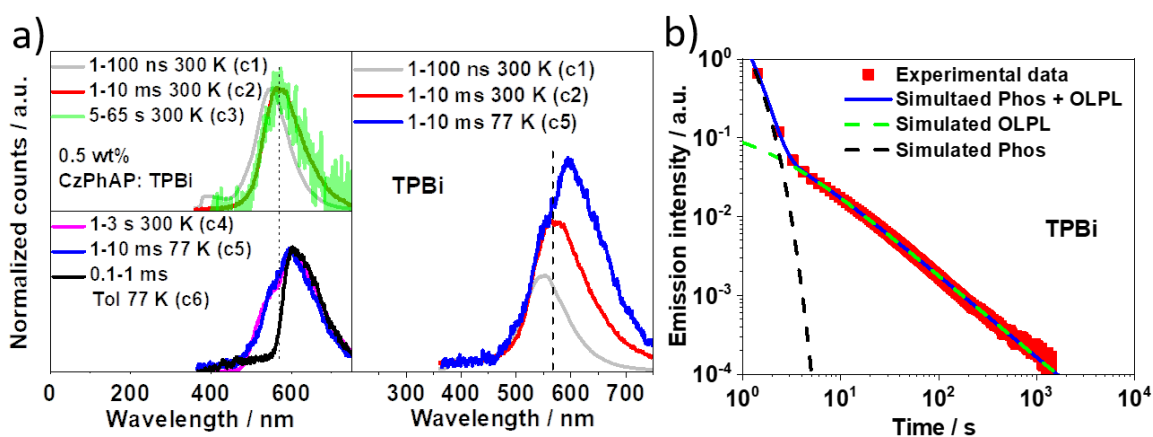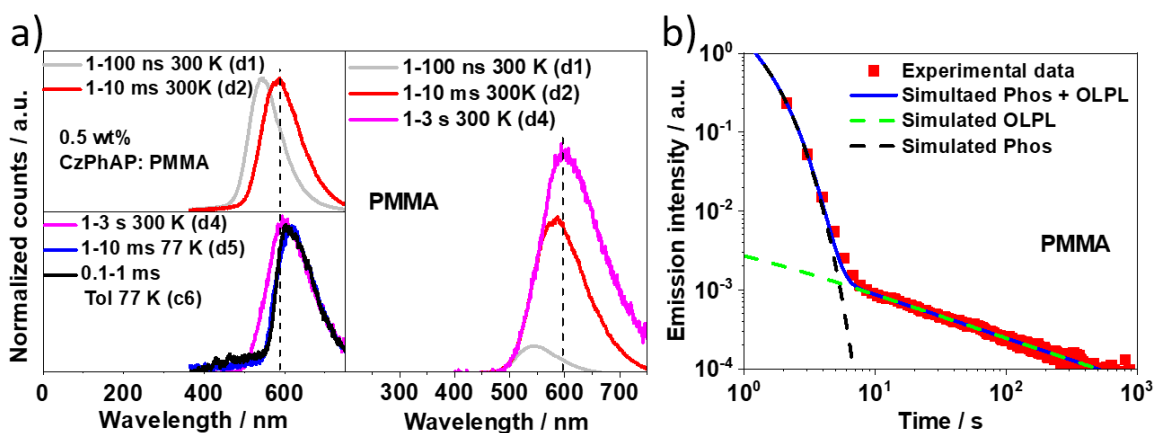

Figure 8.6. a) TRPL spectra of 0.5 wt% **CzPhAP**:PMMA films and **CzPhAP** in toluene (λ_{exc} = 343 nm). b) OLPL decay fitting of the 0.5 wt% **CzPhAP**:PMMA film

In summary, there are four main conclusions that can be drawn from the TRPL decay and the TRPL spectrum studies: (a). For all these three films at 300 K, the emission in the first decay regime (1-5 s for the PPT and TPBi films, 1-7 s for the PMMA film) have contributions from both the S_1 and T_1. (b). For the PPT and TPBi films at 300 K, the emission in the second decay regime (5 s after excitation) is mainly from the S_1. (c). For all these films at 300 K, the whole decay processed can be fitted by Equation **8.3** which is a combination of RTP and OLPL. However, the

validity of this equation requires further investigation. d) For the PPT and TPBi films at 77 K, the onset of the 1-10 ms spectra cannot be used for the T_1 energy level determination of **CzPhAP**, but that of the PMMA film can be used for this purpose. It is because, S_1 emission was found in the 77 K PPT and TPBi films measured in the 1-10 ms time window.

8.3.2 Charge separation mechanism

Although photo-induced charges were assigned to be the origin of the OLPL from **CzPhAP** doped films, the mechanism of this charge separation process and how it is related to the TADF properties are **CzPhAP** is still not entirely clear. This section presents all the experiments that have been done to investigate the photo-induced charge separation process in **CzPhAP** doped films. Among all the charge separation models (successive two-photon ionisation, CT exciton dissociations and SOP) that have been discussed in Chapter **7**, successive two-photon ionisation was found to be the most likely mechanism. In the successive two-photon ionisation process, emitters at the ground state are first populated to the excited states (S_1 and T_1). When the excitation source is sufficiently intense, these excited emitters can absorb another photon before they decay to the ground state, so that the emitters get ionized. Therefore, a longer lifetime of S_1 or T_1 will be ideal for the realization of successive two-photon ionisation. There are many experimental proofs that support the choice of this mechanism here: (a). **CzPhAP** has a large ΔE_{ST}, rigid molecular structure and the subsequent long-lived T_1 state, which is ideal for triplets to build up. To demonstrate the importance of the long-lived T_1, two other TADF emitters with much shorter T_1 lifetimes, namely 2,4,5,6-Tetra(9H-carbazol-9-yl)isophthalonitrile (4CzIPN) and 2CzIPN were tested. A fluorescent material, aluminium 8-hydroxyquinolinate (Alq$_3$), was also tested. Each of these materials was doped into PMMA, but OLPL was not observed. This is consistent with the successive two-photon ionisation mechanism for OLPL. (b). The OLPL from **CzPhAP** cannot be triggered when the excitation intensity is low which is not ideal for multi-photon absorption process. (c). Efficient T_1 absorption was observed in the 0.5 wt% **CzPhAP**:PMMA film, and the offset energy of the photoinduced absorption (PIA) spectrum matches well with that predicted by the energy difference between the LUMO of PMMA and the T_1 of **CzPhAP**. Proof (b) and (c) are discussed in detail as follow:

8.3.2.1 Excitation intensity dependency

The major difference between successive two-photon ionisation and other possible mechanisms is that successive two-photon ionisation is a two-photon process. Therefore, this process cannot be triggered with low excitation intensity. Consequently, the TRPL decay of the 0.5 wt% **CzPhAP**:PPT film was measured at 300 K under vacuum using different excitation intensities varying from 23.20 mW/cm^2 to 0.37 mW/cm^2. As shown in Figure **8.7**, with the excitation intensity less than 0.7 mW/cm^2, no OLPL but only RTP can be harvested, which is in line with the mechanism of successive two-photon ionisation.
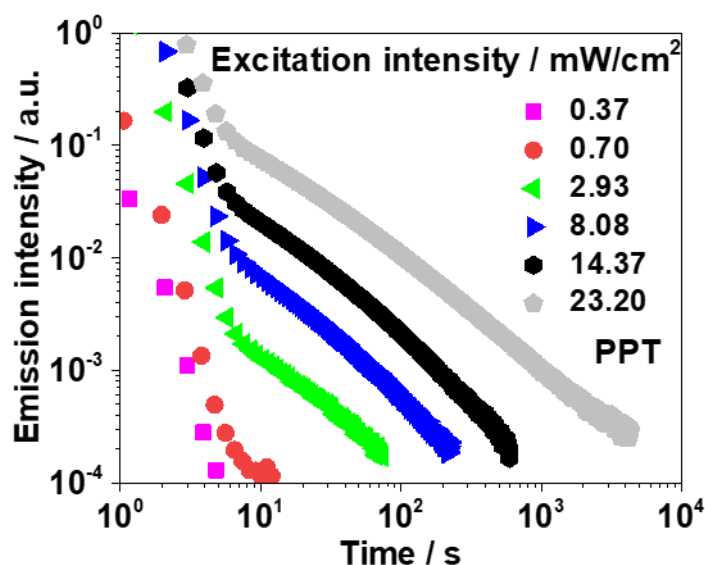
Figure 8.7. Excitation intensity dependent TRPL decay curves of the 0.5 wt% **CzPhAP**:PPT film measured under vacuum at room temperature. (λ_{ext} = 365 nm, excitation duration = 60 s)

8.3.2.2 Photoinduced absorption

Further evidence of successive two-photon ionisation is the strong T$_1$ absorption observed in the 0.5 wt% **CzPhAP**:PMMA film. A schematic energy diagram of the successive two-photon ionisation process of this film is presented in Figure **8.8b**. Assuming the ionized electrons are trapped in the LUMO of PMMA, the lowest energies required to ionize the **CzPhAP** molecules at S$_1$ and T$_1$ are 1.14 eV and 1.77 eV which correspond to wavelengths of 1088 nm and 701 nm, respectively. Therefore, in the PIA measurement of **CzPhAP**, spectrum offsets should be observed at 1088 nm and 701 nm.

Figure 8.8. a) HOMO and LUMO energy levels of **CzPhAP** and PMMA. b) Schematic diagram of the energy levels for the electron transitions between **CzPhAP** and PMMA.

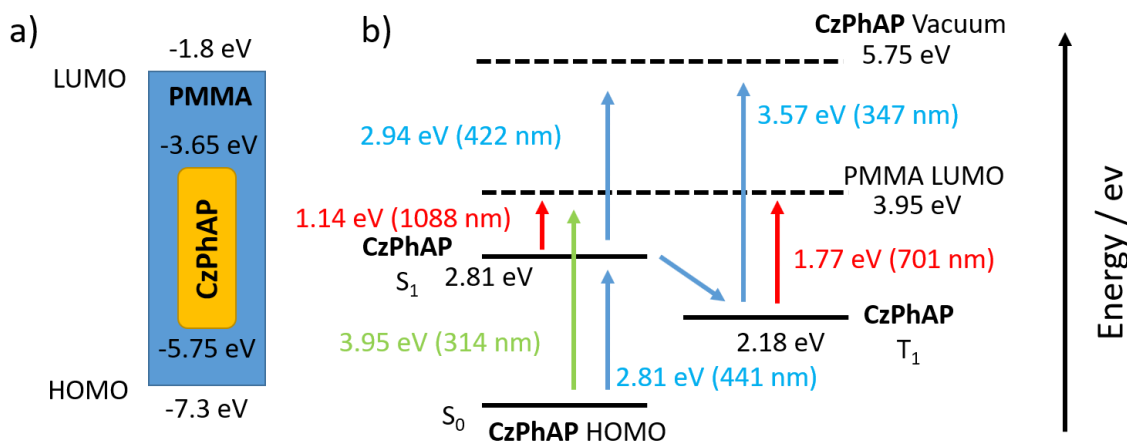To investigate this, a PIA measurement setup was built, and its schematic diagram can be seen in Figure **8.9**. In this setup, the pump beam was a 343 nm femtosecond laser running at a repetition rate of 100 kHz. The probe beam was a tungsten lamp. As the iCCD (the one described in Section **3.5.5**) is not sensitive for infrared detection, only the absorption spectrum offset at 701 nm was studied instead of the 1088 nm one. In this setup, the probe beam from the tungsten lamp was firstly attenuated by a neutral density filter to obtain a lower intensity than that of the pump beam. The beam was then focused on the sample film to have its light spot perfectly overlapped with that of the pump beam. After passing through the sample, the probe beam was then collected by two lenses and finally sent into a spectrograph combined with the iCCD. The intensities of the probe and the pump beams were 8.96 mW/cm^2 and 135.56 mW/cm^2, respectively. The sample was measured under vacuum with an active turbo pump which provided a pressure lower than 10^{-4} mbar. To avoid detecting the strong prompt emission from the sample, the iCCD only integrates the signal collected between 1 μs – 2 μs after photoexcitation. In this time window, most of singlets have been drained through the fluorescence channel, while the majority of triplets are still remained which can be used for the PIA study. Furthermore, each spectrum was accumulated from 200 frames of single measurements, which was used to average the noise from the iCCD.
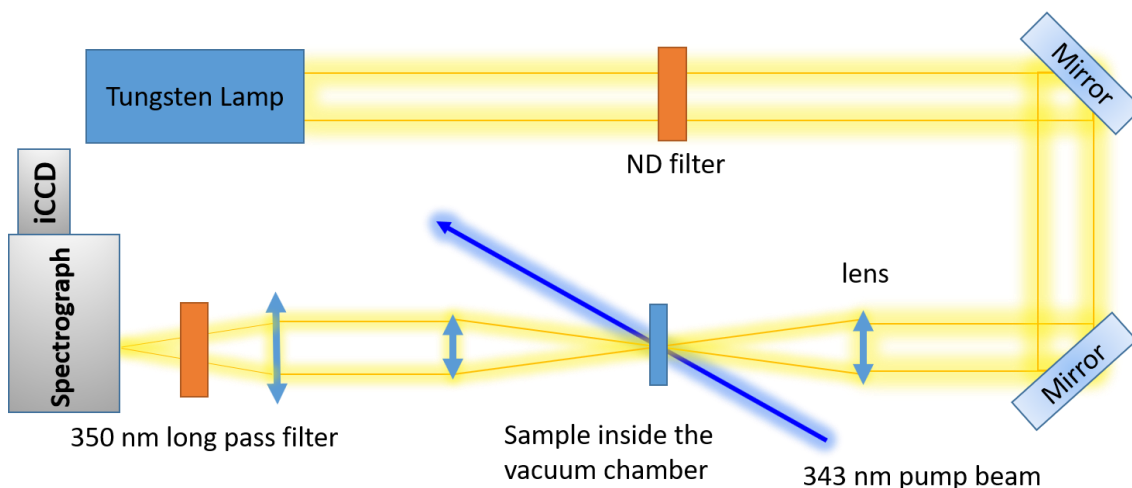
Figure 8.9. Schematic diagram of the photoinduced absorption measurement setup

The procedure of the PIA measurement for the 0.5 wt% **CzPhAP**:PMMA film was:

a. Block both the tungsten lamp and the laser. Measure the background signal from the iCCD (dark noise) and the environment. The measured spectrum is labelled as **BG1**.

b. To measure the spectrum of the probe beam alone, unblock the tungsten lamp and take a measurement. This spectrum is then corrected through subtracting the **BG1** from it. The consequent product is the probe beam spectrum after it passes through the sample, which is labelled as **T** and is shown in Figure **8.10a**.

c. To measure the signal created by all of the iCCD dark noise, the environmental light and the delayed emission from the sample, block the tungsten lamp and unblock the laser. The consequent measured spectrum is labelled as **BG2**.

d. Finally, to measure the probe beam spectrum when the pump beam is on, unblock both the tungsten lamp and the laser, and take a measurement. This spectrum is then corrected through subtracting the **BG2** from it. This spectrum is presented as the blue solid line in Figure **8.10a**. The difference between the blue and red spectra, labelled as **ΔT**, is the absorption caused by the **CzPhAP** molecules at excited states.

To work out the percentage of the light that is absorbed from the probe beam, **ΔT/T** was calculated and presented in Figure **7.10b**. The **ΔT/T** spectrum shows that the sample at the excited state has strong absorption around 600 nm. Furthermore, there is an absorption offset observed around 700 nm (as labelled by the dashed line) which is in the expected position for the transition between the T_1 of **CzPhAP** and the LUMO of PMMA. Therefore, these experimental results further support the choice of successive two-photon ionisation as the charge-separation mechanism in these OLPL materials.

Figure 8.10. a) The probe beam spectrum after passing through the 0.5 wt% **CzPhAP**:PMMA film (red) and probe beam spectrum when the pump beam is on. b) The spectrum of **ΔT/T**.

The schematic energy diagram of the 0.5 wt% **CzPhAP**:PPT film (Figure **8.11b**) shows that the energy gap between the T_1 of **CzPhAP** and the LUMO of PPT is 0.77 eV (1610 nm), indicating all the photons in the visible wavelength ranges have sufficient energy to ionize the T_1 of **CzPhAP**.
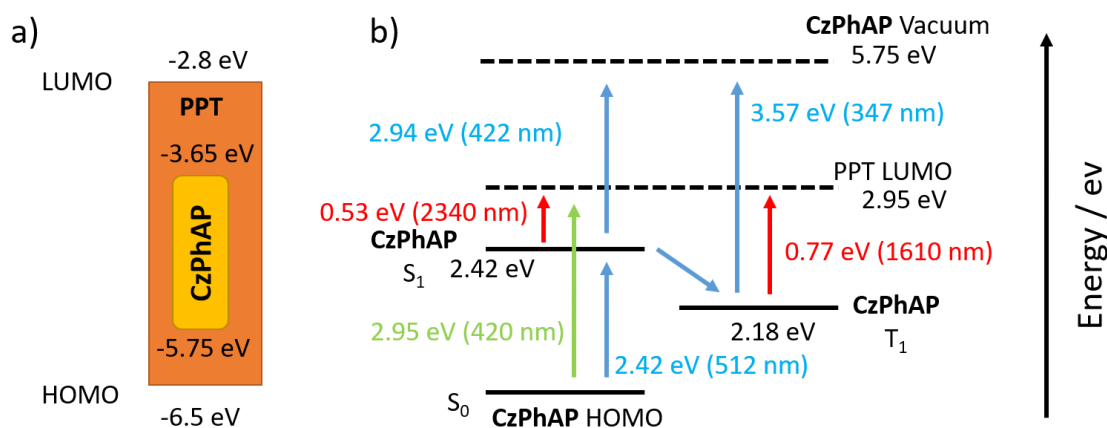
Figure 8.11. a) HOMO and LUMO energy levels of **CzPhAP** and PPT. b) Schematic diagram of the energy levels for the electron transition between **CzPhAP** and PPT.

Similar measurements were also carried out on the 0.5 wt% **CzPhAP**:PPT film and the results are presented in Figure 8.12. The **ΔT/T** spectrum of this film is generally broad, suggesting all the photons in this wavelength range presented in Figure **8.12b** can be absorbed.
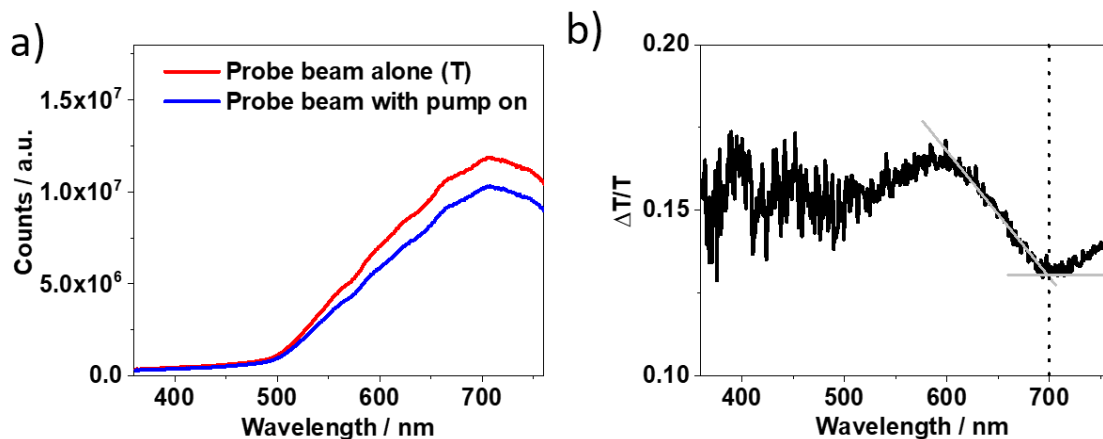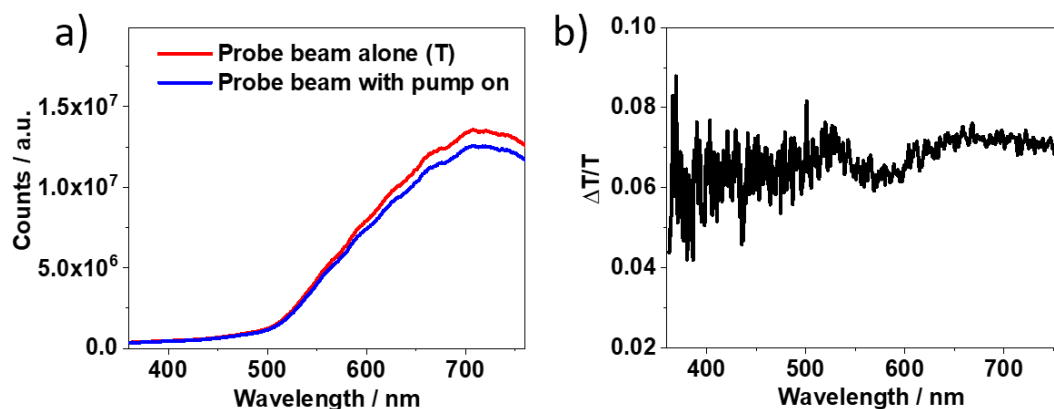
Figure 8.12. a) The probe beam spectrum after passing through the 0.5 wt% **CzPhAP**:PPT film (red) and probe beam spectrum when the pump beam is on. b) The spectrum of **ΔT/T**.

One more concern about the mechanism of the OLPL formation in this work is that a recent paper shows a carbazole isomer can also contribute to long-lived afterglow (22). This isomer can be widely found in most of the commercial carbazole, and **CzPhAP** may also contains it. However, after comparing that paper and the experiment here, it can be concluded that the carbazole isomer is unlikely to be the origin of OLPL in the **CzPhAP** doped films. The reasons follow:

(a). No OLPL can be harvested when **CzPhAP** is doped in ZEONEX. If emission is from the isomer on its own, then we should see long-lived emission.

(b). The spectra of the afterglow in the paper are completely different from those of the **CzPhAP** doped films. Figure **8.12a** shows the afterglow spectra (red curves with circles) of the carbazole isomer in the paper. Figure **8.12b** shows the afterglow spectra of the 0.5 wt% **CzPhAP**:PPT film.

(c). The PL decays of the carbazole isomer follow exponential decay law instead of power law. Therefore, the origin of its long-live emission should be different from that of **CzPhAP**.

Figure 8.13 a) TRPL spectra of the emission from the carbazole isomer. Figure adapted from (22). b) OLPL emission spectrum of the 0.5 wt% **CzPhAP**:PPT film 5-65 s after photoexcitation at 300 K.

(d). Most importantly, we also fabricated **2CzIPN** doped films in the same manner as the **CzPhAP** doped films, but we 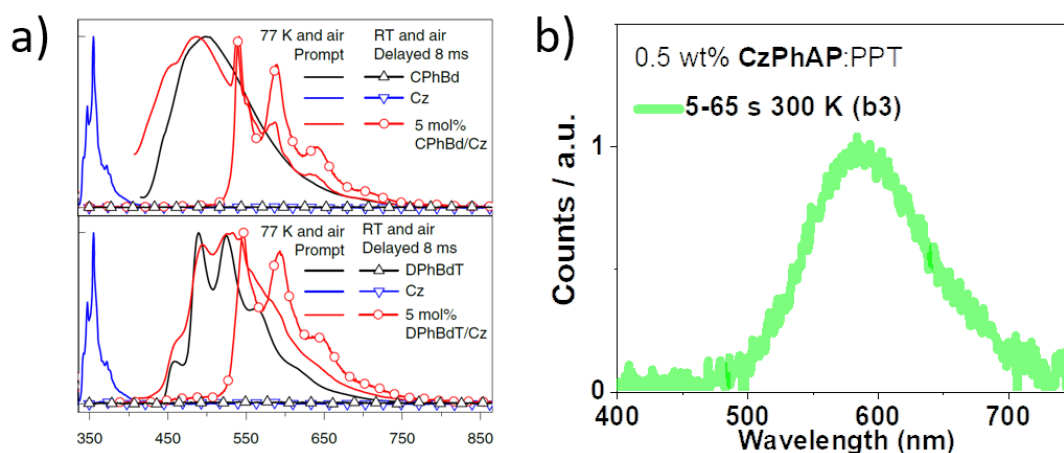did not observe OLPL from the **2CzIPN** doped films. As **2CzIPN** was also synthesized in this lab (Chapter **6**), and it contains two carbazoles, it should also show OLPL if the long-lived emission is from the carbazole isomer.

Therefore, the carbazole isomer should not be the origin of OLPL in this work.

8.4 Multi-colour emission from TADF-compound-based OLPL emitters

One of the biggest advantages of TADF-compound-based OLPL emitters over exciplex-based OLPL emitters is that TADF compounds have more flexible molecular designs and can more easily realize deep-blue emission. Also, the prerequisite of obtaining TADF-compound-based OLPL emitters seems only the choice of TADF materials with long-lived T_1. Therefore, the 1,3,4-oxadiazole-based emitters studied in Chapter **6** should be good candidates for deep-blue OLPL because all of them have long PL decay durations and some of them have deep-blue emission. Figure **8.11b** show the TRPL decay curves of a 0.5 wt% *i*-**2CzdOXDPh**:PMMA film and 10 wt% *i*-**2CzdOXD4CF₃Ph**:PPT/PMMA films measured under vacuum at room temperature. The excitation source was a 365 nm LED with excitation duration of 60 s and excitation intensity of 23.2 mW/cm^2. The fabrication methods of these films are all different because the author was still exploring the film fabrication technique when the TRPL decay measurement was carried out. The 10 wt% *i*-**2CzdOXD4CF₃Ph**:PPT film was prepared through melt-casting mixed host and guest powders on glass substrate at 250 °C, which is similar to the fabrication method of the 0.5wt% **CzPhAP**:PPT film; the 10 wt% *i*-**2CzdOXD4CF₃Ph**:PMMA film was fabricated through drop casting the solution of mixed host and guest in chloroform, with a consequent thermal annealing at 200 °C (similar with the sample as presented in Figure **9.3b**). The 0.5 wt% *i*-**2CzdOXD4CF₃Ph**:PMMA film was fabricated through synthesizing from the monomer of PMMA (sample picture is presented in Figure **9.7b2**). More details of the sample fabrication technique are discussed in Chapter **9**. It can be seen in Figure **8.11** that all the films have afterglow duration over 600 s. The power law decay rates also suggest OLPL is responsible for the long-lived emission. Although the OLPL emission spectra were not studied due to the lockdown of the lab, the photos of the 0.5 wt% *i*-**2CzdOXDPh**:PMMA film 3 s and 6 s after excitation are presented in Figure **8.11c**, which can provide a clue of its spectral evolution. As the emission colour of the top picture in Figure **8.11c** is greenish-blue, but the bottom one is deep-blue, it indicates the emission at 3 s may contain both the contributions from fluorescence (S_1) and phosphorescence (RTP), while the

emission at 6 s mainly contain S_1 emission. Therefore, its spectral evolution behaviour is probably similar to that of the 0.5 wt% **CzPhAP** doped film as shown in Figure **8.3**. Importantly, as has been studied in Chapter **6**, the S_1 emission from *i-***2CzdOXDPh** has CIE coordinate of (0.17, 0.17), it indicates the OLPL from this film is truly deep-blue. However, due to the time limitation, the OLPL properties of the 1,3,4-oxadiazole-based TADF emitters were not fully studied. Nevertheless, the results presented here are sufficient to demonstrate the wide application of this strategy to obtain multi-colour OLPL
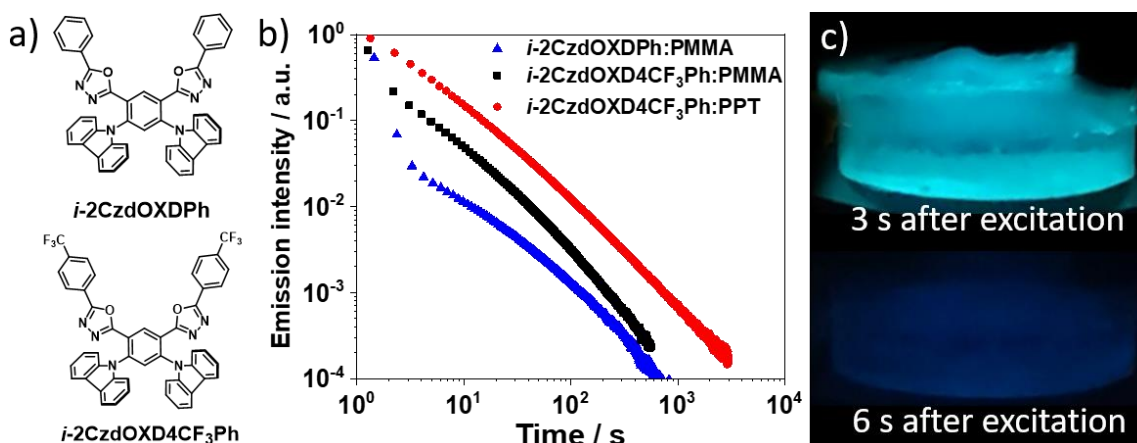
Figure 8.14 a) Molecular structure of *i-***2CzdOXDPh** and *i-***2CzdOXD4CF₃Ph**. b) TRPL decay curves of a 0.5 wt% *i-***2CzdOXDPh** film and 10 wt% *i-***2CzdOXD4CF₃Ph**:PPT/PMMA films under vacuum at room temperature. (λ_{ext} = 365 nm, excitation duration = 60 s, excitation intensity = 23.2 mW/cm^2). c) Photos of the 0.5 wt% *i-***2CzdOXDPh**:PMMA film 3 s and 6 s after excitation. (λ_{ext} = 365 nm)

8.5 Conclusion

This chapter demonstrates that an inefficient TADF compound, **CzPhAP**, can also realize room-temperature OLPL when it is doped into common host materials such as PPT, TPBi and PMMA. In addition, the OLPL from the doped PPT and TPBi films have afterglow durations of thousands of seconds, which is comparable with those of the state-of-art exciplex-based room-temperature OLPL emitters. Furthermore, the TRPL decay and the TRPL spectrum analysis of this OLPL material reveals that there are two decay regimes in the PL decay 1 s after photoexcitation. In the short-time regime (1-5 s for the PPT and TPBi films and 1-7 s for the PMMA film), the emission is from both S_1 and T_1 (from RTP). In the long-time regime (> 5 s for the PPT and TPBi films), the emission is mainly from S_1 generated by charge recombination. Therefore, the whole decay process can be treated as the superposition of RTP and OLPL, which can be expressed by Equation **8.3**. Although Equation **8.3** fits well with the experimental data in this study, its validity

requires further analysis. One more discovery of the TRPL spectrum analysis is that, in the 77 K PPT and TPBi films, singlets can be continuously generated through the recombination of photo-induced charges in the 1-10 ms time window after photoexcitation. Therefore, the onset of the spectrum taken in this condition (1-10 ms, 77 K) cannot necessarily be used for the T_1 energy level determination of a TADF emitter.

The mechanism of the photo-induced charge separation in this OLPL material was assigned to successive two-photon ionisation because of the following experimental evidence: a) The long-lived T_1 is crucial for OLPL formation: not only **CzPhAP**, but also other 1,3,4-oxadiazole-based TADF emitters which have long-lived T_1 show OLPL. In contrast, TADF molecules with short T_1 lifetimes do not show OLPL when doped in PMMA. b) OLPL cannot be observed when the excitation intensity is lower, suggesting the photo-induced charge separation is a multi-photon process. c) Strong T_1 absorption was observed in the 0.5 **wt% CzPhAP**:PMMA film, and the offset energy of the PIA spectrum matches well with that predicted by the energy difference between the LUMO of PMMA and the T_1 of **CzPhAP**. d) Using hosts with lower LUMO energy level leads to longer-lived OLPL.

Moreover, in this work, OLPL properties were found to depend on the host materials. For example, as shown in Figure **8.3a**, OLPL decay slopes in log-log plots vary from -0.55 to -1 in different hosts, which may be due to different electron traps in different hosts. Also, at 77 K, the charge recombination rate in the PMMA film is so low that S_1 emission can hardly be seen in the 1-10 ms time window, which is completely different from the PPT and TPBi cases. As host materials consist of 99.5 wt% of our films, which is responsible for trapping photo-induced charges, they certainly have a strong influence on the OLPL performance. Some of these effects have been studied by Ohkita *et al.* (23) through using different polymers as hosts in 1997, leading to different decay slopes and durations of OLPL. However, the main focus of my work is to demonstrate that putting a TADF emitter into readily available hosts (including PMMA) is another way to realize long-lived room-temperature OLPL. Therefore, more detailed host material dependency was not further studied.

At the end of this work, OLPL was found in the 1,3,4-oxadiazole-based TADF emitters doped films, demonstrating this strategy can be widely applied to other TADF emitters for room-temperature OLPL with different colours.

8.6 References

1. Matsuzawa T. A New Long Phosphorescent Phosphor with High Brightness, SrAl[sub 2]O[sub 4]:Eu[sup 2+],Dy[sup 3+]. J Electrochem Soc. 1996;143(8):2670. Available from: https://iopscience.iop.org/article/10.1149/1.1837067

2. An Z, Zheng C, Tao Y, Chen R, Shi H, Chen T, Wang Z, Li H, Deng R, Liu X, Huang W. Stabilizing triplet excited states for ultralong organic phosphorescence. Nat Mater. 2015;14(7):685–90. Available from: http://www.nature.com/articles/nmat4259

3. Debye P, Edwards JO. Long-Lifetime Phosphorescence and the Diffusion Process. J Chem Phys. 1952;20(2):236–9. Available from: http://aip.scitation.org/doi/10.1063/1.1700385

4. Ohkita H, Sakai W, Tsuchida A, Yamamoto M. Charge Recombination via Electron Tunneling after Two-Photon Ionization of Dopant Chromophore in Poly(butyl methacrylate) Film at 20 K. Bull Chem Soc Jpn. 1997;70(11):2665–70. Available from: http://www.journal.csj.jp/doi/10.1246/bcsj.70.2665

5. Ohkita H, Koizumi T, Sakai W, Osako T, Ohoka M, Yamamoto M. Stabilization of photoejected electrons produced through two-photon ionization of dopant chromophores in electron-accepting polyester film. Chem Phys Lett. 1997;276(5–6):297–302. Available from: https://linkinghub.elsevier.com/retrieve/pii/S0009261497008713

6. Kabe R, Adachi C. Organic long persistent luminescence. Nature. 2017;550(7676):384–7. Available from: http://www.nature.com/articles/nature24010

7. Jinnai K, Nishimura N, Kabe R, Adachi C. Fabrication-method Independence of Organic Long-persistent Luminescence Performance. Chem Lett. 2019;48(3):270–3. Available from: http://www.journal.csj.jp/doi/10.1246/cl.180949

8. Lin Z, Kabe R, Wang K, Adachi C. Influence of energy gap between charge-transfer and locally excited states on organic long persistence luminescence. Nat Commun. 2020;11(1):191. Available from: http://dx.doi.org/10.1038/s41467-019-14035-y

9. Nishimura N, Lin Z, Jinnai K, Kabe R, Adachi C. Many Exciplex Systems Exhibit Organic Long-Persistent Luminescence. Adv Funct Mater. 2020;2000795:2000795. Available from: https://onlinelibrary.wiley.com/doi/abs/10.1002/adfm.202000795

10.   Lin Z, Kabe R, Nishimura N, Jinnai K, Adachi C. Organic Long-Persistent Luminescence from a Flexible and Transparent Doped Polymer. Adv Mater. 2018;30(45):1803713. Available from: http://doi.wiley.com/10.1002/adma.201803713

11.   Yuan Y, Hu Y, Zhang Y-X, Lin J-D, Wang Y-K, Jiang Z-Q, Liao L-S, Lee S-T. Over 10% EQE Near-Infrared Electroluminescence Based on a Thermally Activated Delayed Fluorescence Emitter. Adv Funct Mater. 2017;27(26):1700986. Available from: http://doi.wiley.com/10.1002/adfm.201700986

12.   Hu Y, Yu Y, Yuan Y, Jiang Z, Liao L. Exciplex-Based Organic Light-Emitting Diodes with Near-Infrared Emission. Adv Opt Mater. 2020;8(7):1901917. Available from: https://onlinelibrary.wiley.com/doi/abs/10.1002/adom.201901917

13.   Xue J, Liang Q, Wang R, Hou J, Li W, Peng Q, Shuai Z, Qiao J. Highly Efficient Thermally Activated Delayed Fluorescence via J-Aggregates with Strong Intermolecular Charge Transfer. Adv Mater. 2019;31(28):1808242. Available from: https://pubs.acs.org/doi/10.1021/jacs.9b09323

14.   Congrave DG, Drummond BH, Conaghan PJ, Francis H, Jones STE, Grey CP, Greenham NC, Credgington D, Bronstein H. A Simple Molecular Design Strategy for Delayed Fluorescence toward 1000 nm. J Am Chem Soc. 2019;141(46):18390–4. Available from: https://pubs.acs.org/doi/10.1021/jacs.9b09323

15.   Hu Y, Yuan Y, Shi Y-L, Li D, Jiang Z-Q, Liao L-S. Efficient Near-Infrared Emission by Adjusting the Guest-Host Interactions in Thermally Activated Delayed Fluorescence Organic Light-Emitting Diodes. Adv Funct Mater. 2018;28(32):1802597. Available from: http://doi.wiley.com/10.1002/adfm.201802597

16.   Yamanaka T, Nakanotani H, Adachi C. Slow recombination of spontaneously dissociated organic fluorophore excitons. Nat Commun. 2019;10(1):5748. Available from: http://dx.doi.org/10.1038/s41467-019-13736-8

17.   Li W, Li Z, Si C, Wong MY, Jinnai K, Gupta AK, Kabe R, Adachi C, Huang W, Zysman-Colman E, Samuel IDW. Organic Long-Persistent Luminescence from a Thermally Activated Delayed Fluorescence Compound. Adv Mater. 2020;2003911:2003911. Available from: https://onlinelibrary.wiley.com/doi/10.1002/adma.202003911

18.   Kabe R, Notsuka N, Yoshida K, Adachi C. Afterglow Organic Light-Emitting Diode. Adv

Mater. 2016;28(4):655–60. Available from:
http://doi.wiley.com/10.1002/adma.201504321

19.   Shinde SM, Kalita G, Tanemura M. Fabrication of poly(methyl methacrylate)-MoS 2 /graphene heterostructure for memory device application. J Appl Phys. 2014;116(21):214306. Available from: http://aip.scitation.org/doi/10.1063/1.4903552

20.   Méhes G, Goushi K, Potscavage WJ, Adachi C. Influence of host matrix on thermally-activated delayed fluorescence: Effects on emission lifetime, photoluminescence quantum yield, and device performance. Org Electron. 2014;15(9):2027–37. Available from: https://linkinghub.elsevier.com/retrieve/pii/S1566119914002067

21.   Ohkita H, Sakai W, Tsuchida A, Yamamoto M. Charge Recombination Luminescence via the Photoionization of a Dopant Chromophore in Polymer Solids. Macromolecules. 1997;30(18):5376–83. Available from: https://pubs.acs.org/doi/10.1021/ma970585q

22.   Chen C, Chi Z, Chong KC, Batsanov AS, Yang Z, Mao Z, Yang Z, Liu B. Carbazole isomers induce ultralong organic phosphorescence. Nat Mater. 2020;4–10. Available from: http://dx.doi.org/10.1038/s41563-020-0797-2

23.   Ohkita H, Sakai W, Tsuchida A, Yamamoto M. Charge Recombination of Electron−Cation Pairs Formed in Polymer Solids at 20 K through Two-Photon Ionization. J Phys Chem B. 1997;101(49):10241–7. Available from: https://pubs.acs.org/doi/10.1021/jp971897y

Chapter 9 Organic Long-Persistent Luminescence Sample Fabrication using Poly(methyl Methacrylate) as the Host

In the last chapter, I demonstrated that using thermally activated delayed fluorescence (TADF) emitters enables poly(methyl methacrylate) (PMMA) to be used as the host for room-temperature organic long-persistent luminescence (OLPL) materials. Compared with 2,8-bis(diphenyl-phosphoryl)dibenzo[b,d]thiophene (PPT) which is widely used in exciplex-based room-temperature OLPL emitters, PMMA has the advantages of much cheaper price, mechanically stronger and it is also more easily moulded. However, the fabrication of OLPL samples using PMMA is more difficult than using small molecules, such as PPT or TPBi, as the hosts. This chapter discussed these difficulties and how they were overcome using the method I developed. Finally, clear and transparent PMMA-based OLPL samples are presented to fully demonstrate the advantage of this method.

The work in this chapter is not yet published but to be continued. It is a collaborative work between I. D. W. Samuel's group and E. Zysman-Colman's group at the University of St Andrews, and C. Adachi's group at Kyushu University. In this chapter, Z. Li and C. Si from Zysman-Colman's group performed the TADF emitter synthesis. K. Jinnai from Adachi's group taught me the method of melt-casting. A. K. Gupta from Samuel's group taught me the PMMA synthesis. C. Smith from Samuel's group modified the bottle jack and fabricated metal mould for the injection moulding of PMMA. I investigated and developed the methods for the OLPL sample fabrication, these methods include melt-casting, solution processing, PMMA polymerization and PMMA moulding.

9.1 Introduction

OLPL is a weak emission phenomenon which can only be observed in dark condition. Thicker and larger OLPL samples can increase the sample absorption and emission, which makes the afterglow more visible. However, as has been discussed in Chapter **7** and **8**, most of current OLPL emitters are using PPT as the hosts which consist of more than 99 mol% (or wt%) of the samples. PPT is not suitable for large-scale OLPL sample fabrication because: (a). the price of PPT is several hundred pounds per gram (1), and so a large-scale (> 10 g) PPT-based OLPL emitters is not easily affordable. (b). PPT contains phosphorus which is toxic, therefore, a wide application of it is not environmental friendly. (c). PPT films are not mechanically strong or flexible, which limits its applications.

Figure **9.1a** and **b** show the photos of OLPL samples using PPT and TPBi as the hosts, respectively. Cracks can be seen in these samples, which were caused by the cooling down process in the last step of the melt-casting sample fabrication (from 250 °C to room temperature). Also, both these films are brittle, and can be easily broken with a few Newtons of force.
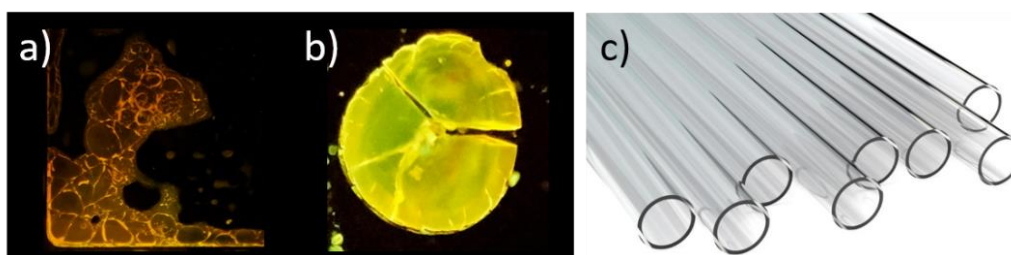
Figure 9.1. a, b) Photos of 0.5 wt% CzPhAP:PPT/TPBi films. c) Photo of PMMA tubes. Picture adapted from (2).

Compared with PPT and TPBi, PMMA is a more suitable host in many ways: (a). the unit price of PMMA (3) is less than 1% of that of PPT. Also, combining the mature PMMA manufacture industry, the final product of the large-scale OLPL layer should be costless; (b). PMMA only contains carbon, hydrogen and oxygen which are not toxic. Moreover, PMMA has a good compatibility with human tissue (4); (c). PMMA is easily moulded above its melting point but is mechanically strong at room temperature, which makes it flexible in sample designs but robust in applications.

9.2 Difficulties of the large-scale PMMA-based OLPL film fabrication

However, making a large-scale (> 1 g) PMMA-based OLPL sample is not easy, as the following requirements need to be fulfilled: (a). TADF emitters should be evenly dispersed inside the PMMA host. (b). The final PMMA products should be completely solvent free. (c). The final PMMA products should not contain bubbles, but should be clear and transparent, as shown in Figure **9.1c**. Among all these criteria, point (b) is especially important for OLPL formation. As has been discussed in Chapter **7** (Section **7.1.3**), OLPL originates from charge recombination. The charges stored in the host materials are extremely sensitive to liquids, so that any liquids (like water and organic solvents) inside the sample will quench the charges and consequently diminish OLPL.

Injection moulding is the most promising way to fulfil all these requirements, which is widely used in PMMA industry (5). However, labs in universities are normally not equipped with the corresponding machines. Therefore, other common methods, namely melt-casting and solution process, were first carried out to test the feasibility of large-scale PMMA sample fabrication. However, neither of these methods can meet all the criteria listed in the last paragraph, which is discussed below.

Melt-casting was first used for sample fabrication. Solid-state PMMA powders or plates were mixed up with TADF-emitter powders, and the mixtures were heated up above the melting point of PMMA (160 °C) on a hotplate, and so the liquid phase PMMA may dissolve the emitter powders. However, the hot PMMA powders and plates were only softened instead of being turned into liquid phase because PMMA is always highly viscous over all the temperature ranges even close to its decomposition temperature (240 °C). Therefore, the TADF emitter powders were unable to diffuse into the PMMA powders or plates but only stayed on their surface. Figure **9.2** shows an example of doping a TADF emitter, **CzPhAP**, into a PMMA plate using this fabrication method. The top right corner of this PMMA plate was heated up to 220 °C on a hotplate with the **CzPhAP** powders on its top corner. It can be seen that the **CzPhAP** powders only aggregated on the plate surface instead of evenly dispersing into the plate. Furthermore, it can be seen in Figure **9.2b** that different regions on the plate show different emission colours (green, yellow and orange) under UV excitation. It is because the doping concentration is out of control, and so the degree of emitter aggregation varied over the sample surface, giving different emission colours. Consequently, although this method has the advantage of making

the fabrication process completely solvent free, the emitter powder cannot be evenly doped in the PMMA matrices.
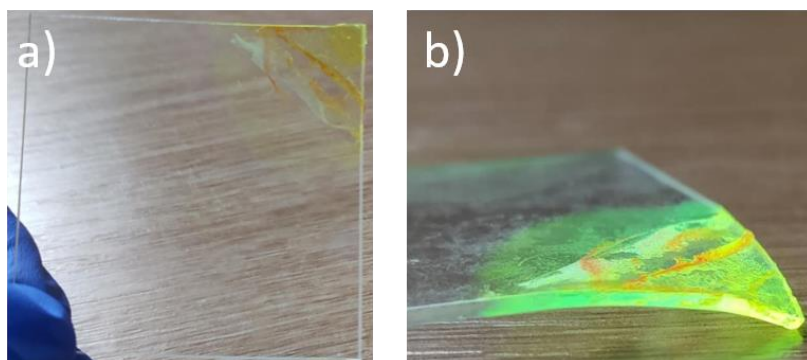

Figure 9.2. a) Front view of the product of doping **CzPhAP** powders into PMMA plate using melt-casting as the doping process. b) Side view of this sample under UV irradiation (λ_{ext} = 365 nm).

In comparison, solution processing can mix up PMMA with the emitter evenly, therefore, was also tried out. In the fabrication process, the PMMA (180 mg/ml) and the emitter powders were first mixed in chloroform according to the required doping concentrations. The mixed solutions were either drop-casted on a glass substrate to form a dried film or left in a glass vial to form a dried solid block after the solvent had evaporated. Spin-coating was not used because the maximum thickness of a spin-coated film is usually a few microns, which is not the 'large-scale' envisaged. The main challenge of fabricating solution processed PMMA samples is the difficulty of removing the organic solvents from the thick samples even when the low boiling-point solvent, chloroform, is used. It is because, in the solvent evaporation process, the surface of PMMA will first be dried and form a rigid surface. This solid surface stops the further evaporation of the solvents inside the PMMA sample, which leads to photo-induced charge being quenched and stops OLPL.

To remove all the remaining solvents, the samples were heated on a hotplate at 200 °C for 3 min inside the glovebox. This temperature is above the melting point of PMMA and the boiling point of the solvent, which disables PMMA's confinement of the solvent molecules, and enables an effective solvent evaporation. The heated samples started to show OLPL under vacuum, demonstrating the importance of a complete solvent removal. However, this method is not suitable for large-scale PMMA sample fabrication. Figure **9.3** shows two solution-processed 0.5 wt% **CzPhAP**:PMMA films after thermal annealing with different thickness. The sample thicknesses were controlled by the volume of the solution drop-casted onto the glass substrates. As shown in Figure **9.3a**, the thin film (a few hundred-of-micron thick) is generally clear and

transparent, but with small bubbles on the edge of the film as the edge is much thicker (~ 1 mm). These bubbles were the voids left by the evaporated solvents when the film is thick, and the film is thicker around the edge of this sample. As Figure **9.3b** shows, the effect of the bubbles is worse in the thicker sample (> 2 mm), which is because more solvent was trapped in it, and so more bubbles were created when the sample was heated up. The colours of the two samples are also different under ambient light: the thin sample (Figure **9.3a**) is yellowish orange but the thick sample (Figure **9.3a**) looks white. The white colour is the result of scattering of ambient light caused by its porous morphology. This does not only affect the attractiveness of the sample, but also decreases the light absorption in the excitation process (because of the light-scattering) and block the emission in the OLPL process (because of the low transparency). Most importantly, it is unlikely to obtain a clear centimetre-scale thick sample by drop-casting.
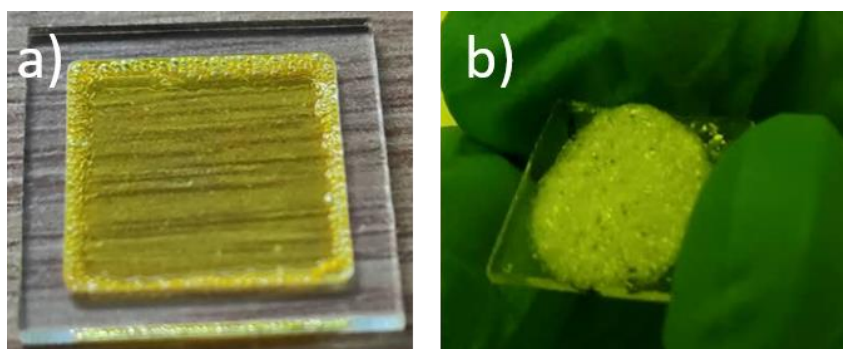

Figure 9.3. a, b) Drop-casted 0.5 wt% **CzPhAP**:PMMA films after being heated to 200 °C inside a glovebox. The volumes of the solution used for these two films are 80 µL and 1500 µL, respectively. (Solution concentration: 180 mg/ml, solvent: chloroform).

Solvent removal from a solution-processed PMMA solid block which is formed inside a glass vial was more difficult as there was more solvent trapped in block samples: a 0.5 wt% **CzPhAP**:PMMA block sample (2 ml) formed inside a glass vial was found to be soft inside but rigid on the surface even after the glass vial had been kept in the glovebox for a week. To remove these solvents, the glass vial was connected to a vacuum pump and the vial was immersed in a 200 °C oil bath. More bubbles were created in the solvent removal process and the final product looked like solid foams instead a transparent PMMA block. The consequent sample morphology was more porous than that shown in Figure **9.3b**. Therefore, although the solution-processed samples have the advantage of a good host-guest mixing, the introduction of solvents creates the trouble of solvent removal and the consequent bubbles. The bubbles not only affect the appearance of the consequent OLPL products, but also decrease the light absorption and emission, and so

decrease the performance of OLPL. Therefore, a different approach to PMMA sample fabrication for large-scale OLPL sample fabrication is needed.

9.3 Fabrication method towards large-scale PMMA-based OLPL samples

In this work, to overcome the shortcomings of melt-casting and solution processing, a new fabrication method was proposed to realize both even emitter dispersion and solvent free final products. Furthermore, a costless moulding setup was invented to shape the PMMA product and remove all the bubbles at the same time. This method opens the door to obtain clear, transparent and multicolour PMMA-based large-scale OLPL samples.

This sample fabrication process starts from dissolving TADF emitters into the monomer of PMMA, namely methyl methacrylate (MMA), which is in liquid phase at room temperature. The MMA should be dehydrated using molecular sieve before being used to dissolve the TADF emitters. After the emitters are completely dissolved in MMA in a glass vial, the MMA solution was polymerized in nitrogen atmosphere with the assistant of a catalyst (0.1 wt%), 2,2'-azobis(2-methylpropionitrile) (AIBN). The reaction temperature was kept at 60 °C in an oil bath heated up by a hotplate. After 10 hours' polymerization, although the sample became rigid, there was still around 15 wt% of the MMA not reacted. This is because the viscosity of the solution gradually increases over the polymerization process. Eventually, the viscosity reaches a point that the catalyst radicals stop diffusing, which also stops further polymerization. This viscosity related polymerization rate is called Trommsdorff effect (6). Therefore, the remaining MMA was still in liquid phase which can quench the photo-induced charges. To remove the remaining MMA, the reaction temperature was set to be 100 °C for 1 hour and then to the glass transition temperature (160 °C) of PMMA for another 2 hours to allow the diffusion of catalyst radicals so as to complete the polymerization, which is called post-curing process. Finally, the samples were cooled down to room temperature, and the PMMA products can be seen in Figure **9.4**. Figures **9.4a** and **b** show a 0.05 wt% *i-***CzdOXD4F3Ph**:PMMA block without and with UV excitation. Figure **9.4c** shows 0.05 wt% *i-***CzdOXD4F3Ph/CzPhAP**:PMMA block with UV excitation. These two samples are clear, rigid and transparent, but with some large bubbles inside. The large bubbles were created because the temperature was not properly control in the polymerization process: the MMA polymerization is an exothermic reaction, and so a combination of high initial reaction temperature and insufficient heat diffusion may speed up the polymerization process and heat up the solution above the boiling point of MAA (101 °C). Therefore, setting the initial reaction

temperature to 60 °C or lower with a proper oil bath is important to avoid these bubbles. The post-curing process does not create more bubbles even the temperature is as high as 160 °C because most of MMA has already been converted into PMMA after 10 hours' polymerization.
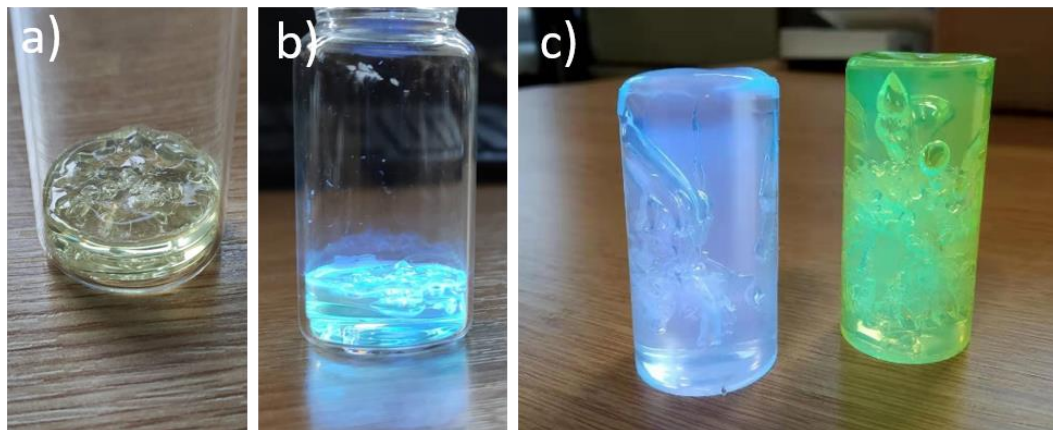

Figure 9.4. a, b) 0.05 wt% *i*-**CzdOXD4F₃Ph**:PMMA sample after polymerization with and without UV excitation. c) 0.05 wt% *i*-**CzdOXD4F₃Ph/CzPhAP**:PMMA samples taken out from glass vials after polymerization with UV excitation.

Ideally, after post-curing, there should be no MMA or moisture remaining. However, it was found that OLPL cannot be observed in the samples presented in Figure **9.4**, but TADF can be seen after photoexcitation. It indicates that photo-induced charges are more sensitive to environments than triplets because triplets can survive inside these samples, but the photo-induced charges cannot. In addition, the survival of triplets implies the absence of oxygen in these samples. Therefore, the photo-induced charges were not quenched by oxygen here. Further experimental results suggested that some other liquids remained in the PMMA sample were responsible for the OLPL quenching. To completely remove all these liquids, the PMMA samples were put under vacuum (< 10^{-1} mbar) at 200 °C for 1 hours. The high temperature can soften the PMMA and allows the liquids to be evaporated. Also, the vacuum helps to extract the vapours from the PMMA. After the solvent removal process, as shown in Figure **9.5**, the final samples become porous, which aligns with the conclusion that are some liquid remained after the post-curing process because the bubbles were created by the evaporated liquids. Nevertheless, these bubbles may come from the decomposition of the PMMA due to the high temperature. However, this factor should not be dominant because the solvent removal temperature (200 °C) is still well below the decomposition temperature (240 °C) of PMMA. Importantly, the PMMA samples after this solvent removal started to show OLPL under vacuum.
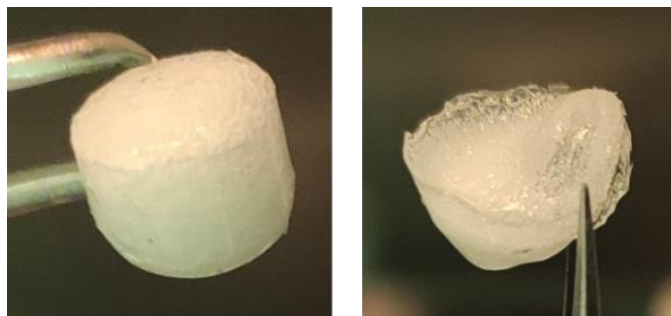
Figure 9.5. 0.5 wt% **i-CzdOXDPh**:PMMA and **i-CzdOXD4F₃Ph**:PMMA samples after the solvent removal process

The origin and the composition of the remaining liquids in the PMMA samples after the post-curing is not clear. This liquid was not expected because the purity of the initial MMA was as high as 99 %. This MMA was also dehydrated before the polymerization. In addition, the polymerization process was carried out in nitrogen environment which should not introduce any liquids. Therefore, a possible explanation of its origin could be the existence of unreacted MMA even though the post-curing temperature was as high as 160 °C. This liquid could also be water even though the MMA was dehydrated. In addition, the 1 % impurity from the initial MMA may remain unreacted in the polymerization process, and could quenched the final OLPL. Understanding the origin of this liquid is beneficial to the large-scale PMMA-based OLPL sample fabrication because the solvent removal process makes the samples porous, which affects the optical properties and the attractiveness of the final PMMA products.

The bubble removal of PMMA was done using injection moulding which requires a combination of high temperature (> 205 °C), high pressure (> 700 bar) and an inert gas environment for water and oxygen prevention (7). Among all these requirements, the high pressure is especially important because it is used to squeeze all the bubbles out when the sample is soft. To obtain these conditions in lab, a home-made thermal forming equipment was created as shown in Figure **9.6**. This setup is composed of a cylinder metal sheath as a mould and a modified hydraulic bottle jack to provide high pressure. As shown in Figure **9.6a**, the metal sheath is made of stainless steel to tolerate the high pressure, and it is responsible for the heat conduction to soften the whole porous PMMA samples. As shown in Figure **9.6b**, this metal mould has three components, namely a solid rod, a hollow cylinder and a base. Porous PMMA samples are loaded into the hollow cylinder sandwiched by the rod and the base. As the diameter of the metal rod is 13 mm, creating a 700-bar pressure from the rod requires around 9000-Newtons of force from the bottle jack. As shown in Figure **9.6c**, a commercial hydraulic bottle jack (8) used here was

modified by adding a homemade metal frame which is sufficiently strong to tolerate the force from the bottle jack.

Figure 9.6. a, b) Photo of the stainless-steel metal mould. c) Photo of the PMMA heat moulding process using the bottle jack and the metal mould.

The procedures of the bubble removal process follow: (1). Load the porous PMMA samples into the metal mould. (2). Heat the metal mould up to 230 °C on a hotplate inside the glovebox for 15 min to soften the whole PMMA sample. (3). Transfer the hot metal mould to the top of the bottle jack (Figure **9.6c**) and increase the pressure to 1000 bar for 30 seconds, which leaves sufficient time for the moulding and distortion of samples. (4). Release the pressure of the bottle jack and take the PMMA sample out after the cooling down process of the metal mould.

Figures **9.7a1** and **b1** show the 0.5 wt% **CzPhAP**:PMMA and *i-***CzdOXDPh**:PMMA samples before the bubble removal process, while Figures **9.7a2** and **b2** show these two samples after the bubble removal process. It can be seen that the initial porous samples were completely changed into compact and bubble free disks, proving this method is an effective way for bubble removal. Importantly, all the afterglow properties, namely TADF, RTP and OLPL, were well maintained in these rigid disks: Figures **8.3a** and **8.14b** in Chapter **8** show the TRPL decay curves of the disks shown in Figures **9.7a2** and **b2**. Both disks have OLPL lasting for hundreds of seconds, demonstrating the bubble removal process did not quench the OLPL.

Figures **9.7a3** and **b3** present these disks under UV excitation inside the glovebox, while Figures **9.7a4** and **b4** show these disks under vacuum with and without UV excitation. Although the samples in Figure **9.7a3** and Figure **9.7a4** are identical, the emission in Figure **9.7a3** look more greenish. This was caused by the colour correction of the camera instead of different sample emission properties. Therefore, all these experimental results demonstrate that this new PMMA fabrication method can meet all the criteria proposed in the first paragraph of Section **9.3**, which enables large-scale PMMA-based OLPL sample fabrication.
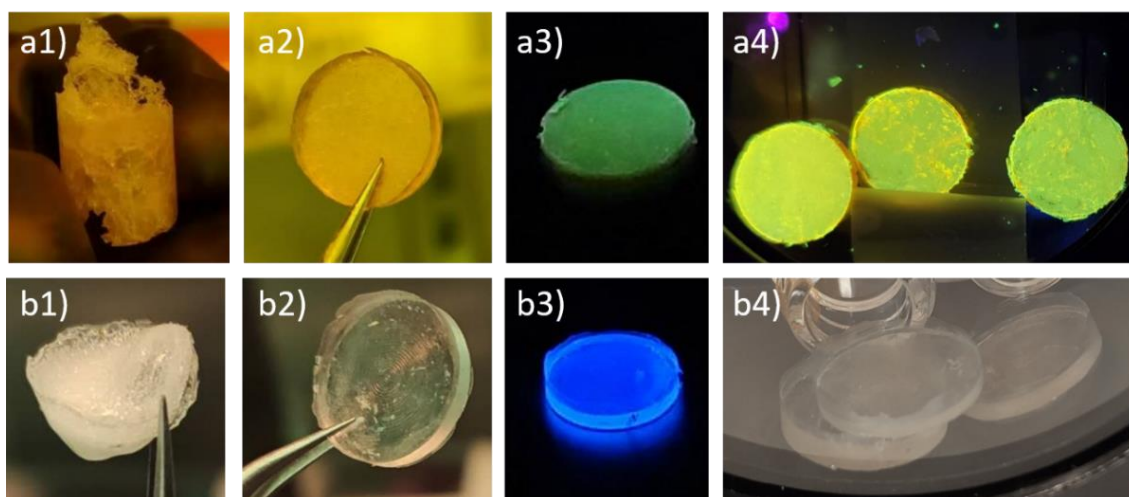

Figure 9.7. a1, b1) PMMA-based OLPL samples after post-curing; a2, b2) after moulding; a3, b3) emission under UV excitation in the glovebox. a4, b4) Photos of the moulded samples under vacuum, with and without the UV excitation. Samples in Figure a are 0.5 wt% **CzPhAP**:PMMA; in Figure b are 0.5 wt% ***i-CzdOXDPh***:PMMA. (λ_{ext} = 365 nm)

In summary, the protocol of making large-scale PMMP-based OLPL sample follows:

a.   Dissolve the emitter in anhydrous MMA in a glass vial with around 0.1 wt% AIBN dissolved as the catalyst.

b.   Purge the inner side of the glass vial with nitrogen for 1 min. Connect the glass vials to the nitrogen source with a rubber hose.

c.   Keep the nitrogen source on. Put the glass vial in the oil batch and set the temperature to 60 °C. Leave the reaction for 10 hours.

d.   After 10 hours, increase the reaction temperature to 100 °C for 1 hour, and then increase the reaction temperature to 160 °C for another 2 hours for post-curing.

e.   To remove the remaining liquids, connect the vial to a vacuum pump to create a pressure of < 10^{-1} bar. Set the temperature to 200 $^{\circ}$C for 2 hours. In this process, many bubbles will be generated and the PMMA sample becomes porous.

g.   Wait until the sample cool down to room temperature. Break the glass vial and take the PMMA sample out.

h.   Fill the PMMA sample into the metal mould. Heat the metal mould up to 200 $^{\circ}$C on a hot plate inside a glove box for 15 min to soften the sample. Quickly transfer the metal mould to the hydraulic bottle jack and increase the pressure to 1000 bar for 30 s.

h.   Release the pressure, remove the metal mould and wait for it to cool down.

Take the PMMA sample out.

9.4 Conclusion

This chapter presents the difficulties of large-scale PMMA-based OLPL sample fabrication, and how the new method proposed in this work overcame these difficulties. Compared with small molecule hosts (such as PPT or TPBi), PMMA is one of the most suitable materials for large-scale OLPL products because of its much lower price and the much higher rigidity. However, the fabrication methods such as melt casting and solution processing fail to meet the requirements of making ideal OLPL samples. Melt-casting has the advantage of being solvent free. However, hot PMMA does not melt, and so emitters do not dissolve in the PMMA host, which causes the problem of uneven emitter dispersion in the host. In comparison, solution processing has the advantage of even emitter dispersions. However, the introduction of the large amount of organic solvents creates the difficulty of a complete solvent removal, which leads to the quenching of OLPL. Solvent removal techniques such as thermal annealing on hotplates are only suitable for thin (hundreds of microns) PMMA doped films, but it will create many bubbles in thick films (> 1 mm). Solvent removal is more difficult for solid block samples (size > 1 cm × 1 cm × 1 cm) formed in glass vials, which have more organic solvents confined in the PMMA.

In comparison, the new fabrication method proposed in this work starts from dissolving the TADF emitters in the monomer of PMMA, which can disperse the emitters evenly in the host without the introduction of other organic solvents. The consequent polymerization process can theoretically convert all the MMA into solid, and so all the liquids can be assumed to change into

the solid phase or evaporated. Although it was found that a small amount of unknown solvents still remaining in PMMA after the polymerization, they were further removed under vacuum at 200 °C. The bubbles generated in this solvent removal process can be eliminated under high pressure at high temperature using the homemade thermal forming equipment. The final PMMA products after these processes become transparent and bubble free, with all the afterglow properties maintained. Therefore, this new fabrication method completely fulfils all the requirements toward making ideal large-scale PMMA-based OLPL samples.

Moreover, this fabrication method is easily scalable: using more emitters, MMA and a more powerful hydraulic press could enable a much larger sample fabrication. Therefore, PMMA-based OLPL toys, daily products or decorations are possible to be obtained. Furthermore, it has been observed that OLPL still operates in inert gas environments, which suggests a proper encapsulation could enable the application of these large-scale OLPL products in ambient environments. Therefore, the introduction of TADF-compound-based OLPL materials and large-scale PMMA fabrication method tremendously expand the applications of OLPL emitters.

9.5 References

1.   Merck. PPT [Internet]. 2020. Available from: https://www.sigmaaldrich.com/catalog/substance/ppt58460101984299911?lang=en&region=GB

2.   RIMETPLAST. PMMA [Internet]. 2020. Available from: https://www.rimetplast.it/en/products/methacrylate-pmma/

3.   Merck. PMMA [Internet]. 2020. Available from: https://www.sigmaaldrich.com/catalog/substance/polymethylmethacrylate12345901114711?lang=en&region=GB

4.   Frazer RQ, Byron RT, Osborne PB, West KP. PMMA: An Essential Material in Medicine and Dentistry. J Long Term Eff Med Implants. 2005;15(6):629–39. Available from: http://www.dl.begellhouse.com/journals/1bef42082d7a0fdf,56437700108bb47c,30f08b9f6c2404c1.html

5.   Anhui jingwei medical material technology co. LTD. Plastic people must understand the PMMA injection molding process knowledge [Internet]. 2020. Available from:

http://www.jwmedpolymer.com/index.php?c=content&a=show&id=32&siteid=2

6.   Ebewele RO. Polymer Science and Technology. CRC Press; 2000.

7.   Fast heat. PMMA [Internet]. 2020. Available from:
        http://www.fastheatuk.com/mdb/pmma.html

8.   Amazon. Hydraulic Bottle Jack 6 Tonne [Internet]. 2020. Available from:
        https://www.amazon.co.uk/Silverline-457050-Hydraulic-Bottle-
        Jacks/dp/B0015NULPU/ref=sr_1_9?dchild=1&keywords=bottle+jack&qid=1591376247
        &sr=8-9

Chapter 10 Concluding remarks

10.1   Conclusion

This thesis briefly reviews the recent developments and the mechanisms of thermally activated delayed fluorescence (TADF) and organic long-persistent luminescence (OLPL), and their promising applications to indoor lighting. In the experimental parts, two groups of TADF emitters were studied regarding their photophysical properties and EL performance in OLEDs. Furthermore, the author innovatively applied these new TADF emitters to OLPL and studied the light emitting properties and relevant mechanisms of this kind of new OLPL systems.

Within the new TADF emitter studies, the orange and yellow emitters (**DMAcPhAP** and **CzPhAP**) were designed using acenaphtho[1,2-b]pyrazine-8,9-dicarbonitrile (**AP**) as their acceptors and the OLEDs based on these two emitters have the EQE_{max} of 13.0% and 11.1%, respectively, at a luminance of 1 cd/m^2. However, the EQEs dropped to 4.67% and 2.80% at 100 cd/m^2, demonstrating that these two emitters are inefficient when working at practical brightness due to their large ΔE_{ST}s (0.34 eV and 0.24 eV), long triplet lifetimes and the consequent annihilation mechanisms (e.g. TTA, STA).

Similarly, in the case of new blue emitters, the EQE values of *i*-**2CzOXDMe,** *i*-**2CzOXDPh,** *i*-**2CzOXD4CF₃Ph** and *i*-**2CzdOXD4MeOPh** based OLEDs dropped from 11.8%, 7.0%, 12.3% and 4.8% at around 1 cd/m^2 to 1.3%, 1.3%, 2.6% and 1.3% at 100 cd/m^2, respectively. Although the use of 1,3,4-oxadiazole derivatives as the acceptors in these new TADF emitters successfully blue-shifted the emission colour from the CIE coordinates of (0.18, 0.30) to (0.17, 0.17) compared with their reference emitter, **2CzIPN**, the low EQEs at 100 cd/m^2 still make these new emitters unsuitable for practical OLEDs.

Therefore, all the new TADF emitters studied in this thesis suffer from significant efficiency roll-off at high luminance due to their large ΔE_{ST}s. Consequently, a future improvement in TADF emitter designs will take the alignment of S$_1$ and T$_1$ into account to boost k_{rISC} and reduce the efficiency roll-off.

Although these emitters have poor performance in OLEDs, they are good candidates for OLPL applications. Their long-lived triplets contribute to the photo-induced charge generation through the mechanism of successive two-photon ionisation. The subsequent slow charge recombination process enables OLPL lasting for thousands of seconds which is comparable with the emission durations of state-of-the-art room-temperature OLPL materials based on exciplex

emitters (1). Importantly, as exciplex formation is not required in the new OLPL system discovered in this thesis, it enables a wide range of host materials, even PMMA, to be used as the host. Compared with the most frequently used small-molecule host, PPT, for room-temperature OLPL emitters (2–5), PMMA possesses many advantages such as much cheaper price (less than 1% of the cost compared with PPT) and much higher rigidity, which enables wider practical applications. In addition, the flexible TADF emitter designs make multiple-colour OLPL emitters easily obtained, such as the deep-blue OLPL materials presented in Section **8.4**, and so this strategy is likely to work for other TADF compounds emitting at different wavelengths.

To take full advantage of the low expense of PMMA, fabrication methods for large-scale PMMA-based OLPL sample were explored. As has been discussed in Chapter **9**, the fabrication methods like melt-casting and drop-casting are not suitable for this purpose because the resulting samples have the problems of uneven emitter doping concentrations, remaining solvents and bubbles in the samples, which lowers the performance or quench OLPL. Therefore, to fabricate high quality large-scale OLPL samples, the author developed a new fabrication method which started from dissolving TADF compounds in the monomer of PMMA, followed by the polymerization of the mixture. However, unexpected remaining solvents were found after the polymerization, which quenched the OLPL. Consequently, these solvents were removed under vacuum at high temperature. To remove the bubbles introduced in the solvent removal processes, the author developed a hydraulic press setup which can effectively eliminate all the bubbles, and this setup is easily accessed in lab conditions.

To understand the origin of the charge separation in this new OLPL system, all the relevant mechanisms that have been proposed since 1996 were considered in Chapters **7** and **8**. It was found that successive two-photon ionisation is the most likely explanation because of three experimental observations: (a). OLPL was not obtained from the TADF emitters with short T_1 lifetimes (4CzIPN and 2CzIPN), suggesting the large T_1 populations play an important role in photo-induced charge separations; (b). OLPL is not generated when the excitation intensity is low, indicating the photo-induced charge separation process involves more than one photon, and so successive two-photon ionisation is the most reasonable explanation; (c). The photoinduced absorption spectrum shows that the T_1 absorption is stronger for photons which have higher energy than that required for the transitions between the T_1 of **CzPhAP** and the LUMO and higher orbitals of the host. On the emission mechanism side, the ejected electrons probably recombine with the positively charge emitter radicals through the mechanism of

continuous-time random walk (CTRW), and so the emission intensity decays follow t^{-m} (0 < m < 1).

Compared with fluorescent emitters and phosphorescent emitters, TADF emitters are particularly suitable for harvesting OLPL through successive two-photon ionisation due to their following properties: a) TADF emitters normally have much higher k_{ISC} compared with fluorescent emitters because the spin-orbit coupling (SOC) between S_1 and T_1 is stronger in TADF emitters (as discussed in Section **4.3**), and so TADF emitters can generate more T_1 in the photoexcitation process. b) The T_1 lifetimes of TADF emitters are usually longer than those of phosphorescent emitters because TADF emitters have weak SOC between T_1 and S_0, which reduces the T_1 loss from the phosphorescence channel. c). TADF emitters are usually designed in rigid structures, which reduces the T_1 loss from non-radiative decay as well. Combining these three properties, TADF emitters make a preferable condition for triplets to accumulate, and the consequent large T_1 population is ideal for photoinduced absorption.

TADF-emitter based OLPL materials still have much to be improved. As has been discussed in Section **8.3.2.2**, photo-induced electrons may come from the transitions between the T_1 of the emitter and the LUMOs of host materials. Therefore, shallower host LUMOs may help to decrease the band gap for the photoionisation during the second photon absorption process. Consequently, a future development of n-type cheap polymer hosts which have shallow LUMOs may help to decrease the photon energy for OLPL photoexcitation and so even green light may be used as the OLPL excitation sources. Shallower LUMOs also help the ionized electrons to be ejected further apart from the emitter ions when using the same excitation wavelength. This contributes to a slower charge recombination process and the subsequent extended OLPL durations. Vice versa, on the emitter side, reducing the HOMO energy levels of emitters will have the same effects. In addition, as long-lived excited states are important, further supressing the non-radiative decays is another pathway for improvement. In addition, in order to enable this new OLPL material to operate in air, encapsulations techniques also need to be developed.

In summary, this thesis presents the study of two groups of new TADF emitters and their applications to OLPL. The discovery of this new class of OLPL emitters not only provides potential applications for TADF emitters that have large ΔE_{ST}s, but also demonstrated the importance of photo-induced charges in TADF emitter doped films, which has never been emphasized before. These new OLPL emitters possess the advantages of low cost, simple moulding, better

mechanical performance, multi-colour selections, which helps the OLPL materials to be commercialized and applied to indoor lightings.

10.2   References

1.   Kabe R, Adachi C. Organic long persistent luminescence. Nature. 2017;550(7676):384–7. Available from: http://www.nature.com/articles/nature24010

2.   Lin Z, Kabe R, Wang K, Adachi C. Influence of energy gap between charge-transfer and locally excited states on organic long persistence luminescence. Nat Commun. 2020;11(1):191. Available from: http://dx.doi.org/10.1038/s41467-019-14035-y

3.   Nishimura N, Lin Z, Jinnai K, Kabe R, Adachi C. Many Exciplex Systems Exhibit Organic Long-Persistent Luminescence. Adv Funct Mater. 2020;30(22):2000795. Available from: https://onlinelibrary.wiley.com/doi/abs/10.1002/adfm.202000795

4.   Jinnai K, Nishimura N, Kabe R, Adachi C. Fabrication-method Independence of Organic Long-persistent Luminescence Performance. Chem Lett. 2019;48(3):270–3. Available from: http://www.journal.csj.jp/doi/10.1246/cl.180949

5.   Jinnai K, Kabe R, Adachi C. Wide-Range Tuning and Enhancement of Organic Long-Persistent Luminescence Using Emitter Dopants. Adv Mater. 2018;30(38):1800365. Available from: http://doi.wiley.com/10.1002/adma.201800365